



Materials and Machine Techniques for Automated Repair of Bituminous Pavements

by

Frank Kofi Asamoah Awuah

A doctoral thesis submitted in partial fulfilment of the
requirements for the award of Doctor of Philosophy in Civil
Engineering at the University of Nottingham

Department of Civil Engineering

Faculty of Engineering

October 2024

“The great thing about this level of automation is that it frees people up. They don’t have to focus on these manual task labour that a machine can do.”

- *Josh Steimle*

“Teams are now doing their jobs faster and easier, a job that would have previously taken two days is now done in less than a day thanks to mistakes or errors being caught in the digital process.”

- *James Monahan*

“Almost all quality improvement comes via simplification of design, manufacturing, layout, processes, and procedures.”

- *Tom Peters*

Abstract

Research has been conducted to evaluate the feasibility of automating crack and pothole repairs in bituminous pavements within a laboratory setting. Traditional manual methods, while effective, are labour-intensive, time-consuming, and prone to variability, underscoring the urgent need for automation to enhance efficiency, precision, scalability, and safety. To address these limitations, machines requiring minimal human input were developed alongside asphalt mixtures tailored for automated applications. A comprehensive review identified 3D printing as an optimal, economical, and user-friendly technology for creating repair machines. Accordingly, a RepRap 3D printer was modified for repair tasks, with parameters such as filling speed and extrusion temperature systematically optimised to improve repair quality.

The research investigated the effects of bitumen type, crack width, irregularity, and hot bitumen flow on the performance of automated crack filling. Results revealed that bitumen flow rate, filling speed, and crack geometry significantly affect fill quality. Specifically, lower temperatures resulted in incomplete filling, while higher temperatures and suboptimal speeds led to overfilling. These findings highlight the critical importance of precisely controlling temperature, flow rate, and filling speed to optimise performance in future fully autonomous robotic systems.

A novel digital methodology, developed using physics engine software with aggregate geometry as a key input, enabled the design of asphalt mixtures tailored to performance requirements such as extrudability, stability, and flow. Validated through independent tests at the Czech Technical University in Prague, the method achieved 78% accuracy in predicting the properties of real mixtures with highly variable compositions. It offers a reliable, performance-based alternative to traditional trial-and-error methods and lays the groundwork for automating asphalt design in road repair operations.

The digital method was further applied to produce asphalt repair cartridges for a screw-extrusion-based automated pothole filling machine, which achieved 86% of the rutting resistance observed in manual techniques. In a transitional phase, this machine could be mounted on trucks for in-situ pothole repairs, providing an immediate and cost-effective solution for practitioners. Over the long term, it has the potential to evolve into advanced, fully autonomous robotic systems, paving the way for more efficient, self-operating road maintenance.

Acknowledgements

- Supervisors:** Nicholas Thom (UoN) and Anand Sreeram (UoN),
for their supervision and intellectual support.
- Internal Assessor:** Carlos Osorio Sandoval (UoN) and Tony Parry, (AtkinsRéalis, former assessor)
for their insightful feedback and guidance.
- Former Supervisor:** Alvaro Garcia Hernandez (RWTH Aachen University),
for his mentorship, supervision and support.
- Collaborators:** Jan Valentin (Czech Technical University) and Mark Miodownik (University College London)
for their invaluable partnership and cooperation.
- Technicians:** Jonathan Watson (Nottingham Transportation Engineering Centre, NTEC, UoN), Richard Blakemore (NTEC, UoN), Martyn Barrett (NTEC, UoN), and Brian Atkinson (X-ray CT specialist, UoN),
whose essential assistance in the lab was invaluable.
- Colleagues:** Mariam Abedraba Abdalla (NTEC, UoN), Rufus Adjetey (NTEC, UoN), Yongping Hu (NTEC, UoN), and Gloria Maruchu (Resilience Engineering Research Group, UoN),
for making the research journey worthwhile.
- Family:** Elvira Pokuah Asamoah,
a budding scholar.
- Funding:** European Union's Horizon 2020 research and innovation program under the Marie Skłodowska-Curie grant, agreement number 765057.

Declaration

The research presented in this thesis was undertaken at the University of Nottingham, specifically within the Department of Civil Engineering at the Nottingham Transportation Engineering Centre (NTEC).

I declare that this work is entirely my own and has not been submitted for a degree at any other university.

Frank Kofi Asamoah Awuah

Nottingham, UK

August 2024

Table of Contents

Abstract.....	ii
Acknowledgements.....	iii
Declaration.....	iv
Table of Contents	v
List of Figures.....	x
List of Tables	xvi
Definition of Keywords.....	xviii
List of Abbreviations and Symbols	xix
List of Publications.....	xx
Chapter 1: Introduction	1
1.1 Background.....	1
1.2 Aims and Objectives	4
1.3 Research Methodology.	5
1.4 Statement of Novelty.....	6
1.5 Thesis Structure.....	6
Chapter 2: Literature Review	9
2.1 Introduction and Structure.....	9
2.2 Overview of Road Transportation in the UK and Its Contribution to Economic Growth.....	9
2.2.1 Road classification system in the UK.....	10
2.2.2 General overview of road maintenance in the UK.....	11
2.3 Road Pavement Structure.....	13
2.3.1 Flexible pavements.....	14
2.3.2 Rigid pavement	15
2.3.3 Composite pavement.....	16
2.4 Asphalt Mixtures	16
2.4.1 Aggregates for asphalt mixtures	16
2.4.2 Bitumen for asphalt mixtures	24
2.4.3 Types of asphalt mixtures.....	26
2.4.4 Asphalt mix design methods.....	28
2.4.5 Asphalt mix design approaches across regions	30
2.4.6 Trends in Asphalt Mix Design	34

2.4.7	Evaluating the workability of asphalt mixtures.....	35
2.4.8	Comparing asphalt mix design methods to flexible pavement design methods.....	38
2.5	Distresses in Asphalt Pavements.....	39
2.5.1	Cracking in asphalt pavements.....	39
2.5.2	Potholes in flexible pavements	54
2.6	Repair of Trenches and Openings in Asphalt Pavements ..	59
2.6.1	Structural integrity of repaired potholes, trenches, and openings.....	60
2.7	Overbanding	61
2.8	Comparing Productivity in Construction to Other Core UK Industries	61
2.9	Automation in Construction and Road Maintenance.....	62
2.10	Additive Manufacturing (3-D printing) of Structures	64
2.10.1	3D printing methods and materials in construction.....	65
2.10.2	Screw extrusion-based additive manufacturing.....	68
2.10.3	3D-printing for road repairs.....	71
2.10.4	Integrating 3D printing with smart technologies in road works.....	72
2.10.5	Major challenges to 3D printing	73
2.11	4D Printing of Structures	73
2.12	Application of Physics Engine in Pavement Engineering....	74
2.13	Literature Review Summary and Its Impact on the Methodology Adopted in the Research	75
Chapter 3: Materials and Methods.....		79
3.1	Introduction	79
3.2	Methods.....	80
3.2.1	Aggregates and bitumen for the asphalt pavement.....	80
3.2.2	Asphalt manufacturing.....	81
3.2.3	The original Prusa MK3 3D printer.....	82
3.3	Methods.....	84
3.3.1	X-ray CT scanning and data processing techniques ...	84
3.3.2	Extraction of crack path and pothole perimeter coordinates.....	86
3.3.3	3D printing process and commands	86
3.3.4	The newly developed workability device	87

3.3.5	Extraction of geometric properties from real aggregates using Image Processing Techniques	91
3.3.6	Generation of virtual asphalt in physics engine and estimation of number of aggregates and volume of mastic.....	92
3.3.7	Design standards.....	95
3.3.8	Standard tests to assess the volumetric and mechanical performance of asphalt and bitumen	95
3.3.9	Statistical derivatives	102
3.4	Summary	106
Chapter 4: Machine Filling of Cracks in Asphalt Pavements.....		108
4.1	Introduction	108
4.2	Laboratory Simulated Cracks in Asphalt Pavement.....	108
4.3	Bitumen for Crack Filling	110
4.4	Developing the ACFM.....	111
4.4.1	The hot-bitumen heating components.....	111
4.4.2	The assembled ACFM.....	112
4.5	The Crack Filling Process	113
4.5.1	Automated crack filling by 3D printing.....	113
4.5.2	Crack filling by hand	115
4.5.3	Determination of the volume of crack filled	115
4.6	Preliminary Assessment of the Flow Rate and Ductility of Extruded Bitumen	116
4.7	Effect of Temperature and Printing Speed on the Volume of Crack Filled with 40/60 Pen-grade Bitumen	118
4.8	Shear Strength of Filled Regular Cracks	120
4.9	Tensile Strength in Filled Regular Cracks	121
4.10	Impact of Crack Widths on Proportions of Crack Volume Filled	121
4.11	Filling in Irregular Cracks with 40/60 Pen-Grade Bitumen	122
4.12	Crack Filling with Polymer-Modified Bitumen	124
4.13	Summary	126
Chapter 5: Digital Design of Asphalt Mixtures		128
5.1	Introduction	128
5.2	Aggregates, Bitumen and Asphalt Mixtures.....	129
5.3	Extracted Geometric Properties from Real Aggregates	134
5.4	Illustration of Virtually Generated Aggregates and Mastic	134

5.5	Properties of the Asphalt Mixtures	136
5.6	Relationships Between Aggregate Geometric Properties, Performance Parameters, Number of Aggregates, and Volume of Mastic	136
5.7	Nomograph for the Design of Asphalt Mixtures	140
5.8	Nomograph validation	143
5.9	Sensitivity Analysis of the Developed Asphalt Design Model	147
5.10	Summary	149
Chapter 6: Machine Filling of Potholes in Asphalt Pavements		151
6.1	Introduction	151
6.2	Development of the Hot-End Screw-Extrusion-Based Asphalt 3D Printer (APFM)	152
6.3	Optimisation of the Operational Parameters of the APFM.....	152
6.4	Measurement of the Extrusion Rate of Mixtures by the APFM	156
6.5	Aggregates and Asphalt Specimens	156
6.6	Laboratory Simulation of Potholes	157
6.7	Development of a Design Model for the Formulation of Suitable Filling Mixtures	159
6.7.1	Creation of virtual aggregates and asphalt mixtures .	159
6.7.2	Performance properties of the asphalt mixtures for pothole filling	159
6.7.3	Assessment of the relationships between asphalt performance parameters, volume of mastic and number of aggregates	160
6.7.4	Creating a nomograph for asphalt design	162
6.7.5	Iterations for the generation of aggregate gradations from the nomograph	164
6.7.6	Validation of digitally designed pothole filling mixtures: comparing nomograph-generated and experimentally tested performances.....	166
6.8	Creation of Asphalt Cartridges	166
6.9	The Extrusion and Pothole Filling Process	168
6.10	Densification of Asphalt Extrudate in Potholes	168
6.11	Pothole Filling by Hand	169
6.12	Evaluation of Filled Pothole Quality	169
6.13	Summary	171

Chapter 7: Conclusions, Future Work and Outlook	172
7.1 Conclusions	173
7.2 Future Works	175
7.3 Outlook	177
References	184
Appendices	210
Appendix A: Gradation and Characteristics of Aggregates Used in the Research	211
Appendix B: Pavement Distresses.....	226

List of Figures

Figure 2-1: Visual representation of road classifications and their administration in Great Britain.	11
Figure 2-2: Average annual maintenance budget allocations and shortfalls in the UK [37].	12
Figure 2-3: Number of potholes filled and cost (£m) (data from 2023/24 financial year)	13
Figure 2-4: Road user compensation claims.	13
Figure 2-5: Section of a typical flexible Pavement.	15
Figure 2-6: Drawings illustrating typical asphalt mixture gradations – well graded, poorly graded and gap graded.	18
Figure 2-7: Aggregate classification based on shape.	19
Figure 2-8: Manual measurement of aggregate shape utilising a Shape Index Gauge in accordance with EN 933-4.	21
Figure 2-9: Illustration of selected geometric properties of coarse aggregates.	22
Figure 2-10: The CAMSIZER 3D particle analyser: (left) side view of the device, and (right) the Dynamic Image Capturing technique.	24
Figure 2-11: Illustration of optimisation of mixture performance to meet cracking and rutting failure criteria.	30
Figure 2-12: Workability measurement of asphalt mixtures from literature: (a) torque wrench with a paddle mixer by Wang et al. [140], and (b) paddle mixer type design by Poeran and Sluer.	36
Figure 2-13: Scattered test data from Poeran and Sluer demonstrate the lower accuracy of paddle mixer test results in measuring workability in HMA.	37
Figure 2-14: Demonstration of problems associated with the paddle mixer type design (a) fine aggregates in HMA segregated and pasted on the container walls, and (b) shear planing in the mixture.	37
Figure 2-15: Asphalt pavement distress interaction.	39
Figure 2-16: Illustration of structural bending and stresses in asphalt pavement from loading.	40
Figure 2-17: Reflective cracking mechanism in flexible pavements.	41
Figure 2-18: Evolution of top-down cracking: (left) scheme in stages, and (right) extracted core of a wearing and binder course.	42
Figure 2-19: Transverse crack of a typical pavement: (a) surface view, (b) pit showing failed CTB, (c) core from the cracked pavement, and (d) cored-profile of in-situ pavement.	42
Figure 2-20: Crack width measurement.	45
Figure 2-21: Induction heating on Dutch Highway A58.	48
Figure 2-22: Asphalt mastic beam containing encapsulated capsules.	48
Figure 2-23: Crack filling by hand using a pour pot.	50

Figure 2-24: Sealzall machine: (a) during longitudinal crack sealing (b) In-lane crack sealing.	51
Figure 2-25: A 3D printing drone developed from the Self-Repairing Cities project at the University of Leeds.	52
Figure 2-26: Vertical Aerospace's electric VX4 flying taxi.	52
Figure 2-27: Illustration of adhesion loss in sealed cracks on site.	53
Figure 2-28: Illustration of the pothole formation process.	55
Figure 2-29: Illustration of the throw-and-go pothole repair method.	58
Figure 2-30: (a) Example of a pothole and (b) a Velocity Spray Injection patching machine filling a pothole.	59
Figure 2-31: Reinstating openings in flexible pavements, (a) ironworks with overbanding, and (b) utility opening.	60
Figure 2-32: Illustration of a settled trench fill (Location: Trent Building, University Park; Date: June 27, 2022).	61
Figure 2-33: Productivity in core UK industries (output per hour worked).	62
Figure 2-34: The robotic Hadrian X for constructing houses.	63
Figure 2-35: Robotic arm installing slab on site.	64
Figure 2-36: Illustration of automated Road Condition Survey from ROMDAS.	64
Figure 2-37: (a) a layer-by-layer arrangement in a concrete 3D printed structure [241], and (b) a 3D printed house by WinSun.	65
Figure 2-38: Extrusion of concrete from a 3D printing nozzle.	67
Figure 2-39: Comparison of FDM 3D printers in the market.	67
Figure 2-40: Comparison of screw-based additive manufacturing with plunger-based and traditional filament-based methods.	69
Figure 2-41: (a) Illustration of die angle and (b) effect of die angle on extrusion force.	70
Figure 2-42: Illustration of an auger in an asphalt paver, captured on site after paving works.	71
Figure 2-43: Spall damage repair using 3D printed concrete: (a) concrete patch produced for the experiment, (b) applying adhesive to the concrete patch, and (c) concrete patch seated in the damaged area.	72
Figure 2-44: 3D printed headwall by Cambridge researchers installed on a section of the A30 road in Cornwall.	72
Figure 2-45: Illustration of the shape changing performance of the 4D printed flower over time.	74
Figure 2-46: Example of a physics-engine-generated virtual aggregate skeleton.	75
Figure 3-47: A flowchart linking the methodologies, chapters, and objectives of the research.	80
Figure 3-48: Aggregate grading curve for SMA-10.	81

Figure 3-49: (a) batching of aggregates, (b) asphalt mixing in accordance with BS EN 12697-35:2016, and (c) manufactured SMA-10 slabs.	82
Figure 3-50: Essential parts of the original Prusa MK3 3D printer.	83
Figure 3-51: The Phoenix v tome x medium (M) ® 240 kV X-ray microCT scanner scanning a beam specimen.	84
Figure 3-52: The Phoenix v tome x large (L) Custom ® 320 kV X-ray CT scanning a block specimen.	85
Figure 3-53: Illustration of porosity analysis for extracting voids from scanned bitumen in cracks.	85
Figure 3-54: G-code extraction for crack paths.	86
Figure 3-55: A detailed dimensional drawing of the penetrometer device (not to scale). ...	88
Figure 3-56: The asphalt penetrometer setup in the laboratory.	89
Figure 3-57: Free body diagram and schematic illustration of the asphalt penetration test.	89
Figure 3-58: Comparison of plunger penetrations with mixing torque across various asphalt mixtures. Inserted device: Illustration of a conventional HMA workability apparatus developed over the years.	90
Figure 3-59: Setup for capturing images of aggregates.	91
Figure 3-60: Illustration of the Image processing steps in ImageJ.	92
Figure 3-61: Geometric projections of typical 8 mm limestone aggregate examined in this research.	93
Figure 3-62: Illustration of the simulation stages used to create the virtual aggregates in the physics engine.	94
Figure 3-63: Illustration of the creation of virtual asphalt models in physics engine software (Unity 3D).	94
Figure 3-64: Bitumen density test with pycnometer.	96
Figure 3-65: Force ductility test setup: (a) force ductility testing machine, (b) filled ductility moulds, and (c) extended bitumen specimen at 400 mm.	97
Figure 3-66: An experimental setup for the shear bond test.	98
Figure 3-67: (a) Experimental setup and (b) free body diagram of the tensile bond test.	99
Figure 3-68: (a) Illustration of the Marshall Stability Tester and (b) a typical Marshall Stability curve.	100
Figure 3-69: Foil-sealed asphalt specimen prepared for bulk density and air void content determination using the sealed specimen method.	101
Figure 3-70: The Wheel Tracking device (Cooper, Ripley, UK) at NTEC.	102
Figure 4-71: A graphical abstract of the automated crack filling investigation with the ACFM	108
Figure 4-72: (a) regular crack in blocks and (b) irregular crack in snapped beam.	109
Figure 4-73: Schematic illustration of a regular crack between identical asphalt blocks. .	109

Figure 4-74: 40/60 pen-grade bitumen pellets.	110
Figure 4-75: Images of extruder components: (a) auger screw attached to stepper motor, (b) band heater, (c) aluminium collar, and (d) funnel-shaped nozzle.....	111
Figure 4-76: The assembled 24 V, 150 W heating chamber.	112
Figure 4-77: Schematic diagram of heating and control systems in the ACFM.	112
Figure 4-78: The ACFM setup.	113
Figure 4-79: 3D printing crack filling process.	114
Figure 4-80: (a) 3D printing in progress to fill a regular crack and (b) the filled crack.	115
Figure 4-81: Crack filling by hand.	115
Figure 4-82: The steady flow rate of 40/60 pen bitumen from the extruder nozzle outlet.	117
Figure 4-83: Comparison between the deformation energy for 3D-printed fills and manual fills.	117
Figure 4-84: Volume of regular cracks filled with 40/60 pen-grade bitumen at different extrusion temperatures and layer printing speeds. The inserted image shows voids trapped in bitumen printed at 160 °C at 1000 mm/min.	118
Figure 4-85: A section of 40/60 pen-grade bitumen in regular cracks printed at 100 mm/min: (a) at 100 °C and (b) at 160 °C.....	119
Figure 4-86: Sections through a 3D printed fill at 1000 mm/min and 160 °C for 40/60 pen bitumen in a regular crack after shear-splitting at 5 °C.....	120
Figure 4-87: Resistance of filled cracks to shear failure for 40/60 pen-grade bitumen: (a) ultimate shear force for filled cracks at 140 °C, 160 °C, and 180 °C at 100 mm/min, and (b) impact of crack volume filled on shear resistance.	121
Figure 4-88: (a) Tensile bond stress for regular cracks filled with 40/60 pen-grade bitumen, and (b) crack-filling volumes for cracks of various widths.	122
Figure 4-89: Isometric view of 3D reconstructed images of 40/60 pen-grade bitumen infill in irregular cracks: (a) 3D printed fill and (b) manual fill.	123
Figure 4-90: Volume of cracks filled with PMB type N1 at a temperature of 180°C at varying printing speeds.	124
Figure 4-91: Tensile bond failure modes in regular cracks filled with PMB type N1 and pulled apart at 5 °C: (a) 3D printing and (b) manual filling.	125
Figure 5-92: An illustration of the asphalt digital design concept using aggregate geometry as a key input.	128
Figure 5-93: Exhibit of selected Marshall specimens for Cat A mixtures.	129
Figure 5-94: Aggregate gradations for predictive modelling specimens: (a) specimen M1 to M14, and (b) specimen M15 to M25 and SMA limits.	130
Figure 5-95: Aggregate gradation for sensitivity analysis specimens: (a) specimen S1 to S8 and (b) specimen S9 to S16.	132
Figure 5-96: A showcase of selected Cat B aggregates.....	133
Figure 5-97: Virtual aggregate gradation example (specimen M8).	134
Figure 5-98: A comparison of real and virtual limestone aggregates for specimen M2....	134

Figure 5-99: An illustration of loose coarse aggregates (> 2 mm) coated with mastic (fines, filler and bitumen mixed) from the physics engine simulation.....	136
Figure 5-100: Impact of aspect ratio on asphalt aggregate content.....	138
Figure 5-101: Relationship between asphalt performance parameters, number of aggregates and volume of mastic.	140
Figure 5-102: Nomograph for the design of asphalt: feasible region defined by performance and SMA limits.	141
Figure 5-103: Nomograph for the design of asphalt: selected coordinates for validation of the nomograph.	142
Figure 5-104: Comparison of virtual and physically manufactured asphalt for specimen V5.	145
Figure 5-105: A comparison between physically measured properties (m) and predicted properties (p) for Cat B mixtures using the developed model.	148
Figure 6-106: A graphical abstract of the automated pothole filling investigation with the APFM.	151
Figure 6-107: Illustration of the (a) spiral feed screw and die angle, and (b) band heater and insulating jacket.	153
Figure 6-108: Assembling the heating system and extruder.	153
Figure 6-109: Illustration of the asphalt extruder mounted onto the 3D printer frame shown in Figure 3-50.	154
Figure 6-110: The complete APFM setup at NTEC during the pothole filling process	154
Figure 6-111: Optimisation of the operational parameters of a DC motor: (a) maximising operating power, and (b) optimising extrusion speed using mixture P8.....	155
Figure 6-112: Aggregate gradation for asphalt specimens, including SMA limits and pothole slabs: (a) P1 to P20, and (b) P21 to P34	157
Figure 6-113: (a) Manufactured slabs, (b) tack-coated base surface, (c) hollow upper slab (core drilling machine inserted), (d) hollow upper slab laid on the base slab, and (e) fully assembled pothole with tack-coated pothole walls.	158
Figure 6-114: Illustration of a pothole: (a) on-site condition and (b) lab simulated.....	159
Figure 6-115: Relationship between number of aggregates, volume of mastic, and (a) extrudability, and (b) stability.	162
Figure 6-116: Nomograph for the design of performance-satisfactory asphalt mixtures for pothole filling.....	163
Figure 6-117: Cumulative gradations for generated aggregates compliant with BS EN 13108-5:2016.	166
Figure 6-118: The asphalt cartridges.	167
Figure 6-119: Cores drilled from filled potholes for the estimation of AVC.....	169
Figure 6-120: Comparative rutting resistance of filled pothole specimens: automated versus hand filling.	170

Figure 7-121: (a) A 3D printing drone prototype developed by Leeds University under the Self-Repairing Cities Project, and (b) an artistic impression of the Robotiz3d road repair robot by the University of Liverpool.....	180
Figure 7-122: Illustration of how a bitumen extruder attached to a repair vehicle for field applications could look in the medium term.	181
Figure 7-123: A futuristic highway scene featuring a robot actively repairing a pothole, with real-time pothole and traffic data provided by a drone.	182
Figure 7-124: Field trial of an autonomous robotic platform in front of NTEC at University Park, University of Nottingham.	183

List of Tables

Table 2-1: Description of selected performance tests on asphalt mixtures.....	33
Table 2-2: Classification of crack density by the MDOT.....	45
Table 2-3: Guidelines for determining the type of maintenance action to take.	46
Table 2-4: Classification of crack filling methods in concrete and asphalt pavements.....	49
Table 2-5: Carriageway pothole response	57
Table 2-6: Comparison of main methods of 3D printing.	66
Table 3-7: Properties of 40/60 pen-grade bitumen used for the asphalt specimen manufacturing.....	82
Table 3-8: Operational parameters of the Phoenix v tome x scanners.	85
Table 3-9: Common G-Code commands used for 3D Printing in this research.	87
Table 3-10: Description of basic data statistics used in the research.	103
Table 4-11: Performance of PMB N1 sealant as supplied by manufacturer.	110
Table 4-12: Crack volume filled with 40/60 pen-grade bitumen and flexural behaviour in irregular cracks.	123
Table 4-13: Crack filling performance of PMB type N1.....	126
Table 5-14: Asphalt mix properties for predictive modelling specimens.	131
Table 5-15: Asphalt mix properties for sensitivity analysis specimens.	133
Table 5-16: Geometric and Weibull characteristics of aggregates.....	135
Table 5-17: Simulated and experimental characteristics of Cat A asphalt mixtures for the predictive modelling.	137
Table 5-18: Simulated and experimental characteristics of Cat B asphalt mixtures for the sensitivity analysis.	138
Table 5-19: Parameters for the fitting equations and goodness of fit.....	139
Table 5-20: Performance limits for the design of asphalt mixtures.	140
Table 5-21: Number of aggregates and volume of mastic for selected coordinates on the nomograph.	143
Table 5-22: Number of aggregates and volume of mastic for different fractions of aggregates, SMA limits and feasible region bounds.....	144
Table 5-23: Generated gradations for validation specimens.	146
Table 5-24: Predictivity of asphalt mixtures' properties designed with the monograph. .	147
Table 5-25: MAPE for physically measured properties compared with digitally predicted properties of Cat B HMA mixtures.....	149
Table 6-26: Parameters for the fitting equations, goodness of fit and design limits.	161
Table 6-27: Number of aggregates and volume of mastic for different fractions of aggregates, SMA limits, and feasible region bounds.....	164

Table 6-28: Number of aggregates and volume of mastic for selected coordinates on the nomograph.	165
Table 6-29: Generated gradations for validation of nomographs.....	165
Table 6-30: Predictivity of performance of asphalt designed with the monograph.	167
Table 6-31: Wheel tracking test results comparing the rutting resistance of automated and hand filled pothole specimens.	170
Table A-32: Gradation of aggregate fractions predominantly used in this research at NTEC.....	212
Table A-33: Geometric and Weibull characteristics of fractions of aggregates at NTEC.	212
Table A-34: Geometric and Weibull characteristics of aggregate fractions provided by the Department of Road Structures, Czech Technical University, Prague.....	213
Table A-35: Characteristics of aggregates for mixtures (Cat A) used in developing the digital design model in Chapter 5. The gradations are also graphically shown in Figure 5-94.	215
Table A-36: Characteristics of aggregates for Cat B mixtures used in validating the digital design model in Chapter 5. The gradations are also graphically shown in Figure 5-95.	217
Table A-37: Characteristics of aggregates for mixtures used in developing the digital design model in Chapter 6.	219
Table A-38: Comparing physics engine output to output from model equations developed in Chapter 5.	222
Table A-39: Properties of asphalt mixtures for the development of a model to select filling mixtures.	223
Table A-40: Simulated and experimental characteristics of asphalt mixtures for digitally designing the pothole-filling mixtures.	225
Table B-41: Cracking types associated with flexible pavements.	227

Definition of Keywords

For the purposes of this research, the following terms and definitions apply.

Aggregates: Crushed stone used in construction. Aggregates form a major part of asphalt and concrete, providing reinforcement to add strength to the overall composite material.

Asphalt Mixtures: A composite material commonly used to surface roads, parking lots, and airports. It mainly consists of aggregates bound together with bitumen.

Automation: The technology by which a process or procedure is performed with minimal human assistance.

Bitumen: A black, viscous mixture of hydrocarbons obtained naturally or as a residue from petroleum distillation. It is used for road construction by being a binder in asphalt.

Crack (in asphalt pavement): A fracture or discontinuation in the pavement surface, which can be caused by stress from traffic loads, thermal fluctuations, and aging of the pavement material.

Extrudability: The ease with which a loose asphalt mixture is extruded from a heating vessel.

Extrusion Rate: The speed at which asphalt mixtures are extruded or pushed. In practice, this is a way of quantifying extrudability.

Flow (of asphalt mixtures): Determines the elasto-plastic characteristics of asphalt, which is considered as the capability of asphalt concrete to adjust to the gradual movements and settlement in the subgrade and underlying layers without cracking.

Machine: A device or system designed to operate with minimal human intervention.

Nomograph: A two-dimensional diagram designed to allow the approximate graphical computation of a function.

Physics Engine: A software component used in computer simulations and video games that simulates physical systems in real-time, including the dynamics of objects in motion, collisions, and other physical phenomena.

Pothole (in asphalt pavement): A depression or hollow in a road surface formed due to the localised failure of the asphalt.

Scalability: The ability of a system, process, or method to efficiently adapt to increased demand, workload, or size without compromising its performance, functionality, or quality.

Stability (of asphalt mixtures): The ability of an asphalt mixture to resist deformation from imposed loads.

Workability (of asphalt mixtures): Refers to the ease with which an asphalt mix can be mixed, placed, compacted, and finished.

List of Abbreviations and Symbols

ABS	Acrylonitrile Butadiene Styrene
ACFM	Automated Crack Filling Machine
APFM	Automated Pothole Filling Machine
A/S	Average in Skip
BS EN	Standard (BS) refers to the national standards of Britain, regulated by the British Standards Institution (BSI). Meanwhile, EN standards denote those adopted by the European community and overseen by the European Committee for Standardisation (CEN).
CMA	Cold Mix Asphalt
Cu	Copper
DGM	Dense-Graded Mix
F	Filter
FDM	Fused Deposition Modelling
HMA	Hot Mix Asphalt
HWMA	Half Warm Mix Asphalt
KV	Kilovolts
M	Volume of mastic (see Chapter 5)
MS	Milliseconds
MV	Volume of mastic (see Chapter 6)
NMAS	Nominal Maximum Aggregate Size (NMAS)
P	Projections
PLA	Polylactic Acid
PMB	Polymer Modified Bitumen
S	Detector Sensitivity
SMA	Stone Mastic Asphalt
SMA 10 surf 40/60	Stone Mastic Asphalt for surface course with maximum aggregates size 10mm and paving grade bitumen 40/60
T	Time
WMA	Warm Mix Asphalt
μA	Microamps
μm	Resolution

List of Publications

Refereed papers in primary journals (from Chapter 4, 5 and 6)

1. Frank K. A. Awuah, A. Garcia, N. Thom. **Automating the repair of potholes using machine techniques and digitally crafted asphalt cartridges**, Construction Robotics 8 (2024).
<https://doi.org/10.1007/s41693-024-00116-y>
2. Frank K. A. Awuah, A. Garcia, J. Valentin. **A digital design method for asphalt mixtures that incorporates aggregate geometry**, Construction and Building Materials 416 (2024).
<https://doi.org/10.1016/j.conbuildmat.2024.135281>
3. Frank K. A. Awuah, A. Garcia. **Machine filling of cracks in asphalt concretes**, Automation in Construction 416 (2022).
<https://doi.org/10.1016/j.autcon.2022.104463>

Contributions to symposia and compiled volumes

1. Frank K. A. Awuah, Alvaro Garcia-Hernandez, Jan Valentin. **A novel performance-based method to design asphalt mixtures**, Proceedings of the Conference Asphalt Pavements, (pp. 50-64), České Budějovice, Czech Republic, November 2023.
<https://svsweb.cz/asfaltove-vozovky/2023/sbornik.pdf>
2. Frank K. A. Awuah, Nick Thom. **Performance-based digital design of asphalt mixtures utilizing the morphology of aggregates**, The 7th Chinese-European Workshop on Functional Pavement, Birmingham, UK, 2023. <https://doi.org/10.1201/9781003387374-32>
3. F. K Awuah, A. Garcia, B. Ghiassi, Yuanyuan Li, M. Torbaghan, R. Jackson, M. Miodownik. **Feasibility of 3D Printing to Fill In-situ Cracks in Asphalt Concretes**, Transportation Research Board, Washington, 2022.
<https://research.birmingham.ac.uk/en/publications/feasibility-of-3d-printing-to-fill-in-situ-cracks-in-asphalt-conc>

Forum:

F. K Awuah (Invited speaker). **Automation of road maintenance**. International innovation forum of doctoral students in road and airport engineering, Tonji University, China, May 2021.

Chapter 1: Introduction

The purpose of this opening chapter is to establish the fundamental groundwork for the entire research. It introduces the central theme of automation within the road maintenance field and offers an outline of the thesis structure.

1.1 Background

Since ancient times, road construction and maintenance have predominantly been manual endeavours. Despite recent technological advancements, this manual nature persists. In the UK, the construction sector is noted for its relatively low hourly productivity compared to key industries such as production, manufacturing, and services [1]. Manual repairs of roads are not only labour-intensive but also expose workers to significant accident risks on highways. Additionally, they generate considerable waste due to lack of precision, result in variable quality dependent on the discretion of the technicians involved, and increase repair costs in some circumstances. For example, in crack filling, labour costs are estimated to account for about 66% of total expenses [2].

Automation in road repair is identified as a crucial solution to address challenges in road maintenance, such as enhancing efficiency, improving safety, ensuring consistent quality, reducing waste, decreasing costs, promoting scalability, and fostering smarter, more sustainable construction practices [3–8]. Reference [9] suggests that the UK could save approximately £15 billion annually by enhancing construction productivity through automation.

In the era of the Fourth Industrial Revolution, marked by a convergence of technologies that blur the boundaries between the physical and digital realms - including robotics, physics engines, sensing, and 3D printing technology - it is surprising that automation in road repair remains nascent, especially when compared to sectors like manufacturing and healthcare. From a pavement engineering viewpoint, the often-inferior quality linked with so-called "automated and improved" repair systems is one of the key reasons for the slow adoption of automation. Even the most advanced repair machines are currently limited to working with cold mix asphalt, which is only suitable for temporary repairs due to its weaker structural performance. Therefore, the effectiveness of these systems relies not just on the sophistication of the robots or machines but crucially on their ability to effectively manage complex materials like bitumen and asphalt mixtures, especially hot mixes. For successful automation, these

materials must be designed to be compatible with machine operations, and the operational and repair parameters of these machines must be comprehensively understood.

Consequently, this research does not pursue the development of highly sophisticated systems comparable to NASA's robotic technologies. Instead, it focuses on engineering more straightforward prototype repair machines at the laboratory scale and advancing digital methodologies for formulating asphalt repair mixtures. This initiative aims to address critical challenges in material design and automated repair techniques within the sector, with a focus on minimising human involvement. Undoubtedly, the results from these feasibility studies have the potential to be applied in subsequent machine up-scaling research, which is aimed at achieving the goal of fully robotic defect repair on asphalt roads in future research endeavours.

Roads are crucial for the transportation of goods and the overall economic development of countries [10]. In 2022, cars, vans, and taxis accounted for 86% of all passenger kilometres travelled for domestic journeys in the UK. Additionally, approximately 81% of freight within the UK was transported by road [11]. About 95% of these UK roads are paved with asphalt mixtures [12]. An asphalt mixture is a composite material primarily consisting of mineral aggregates bound together with a sticky substance called bitumen. These mixtures are designed by selecting the appropriate combination of aggregates and bitumen to achieve desired properties, such as stability under traffic loads.

Although engineered to last a set number of years, it is common for asphalt mixtures to develop defects such as cracks and potholes before their service life is due. These damages can be triggered by repeated loading from vehicles, extreme weather conditions, loss of flexibility due to aging, subgrade settlement, and chemical and oil spills. Cracking refers to the development of fractures in the pavement, while potholes are localised road surface areas that develop surface layer cracks, which subsequently fracture due to the repetitive stress induced by passing traffic, forming a depression with irregular vertical boundaries. Timely crack repairs can prevent the occurrence of potholes and other severe defects.

Both cracks and potholes significantly compromise the safety of road users and reduce the service life of pavements. Cracks allow water to penetrate the inner part of the pavement, causing further defects such as potholes. Potholes remain

a significant and costly challenge to pavement maintenance, posing risks to road safety, vehicle integrity, and economic well-being [13]. As a result, both crack and pothole repairs are classified as routine maintenance [13,14] by road agencies, which implies that they should be repaired at early stages when detected in pavements. In repairs, bitumen is used to fill cracks, while asphalt mixtures are used for pothole repairs. This approach is adopted because asphalt mixtures, being less fluid than bitumen, are unable to effectively fill the "narrow" crevices of cracks. Conversely, bitumen alone does not have the structural integrity required to adequately repair "widely open" potholes.

Current crack filling methods predominantly involve pouring hot or cold bitumen into clean and dry cracks. Hot-pour sealants are typically applied at temperatures above 177°C, while cold-pour sealants are used at ambient temperatures [15]. Hot pour crack filling is known to be more durable than cold pour fillings [16]. Like crack filling, potholes could be filled with either hot or cold asphalt mixtures. Cold filling is less problematic to manage on site, but they are less durable, making hot filling still a preferred option. In most cases, cold asphalt filling or patching are done mainly as emergency or temporary repairs.

Tracing back through history, the desire to automate road repairs began decades ago. One of the early machines that approached automated operations is the Sealzall machine [17], developed in 2009 by the Advanced Highway Maintenance and Construction Technology Research Centre. Since then, there has been little advancement in this area. The Sealzall is simply a truck with a crack filling pour pot attached to the driver side. The driver would have to gauge the pour pot outlet to follow cracks while the liquid sealants drip into the cracks. This made the machine suitable for longitudinal cracks only. Moreover, the accuracy of the filling operation depended on the expertise of the driver. Worse still, the machine was unable to fill in-lane cracks such as fatigue cracking, which are typically made up of a group of interconnected cracks. In such situations, the in-lane cracks were filled manually with a hose and nozzle, making the repair process still largely manual.

Pothole repair, on the other hand, has perhaps seen greater advancement in the last decade. Advanced machines such as those cited in references [18,19] utilising spray injection techniques [14], have emerged in the road industry. However, like the throw-and-go method, spray injection techniques [20] simultaneously blow bitumen emulsion and aggregates into potholes [21], a

technique generally characterised by its lower durability and predominance in temporary or emergency repairs [22]. Also, the nozzle of these spraying machines has to be manually oriented by labour gangs. As such, the development of a machine that can automatically follow and fill cracks and potholes remains a gap in the road construction industry's toolkit.

In this research, modified RepRap 3D printers are utilised as laboratory machines due to their capability to handle large payloads, follow complex shapes, maintain consistent operational temperatures and speeds, and their simplicity and cost-effectiveness. An automated crack filling machine (ACFM) has been constructed using a modified 3D printer outfitted with a bitumen dispenser. Similarly, automated pothole filling machines (APFMs) have been developed by adapting a 3D printer with a screw-based extruder, which functions similarly to the augers used in asphalt pavers in the field. These extruders are equipped with heating bands that heat solid asphalt pieces, referred to as asphalt cartridges, whilst the integrated screws push the heated asphalt through the nozzle outlet into the pothole.

Although hot-mix asphalt is preferred for its enhanced durability in road repairs, the challenge of formulating it to be extrudable by autonomous machines while still meeting standardised volumetric and mechanical performance criteria remains a significant gap in the field. Commonly, mixtures that are extrudable or pumpable are associated with compromised durability [23,24]. Moreover, for an effective autonomous system applicable in future scenarios, machines should be capable of autonomously selecting optimal asphalt recipes, particularly the right proportions of aggregates and bitumen, with minimal human oversight. This necessitates a new digital design methodology that can reduce the reliance on time-consuming and labour-intensive physical and mechanical tests to ascertain the properties of new asphalt mixtures. This research has tackled this challenge by incorporating a physics engine [25–28].

1.2 Aims and Objectives

The primary objective of this research was to develop prototype automated machines for filling cracks and potholes that require minimal human intervention in the laboratory, and to compare the quality of their automated repairs with that of manual repairs.

To achieve this aim, the following objectives (OB) were developed:

- OB 1: Develop a modified bitumen 3D printer and demonstrates its ability to follow regular and irregular cracks in asphalt pavements and fill them with hot modified and non-modified bitumen.
- OB 2: Develop a digital design method to rapidly design asphalt mixtures that can be extruded with screw-based pothole filling machines and meet industrial quality standards.
- OB 3: Develop a pothole filling machine and demonstrate its ability to extrude hot mix asphalt (developed in OB 2) to fill lab-simulated potholes.
- OB 4: Investigate the quality of automated crack and pothole fills in objectives OB 1 and OB 3 and compare their performance to manual repair methods.

1.3 Research Methodology

This research adopts a multi-faceted methodology aligned with the objectives outlined in [Section 1.2](#). A modified RepRap 3D printer served as the core repair machine, equipped with a customised hot-end extruder to function as an autonomous arm for both crack- and pothole-filling applications. Utilising Fused Deposition Modelling (FDM), the printer applied a layer-by-layer material extrusion technique for repairs, with movement and operational parameters like printing speed controlled via Repetier 3D printing software [29].

For quality assessment, manual crack and pothole repair methods were used as controls. Objective 2, focusing on digital asphalt design, incorporated a physics engine [26,30,31] to simulate asphalt performance. This involved extracting aggregate geometric properties using image processing, generating virtual asphalt models, and validating results against traditional laboratory designs from Nottingham Transportation Engineering Centre (NTEC) and Czech Technical University (CTU).

Asphalt mixture preparation adhered primarily to British Standards. Where deviations or novel methods were required, these were fully justified. For example, a bespoke penetrometer was developed to evaluate asphalt workability under specific conditions. Performance tests, including shear bond strength, tensile bond strength, wheel tracking, and X-ray CT scanning, were

employed to assess the integrity of crack and pothole repairs.

Finally, statistical tools such as regression analysis and performance metrics (R-squared, RMSE) provided quantitative validation of experimental findings.

These methodologies are systematically aligned with research objectives and visually summarised in [Figure 3-47](#) to ensure coherence and reproducibility.

1.4 Statement of Novelty

The research has demonstrated the viability of automating the repair of cracks and potholes in asphalt pavements using hot bitumen and asphalt mixtures, achieved through 3D printing technology and digital design of repair asphalt mixtures. Specifically, this research showcases innovation in the following areas:

1. 3D Printing to fill cracks in asphalt pavements.¹
2. Automation of pothole filling with screw-extrusion based 3D printers using digitally crafted hot-mix asphalt cartridges.¹
3. A new Data-Driven digital approach for selecting aggregates and bitumen content in hot-mix asphalts. This method aims to reduce the need for time-consuming and labour-intensive physical and mechanical tests to determine the properties of new asphalt mixtures. Additionally, it can be integrated into future robotic systems, enabling automatic and on-demand production of repair asphalt mixtures with tailored functionalities.
4. A new penetration device for measuring the workability of asphalt mixtures.

1.5 Thesis Structure

The contents of the remaining chapters in the thesis are briefly described below:

Chapter 2: Literature Review

This chapter presents a comprehensive overview of the state of the art in several key areas: the status of road networks in the UK, the deterioration of asphalt roads, defect evaluation, conventional methods for repairing road defects, the application of additive manufacturing (3D printing) in civil infrastructure development and maintenance, the use of autonomous systems

¹ Lab-scale repair machines developed in this research can be upscaled by the industry and attached to repair vehicles.

in construction and maintenance, and the application of physics engines in addressing engineering challenges. The review concludes by identifying gaps in the field of automated road repairs that require further attention and by discussing critical knowledge from the literature that could be leveraged to address these challenges.

Chapter 3: Materials and Methods

This chapter describes asphalt materials, including aggregates, fillers, and bitumen, used in specimen manufacturing processes. It also covers crack filling materials, the additive manufacturing process, and a description of the Original Prusa MK3 3D Printer adopted for modification. Additionally, the chapter provides details on the design standards used in this research, as well as a description of the analytical methods and statistical derivatives applied in the data analysis.

Chapter 4: Machine Filling of Cracks in Asphalt Pavements

This chapter covers the development of the ACFM and examines how filling speed, temperature, bitumen type, crack width, crack irregularity, and the flow of hot bitumen affect the quality of filled cracks. It also presents details of the commercial sealants that were used in the crack filling work. A detailed analysis of the characterisation of filling quality in terms of porosity, shear, and tensile strength is also presented. Additionally, a comparison is made between the quality of cracks filled by automated techniques and those filled manually, establishing the feasibility of automated crack filling techniques.

Chapter 5: Digital Design of Asphalt Mixtures

This chapter introduces a new digital asphalt mix design method that streamlines the traditional process using physics engine software. It ensures that mixtures selected for use in the APFM (see [Chapter 6](#)) are extrudable (easily dispensed from the extruder) and adhere to industrial standards, including Marshall stability, Marshall flow, and AVC limits. This method is applicable not only to automated repair mixtures but also to everyday asphalt design.

The section also covers the validation of the newly developed design method using experimental mixtures independently verified through physical testing at the Department of Road Structures at the CTU in Prague.

Chapter 6: Machine Filling of Potholes in Asphalt Pavements

This chapter details the development of an Automated Pothole Filling Machine (APFM) and the optimisation of its operational parameters to improve the filling of lab-simulated potholes. The APFM consists of a 3D printer equipped with an extruder that heats asphalt cartridges (manufactured asphalt mixtures cut into pieces) and expels the heated material through the extruder nozzle into potholes. The chapter provides a detailed account of how potholes were simulated in the laboratory. Additionally, the quality of the potholes filled automatically has been assessed using the Hamburg Wheel Tracking test and compared with those filled manually.

Chapter 7: Conclusions, Future Work and Outlook

This chapter provides a summary of the main conclusions from the research, along with recommendations for future research. Additionally, the Outlook section provides a comprehensive view of the implications of this research's findings and their relevance to both future upscaling research efforts and real-world applications.

Chapter 2: Literature Review

2.1 Introduction and Structure

This literature review examines four key areas crucial to the development of materials and techniques for the automated repair of bituminous pavements.

First, it provides a comprehensive overview of road transportation in the UK, emphasising its critical role in supporting economic growth and the necessity of timely, efficient defect repairs. Additionally, it examines the structural composition of asphalt pavements and the formulation of asphalt mixtures.

Second, it explores the nature of defects in asphalt pavements and compares manual and automated repair methods. The strengths and limitations of both approaches are assessed, offering insights for enhancing the efficiency and durability of automated repair systems.

Third, the review investigates emerging automation technologies, with particular emphasis on the application of 3D printing in pavement repair. It evaluates how additive manufacturing can enhance repair automation by drawing parallels with its successful use in concrete construction and other infrastructure applications. Additionally, the potential for 3D printing to streamline repair processes, increase precision, and reduce manual intervention is assessed.

Finally, the review evaluates the application of physics engines in simulating asphalt mixture behaviour, optimising the design of repair materials, and supporting the digitalisation and streamlining of material development for pavement repairs.

Throughout the review, key gaps in current automated repair technologies and insights from conventional repair practices are identified. The chapter concludes by discussing how these findings inform the methodologies adopted in this research, particularly in developing more workable and durable automated repair mixtures, such as those used for pothole filling in bituminous pavements.

2.2 Overview of Road Transportation in the UK and Its Contribution to Economic Growth

Road transportation is integral to the UK's economic vitality, influencing various sectors both directly and indirectly, and is essential for sustaining economic growth and development. The extensive network of motorways and roads spans

the entire region, facilitating the safe, reliable, and efficient movement of people and goods [10]. In the UK, roads carry over 86% of passenger travel and about 81% of domestic freight [11]. Consequently, investments in road infrastructure are seen as vital economic stimulators. Maintaining, renewing, and improving road networks makes journeys safer, more reliable, and more efficient [10]. Furthermore, improved road infrastructure attracts foreign investment and supports tourism, further bolstering economic growth [10,32,33]. Different ranks of road infrastructure have varying impacts on the economic fabric of a nation; consequently, road networks in the UK are systematically classified to strategically prioritise their development and maintenance.

2.2.1 Road classification system in the UK

The UK road classification system categorises roads based on their function, importance, and traffic volume. The various classes include motorways, A roads, B roads, and minor roads. This classification is crucial for road management, maintenance prioritisation, and strategic planning to ensure efficient traffic flow and safety across the country. The roads are either centrally managed or locally managed.

Centrally managed roads are typically major routes and highways that form part of the Strategic Road Network (SRN) [34]. This includes motorways and some major A roads (trunk roads) designated as part of the national transportation network. Responsibility for centrally managed roads lies with national agencies such as National Highways in England, Transport Scotland in Scotland, and the Welsh Government in Wales. Maintenance, upgrades, and investment decisions for centrally managed roads are made at the national level, with a focus on ensuring connectivity, safety, and efficiency for long-distance travel and freight movement.

On the other hand, locally managed roads are typically under the jurisdiction of local authorities, such as county councils or unitary authorities. Local roads include residential streets, minor roads, and some A and B roads within urban and rural areas. Local authorities are responsible for the maintenance, repair, and improvement of these roads, including pothole repairs, signage, and traffic management.

The total length of roads in Great Britain was recently estimated to be 247,800 miles. Major roads in Great Britain cover 31,900 miles, consisting of 2,300 miles of motorway (99% trunk, 1% principal) and 29,500 miles of 'A' road (18% trunk,

82% principal). Additionally, there were 216,000 miles of minor road in Great Britain, comprising 18,900 miles of 'B' road and 197,100 miles of 'C' and 'U' roads [35]. [Figure 2-1](#) illustrates the UK road classification structure.

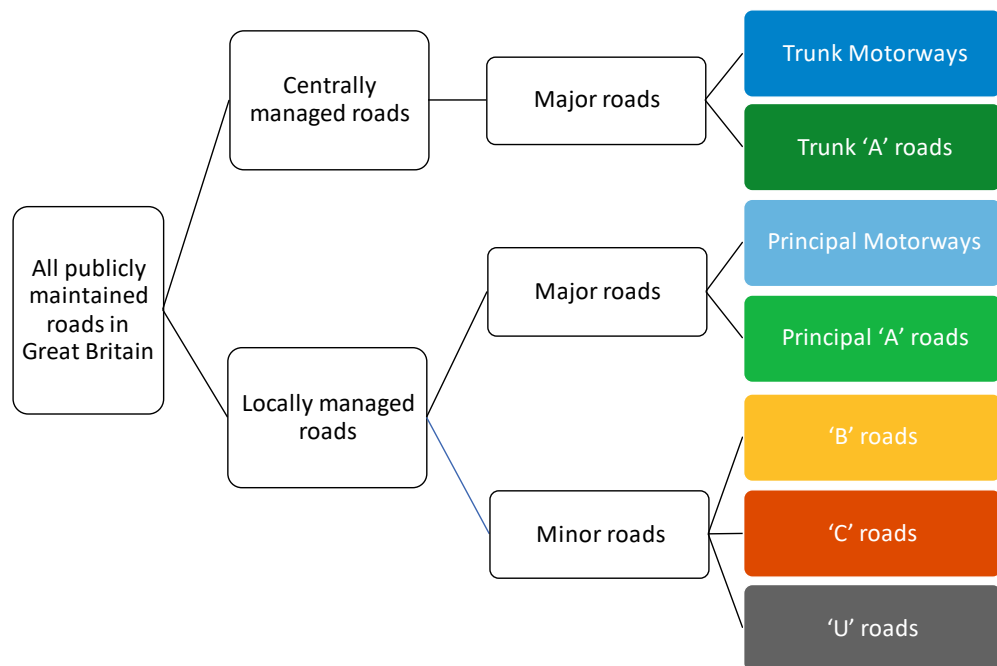


[Figure 2-1: Visual representation of road classifications and their administration in Great Britain \[36\].](#)

2.2.2 General overview of road maintenance in the UK

A review of literature on road maintenance in the UK reaches a definite conclusion – resources for road maintenance by road authorities are stretched [37,38]. Specifically, reference [37] indicates that local road authorities will require approximately 10 years to clear carriageway maintenance backlogs in the UK, at a one-time cost of £16.3 billion. Although the ALARM Surveys [37,38] attribute this backlog to shortfalls in budgets (see [Figure 2-2](#)), it is apparent, from the technical point of view, that both the techniques and materials used for pothole repairs need to be reevaluated.

Pothole repairs constitute a significant portion of this backlog, with 2 million potholes filled each year between 2020 and 2023 - up more than 40% from 1.4 million in the previous year, equivalent to one repair every 16 seconds in England (including London) and Wales. The 2024 Alarm survey [37] reports that the rise in repairs correlates with increasing weather-related damage across the road network, including floods and landslides. Be that as it may, the cost disparity between planned and reactive pothole repairs is evident in [Figure 2-2](#), with the average repair cost now £72.26. Consequently, the total expenditure in

England and Wales last year was approximately £143.5 million, a 50% increase from £95.6 million, illustrating the combined effects of more frequent repairs and recent inflation spikes.

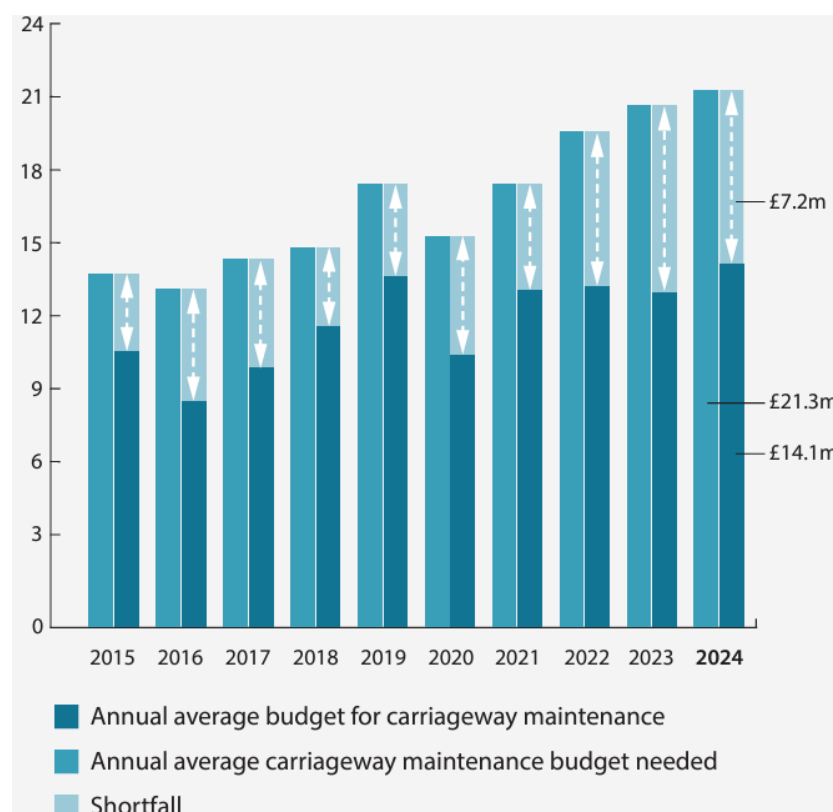


Figure 2-2: Average annual maintenance budget allocations and shortfalls in the UK [37].

The growing prevalence of potholes on UK roads is exerting pressure on the maintenance budgets of road authorities (as depicted in Figure 2-3) and driving up road user compensation claims (illustrated in Figure 2-4). In the 2023/24 financial year, local authorities in England and Wales experienced an 80% increase in the average number of claims per authority, reaching 421, with 89% directly related to potholes. This increase in claims has led to a 31% rise in compensation payouts, now averaging £15.2 million per authority. An additional £13.6 million was spent on staff costs to handle these claims, pushing the total expenditure on claim-related issues to £28.8 million across England, London, and Wales - a 27% increase from the previous year's £22.7 million. This amounts to £142.15 paid out per mile of road in 2023.

From the preceding considerations, the pothole problem on UK roads presents not only safety and health concerns but also significantly impacts the UK economy.

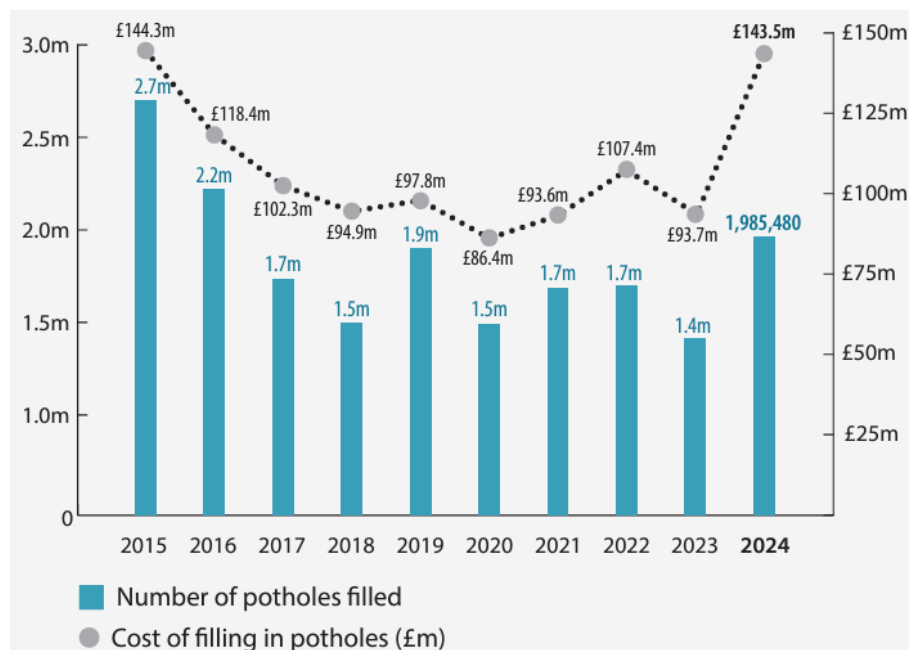


Figure 2-3: Number of potholes filled and cost (£m) (data from 2023/24 financial year) [37].

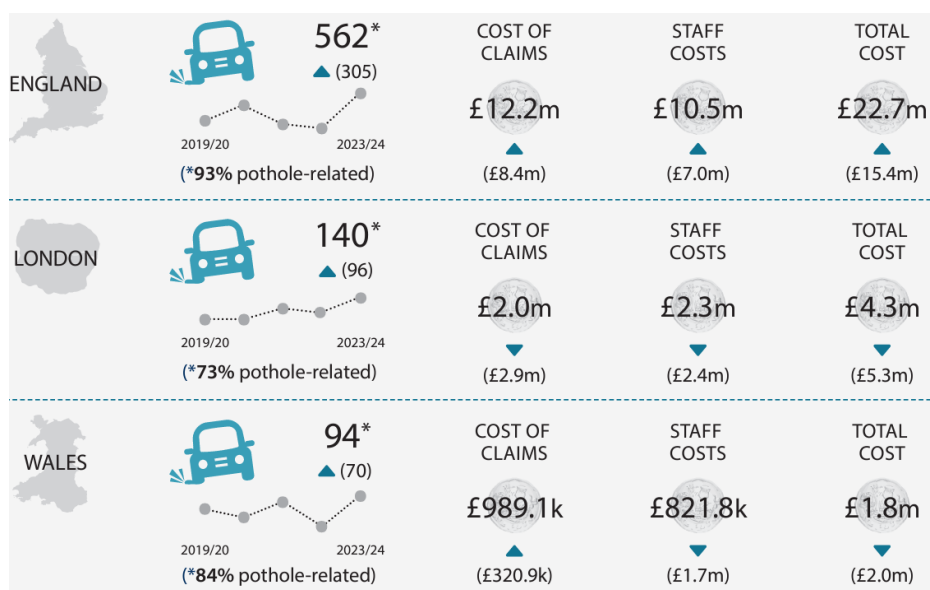


Figure 2-4: Road user compensation claims² [37].

2.3 Road Pavement Structure

A road pavement comprises layers of processed materials placed atop the natural soil subgrade. Its primary function is to distribute the vehicle loads applied to the top layer to the underlying layers and eventually to the subgrade.

² Average number of claims per authority in the past year and the total cost (£) of handling these claims (previous year's figures in brackets for 2022/23).

This ensures that the transmitted stresses from wheel loads are adequately reduced, preventing them from exceeding the bearing capacity of the subgrade [39,40].

The pavement structure should be able to provide a surface of acceptable riding quality, adequate skid resistance, effective drainage, and durability against weathering and traffic wear [40,41]. Road pavements are categorised as flexible pavement, rigid pavement, and composite pavement based on their structure and material compositions, which influence the way traffic loads are distributed to the subgrade.

2.3.1 Flexible pavements

Flexible pavements are typically constructed using bituminous materials and employ surface treatments [41,42] or asphalt courses [42,43]. These pavements distribute wheel load stresses through grain-to-grain transfer, allowing for multiple layers to accommodate varying stress levels. The top layer requires high quality to withstand maximum stress and wear, while lower layers can use lower-quality materials. Design considerations focus on overall performance and stress management within allowable limits for each layer. Due to the flexible nature of these layers, deformations in the subgrade and lower layers can manifest in the top layers of the pavement. Key components of an asphalt pavement include the following:

Surface Course: The topmost layer of the pavement, designed to provide skid resistance, ride quality, and drainage. This layer also facilitates the efficient removal of surface water to prevent water-induced damage and pavement deterioration. Additionally, it ensures a smooth and comfortable driving experience by minimising surface roughness and irregularities. Due to their direct contact with vehicle wheel loads and exposure to weather conditions, most pavement deterioration - such as cracking and potholes, which are the focus of this research - develop within this layer.

Binder Course: This course or layer is located beneath the surface course and serves as an intermediate layer between the surface and base courses. It is composed of bitumen mixed with aggregates, providing structural support and flexibility.

Base Course: This layer is positioned beneath the binder course, responsible for distributing traffic loads and preventing deformation. It is typically

constructed using aggregates of varying sizes bound together with bitumen or cement.

Subbase: Situated below the base course, serves as a transition layer between the pavement structure and the subgrade. It comprises coarse aggregates or recycled materials, offering additional support and drainage capabilities.

Subgrade: The natural subsoil or prepared foundation beneath the pavement layers provides load-bearing capacity. Although this layer receives the least loading from traffic, it requires proper stabilisation to minimise settlement and deformation under traffic loads. If too extreme, its deformation can lead to damage of all the entire pavement structural layers that sit on top of it.

Figure 2-5 shows the layers that makes up a typical flexible pavement.



Figure 2-5: Section of a typical flexible Pavement³.

2.3.2 Rigid pavement

Rigid pavements are typically composed of cement concrete or reinforced concrete slabs. These pavements exhibit substantial rigidity and modulus of elasticity, facilitating the dispersion of loads over a wide soil area. Unlike their flexible counterparts, minor fluctuations in subgrade strength exert minimal influence on the structural resilience of rigid pavements. In the design of rigid pavement systems, the paramount consideration is the flexural strength of concrete, superseding subgrade strength [44]. This property enables the concrete slab to effectively bridge localised subgrade deficiencies and regions with inadequate support, thereby upholding pavement integrity.

³ Asphalt Investigations: <https://www.guidelinegeo.com/asphalt-investigations/>

2.3.3 Composite pavement

Composite pavements combine the benefits of both flexible and rigid pavement systems. They utilise a combination of materials and layering techniques to provide enhanced performance and durability. The concrete base layer provides structural capacity, while the asphalt surface layer serves as the wearing surface course [45,46]. By combining the properties of both layers, composite pavements can achieve greater strength and longevity, offering a practical solution for various road conditions [45].

2.4 Asphalt Mixtures

An asphalt mixture is a composite material that is commonly used to construct the structural layers of roads, parking lots and airports. In the UK, these mixtures are designed predominantly in accordance with the BS EN 13108 standards [47], which ensure consistency and quality in asphalt mixtures for various applications. The aggregates form a solid skeleton that provides the required compressive strength, while the bitumen keeps the aggregates together. The smallest aggregates, for example, those under 2 mm and the filler (<0.063 mm) [48], help fill the space between the biggest aggregates [49]. The aggregate gradation, filler content, bitumen type, and amount are carefully selected to provide the best cost, strength, resistance to loading and environmental degradation, and vehicle traction. Then, the aggregates and the bitumen are mixed at an asphalt plant and compacted onsite to provide a stable solid skeleton that can carry loads by interlocking the aggregates [50]. An asphalt mixture typically consists of 90-95% aggregates (by mass) and 5-10% bitumen [43]. To meet increasing traffic demands, asphalt mixtures are increasingly nowadays modified with materials such as fibres to enhance their mechanical properties [51]. Also, moving towards a sustainable approach, existing asphalt is now being recycled for reuse. Furthermore, to achieve specific asphalt properties such as enhanced traffic noise reducing abilities, some additives may be added to the asphalt mixture. An example is a rubberised asphalt which is made by blending crumb rubber (finely ground scrap tires) into an asphalt mixer [52–54]. Also, asphalt may be coloured for aesthetics and to reduce heat absorption [55–57].

2.4.1 Aggregates for asphalt mixtures

Aggregates in asphalt mixtures are selected based on their ability to form a stable skeleton, ensuring load-bearing capacity and effective interaction with

bitumen for enhanced durability and strength. The BS EN 13108 standards [47] provide detailed guidelines for the selection of suitable aggregates and fillers, ensuring optimal performance for specific asphalt types used in roads, airfields, and other trafficked areas.

These aggregates can be of different mineral origins, which causes them to have different shapes. Their proportions are selected based on the ranges outlined in the BS EN 13108 standards [47], such as aggregate gradation. However, these ranges are flexible to accommodate the varying shapes of local aggregates, which influence how the aggregates pack together. The shape of the aggregates is described by properties like Feret diameter, chord length, aspect ratio, area, perimeter, sphericity, shape factor, form factor, flatness, elongation, and roundness, among others [58]. These morphological characteristics are known to affect key pavement properties, including crack and skid resistance [59], stability [60], workability [61], and compactibility [62].

Aggregates used in asphalt mixtures can be either natural or artificial. For instance, natural coarse aggregates are typically sourced from crushed rock or natural gravel, while artificial coarse aggregates, such as slag, calcined bauxite, and synthetic materials, are also commonly used. Similarly, fine aggregates are derived from crushed rock fines or natural sand. In addition, common fillers like hydrated lime, Portland cement, and limestone dust are used to enhance the mixture's performance.

Moreover, recycled aggregates, sourced from construction and demolition waste, serve as secondary aggregates and have been widely used in the UK, as reflected in standards like PD 6691:2022 [63]. Consequently, these materials promote sustainability by reducing reliance on natural resources while maintaining comparable durability and stability when properly processed [64].

Various properties of aggregates employed in asphalt mixtures include gradation, particle shape, strength, durability, specific gravity, unit weight, absorption, volume stability, and the presence of deleterious components.

Gradation of aggregates

According to the American Society for Testing and Materials (ASTM), gradation refers to the particle size distribution within a set of aggregates [65]. While the required gradations for asphalt mixtures are not fixed, acceptable limits are specified. The traditional approach to measuring aggregate gradation is through

sieve analysis. Depending on the type of gradation, this process results in different percentages of voids between mineral aggregates, tailored to meet specific design requirements in asphalt mixtures. Gradation specifications can vary slightly across regions, with notable differences in terminology between Europe, the United States, and other non-European countries. For example, the ASTM standard uses a 2.36 mm sieve to distinguish fine from coarse aggregates, whereas the European Committee for Standardisation (CEN) defines this division at 2.00 mm [47,65].

There are three typical gradation types for asphalt mixtures: well-graded, which includes a full range of particle sizes; poorly graded, which has a uniform particle size distribution; and gap-graded, which excludes a range of medium-sized particles. Figure 2-6 illustrates these gradation types.

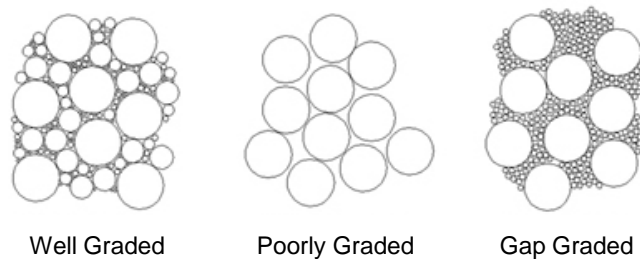


Figure 2-6: Drawings illustrating typical asphalt mixture gradations – well graded, poorly graded and gap graded [66].

When describing the sizes of aggregates in gradations, Maximum Size and Nominal Maximum Size are often used. Maximum size represents the largest particle size present in the aggregate, while nominal maximum aggregate size (NMAS) represents the sieve size through which most of the aggregates pass. Superpave (Superior Performing Asphalt Pavements) [67,68] specifies the maximum aggregate size as one sieve larger than the nominal maximum size. Additionally, it defines the nominal maximum aggregate size as "one sieve size larger than the first sieve to retain more than 10 percent of the material."

The maximum aggregate size can impact asphalt mixtures in various ways. For instance, instability may occur when the maximum aggregate size is too small, whereas excessively large sizes can lead to poor workability and/or segregation [69]. A previous study examining the effect of the maximum nominal aggregate size (NMAS) on Stone Mastic Asphalt (SMA) performance demonstrated that increasing NMAS enhances the mixture's resistance to deformation and rutting [70]. Conversely, decreasing NMAS helps to prevent cracking and ravelling. Furthermore, reducing NMAS brings aggregate particles closer together,

thereby resulting in fewer voids in the mix. This reduction in voids subsequently decreases the permeability of the mix, as fewer pathways are available for water infiltration through the pavement.

Therefore, the gradation of coarse aggregates significantly influences various characteristics of bituminous mixtures, including workability, stability, flow, permeability, and economy. Consequently, it is essential to thoroughly understand how changes in aggregate size distributions affect the performance of asphalt mixtures [71,72].

Classification of aggregate shapes

Aggregate is classified according to shape as rounded, irregular or partly rounded, angular, flaky, elongated, and flaky and elongated [73]. These shapes have been illustrated in Figure 2-7. Changes in aggregate shape influence the volumetric and mechanical performance of the structures they form, such as asphalt mixtures [59,74–78].

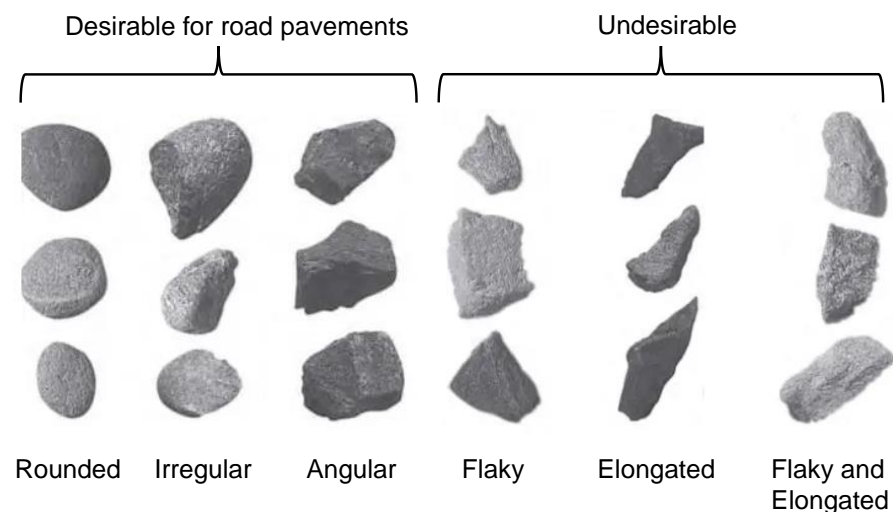


Figure 2-7: Aggregate classification based on shape.

Also, the presence of flaky, elongated, and flaky and elongated aggregates can compromise the integrity, durability, and long-term performance of asphalt mixtures. Consequently, most regulations have restrictions with respect to these undesirable aggregates as they can break during compaction, changing the gradation and voids percentage in the mixture. Aggregate shape properties, such as aspect ratio (AR), denote the relative prevalence of the two characteristic surfaces of aggregates and are typically defined as the ratio of the minor axis dimension to the major axis dimension, or vice versa [79]. This aspect affects the arrangement of aggregates in asphalt mixtures. AR is also

considered a key geometric parameter for optimising the performance of granular materials. Generally, high AR nanomaterials have been found to impact granuloma induction in biomedical science, while high AR fibres in self-compacting concrete enhance tensile and fracture strength. Therefore, accurately quantifying aggregate geometric properties, such as AR, is vital for selecting appropriate aggregate gradations and achieving desirable properties or performances of asphalt mixtures. Generally, it is essential to use well-graded aggregates with predominantly cubical or angular shapes to ensure the quality and longevity of bituminous pavements [80,81]. Also, different proportions of these aggregates may be combined to meet optimised mixture properties such as meeting workability and stability requirements. Below are definitions for each aggregate shape category:

Rounded aggregates: Smooth-surfaced aggregates formed by natural erosion, typically used in low-resistance concrete due to their low void percentage (32-33%), ensuring good workability [80].

Irregular or partly rounded aggregates: Created through attrition, these aggregates have a slightly higher void percentage than rounded aggregates, offering slightly more resistance but still unsuitable for high-strength cements or asphalt mixtures [80].

Angular aggregates: Defined by well-defined edges, obtained through crushing methods. They yield a high void percentage (38 - 45%), enhancing compression resistance through better interlocking between aggregate and mortar. Although less workable, they are suitable for high-strength concrete and ideal for asphalt mixtures due to high internal friction and excellent adhesion [73,80].

Flaky aggregates: Aggregates with thickness much smaller than length and width, typically considered flaky when thickness is around 60% less than average size, although specifications may vary [80].

Elongated aggregates: Classified as aggregates with length 180% greater than average dimension.

Flaky and elongated aggregates: Aggregates possessing both flaky and elongated properties.

Methods for measuring aggregate geometry

Manual techniques [82] and Digital Image Processing (DIP) [78,83,84] are common methods for measuring aggregate geometry, each introducing distinct indices to quantify size and shape at macro, meso, and microscales. However, both methods come with limitations. For example, manual measurement entails assessing the length, width, and thickness of individual aggregates, often using a shape index gauge, as shown in Figure 2-8. While this approach offers high accuracy, it is labour-intensive and generally reliable only for aggregate sizes exceeding approximately 4 mm.

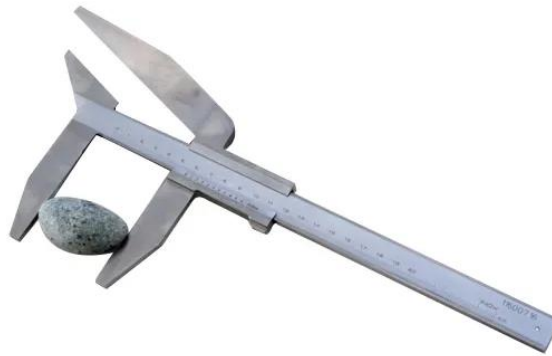


Figure 2-8: Manual measurement of aggregate shape utilising a Shape Index Gauge⁴ in accordance with EN 933-4.

Digital Image Processing (DIP) methods are increasingly popular for aggregate shape characterisation due to their simplicity compared to manual techniques. Two-dimensional (2D) characterisation, for instance, involves analysing images of aggregates taken from a top-down perspective, which efficiently captures aggregate shape with minimal manual intervention. While 2D characterisation provides valuable insights, it may not fully represent the complexity of aggregate morphology, often requiring complementary three-dimensional (3D) analyses to achieve a comprehensive understanding.

Three-dimensional characterisation, however, necessitates specialised equipment, which can be costly, thus limiting its widespread application. Recently, advanced digital imaging technologies have been developed and commercialised, such as the Aggregate Imaging System (AIS) [85]. Furthermore, techniques like computed tomography (CT) [86] and three-dimensional laser scanning [87] offer highly detailed representations of aggregate morphology, elevating characterisation capabilities to a new level.

⁴Geotechnical Testing Equipment: <https://geotechnical-equipment.com/product/shape-index-gauge/>

Despite their potential, these advanced methods are relatively new to the field, and they require the development of new characterisation indices to fully utilise their capabilities.

Figure 2-9 illustrate some basic geometric properties of aggregates.

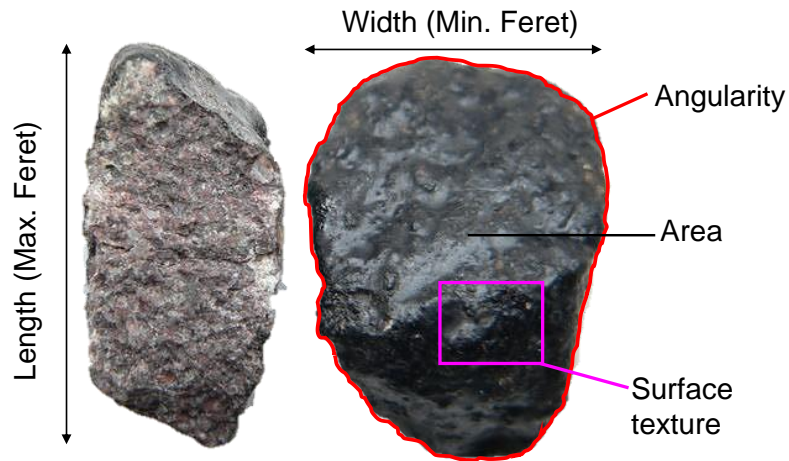


Figure 2-9: Illustration of selected geometric properties of coarse aggregates.

Digital image analysis methods and equipment

ImageJ image analysis software

ImageJ (also called Fiji) is a popular open-source software extensively employed for visualising, examining, quantifying, and validating scientific image data [79]. It was developed by Wayne Rasband at the National Institute of Health in 1987 [81]. BioVoxxel plugin, developed by Jan Brocher [88], can be employed in ImageJ to compute representative shape factors for aggregates. The plugin includes functions such as the extended particles analyzer [88], which calculates the morphological parameters of aggregates.

Aggregate Imaging System (AIMS)

The AIMS measures the angularity, shape, and texture of coarse aggregates and fines. It analyses aggregate particle characteristics distribution, utilising a microscope, light, and software. AIMS employs 3D analysis to identify flat and elongated particles and uses wavelet methods for shape and texture quantification. A video-microscope is utilised to measure the depth of aggregates to obtain the third dimension. Particle projections for shape measurement are derived from 2D images [89].

University of Illinois Aggregate Image Analyzer (UIAIA)

The University of Illinois Aggregate Image Analyzer (UIAIA) has gained prominence for assessing particle morphology. This innovative technique involves capturing images of coarse aggregates and applying segmentation algorithms within the UIAIA system. By analysing these images, the method quantifies both particle size and shape. Notably, UIAIA focuses on two-dimensional image analysis, distinguishing it from previous approaches. In addition to UIAIA, other static methods have been explored by researchers for aggregate characterisation. These include Fernlund's method and another developed by Texas-Austin. Interestingly, these less popular methods operate in a manner similar to the UIAIA approach [81,90–92].

The UIAIA system employs specifically developed algorithms to characterize the flat and elongated ratio (F&E ratio), angularity, and surface texture of aggregate particles. These quantitative indices provide valuable insights into aggregate properties [91]. Furthermore, UIAIA's accurate determination of volume and shape factors for individual particles contributes to improved aggregate analysis [90]. Thus, UIAIA's image-based approach enhances our understanding of aggregate characteristics, benefiting fields such as asphalt pavement design.

Dynamic Image Analysis

Dynamic Image Analysis (DIA) is a technique used to analyse particles in motion. Unlike traditional static image analysis, where particles are stationary, DIA involves capturing images of particles as they move through a fluid or across a surface. This method allows for the analysis of dynamic processes such as particle size distribution, shape, and morphology changes over time. However, these devices have a significant drawback: they tend to be expensive.

The VDG-40 Videograder [93], is one of the earliest devices to use DIA. Initially designed to determine aggregate gradation, it has since evolved to measure geometric properties like flatness, elongation, and fractured faces. The process involves introducing aggregates into a feed hopper, transporting them via a vibratory channel to an extraction drum, and capturing images during particle descent. Real-time monitoring and calculations occur via a processing unit.

Another similar machine is The Computer Particle Analyzer [94], primarily used for particle sieving and shape approximation. It measures aggregate shape

without considering angularity or surface texture which is one of its drawbacks. Similarly, the Buffalo Wire Works system, developed at the University of Tennessee, provides size and shape information while also idealising aggregate shape.

Figure 2-10: The CAMSIZER 3D, developed by Microtrac Retsch GmbH, operates according to BS ISO 13322-2 [95] and advances particle size and shape analysis of bulk solids. Unlike traditional methods, it employs patented 3D particle tracking, capturing up to 30 images per particle as they tumble through its sensing zone. This approach enables precise measurements of particle morphology, including length, width, and thickness, with distributions calculated based on these dimensions. With its dual-camera system—a 9 MP zoom camera for fine particles and a 5 MP basic camera for coarser ones—the CAMSIZER 3D achieves a wide measuring range (20 μm to 30 mm) without hardware adjustments. Additionally, it offers rapid measurement times of 2–5 minutes, excellent reproducibility, and compatibility with sieve analysis. The system's ability to detect particle defects and provide detailed shape information makes it a transformative tool across various industries, including construction, pharmaceuticals, and food processing, where particle size and morphology significantly impact product performance and quality [84].

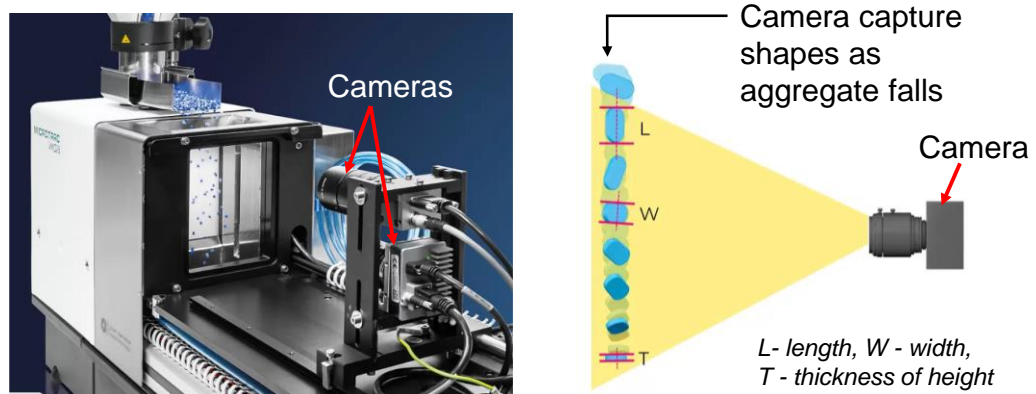


Figure 2-10: The CAMSIZER 3D particle analyser: (left) side view of the device, and (right) the Dynamic Image Capturing technique [84].

2.4.2 Bitumen for asphalt mixtures

Bitumen, a critical component of asphalt mixtures, typically constitutes less than 10% by mass, according to most standards [43]. Despite its minor proportion, bitumen plays a vital role in binding aggregate particles together. The choice of the appropriate bitumen grade significantly impacts pavement durability, stability, and resistance to various stresses. Key properties used to differentiate

bitumen grades include needle penetration, viscosity, ductility, and compatibility [96].

Bitumen emulsion [97], an adaptable alternative to traditional hot bitumen, offers several advantages. Unlike hot bitumen, which requires heating, emulsion bitumen's low viscosity allows it to be used directly without additional energy-intensive preparation steps. Additionally, it uses water instead of petroleum solvents, making it more environmentally compatible. Furthermore, emulsion bitumen remains workable even in colder conditions, improving workability at lower temperatures. Its versatility extends to applications in road construction, waterproofing, and civil engineering projects. However, one drawback of bitumen emulsion is its relatively low durability [98].

To enhance asphalt performance, especially with increased traffic demands, modifications to bitumen properties are essential. Commonly used bitumen modifiers include plastomers, natural rubbers, and synthetic rubber elastomers [99]. These modifications aim to achieve various improvements: lower stiffness (viscosity) at high temperatures to enhance workability, higher stiffness at high service temperatures to reduce rutting and shoving, lower stiffness and faster relaxation properties at low service temperatures to minimise thermal cracking, and increased adhesion to aggregate in moist conditions to prevent stripping of bitumen from the aggregate [100].

Bio-Bitumen

Bio-bitumen, also known as bio-binders, is an emerging sustainable alternative to traditional petroleum-based bitumen. Derived from renewable sources such as lignin, vegetable oils, animal fats, and agricultural residues, bio-bitumen offers the potential to significantly reduce the carbon footprint of asphalt pavements. Its adoption aligns with global sustainability goals and supports circular economy principles by repurposing waste materials.

Recent studies have highlighted bio-bitumen's promising performance characteristics [101,102]. For instance, lignin-based bio-bitumen demonstrates enhanced stiffness and resistance to oxidative ageing, making it suitable for high-temperature regions. Similarly, bio-oil-based binders derived from the pyrolysis of biomass exhibit improved flexibility and low-temperature cracking resistance. Laboratory tests have also shown that, with appropriate additives such as polymers or nanomaterials, bio-bitumen can achieve performance

levels comparable to conventional bitumen, particularly in terms of rutting and fatigue resistance.

However, the technology is still in its early stages and faces several limitations, which have hindered its widespread adoption and practical application [103]. A significant challenge is the variability in the chemical composition of bio-bitumen, which depends on the source material and production process. This inconsistency can lead to unpredictable performance, particularly under long-term service conditions. Additionally, bio-bitumen often requires extensive modification with additives to meet the rigorous performance demands of modern road infrastructure, which increases production complexity and costs.

Durability is another critical concern, as some bio-based binders exhibit inferior resistance to moisture-induced damage (stripping) and thermal ageing compared to petroleum-based counterparts. Furthermore, data on the long-term performance of bio-bitumen in real-world conditions is limited, as most studies have focused primarily on laboratory-scale evaluations. While bio-bitumen holds significant promise, its integration into asphalt pavements requires further research to fully understand its properties, address existing challenges, and ensure consistent and durable performance [104,105].

2.4.3 Types of asphalt mixtures

According to BS EN 13108 standards [47], standard asphalt mixtures encompass a variety of types, each suited to specific applications. These include Asphalt Concrete (BS EN 13108-1), Hot Rolled Asphalt (BS EN 13108-4), Stone Mastic Asphalt (BS EN 13108-5), Mastic Asphalt (BS EN 13108-6), and Porous Asphalt (BS EN 13108-7). Additionally, BS EN 13108-3 addresses soft asphalt for roads with lower stability or lighter traffic volumes, while BS EN 13108-8 focuses on reclaimed asphalt for sustainable applications.

Asphalt Concrete (AC) is defined as a dense, well-graded mixture of aggregates, filler, and bitumen, creating a nearly impermeable material. Known for its durability and strong load-bearing capacity, AC is widely utilised as a wearing course on high-traffic roads. It can be classified into coarse or fine-graded types, depending on particle size distribution, to meet varying application needs.

Hot Rolled Asphalt (HRA) is a gap-graded mixture with a high binder content that includes fine aggregates and coarse aggregate chippings rolled into the

surface layer. This design results in a smooth, durable, and waterproof surface, making HRA ideal for urban areas with high traffic where resistance to deformation and wear is essential.

According to BS EN 13108-5, Stone Mastic Asphalt (SMA) is formulated to achieve stone-on-stone contact within the mix, which enhances rutting resistance and stability. Due to its composition, SMA requires high-quality aggregates, raising production costs but delivering durability that makes it well-suited for high-traffic areas prone to mechanical stress.

Mastic Asphalt, outlined in BS EN 13108-6, is a highly dense, impermeable mixture with a high binder content, typically applied in thin layers. It offers unique flexibility and waterproof properties, making it suitable for specialised applications, including bridge decks, tunnels, and other infrastructure needing durable waterproofing.

Porous Asphalt, defined in BS EN 13108-7, is an open-graded mixture designed to allow water to permeate its structure. This enhances drainage and minimises surface water, making it especially valuable in areas where noise reduction and splash control are desired, such as highways. Its porosity also improves road safety by reducing water spray in wet conditions.

BS EN 13108-3 specifies Soft Asphalt for low-traffic or low-stability roads, like those in rural areas or lightly trafficked settings. Its flexible composition makes it more resilient to movement but less suitable for high-load conditions, fitting applications where heavy-duty asphalt performance is unnecessary.

Finally, in line with BS EN 13108-8, Reclaimed Asphalt facilitates recycling by incorporating used materials into new mixtures. This approach conserves resources and reduces waste while maintaining performance standards, making it a sustainable choice for lower-demand applications.

Asphalt mixtures are produced as Hot Mix Asphalt (HMA), Warm Mix Asphalt (WMA), or Cold Mix Asphalt (CMA), each suited to specific applications [106,107]. HMA, produced at 150°C–190°C, offers high strength, stiffness, and durability, making it ideal for high-traffic areas. WMA, manufactured at 100°C–140°C, reduces emissions [108], improves working conditions, extends haul times, and enables better compaction at cooler temperatures [98],[108], making it a sustainable alternative for moderate-performance applications. CMA, produced with unheated aggregates and emulsified or foamed bitumen, is

energy-efficient and eco-friendly but lacks the strength of HMA, limiting its use to low-traffic areas and temporary repairs.

2.4.4 Asphalt mix design methods

The design of asphalt mixtures is a key aspect of pavement engineering, aimed at optimising performance under varying traffic and environmental conditions. It involves selecting and proportioning aggregates and bitumen to achieve desired properties, such as stability and durability. Asphalt design methods are broadly categorised into empirical, mechanistic-empirical, and performance-based approaches, each with unique strengths and limitations. Recently, the Balanced Mix Design, a hybrid of mechanistic-empirical and performance-based methods, has gained popularity for its ability to balance multiple performance requirements effectively.

Empirical design methods

Empirical methods, such as the Marshall Mix Design [109], and Hveem Stabilometer Method [110], were widely used in the early 20th century and are still applied in specific contexts today. The Marshall Mix Design [109] selects aggregate gradations within specific limits and a binder content that satisfies minimum stability and flow requirements. Under traffic, Marshall stability describes how bituminous materials resist displacement and shearing stresses. Flow determines the elasto-plastic properties of asphalt, which are described as the ability of asphalt to adapt to settlements and gradual movement without cracking [111]. Similarly, the Hveem Method emphasises stability through volumetric calculations and performance parameters, although it is more commonly used in the western United States [110]. These methods are relatively simple but rely on limited laboratory testing, making them less adaptable to modern, high-traffic pavements [69].

Mechanistic-empirical design methods

Mechanistic-Empirical (M-E) methods represent a significant advancement over purely empirical approaches, as they incorporate structural responses, such as strain and stress, under real-world loads. The design approach uses mechanistic principles along with empirical data to predict mix performance. A typical example of this approach is the Superpave design method [50,67,112] which offers a more comprehensive approach. The method offers different mix design levels that allow for adjustments based on the available resources,

construction methods, and performance requirements. The process considers the selection of aggregates by determining their proportions according to grade, shape, and durability specifications, and determining the binder content based on some volumetric or mechanical properties of the asphalt. In this approach, the selection of exact aggregate portions is crucial to the performance of the asphalt mixes. However, the selection procedures are mostly based on an experimental trial-and-error process that is tedious and time-consuming.

Performance-based methods

Performance-based methods focus directly on achieving specific performance criteria (such as resistance to rutting, cracking, or durability) based on how the pavement should perform under real-world conditions. These methods are highly adaptable and often consider local factors but may require advanced testing and modelling capabilities.

The Performance mix design (PMD) [113], a more advanced version the performance-based method, fits within the performance-based approach category. PMD focuses on creating asphalt mixtures that meet specific performance criteria, such as resistance to rutting, fatigue cracking, or thermal cracking, under anticipated real-world conditions. As referenced in previous studies [59,61,75], these distresses are influenced by the relative quantities of aggregate and asphalt binder [109,114]. Consequently, control over the characteristics and quantities of aggregates and bitumen in a mixture could lead to the development of mixtures with customised functionalities.

PMD methods often use advanced performance tests, such as the Wheel Tracking Test for evaluating rutting resistance [115] and the Dynamic Modulus Test ($|E|$)* for assessing stiffness [116], as well as modelling to determine how a mix will perform over time, under various loads, and in specific environmental conditions. Although PMD requires a more sophisticated testing infrastructure, it provides a flexible and reliable approach to optimising pavement longevity and functionality by directly addressing performance requirements rather than relying solely on volumetric or empirical measures.

Balanced mix design (BMD)

The Balanced Mix Design establishes specific performance thresholds for rutting and cracking, ensuring that neither property is compromised during the design process. For example, increasing binder content can improve cracking

resistance by enhancing the mixture's flexibility and reducing susceptibility to fatigue. However, excessive binder may reduce stiffness, increasing the likelihood of permanent deformation (rutting) under heavy traffic loads. Conversely, optimising the aggregate structure for high stiffness and rut resistance can result in a more brittle mix, making it prone to cracking under repeated loading or temperature variations. To address this trade-off, BMD incorporates rutting and cracking criteria into the design process.

The method often incorporates both empirical and mechanistic tests [117], such as the Wheel Tracking Test for rutting resistance and the Indirect Tensile Cracking Test (IDEAL-CT) [118] for cracking. Additionally, BMD can include other tests, such as the Dynamic Modulus Test ($|E|$), to address broader performance needs beyond its primary focus.

Figure 2-11 illustrates a balance mix graph for optimising the fatigue cracking and rutting performance of a mixture [113].

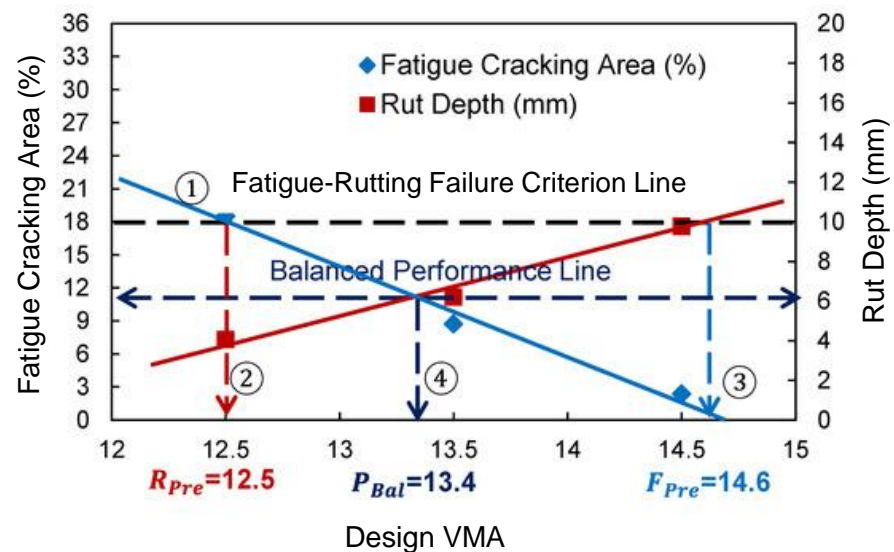


Figure 2-11: Illustration of optimisation of mixture performance to meet cracking and rutting failure criteria [113].

2.4.5 Asphalt mix design approaches across regions

Asphalt mix design varies across regions to suit distinct traffic demands, climates, and material availability. This section examines key approaches across developed and developing regions.

United States

In the United States, the Superpave (Superior Performing Asphalt Pavement) mix design method, developed under the Strategic Highway Research Program

(SHRP) in the 1990s, has become the most widely adopted approach for asphalt mixture design. It has largely replaced traditional methods like Marshall and Hveem due to its performance-based framework, which incorporates climate-specific conditions, traffic loads, and material properties into the design process. Superpave's ability to produce durable and reliable asphalt mixtures tailored to a wide range of environmental and traffic conditions has established it as the standard in modern pavement engineering.

A key feature of the Superpave system is the Performance-Graded (PG) binder specification, which classifies bitumen based on its resistance to rutting, fatigue cracking, and thermal cracking under regional temperature extremes. The mix design incorporates volumetric analysis, including voids in mineral aggregate (VMA) and air voids, alongside advanced tests like gyratory compaction to simulate field conditions and assess deformation resistance. Its widespread adoption highlights its effectiveness in addressing critical performance demands, particularly for high-traffic roads and highways.

Europe

European countries, guided by harmonised CEN standards, emphasise performance-based asphalt mix design. While the Marshall method is still used in countries like France and the UK, it is often supplemented with advanced testing. France, for example, uses the Gyratory compactor for accurate volumetrics and specific tests like the Duriez test for water sensitivity, the Laboratoire Central des Ponts et Chaussées⁵ (LCPC) wheel tracking for rut resistance, and trapezoidal bending for stiffness and fatigue. These methods enable the characterisation of deformation resistance, stiffness, and fatigue life, ensuring asphalt durability and structural integrity under varying climates and heavy traffic loads.

The French asphalt mix design method

The French design method for asphalt mixtures is based on a performance-oriented approach that emphasises laboratory validation through empirical testing to achieve durability and resistance to deformation under load. This method primarily assesses parameters such as stiffness, fatigue resistance, and rutting resistance, ensuring that the mix can withstand various traffic loads and climatic conditions over time. The French methodology principally utilises

⁵ Translated to English as 'Central Laboratory of Bridges and Roads.'

the LCPC Wheel Tracking Test and Fatigue Beam Test to evaluate performance, particularly for high-performance asphalt types like Enrobé à Module Élevé⁶ (EME), which is widely used for high-stress applications. The French design approach also considers local materials and regional climatic conditions, adapting the mix to optimise resistance to aging and environmental stresses [119,120].

The UK asphalt mix design: recipe-based approach

The UK design approach, as specified in PD 6691:2022 [63], complements the BS EN 13108 standards [47], by providing a recipe-based framework for asphalt mix design. This method defines mixture proportions for aggregates, binders, and fillers according to standardised compositions for different applications, facilitating consistency and ease of production. PD 6691 specifies various asphalt mixtures, including Asphalt Concrete (AC), Hot Rolled Asphalt (HRA), and Stone Mastic Asphalt (SMA), with targeted properties aligned with the functional layer in which each type is used (e.g., surface, base, or binder course). This recipe approach is grounded in historical performance and empirical knowledge, allowing contractors to select appropriate mixtures for specific applications, particularly where rapid application and consistency are prioritised. [Table 2-1](#) presents a selection of laboratory tests, chosen from among many, that are performed to evaluate the performance of asphalt mixtures in the UK.

Asia

Asian countries, including Japan, India, and China, adopt diverse asphalt mix design approaches to address rapid urbanisation, heavy traffic, and varying climatic conditions. Japan frequently employs Stone Mastic Asphalt (SMA) for high-traffic areas, focusing on durability and resistance to deformation. India relies heavily on the Marshall mix design, modified with locally available aggregates and additives, to optimise cost-effectiveness. In China, performance-based methods, including polymer-modified binders and rutting resistance tests, are increasingly utilised for infrastructure durability under high axle loads and extreme weather variability.

⁶ Translate to English as 'High Modulus Asphalt.'

Table 2-1: Description of selected performance tests on asphalt mixtures (selection informed by the scope of the research).

Performance	Description	Test name	Reference	Limit ⁷ [121,122]
Stability	The asphalt's resistance to deformation under load.	<ul style="list-style-type: none"> • Marshall test • Indirect tensile strength • Resistance to fatigue • Wheel tracking 	BS EN 12697-34:2020 [123] BS EN 12697-23:2003 [118] BS EN 12697-24:2018 [124] BS EN 12697-22:2020 [115]	≥ 5.0 kN
Flow	Determines the asphalt's elasto-plastic characteristics, reflecting its ability to adapt to subgrade movements and settlements without cracking.	Marshall test	BS EN 12697-34:2020 [123]	2 mm to 4 mm
Air void content	The air void volume in compacted mix is vital for designing and evaluating asphalt pavements, impacting their durability, strength, and environmental resistance.	Determination of bulk density of bituminous specimens	BS EN 12697-6:2020 [125]	3% to 7%
Workability	The ease of placing, compacting, and shaping asphalt mixtures during construction.	No known standard method ⁸	-	-

⁷ Performance limits typically applied in the field for asphalt mixtures.

⁸ Some non-standard techniques for evaluating the workability of asphalt mixtures are presented in [Chapter 2](#), given the significance of this performance parameter to the research.

Africa

In Africa, the Marshall method remains the predominant mix design due to its simplicity and adaptability to local materials. Cost and resource limitations drive innovations like the use of reclaimed asphalt and unconventional aggregates. Performance modifications are typically aimed at improving binder adhesion and resistance to stripping in regions with high moisture and temperature variations. Despite limited adoption of advanced techniques, pilot studies using Superpave and polymer-modified binders are emerging in South Africa for high-traffic roads.

Australia and New Zealand

Australia and New Zealand prioritise sustainability in asphalt mix designs by incorporating reclaimed asphalt pavement (RAP) and industrial by-products, such as slag and fly ash. Both countries utilise performance-based specifications, particularly in high-temperature and moisture-prone regions. The use of Wheel Tracking Tests and Dynamic Modulus Tests ensures mixes are suited for rut resistance and fatigue life. Sustainability frameworks guide material selection and mix optimisation, balancing durability with environmental objectives.

Middle East

Middle Eastern countries focus on developing asphalt mixes that withstand extreme heat and heavy axle loads. Polymer-modified binders (PMBs) and Performance-Graded (PG) systems are widely utilised to enhance rut resistance and thermal stability. Tests such as the Hamburg Wheel Tracking and Indirect Tensile Strength are integral for assessing performance under severe conditions. The inclusion of anti-stripping agents and reflective surfaces also addresses durability and longevity in arid climates.

2.4.6 Trends in Asphalt Mix Design

Globally, asphalt mix design is increasingly adopting performance-based frameworks that incorporate climate, traffic, and sustainability considerations. Advances in materials, such as polymer-modified binders, recycled components, and innovative additives, have significantly improved the durability and environmental impact of asphalt mixtures. Regional approaches, such as Superpave in the United States, European Committee for Standardisation (CEN) methodologies, and adaptations in Asia and Africa, aim to address

specific environmental and traffic conditions while ensuring long-term pavement performance.

The introduction of digital technologies [126], including virtual aggregate modelling [30], digital twins [127], and AI-driven optimisation [127,128], has shown promise in enhancing the precision and adaptability of asphalt mix designs across diverse regions. Furthermore, innovative methods for assessing mixture workability are emerging to address practical challenges in construction and ensure consistency in field performance.

Future research in this area is expected to focus on integrating sustainable materials, refining digital design tools, and developing advanced performance testing methods to create durable, regionally adaptable, and environmentally conscious pavement solutions [129,130].

The UK method's reliance on pre-defined recipes simplifies the design process, although it may lack the flexibility of performance-based methods like the French approach.

2.4.7 Evaluating the workability of asphalt mixtures

The factors that influence the workability of asphalt mixtures have been well documented in literature. [8] indicated that the workability of HMA is affected by the temperature, binder type, aggregate type, and nominal maximum aggregate size. For aggregate gradation, an increase in the percentage of filler is known to reduce the workability of HMA [131–134]. Reference [61] also established that the workability of asphalt mixtures decreases with decreasing flaky aggregate content. Furthermore, [70] showed that 12.5 mm nominal maximum aggregate sized mixtures are more workable than 19.0 mm nominal maximum aggregate size mixture in both WMA and HMA. Also, crushed gravel HMA mixtures have better workability than limestone aggregate mixtures [70] which indicates that the type and geometry of aggregates influence the characteristics of asphalt mixtures. Reference [70] further indicated that the workability of asphalt mixtures decreases with increasing binder viscosity.

In pavement construction, asphalt pavers are used to distribute, shape, and partially compact the asphalt layers. Paving rollers are then used to press down the laid asphalt to reduce its thickness, reorient aggregates and obtain targeted densification. The density obtained directly impacts the quality and lifetime of that pavement. In effect, mixtures that are more workable and compactable are

likely to last longer. Also, workable mixtures require less energy for distribution and compaction which saves resources.

In manual levelling of HMA mixtures with asphalt shovels, workable mixtures are easy to push around. In recent years, electronic pavers that are capable of laying asphalt to the precise thickness and compacting the mixtures to significant degrees are becoming common on the market. To quantify the ease of working with a variety of bituminous mixtures and predetermine its success of use on-site, several workability-related studies have been conducted in the past four decades. The investigations mainly follow two major paths: the use of compaction index methods [134–136] and paddle mixer type designs [131,132,137,138]. The compaction index involves using Superpave Gyratory Compactor densification curves. Also, from direct gyration readings, a small gyration number indicates better compactability of the mixture [139].

The paddle mixer type design, the oldest of all, utilises the torque generated from the resistance that the paddle blade encounters as it stirs an asphalt specimen, usually 12 kg to 20 kg. It primarily consists of a motor to turn a mixing blade, a mixing paddle with the blades, a blade revolution torque measuring unit, and a mixing bowl, as shown in Figure 2-12.

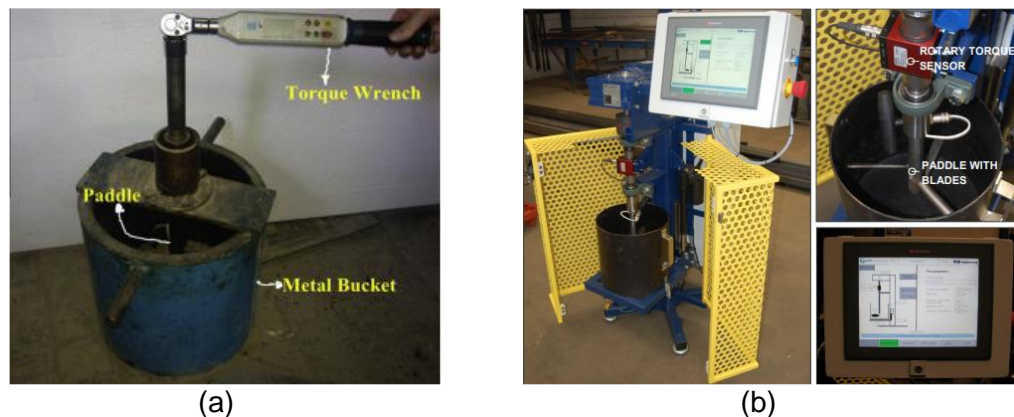


Figure 2-12: Workability measurement of asphalt mixtures from literature: (a) torque wrench with a paddle mixer by Wang et al. [140], and (b) paddle mixer type design by Poeran and Sluer [131].

Either the mixing blade or bowl could be rotated to generate the torque at the desired specimen temperature. A lower torque value is used as an indicator of good workability. In a recent study, reference [141] modified a motorised Vane Shear Test (VST) apparatus, a device used to measure the shear strength of soils, to quantify the workability of asphalt mixtures. One major concern that has characterised these methods in literature has been the wide variability in test results. The raw data of workability measurement of SMA 70/100 showing wide

variability from an improved version of the paddle mixer type design by [131] is shown in Figure 2-13. The high errors have been attributed to fine material segregation and shear planing in asphalt mixes caused by the blades in the paddle-torque devices. An example of the segregation, from reference [131], is illustrated in Figure 2-14.

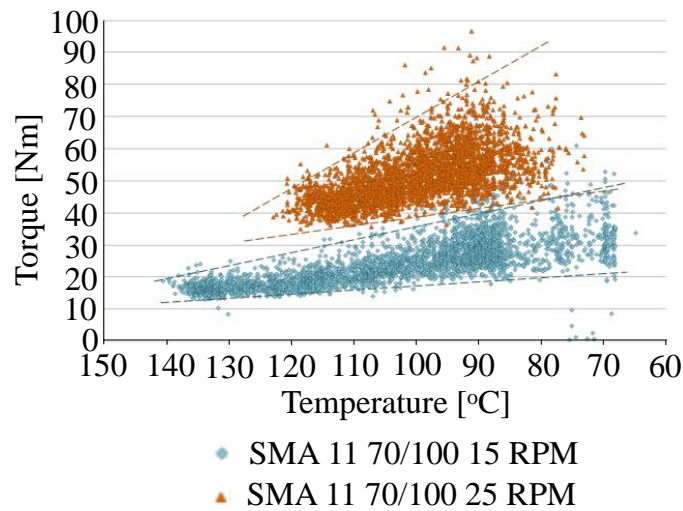


Figure 2-13: Scattered test data from Poeran and Sluer [131] demonstrate the lower accuracy of paddle mixer test results in measuring workability in HMA.

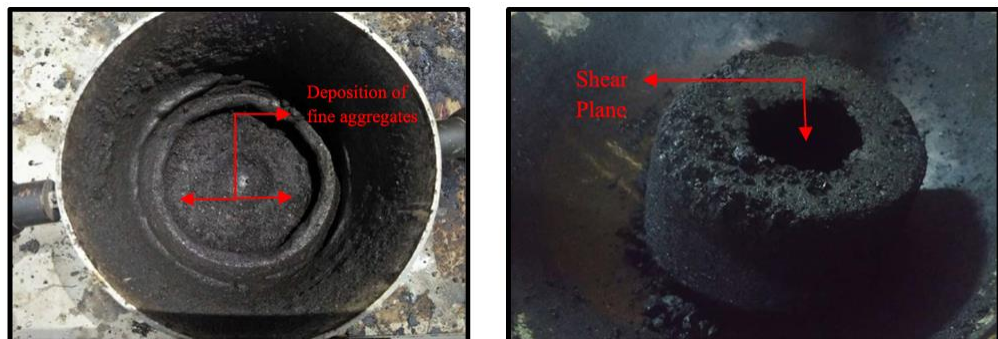


Figure 2-14: Demonstration of problems associated with the paddle mixer type design (a) fine aggregates in HMA segregated and pasted on the container walls, and (b) shear planing in the mixture

Computational methods

Additionally, computational methods are gaining popularity in asphalt mixture designs. For instance, researchers have utilised Data-Driven methods, such as simple rules and artificial intelligence, to create models predicting asphalt mix behaviour based on its composition [26–28,30,31,142–147]. However, data-driven methods still struggle to accurately predict asphalt mix compositions due to the numerous variables involved.

Also, researchers have employed discrete element methods to simulate virtual 3D representations of asphalt mixtures and compact them. This approach enables the prediction of volumetric properties such as air void content. When creating these virtual 3D asphalt mixtures, it is crucial to consider the geometry of aggregates and accurately replicate them to generate precise virtual aggregate assemblies [58,62,111,148].

2.4.8 Comparing asphalt mix design methods to flexible pavement design methods

Asphalt mix design and flexible pavement design share similar foundational approaches—empirical, mechanistic-empirical, and performance-based—though their focus within pavement engineering differs substantially. Asphalt mix design, as previously discussed, concentrates on achieving an optimal material composition for the asphalt layer. In contrast, flexible pavement design applies these methodologies to the entire pavement structure, addressing the distribution of loads across multiple layers, from the asphalt surface down to the subgrade.

Flexible pavement design aims to ensure that loads are distributed effectively to protect the lower layers, particularly the subgrade, which provides foundational support for the pavement. Empirical methods like the AASHTO 1993 [149] design use historical data to guide layer thickness, while mechanistic-empirical approaches, such as the Mechanistic-Empirical Pavement Design Guide (MEPDG) [150], model stresses and strains within each layer to predict how the structure will respond to different loads and environmental conditions. Performance-based methods, meanwhile, evaluate pavement layers based on criteria like fatigue and deformation resistance, ensuring each layer performs as intended over its lifecycle.

By considering factors such as load-bearing capacity, subgrade resilience, and interlayer bonding, flexible pavement design achieves a stable, durable structure capable of withstanding anticipated traffic and environmental stresses. This focus on structural integrity across layers distinguishes it from asphalt mix design, where the emphasis is specifically on optimising material composition within the asphalt layer itself. Together, these design approaches enhance both material performance and overall pavement durability in complex, real-world conditions.

2.5 Distresses in Asphalt Pavements

When traffic traverses the road pavement, it takes life out of it. The loads are repetitive and lead to fatigue in the pavement layers. Also, as pavements are exposed to the environment, variations in the weather weaken the strength of the asphalt. Traffic, environmental and material factors cause road distresses (also called defects) such as cracks, bleeding of binder, corrugation, rutting, shoving and potholes. Reference [151] identifies pavement cracking as the most common road defect and it can progress into other distresses if not fixed. Cracking in road layers can result from factors such as heavy traffic loads, variations in climatic conditions, asphalt aging, deficiencies in construction practices, or movements in the subgrade. Cracks, especially intersecting ones affected by water ingress and traffic impact, lead to the formation of potholes. Ravelling, on the other hand, occurs due to the progressive disintegration of asphalt caused by the dislodgement or segregation of asphalt aggregates. Moreover, excessive axle loads exacerbate rutting, while shoving and corrugation occur as a result of braking forces exerted by vehicles. According to Odoki [152], all pavement defects interact with roughness as illustrated in [Figure 2-15](#). As such, roughness is primarily used as a key parameter in pavement performance modelling [152–154].

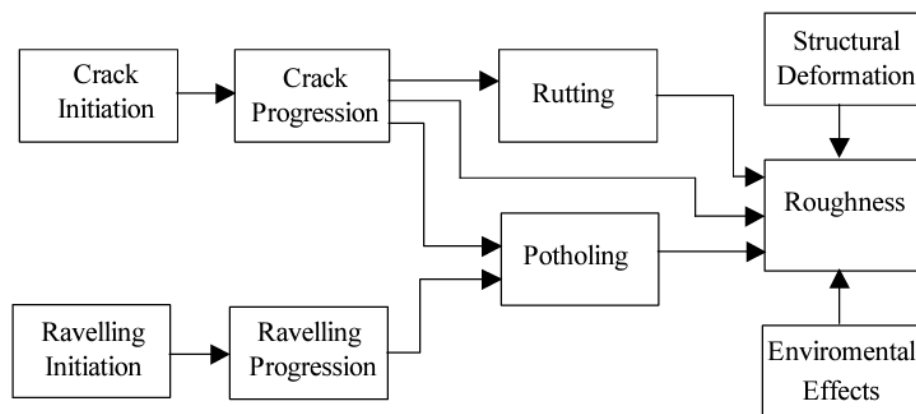


Figure 2-15: Asphalt pavement distress interaction [154].

2.5.1 Cracking in asphalt pavements

It is an undeniable fact that pavements crack; and cracking is the most common distress in flexible pavements making up about 70% of all defects [151]; and its presence signifies a deteriorating pavement.

Impact of cracks on road pavement

Cracking is the most common distress in flexible pavements [151,155,156], and can significantly decrease the service level and service life of an asphalt pavement [157]. There is a significant positive relationship between cracking and road surface roughness [158]. Cracking destroys the structural integrity and decreases the bearing capacity of the pavements [157]. Cracks also allow water to penetrate the inner part of pavements [159], causing other serious distresses such as water bleeding, pumping, and potholes [160,161]. Therefore, it is of great importance to promptly fill and seal the cracks. Delaying crack repairs can reduce serviceability and lifespan while increasing vehicle, operational, and maintenance costs [162].

Crack types and cracking mechanism

Common cracks associated with flexible pavements are detailed in [Table B-41](#) in [Appendix B](#). Generally, cracks may be related to fatigue or ageing [163] and climate impact. That is, generally, cracking in asphalt can be load-associated or non-load associated [164]. Fatigue cracking can initiate both at the top and the bottom of a pavement and may be initiated by shear stresses from vehicular tyres [165–167] and may depend on the material characteristics of the wearing course [168,169]. In [Figure 2-16](#), reference [167] illustrates how loading causes top-down cracking. The figure reveals that load related top-down cracks often develop outside wheel paths in a tension region.

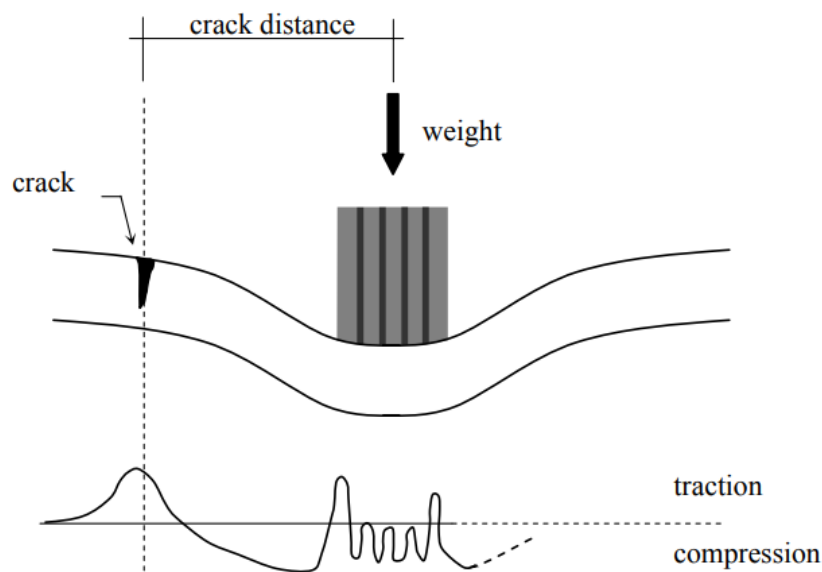


Figure 2-16: Illustration of structural bending and stresses in asphalt pavement from loading [167].

Also, reflective cracking in asphalt overlay refers to the phenomenon where cracks from the existing pavement surface reappear or "reflect" through the newly applied overlay. This type of cracking typically occurs due to the propagation of existing cracks in the underlying pavement through the overlay, often caused by movements in the underlying pavement layers, thermal fluctuations, or inadequate bonding between the overlay and the existing pavement. Figure 2-17, illustrates the reflective cracking phenomenon in asphalt overlays according to reference [170].

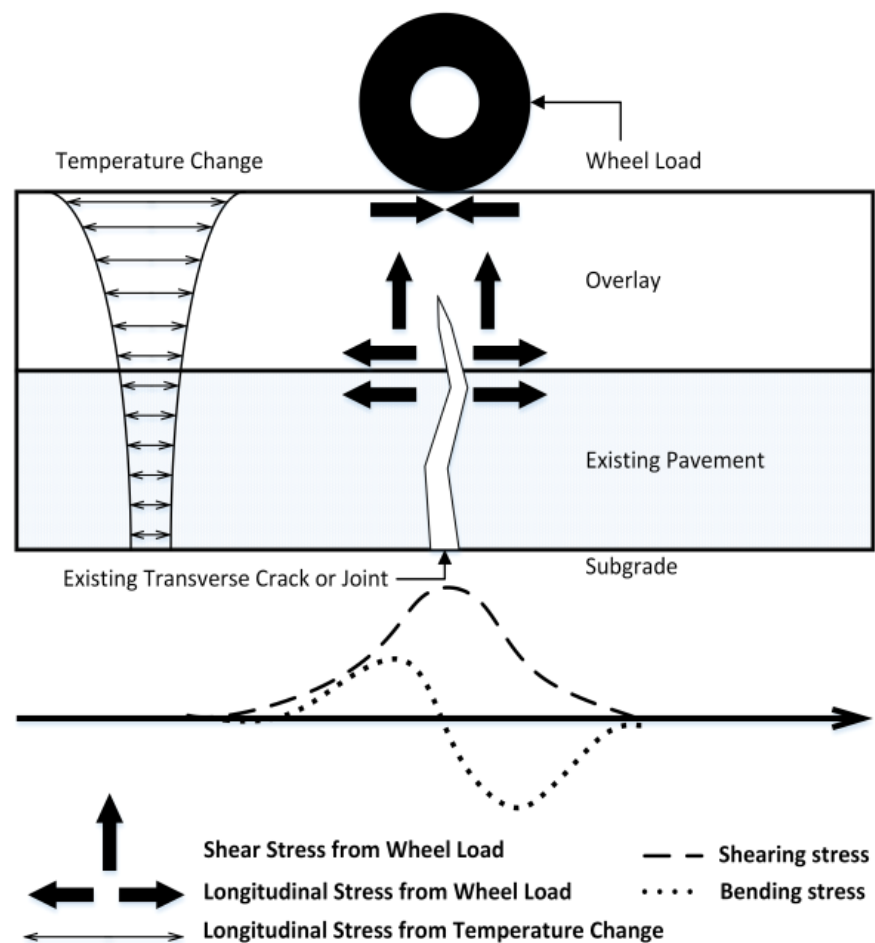


Figure 2-17: Reflective cracking mechanism in flexible pavements [170].

Additionally, temperature-induced fatigue is often top-down. Once developed, at the top, traffic loading and water ingress can exacerbate the cracks' downward propagation [169]. Figure 2-18 illustrates a schematic representation and a real image of a top-down crack in an extracted core from an Italian motorway pavement. However, bottom-up fatigue cracks which are mostly started at the lower sections of a pavement layer, are caused by tensile strains that results from repetitive wheel loads. Recent literature however suggests that not all bottom-up cracks are load associated [164]. All asphalts undergo aging

when in service which reduces their ability to resist repeated deflections from loading. This makes aged asphalts more susceptible to cracking. In a mechanistic approach, bottom-up fatigue cracking is used as the pavement thickness design criterion [168]. In Figure 2-18, the cores reveal characteristics that are typical of transverse cracks. Notably, pavements with lower quality materials will crack at a faster rate. For instance, inadequate interlayer bonding between asphalt concrete and the Cement-Treated Base (CTB), as well as insufficient pavement thickness, can be major causes of accelerated cracking in asphalt pavements [64]. A in-situ transverse crack through the entire profile of a flexible pavement is shown in Figure 2-19.

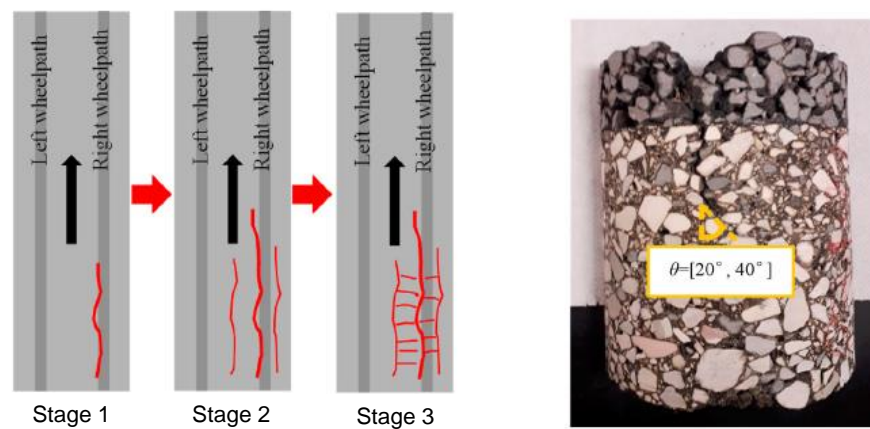


Figure 2-18: Evolution of top-down cracking: (left) scheme in stages, and (right) extracted core of a wearing and binder course [171].

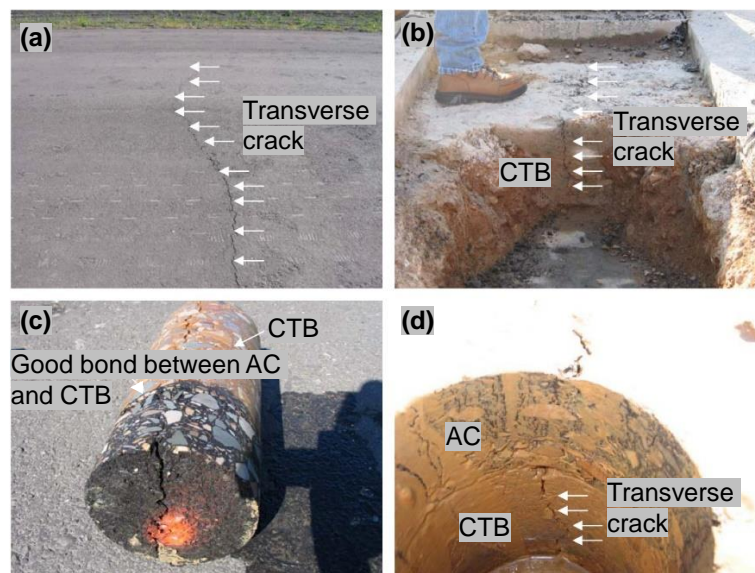


Figure 2-19: Transverse crack of a typical pavement: (a) surface view, (b) pit showing failed CTB, (c) core from the cracked pavement, and (d) cored-profile of in-situ pavement [172].

Crack initiation and progression prediction

Due to the multiple factors that influence cracking in pavements, its prediction is that of a complex phenomenon. Accurately predicting crack development is not just important for road maintenance management but also, to aid in the design of more resilient flexible pavements. Although there have been several efforts both in the past [65] and in recent times [66]–[68] to understand the initiation and propagation of cracking, especially fatigue cracking, their time of initiation and damage distribution are yet to be fully understood, probably due to their stochastic nature. Reference [173] observed that the tensile strain developed in an asphalt under load was the cause of fatigue. This observation remains relevant even in modern research, four decades later.

The fundamental understanding of all crack propagation models in literature is that asphalt mixtures designed with higher strain tolerance have higher resistance to cracking and once the fatigue resistance of an asphalt is exceeded, it could take smaller loads to cause further cracking.

In recent studies, empirical crack propagation models have been developed to guide practicing engineers. However, the effective application of most of these models relies much on the experience of the pavement engineer. One of the well-established models is that found in HDM-4 which predicts crack initiation and progression for rehabilitated pavements. The crack initiation model for rehabilitated pavements is indicated in Equation (2-1) and the crack progression model shown in Equation (2-2) [174]. In terms of crack progression after initiation, HDM-4 illustrates that crack initiation and progression remain in incremental progression throughout the asphalt's life if the cracks are not maintained. In effect, the only time the progression peaks is the stage where the asphalt has collapsed.

Initiation of all structural cracking:

$$ICA = K_{cia} \{CDS^2 \times a_0 \times \exp \left[a_1 \times SNP + a_2 \left(\frac{YE_4}{SNP^2} \right) \right] + CRT\} \quad (2-1)$$

Progression of all structural cracking:

$$d_{ACA} = K_{cpa} \left(\frac{CRP}{CDS} \right) Z_A \left[(Z_A \times a_0 \times a_1 \times \delta t_A + SCA^{a_1})^{\frac{1}{a_1}} - SCA \right] \quad (2-2)$$

where:

- ICA* - time necessary for initiation of all cracks in the construction (years)
- K_{cia} - calibration coefficient for the initiation of all structural cracks
- CDS* - indicator of the defects in the asphalt surface construction (*CDS* = 0 for well-built pavements; *CDS* = 1 for correctly built pavement with a few defects; *CDS* = 2 badly built pavements with a combination of defects)
- SNP* - average annual modified structure number of the pavement
- YE_4 - average annual number of equivalent axes as per the standard (millions/lane)
- CRT* - lagging time in the formation of the crack due to maintenance (years)
- d_{ACA} - the incremental change in area of all structural cracking during analysis year, in per cent of total carriageway area
- K_{cpa} - the cracking progression factor
- CRP* - retardation of cracking progression due to preventive treatment
- SCA* - $\min(ACA_a, (100 - ACA_a))$ and ACA_a is the area of all structural cracking at the start of the analysis year, in per cent.
- a* - model coefficients

NB: Progression of all cracking commences when $\delta tA > 0$ or $ACA_a > 0$.

Crack characterisation and measurement

Manual surveys such as crack mapping and visual observations [175], and automatic photographic techniques such as laser surveys [176,177], automatic road analysers and PASCO systems [177,178] are extensively used in pavement management systems for crack detection and measurement. The conventional approach and basics for measuring crack width are illustrated in [Figure 2-20](#) [179].

HDM-4, cited by reference [174], measures cracks as a percentage of the total carriageway. This means that the cracking area is estimated as the sum of rectangular areas circumscribing manifest distress (line cracks are assigned a width of 0.5 m), expressed as a percentage of the carriageway area. Additionally, structural cracking is categorised as narrow cracks or wide cracks, with the crack range of (1-3 mm crack width) and (> 3 mm crack width) respectively. The HDM-4 linear classification is similar to the Federal Highway

Administration 2009 classification [180], where the latter classifies linear crack (transverse and longitudinal) severity levels as low (cracks with a mean width of < 0.25 in (6 mm)), medium (cracks with a mean width > 0.25 in (6 mm) and ≤ 0.75 in (19 mm)), and high (cracks with a mean width > 0.75 in (19 mm)). In contrast, fatigue cracks are quantified in areas due to their wide coverage.

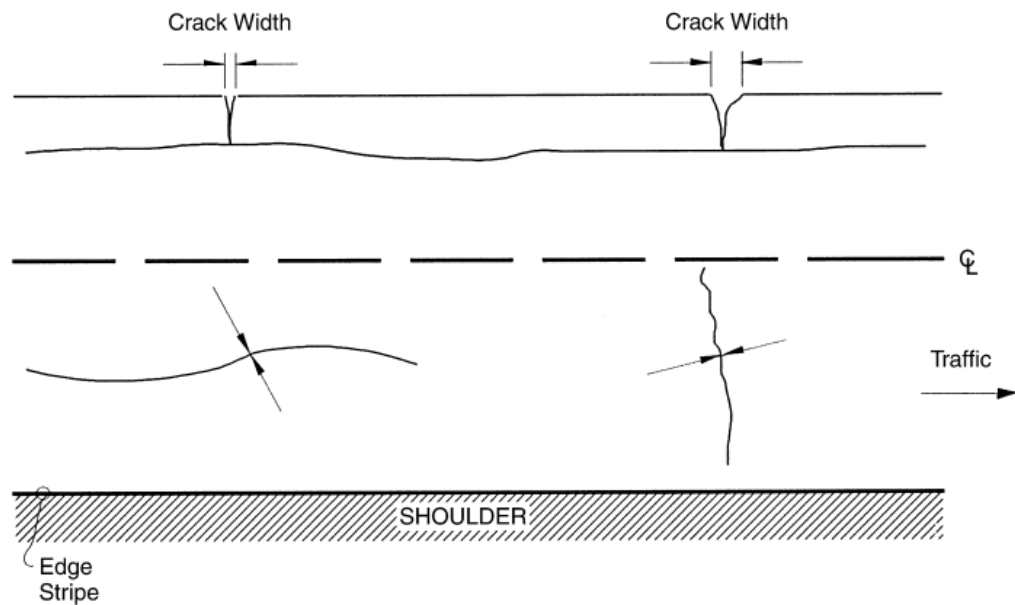


Figure 2-20: Crack width measurement [179].

According to [180], low fatigue cracks are areas of cracks with no or very few interconnecting cracks, where cracks are ≤ 0.25 in (6 mm) in mean width and are not spalled. Medium fatigue cracks cover interconnected cracks that form a complete pattern with crack > 0.25 inches (6 mm) and ≤ 0.75 in (19 mm). Medium fatigue cracks may be slightly spalled. Lastly, high cracks are observed to be interconnected and form a complete pattern with cracks > 0.75 in (19 mm). High fatigue cracks may be moderately or severely spalled. Specifically, the Michigan Department of Transportation (MDOT) evaluates the density of cracks within 100 m sections of a roadway with details shown in Table 2-2.

Table 2-2: Classification of crack density by the MDOT [181].

Total crack length per 100m section of pavement	Density category
$< 10\text{m}$	Low
10m to 135m	Moderate
$> 135\text{m}$	High

Repairing cracks

Cracks in both asphalt and concrete are usually repaired by sealing or filling the crack with binders. In asphalt, bitumen is the most used repair material whereas other sealants and epoxies are commonly used in concrete. It is also common to see cement grouts injected into cracks especially in rigid pavements [181]. Earlier studies do not provide evidence of the use of bitumen in concrete nor cement grout in asphalt. This could be due to the desire for the filling material to bond with the crack wall and effectively prevent water seepage. Sealing techniques also include covering cracks with overbands⁹ [182]. In recent years, new techniques to make the pavement material self-heal are being considered. The concept of self-healing in asphalt was introduced by White et al [183] in 2001. It involves bursting embedded microcapsules when subjected to applied force and releasing healing agents. Common maintenance actions that could be applied to cracked roads are presented in Table 2-3, from FHWA guidance [184].

Although the FHWA did not explain the reasons for taking no action on low-density cracks, its proposal could be attributed to the management of workforce and maintenance budgets. In realistic terms, every identified crack should be sealed at the earliest opportunity to avoid further degradation. Many pieces of literature recommend that if fatigue cracks are not treated at early stages, their treatment at later stages would not result in substantial improvement in pavement performance [162,185]. This could be because fatigue cracks indicate failed pavements, and as such, the failed material would have to be replaced.

Table 2-3: Guidelines for determining the type of maintenance action to take [184].

Crack Density	Percentage of crack length		
	Low (0-25)%	Moderate (26-50)%	High (51-100)%
Low	Do nothing	Do nothing	Repair crack
Moderate	Treat crack	Treat crack	Repair crack
High	Surface treatment	Surface treatment	Rehabilitate road

⁹ The overband material, typically a bituminous sealant or a specialised polymer-modified bitumen, is applied hot and allowed to cool and harden, thereby forming a protective barrier over the crack.

Crack sealing and filling in asphalt

The most used treatments for cracks are sealing or filling [159,163]. This approach is categorised as preventive maintenance [14,161]. The manual approach to crack filling or sealing can however be associated with poor performance and low efficiency [80].

Crack sealing is a localised treatment method used to prevent water and debris (incompressible material) from entering a crack, which can weaken the base material and prevent the pavement from expanding and contracting freely. Cracks are typically less than 19 mm wide [186]. The optimal choice for sealing asphalt cracks is a flexible, polymer-modified, rubberised asphalt blend. This material adheres well to crack walls, prevents water infiltration, and maintains its ability to expand and contract with temperature changes.

Crack filling differs from crack sealing mainly in the preparation given to the crack prior to treatment and the type of sealant used. Crack filling is typically reserved for more worn pavements with wider, more random cracking (usually wider than 19 mm). While crack sealing primarily aims to prevent moisture penetration, crack filling is intended to reinforce the pavement's structural integrity. Materials such as asphalt rubber, polymer-modified asphalt, and cold-pour crack sealants are commonly used. Cracks may also be filled with micro-surfacing material or slurry.

From literature, repairing cracks in moderately cool temperatures provides two main benefits. Firstly, cracks tend to open partially, allowing for sufficient material placement within the crack even without cutting. Secondly, the crack channel width, whether cut or uncut, typically falls within its optimal range. This is crucial for the performance of the sealant material, as it minimises the need for excessive extension or contraction [161].

Self-healing techniques for cracks

At high temperatures, bitumen in asphalts may flow and close cracks which is described as self-healing [187,188]. Several research works are therefore taking advantage of this bitumen property by experimenting with techniques that could enhance breaking the static equilibrium of bitumen by modifying temporarily their viscosity to force it to drain into cracks [189]. This is achieved through microwave and induction heating of ferrous fibres [190–196], or the embedment capsules [197–202] in the asphalt mixture. Although microwave

heating heals cracks better than induction, reference [192] reports that it can damage the rheological properties of the bitumen. Also, both heating methods reduce the air void content in the asphalt mixture thereby altering its volumetric properties. It is also perceived that the self-healing technique may not be ideal for moderate and severe fatigue cracks. Figure 2-21 and Figure 2-22 show the first in-situ induction and an asphalt beam with capsules, respectively. Currently, there are no known techniques for self-repairing potholes.



Figure 2-21: Induction heating on Dutch Highway A58 [203]

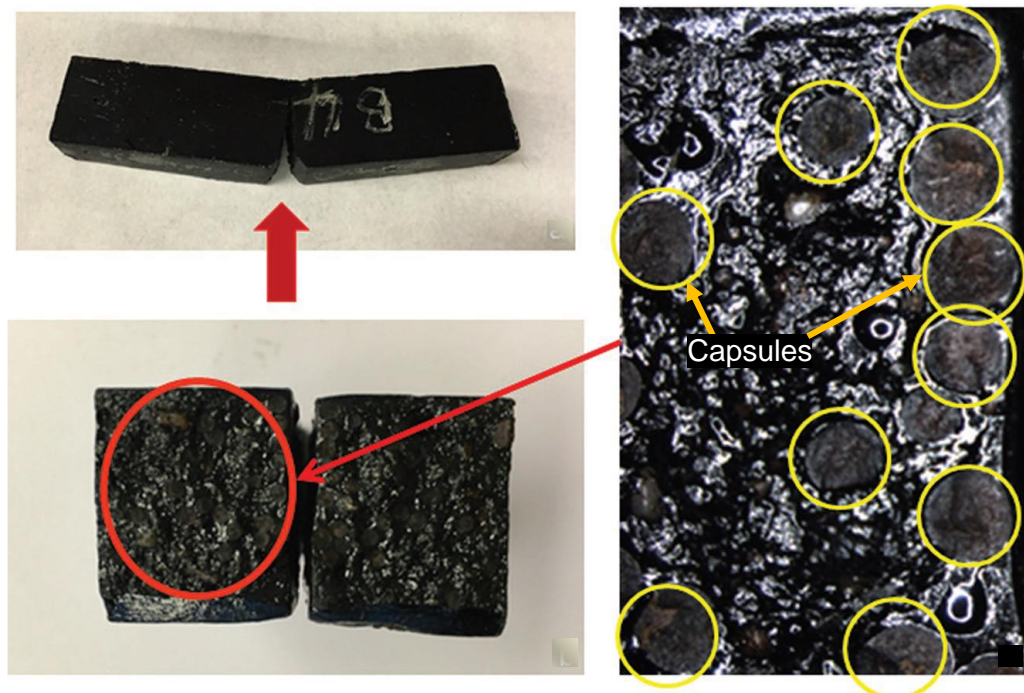


Figure 2-22: Asphalt mastic beam containing encapsulated capsules [203].

Table 2-4 categorises selected common methods of crack filling in concrete and asphalt pavements.

Table 2-4: Classification of crack filling methods in concrete and asphalt pavements.

Author	Repair materials	Approach	Category	Pavement
White et al [184], Vila-Cortavita et al [204], Gomez-Meijide et al [194], Monozzi et al [193]	Conductive particles and encapsulated rejuvenators	Heating of ferrous metals in asphalt mixture through electromagnetic induction and microwaves heating; breaking of capsules	Self-healing	Asphalt
Yin et al [205]	Epoxy resin–sealing materials	Epoxy asphalt on steel bridge deck surfacing	Sealing	Asphalt and concrete
Li et al [186]	seal band (bitumen pellets)	Band pasted over crack and squeezed into by traffic.	Sealing	Asphalt
Li et al [205], Huang et al [206], Lo-presti [54]	fibre materials and rubber modified bitumen	Increase in low temperature cracking resistance with addition of fibre material; and use RMB as binder.	Resilience/preventive	Asphalt
Winterbottom et al [207]	Epoxy, stiches, bandage, dowels	Introduce expansion joints. Other methods include epoxy injection, stitching, post-tensioning, doweling, and bandaging.	Structural crack repairs	Concrete
Winterbottom et al [207]	Epoxy compounds, elastomeric sealants, urethane, cement hydration	Routing and sealing, injection and vacuum impregnation, the gravity-soak technique, overlays and toppings, hydraulic cement-based methods, and autogenous healing.	Non-structural crack repairs	Concrete

In-situ crack filling procedures

To get good performance from crack filling and sealing, it is imperative that correct working procedures are followed. One activity that remains controversial in crack filling is the cutting of crack edges and literature does not explain its advantages and disadvantages. The decision here is therefore mostly left to the discretion of the engineer. However, one activity that is common to all crack repair works is crack cleaning and drying. This is done to achieve adequate adhesion. For cleaner crack surfaces, compressed air and vacuum systems are adopted. Likewise, hot air lances are used to enhance crack drying. After crack cleaning and drying, the sealant is heated to proper application temperature and poured to fill the crack. Crack sealants could be hot-pour or cold-pour [15]. Hot pour-sealants are typically heated above 177 °C before application while cold-pour sealants, usually emulsions, are applied at ambient temperature [15]. Although hot pour is dominant in crack repair, its heating takes a lot of time and poses risk to the labour force. Cold-pour asphalts, however, require a longer curing time. Figure 2-23 shows a crack filling operation by hand with a pour pot.

Technically, all crack treatment techniques are executed by labour forces, and several workers are needed during the maintenance. This condition makes crack treatment uneconomical, time consuming and exposes the labour gang to traffic accidents. According to the Nebraska Department of Roads Pavement Maintenance Manual [2], about 66% of cracks sealing cost is on labour force; and 22% spent on equipment. Interestingly, only 12% of the cost is spent on sealing materials.



Figure 2-23: Crack filling by hand using a pour pot¹⁰.

¹⁰ Roadtech Groups: <https://www.roadtechs.net/highway/cracks-and-joints/>

Machines for crack repairs

The last two decades have seen some advancements in the development of machines inching closer to achieving autonomous crack filling. The Sealzall machine [17] (shown in Figure 2-24), developed by the Advanced Highway Maintenance and Construction Technology Research Centre in California, is a demonstration of such advancements. However, the machine could only fill longitudinal cracks. Even so, a driver had to manually control the vehicle and ensure that a pour pot (a device for dispensing bitumen into cracks) was manually aligned with the crack path. Furthermore, the machines could not fill in-lane cracks, which often have complex alignments. In such circumstances, the work crew had to manually control the hose and nozzle, making the repair process largely labour-intensive.



Figure 2-24: Sealzall machine: (a) during longitudinal crack sealing (b) In-lane crack sealing [17].

A more recent attempt was made by the Self-Repairing Cities project at the University of Leeds [208], demonstrating the possibility of using a drone to perch at sites and fill cracks. The heating system in the drone was adopted from reference [209]. The drone's setup is shown in Figure 2-25. However, the Self-Repairing Cities project did not investigate how cracks were filled or the quality of repairs. Nevertheless, it confirms the possibility of perching at defect sites with autonomous control systems and provides motivation for future automation of pavement repairs.

The drone approach also faces payload limitations, an issue that could be addressed in the future as larger unmanned aerial vehicles, such as flying taxis¹¹, emerge. A picture of a flying taxi is shown in Figure 2-26. Even with this

¹¹ GOV.UK: Flying taxis: <https://www.gov.uk/government/news/the-age-of-the-flying-taxi-draws-closer-with-the-future-of-flight-action-plan>

advancement, lane closures for repair, due to its large size and implications for traffic management, may undermine the sustainability of this approach.

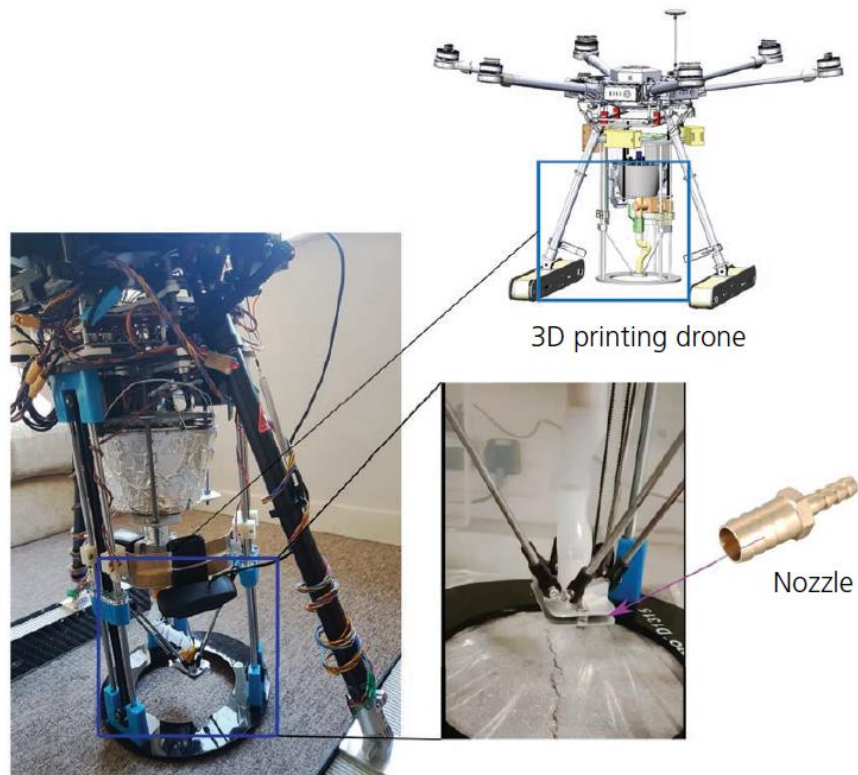


Figure 2-25: A 3D printing drone developed from the Self-Repairing Cities project at the University of Leeds [208].



Figure 2-26: Vertical Aerospace's electric VX4 flying taxi¹².

¹² Vertical Aerospace: Prototype of the VX4 – <https://flyer.co.uk/first-take-off-for-uks-vertical-aerospace-vx4-evtol/>

Performance of asphalt-crack repairing materials and repaired cracks

The efficiency of crack repairing materials depend on their proper technical performance. This largely depends on their ability to withstand being spilled over or squeezed out by the compressive stresses from traffic loading [16]. Materials meeting this requirement should usually bear a large shearing stress, vacuum suction and dynamic water pressure to prevent it from snapping. It should have a good extensibility and cracking resistance as it is being sandwiched between the two cracked blocks which will subject it to compressive forces [16]. Irrespective of how tough a repair material may appear; it must have a good adhesive capability. These performance factors explain why bituminous materials remain an ideal choice for crack repair in asphalt. To improve the technical performance, bitumen is usually modified. Examples of such modified bitumen are styrene-butadiene-styrene (SBS) and styrene butadiene rubber (SBR) [210–212]. Airey [212] revealed that when a continuous polymer network is achieved in the modification process, the alteration gets driven by a highly elastic network which produces an enhanced elastic response, viscosity and stiffness of the polymer modified bitumen (PMB), especially at high service temperatures. Accordingly, polymer modified bitumens are more likely to meet the above indicated performance than unmodified bitumen. However, modified bitumens are difficult to work with and require high temperature heating. Recently, the economic and sustainable impacts of crack repair materials have also become key factors to consider.

It is important to note that repaired cracks can further crack or sustain damage if correct procedures are not followed. An example of such damage is shown in Figure 2-27.



Figure 2-27: Illustration of adhesion loss in sealed cracks on site.

This makes hot-poured bituminous repair materials superior, especially on high-traffic roads, irrespective of their heating challenges. One crucial element of crack sealing is adequate adhesion between the sealed blocks to ensure

resistance to shearing and fatigue. As such, shear bond tests, tensile bond tests, and flexural strength tests have been key tests to assess the performance of repaired cracks in the laboratory [213].

2.5.2 Potholes in flexible pavements

A recurring issue in asphalt pavements is the formation of potholes, which are bowl-shaped holes of various sizes on the pavement surface. These potholes typically arise due to moisture intrusion, freeze-thaw cycles, and traffic-induced loads. Moisture seeps into cracks and holes formed by lost aggregates, expanding when frozen and contracting when thawed, thereby weakening the asphalt. Traffic further exacerbates this deterioration over time, leading to depressions. Factors such as inadequate construction, drainage, or aging can worsen this phenomenon [214,215].

Potholes attract significant media attention, positioning them as key indicators of road quality in the public's perception. Both the public and road authorities regard potholes as particularly undesirable forms of road damage because they can damage vehicles and compromise the safety of road users. Due to limited funding and a lack of knowledge on effective prevention methods, local highway authorities often resort to emergency repairs to maintain safety and functionality. However, these emergency measures tend to be temporary if the materials and methods used are not suited to the existing conditions [215].

Furthermore, there is an increasing trend of heavy vehicles using roads designed for lower traffic volumes, which were not engineered to withstand such loads, resulting in rapid deterioration [215]. This problem is acknowledged globally; inadequately constructed roads break down, diverting traffic to alternative routes and creating similar issues. Pothole repairs are not consistently durable; they can deteriorate swiftly after being made. Sometimes, these repairs may outlast the surrounding pavement, causing greater deflections in adjacent areas. This often leads to deterioration in the nearby pavement, necessitating further repairs. Thus, the durability and effectiveness of repair materials are vital, raising questions about the materials and techniques currently employed in pothole repairs in the UK [13,22,183,215,216].

Prediction of pothole formation

The mechanisms leading to the formation of potholes have been well documented, as seen in references [217–219]. A prevalent theme in the

literature on pothole formation is that water seeps into the pavement through cracks originating at the surface or other surface imperfections. The pressure from vehicle tyres on this water within the cracks and defects weakens the bonds between aggregate particles and layers near these imperfections, leading to asphalt fragmentation. Continuous traffic load exacerbates the issue by dislodging these fragments, deepening the depression. As these depressions enlarge, they hold more water, hastening the damage. Eventually, water reaches the pavement's foundation, softening it and reducing local stiffness, which further accelerates deterioration and creates a pothole. [Figure 2-28](#) illustrates the pothole formation process, adopted from [220] and in agreement with the basic factors causing the formation of potholes from reference [221].

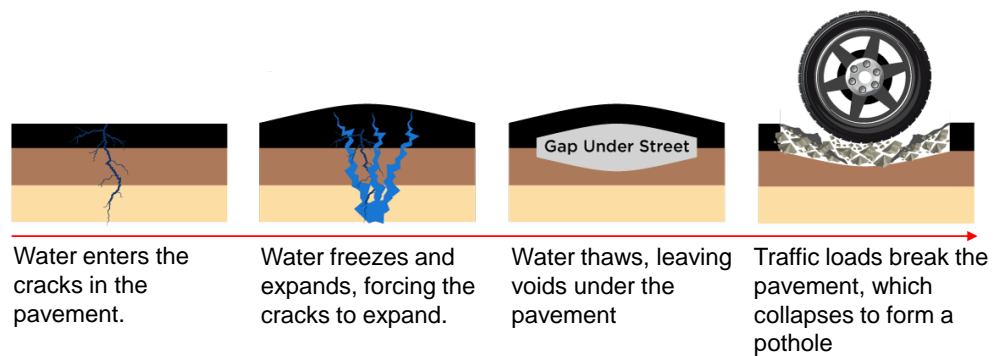


[Figure 2-28: Illustration of the pothole formation process](#) [220].

Despite decades of research into the mechanisms of pothole formation, the literature suggests that further study is still required in this area. This ongoing need for research may be due to evolving construction materials and techniques, as well as changes in climatic conditions.

In the realm of pothole prediction, established models are not known in literature, contrasting sharply with the more developed sector of crack prediction. Certain research efforts, such as those documented in reference [217] have ventured into constructing theoretical models for pothole prediction. However, these models are yet to undergo rigorous validation processes, and their adoption by road authorities as reliable tools remains unconfirmed. [Equation \(2-3\)](#) and [Equation \(2-4\)](#), derived from reference [217], attempts to quantify potential pothole formation within a road network, drawing on the presence of other surveyed road distresses. It's crucial to understand that Abed's model is a statistical correlation that suggests that road sections exhibiting specific distresses may be more prone to pothole development.

Number of potholes on a flexible pavement:

$$NP_{i,k} = PSD_{i,k} \times L_{i,k} \quad (2-3)$$

$$NP = \sum_{k=1}^s NP_{i,k} \quad (2-4)$$

$NP_{i,k}$ represents the total potholes appearing on road segments classified by condition i and severity k . $L_{i,k}$ denotes the cumulative length of these segments, while $PSD_{i,k}$ is defined as the density of potholes, expressed in terms of potholes per kilometer of road (NP/km).

As such, this approach, harbours the potential for misinterpretation, particularly in the absence of concrete evidence linking the severity of one type of defect, such as rut depth which is predominantly used in the modelling, directly to pothole formation. Drawing insight from reference [154], it is evident that rutting does not have a direct relationship with pothole formation, as illustrated in [Figure 2-15](#). This is because the underlying causes and mechanism of rutting and potholes are fundamentally distinct. Consequently, relying solely on such models without acknowledging their limitations and the necessity for empirical validation could lead to misguided maintenance strategies.

Characterisation and measurement of potholes

According to reference [180], potholes should have a minimum plan dimension of 150 mm. Consequently, circular potholes should have a minimum diameter of 150 mm. However, in most road repair manuals, pothole classification is based on depth rather than width. Moreover, road authorities plan repair responses based on the depth of the pothole and the category of the road. Despite the application of these response times, the judgment of the defect inspection officer and the availability of resources remain key factors in determining repair timing. Typically, potholes need to exceed 40 mm in depth to prompt repair action by authorities. An example of a pothole response schedule for Northamptonshire County Council [222] in the UK is presented in [Table 2-5](#). The County response timeframes are implemented prioritising the most urgent response first:

- Emergency: This demands a response within two hours. Instances include road collapses.
- Category 1: Repairs must be completed within five working days.

- Category 2: Repairs are mandated within four calendar months for carriageway potholes and within two calendar months for footway potholes.

Table 2-5: Carriageway pothole response [222] .

Depth	Local Access Road	Link Road	Secondary Distributor	Strategic Route
≥ 40 mm - < 50 mm	No action		Category 2	
≥ 50 mm - < 75 mm (> 30 mph)	Category 2		Category 1 or Category 2	Category 1
≥ 50 mm - < 75 mm (> 30 mph)	Category 1 or Category 2		Category 1	
≥ 75 mm	Category 1			

Pothole repair materials

Several mix types are frequently utilised for pothole repairs, such as hot mixes, cold mixes, warm cold mixes, and mixes that incorporate recycled materials. Hot mixes are generally regarded as the best option for repairing potholes, as suggested by references [69,70]. Nonetheless, these mixes require considerable manual labour to apply. Many organisations employ one or more of the following three types of cold asphalt mixes: mixes prepared by local asphalt facilities using locally sourced aggregates and binders, mixes created as per agency guidelines that specify suitable aggregates and asphalt types, and specialised cold mixes developed with unique binders [223].

Traditional pothole repair techniques

Common repair techniques employed for pothole patching, as described in [22,224,225], include the following:

Throw-and-Go: This method involves depositing the repair mixture into potholes with minimal or no compaction. While it is the quickest and most inexpensive approach for emergency pothole repairs, its lack of proper compaction significantly reduces the repair's durability and effectiveness. This method often results in material displacement under traffic loading, leading to rapid deterioration and the need for frequent re-repairs. Consequently, although the initial costs are low, the cumulative expenses over time can be much higher due to repeated maintenance. Throw-and-go is typically used as a temporary measure during adverse weather conditions or when resources and time are

limited, but it is not recommended as a long-term solution for pavement maintenance. [Figure 2-29](#) depicts the throw-and-go repair technique.



Figure 2-29: Illustration of the throw-and-go pothole repair method¹³.

Throw-and-Roll: This technique includes filling the pothole with patching material and then using truck tires to compact the patch. The compacted patch features a crown ranging from 3 mm to 6 mm.

Semi-Permanent: This approach involves clearing the pothole of water and debris, shaping the sides of the patch area into squares, and then filling it with the mixture, which is subsequently compacted.

Spray Injection: This technique entails clearing the pothole of water and debris, coating the sides and bottom with a tack layer of binder, mixing aggregate with heated asphalt emulsion and then spraying this mixture into the pothole, followed by topping the patched area with a layer of aggregate. The spray injection method does not necessitate compaction.

Edge Seal: Like the throw-and-roll technique, this method consists of filling the pothole with the mixture and then compacting it with truck tires. After the patch has dried, a strip of asphaltic tack material is applied around the edge of the patch, followed by a layer of sand over the tack material.

Advanced pothole repair techniques

Autonomous pothole repair offers several advantages including continuous operation, reduced fatigue, decreased accidents to labour gangs, consistent quality, waste reduction, and possible integration with smart infrastructure, distinguishing it from traditional methods [7]. As a result, there has been a shift

¹³ Start safety Blog: <https://blog.startsafety.uk/2012/09/permanent-pothole-repair-ultracrete/>

in industrial focus towards reducing human involvement in pothole repair. Over the past decade, advanced machines such as those utilising spray injection techniques have emerged [226,227]. An example is the Velocity Spray Injection machine shown in Figure 2-30. However, similar to the throw-and-go method, spray injection techniques simultaneously blow bitumen emulsion and aggregates into potholes [19], a method typically associated with lower durability and primarily used for temporary or emergency repairs [20].

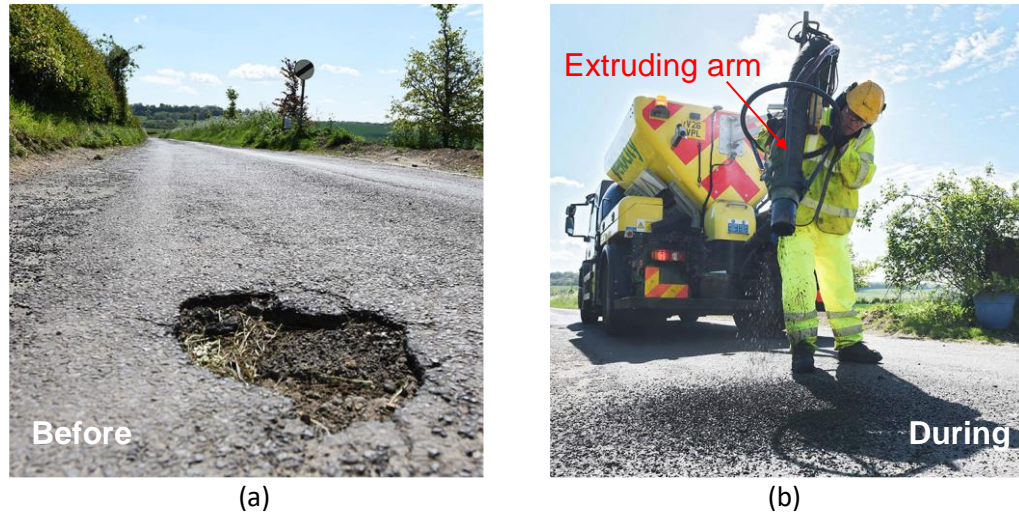


Figure 2-30: (a) Example of a pothole and (b) a Velocity Spray Injection patching machine filling a pothole [19].

Although hot-mix asphalt offers better durability and bonding with existing pavement, regulating its temperature and obtaining a mixture that is extrudable (ability to push through the extruder of repair machines) presents a significant challenge [20,215]. Current flowable or pumpable mixtures (cold mix) commonly used are often linked to reduced durability [21,22]. Additionally, despite being labelled as 'autonomous', these machines do not have the capability to autonomously follow potholes and fill them. Manual intervention is required to control and rotate their extruding arms.

2.6 Repair of Trenches and Openings in Asphalt Pavements

Trenches and openings in highways refer to sections of asphalt or rigid pavements that are excavated temporarily or permanently for purposes such as construction, maintenance, or the installation of utilities and services beneath the road surface. Examples include openings around ironworks, as shown in Figure 2-31. In the UK, the repair and reinstatement of trenches and openings are governed by the Specification for the Reinstatement of Openings in

Highways [228], which prescribes materials, workmanship, and performance standards to ensure durability and compliance.

The repair process often mirrors procedures used in semi-permanent pothole repairs (see Section 2.5.2). For instance, wide cracks or damaged sections that must endure heavy traffic are typically filled with a bitumen mixture combined with aggregate (asphalt) to enhance structural integrity. Advanced methods, such as performance mix designs (see Section 2.4.4) and rigorous compaction techniques, are also applied to ensure that repaired sections effectively withstand traffic loads and environmental stresses.

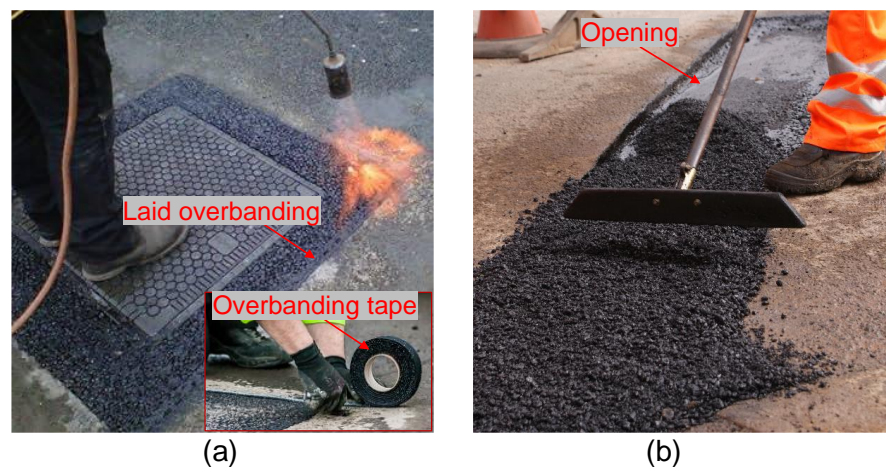


Figure 2-31: Reinstating openings in flexible pavements, (a) ironworks with overbanding, and (b) utility opening¹⁴.

2.6.1 Structural integrity of repaired potholes, trenches, and openings

The quality of filled potholes is typically assessed by determining how they deform under traffic loading. The wheel tracking test has been a common standard test used for this assessment in the laboratory. Similarly, reinstated trenches and openings are expected to deform within certain tolerable limits; beyond these limits, the reinstatement work would be classified as failed. For example, for a reinstatement width of 1.0 m, a cumulative settlement above 30 mm is not tolerated under normal ground conditions [228]. To ensure that laid asphalt mixtures meet these performance requirements, the stability and flow properties of repair mixtures [123,229] have to be enforced. An example of a settled reinstated trench on the University of Nottingham's University Park's campus, in front of the Trent building is shown in Figure 2-32.

¹⁴ Tarmac: <https://tarmac.com/products/asphalt/enhanced-reinstatement-asphalt/>



Figure 2-32: Illustration of a settled trench fill (Location: Trent Building, University Park; Date: June 27, 2022).

2.7 Overbanding

Overbanding is a road maintenance technique used to seal cracks, joints, or the edges of repairs in pavement surfaces, such as those in potholes, trenches, and openings. This process involves applying a strip of sealing material over the repaired area or crack to create a waterproof barrier. The materials used for overbanding typically include bituminous products, resins, or specialised tapes that adhere well to the pavement and provide a durable, flexible seal. The choice of material can depend on the traffic volume, expected wear, and environmental conditions. The application typically involves heating the overbanding material to ensure a good bond with the pavement surface [182]. An example of an overbanding tape and its application is shown in Figure 2-31.

2.8 Comparing Productivity in Construction to Other Core UK Industries

As illustrated in Figure 2-33, the construction sector has exhibited the lowest productivity performance over the past two decades compared to other key UK industries, such as production, manufacturing, and services [1].

Productivity in manufacturing, for example, is higher than in construction primarily due to the extensive adoption of automation technologies. In manufacturing, repetitive and precision tasks can be efficiently performed by automated machinery, robotics, and computer-controlled processes. These

technologies streamline production lines, reduce human error, and increase output consistency, resulting in higher overall productivity.

In contrast, construction projects often involve bespoke designs, variable site conditions, and a high degree of manual labour. The complexity and variability inherent in construction projects make it challenging to implement automation to the same extent as in manufacturing. While advancements in construction technology, such as prefabrication and modular construction, are beginning to bridge this gap, the sector still lags behind manufacturing in the widespread adoption of automation, leading to comparatively lower productivity.

According to reference [9], the UK could potentially save approximately £15 billion annually by enhancing construction productivity. Automation has been identified as a pivotal factor in achieving this improvement [3,214,226,230].

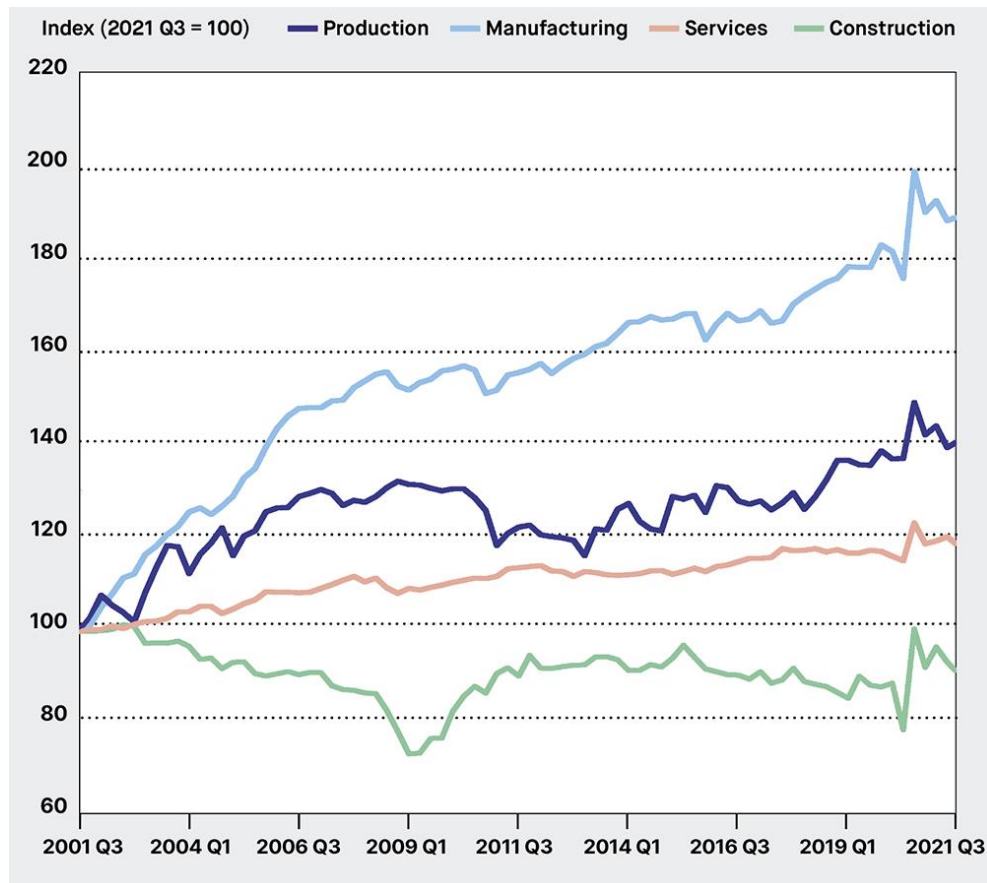


Figure 2-33: Productivity in core UK industries (output per hour worked) [1].

2.9 Automation in Construction and Road Maintenance

The integration of automation in construction and road maintenance represents a significant opportunity for improving infrastructure globally. As technology advances, automation holds immense promise for revolutionising the way roads

are built and maintained, leading to safer and more efficient transportation networks.

Several studies have highlighted the potential benefits of automation in construction and road maintenance [3–8]. For example, research has shown that automated construction processes can increase productivity, reduce costs, and enhance safety by minimising human error and exposure to hazardous conditions [231–233]. Furthermore, the use of autonomous machinery and robotics in road maintenance can improve efficiency and accuracy in tasks such as pothole repair and pavement inspection. Moreover, the adoption of automation in construction and road maintenance aligns with broader efforts to modernise infrastructure and embrace sustainable practices [234]. Automated systems could also contribute to reducing carbon emissions and minimising environmental impact by optimising resource usage and reducing waste.

Figure 2-34 shows the Hadrian X [235], a prominent robotic construction machine capable of swiftly and efficiently erecting walls for family homes and commercial structures of up to 2.5 storeys. The latest version of the Hadrian X can construct a standard family home in around two days. The upcoming iteration is planned to achieve a maximum speed of laying of approximately 60 square metres of wall per hour. Figure 2-35 also shows a robotic arm installing slabs in-situ. These exemplify how automation can enhance productivity in the construction industry.



Figure 2-34: The robotic Hadrian X for constructing houses [236].

In road maintenance, defect identification techniques powered by machine learning algorithms have enabled rapid and accurate assessment of road conditions in the field. By analysing data from various sources such as images, videos, and sensor readings, these techniques can detect and classify defects with high precision, allowing maintenance crews to prioritise repairs and allocate

resources effectively. Figure 2-36 illustrates an example of an automated road condition survey system by Data Collection Ltd's ROad Measurement Data Acquisition System (ROMDAS) [237].



Figure 2-35: Robotic arm installing slab on site [238].

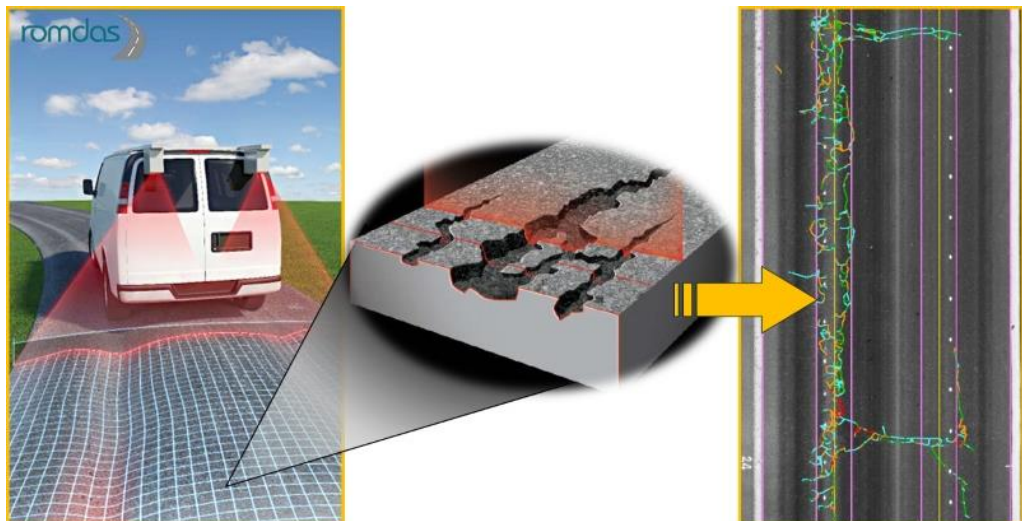


Figure 2-36: Illustration of automated Road Condition Survey from ROMDAS¹⁵.

2.10 Additive Manufacturing (3-D printing) of Structures

Three-dimensional printing involves the production of physical objects through the sequential layering of thin materials. In 1989, Sachs et al. [239], scientists at the Massachusetts Institute of Technology, were the first researchers to patent the term "3D printing" in the acronym 3DP. Through 3D printing technology, a digital model can be transformed into a physical object. Digital models are typically designed using CAD programs, which are then sliced into two-dimensional layers and converted into printing commands. The sequential building of slices in 3D printing, one layer on top of another, gives it the name

¹⁵ ROMDAS: <https://romdas.com/romdas-system.html>

additive manufacturing. The additive manufacturing process differs from consolidation and subtractive processes, which involve casting or moulding objects, and cutting and machining, respectively. Through 3D printing, complicated and customised shapes can be printed with ease and speed, resulting in less waste. However, 3D printing is mainly applicable to comparatively smaller objects, making the printing of large objects tedious and expensive. Consequently, most industries adopt additive manufacturing for prototyping parts, which will then be produced on a mass scale using traditional manufacturing methods. Additionally, there are limitations on the materials that can be used for 3D printing [240].

2.10.1 3D printing methods and materials in construction

Major 3D printing techniques include fused deposition modelling, powder bed fusion, inkjet printing and contour crafting, stereolithography, direct energy deposition, and laminated object manufacturing. Table 2-6 provides a summary of the main methods used in additive manufacturing and their materials, field of application, benefits and drawbacks. Materials widely used include resin, thermoplastics, alloys, paper, and concrete. The 3D printing method has already become a mature technology. It is being applied in areas such as civil engineering, architecture, and the development of structural components [4,241]. For instance, [241] used a 3D printing machine with a V-shape extruder to design six different ratios of concretes and optimised the mix ratio of cement concrete based on its extrudability and buildability. Reference [242] discussed the design, printing, and assembly of a 3D printed concrete bridge, which has been in service since October 2017. Figure 2-37 shows a 3D-printed wall and a house, while Figure 2-38 shows a concrete extruding nozzle developed by [241].



Figure 2-37: (a) a layer-by-layer arrangement in a concrete 3D printed structure [241], and (b) a 3D printed house by WinSun [243].

Table 2-6: Comparison of main methods of 3D printing.

Methods	Material	Applications	Benefits	Drawback
Stereolithography [244]	Resin and hybrid polymer-ceramics	Prototyping and biomedical	High quality with fine resolution	Printing is slow and uses very limited materials
Fused deposition modelling [244]	Continuous filament of fibre-reinforced and thermoplastic polymers	Advanced composite parts and rapid prototyping	Simple and cheap yet operates at high speed	Uses only thermoplastics and has weak mechanical properties
Laminated object manufacturing [245]	Metal rolls, ceramics, paper, polymer composites and metal-filled tapes	Smart structures, foundry industries, paper manufacturing and electronics	Fast, cheap, uses variety of materials, great for producing larger objects	Lacks dimensional accuracy and has inferior surface quality.
Powder bed fusion (SLM, SLS, 3DP) [244]	Alloys, limited polymers (SLM or SLS); polymers and ceramics (3DP)	Electronics, Biomedical, heat exchangers and lattices	Fine quality and high resolution	Slow printing and expensive
Direct energy deposition [246]	Ceramic, polymers and alloys	Biomedical, repair, aerospace, cladding, retrofitting	Fast and cheap, accurate composition control, great for repair	Low surface quality
Inkjet printing and contour crafting [247]	Dispersion of particles in a liquid, ceramic, soil and concrete	Biomedicals, building and large structures	Fast printing of large structures	Lack of adhesion between layers



Figure 2-38: Extrusion of concrete from a 3D printing nozzle [241].

Fused Deposition Modelling 3D printers

In literature, Cartesian 3D printers, Polar 3D printers, Delta 3D Printers and Robot arm 3D printers are the main categories of Fused Deposition Modelling (FDM) 3D printing technologies [245,248]. Figure 2-39 shows examples of the four FDM printers and compares their printing time, quality, and cost. Most cutting-edge printers utilise Cartesian systems [248]. Characterised by its linear motion system along three axes (X, Y, and Z), Cartesian printers feature a rectangular build platform and vertical movement of the print head. Their versatility, simplicity, and ease of customisation have made them a popular choice among researchers [248].

	Cartesian 3D Printer	Polar 3D Printer	Delta 3D Printer	Robot arm Printer
	3 Axis	3 Axis	3 Axis	3 Axis
Printing Time				
Surface Quality				
Investment Costs				
Examples				
	Ultimaker S3 ¹	Polar 3D ²	Delta Go ³	Yizumi SpaceA ⁴

Graduation:

high

middle

low

Sources:

1) <https://ultimaker.com/en/products/ultimaker-3/specifications>

2) <https://polar3d.com/>

3) <https://www.deltaprinter.com/product/delta-go/>

4) <https://www.yizumi-germany.de/spacea-additive-fertigung/>

Figure 2-39: Comparison of FDM 3D printers in the market [248].

Polar 3D printers, on the other hand, employ a rotating build platform and a print head that moves radially and vertically. Utilising polar coordinates, with movement typically defined by angles and radii, Polar printers offer unique design possibilities and can be advantageous for certain applications, such as printing cylindrical objects or intricate designs.

Delta 3D printers feature three vertical columns with movable arms connected to a central carriage. Using a parallel arm mechanism to move the print head in a precise and coordinated manner, Delta printers are known for their fast-printing speeds and smooth, continuous movements. This makes them suitable for producing objects with curved surfaces or complex details.

Robot Arm 3D printers employ robotic arms with multiple degrees of freedom to manoeuvre the print head. Offering exceptional flexibility and the ability to access various orientations and angles, Robot Arm printers are often used in industrial settings where precise control and versatility are required. Industries such as aerospace or automotive manufacturing benefit from the capabilities of Robot Arm printers for complex printing tasks.

Among these configurations, the Cartesian printer stands out for its ability to handle high payloads, cost-effectiveness, ease of operation, and efficient printing times. With its robust linear motion system, Cartesian printers are capable of handling heavier payloads, making them suitable for printing large objects or using multiple extruders simultaneously. Additionally, their straightforward mechanical design and widely available components contribute to their affordability and ease of maintenance. The Cartesian coordinate system, aligning with familiar mathematical and graphical principles, results in user-friendly software interfaces and simplified calibration processes, reducing the learning curve for users. Finally, Cartesian printers are known for their precise and rapid movements along the X, Y, and Z axes, resulting in faster printing speeds. This efficiency is particularly valuable in industrial settings where time is critical and high production volumes are required.

2.10.2 Screw extrusion-based additive manufacturing

Screw extrusion-based additive manufacturing (SEAM) represents a significant advancement in the field of 3D printing, merging traditional extrusion techniques with modern additive manufacturing processes. This technology utilises a screw mechanism to extrude materials, such as polymers or composites, layer by layer to form three-dimensional objects. The evolution and application of SEAM have been subjects of extensive research and development, offering unique advantages in terms of material versatility, efficiency, and the capability to produce parts with complex geometries. [Figure 2-40](#) compares screw-based additive manufacturing with plunger-based and traditional filament-based methods.

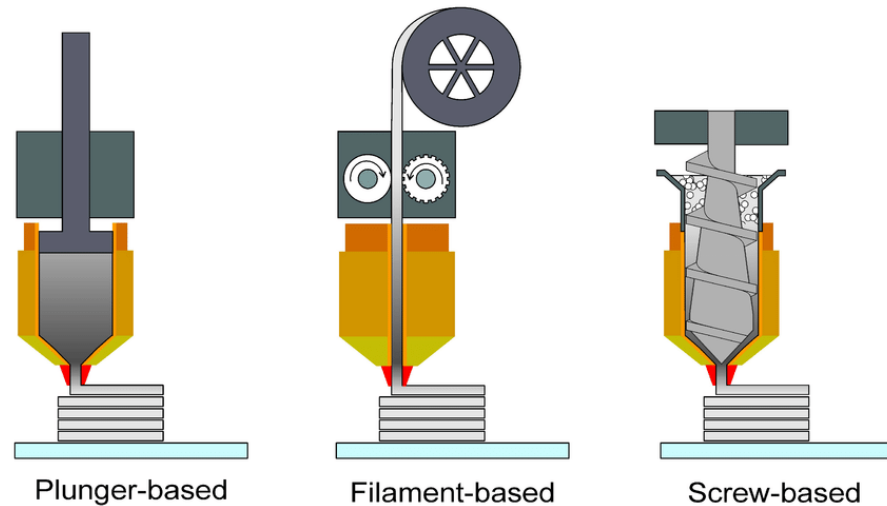


Figure 2-40: Comparison of screw-based additive manufacturing with plunger-based and traditional filament-based methods [249].

In the early 2000s, advancements in material science and mechanical engineering facilitated the development of SEAM systems capable of processing a wider range of materials, including high-performance thermoplastics [250–252], thermoset polymers [253], metals [254,255] and composite materials [241,256]. This period also saw the integration of computer-aided design (CAD) and computer-aided manufacturing (CAM) software with SEAM, enhancing the precision and repeatability of the manufacturing process.

Studies have explored the influence of screw design, extrusion parameters, and material formulations on the mechanical properties and microstructure of printed parts. References [250,257–260] have contributed significantly to understanding material flow behaviour and optimisation techniques for enhanced material properties. Also, research has been dedicated to optimising process parameters such as screw speed, temperature profiles, and layer height. The work referenced in [250,258], for example, has shown that careful control of these parameters can significantly improve the surface finish, dimensional accuracy, and structural integrity of parts produced by SEAM.

Furthermore, one critical parameter in the design of extruder barrels is the die angle. This is the angle formed by the walls of the die as they converge towards the die opening where the material exits as illustrated in Figure 2-41. This angle plays a significant role in determining the amount of friction between the material and the die walls, which in turn influences the extrusion force needed and the possible formation of defects in the extruded product.

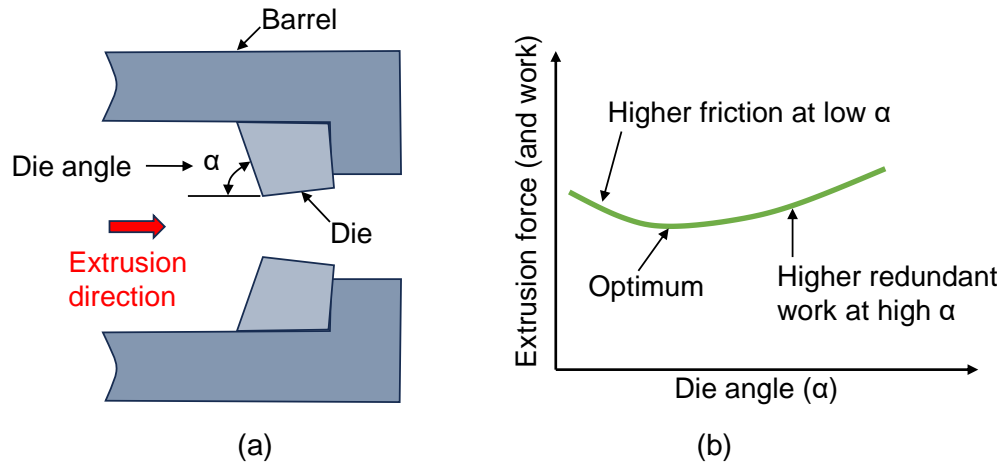


Figure 2-41: (a) Illustration of die angle and (b) effect of die angle on extrusion force (adapted from reference [256]).

A smaller die angle can increase the material's contact with the die, raising friction and potentially improving surface finish but requiring higher force for extrusion. Conversely, a larger die angle may reduce friction and extrusion force but can lead to less precise surface finishes. The optimal die angle is therefore dependent on the material being extruded, the desired properties of the final product, and the specific requirements of the extrusion process.

O'Neill et al. [261] conducted a study on extruding calcium phosphate paste (a non-Newtonian fluid), shedding light on how die angles in the chamber impact concrete extrusion. Using extruders with die angles 90° , 55° and 45° for testing, the observed liquid powder ratios¹⁶ (LPRs) were 0.492, 0.449, and 0.434, respectively. Findings revealed that a 45° die angle significantly lowers the LPR requirement and decreases phase separation¹⁷, attributed in part to reduced extrusion pressure [262]. While similar outcomes were reported by references [263,264], Nienhaus et al. [265] discovered that a very acute die angle of 28° resulted in a relatively low extrusion force (about 20.5 N) compared to 45° (about 22.7 N) and 70.5° (about 23 N). Nonetheless, an even smaller die angle of 15.5° did not further reduce the extrusion force (about 21.7 N). Moreover, the study highlighted an additional advantage of die angles in preventing dead

¹⁶ The liquid to powder ratio (LPR) in concrete refers to the proportion of liquid components (usually water) to the powder components (such as cement, fly ash, silica fume, and other cementitious materials) in the concrete mix.

¹⁷ Phase separation in concrete extrusion refers to the phenomenon where the components of the concrete mix segregate or separate from each other during the extrusion process.

zone¹⁸ formation near the outlet, thereby reducing blockages and enhancing extrusion quality [261].

Practically, the screw-based extrusion is the closest to the auger-extrusion method used in real asphalt paving machines, as shown in Figure 2-42. This likely gives the screw-based method a high chance of success in being adopted for creating asphalt extruding 3D printers or miniaturised pavers in the laboratory.



Figure 2-42: Illustration of an auger in an asphalt paver, captured on site after paving works.

With an increasing focus on sustainable manufacturing practices, literature has also begun to explore the use of bio-based and recycled materials in SEAM. Research by references [266–268] highlights the potential of SEAM in promoting circular economy principles within additive manufacturing. In recent studies, reference [241] adopted SEAM for building concrete structures, a technique that could be highly adapted for asphalt concrete. Certainly, unlike with concretes, controlling the heating of bitumen in asphalt to achieve desirable asphalt performance remains a gap in the science.

2.10.3 3D-printing for road repairs

The use of real 3D printed specimens in repairing pavement layers was primarily demonstrated by [269] where a printed 3D block was used to repair spall damage in concrete roads. Concrete patches were printed off-site and then glued to the spall surface at the site. It could be argued that the structural stability of the repair work was rather more dependent on the adhesive force of the adhesives holding the concrete patch in place. Nonetheless, the repair work

¹⁸ A dead zone in the extrusion of materials refers to an area within the extrusion equipment, typically near the die in the barrel, where the material flow is stagnant or significantly slower compared to the rest of the material being extruded.

looked promising as the 3D concrete patches exhibited high structural stability with a tolerable shear load of up to 15.7 MPa. However, this repair technique was applied to rigid pavements, and there is no evidence of the same method's success in flexible pavements. Figure 2-43 illustrates the spall patching procedure.

Currently, there is no evidence of successful in-situ repair of potholes with 3D printing techniques.

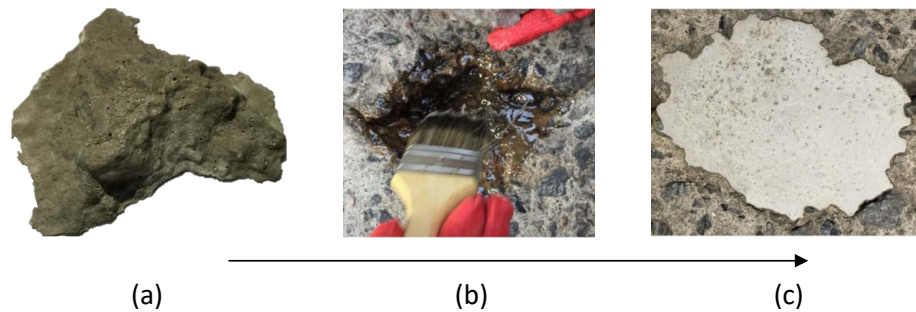


Figure 2-43: Spall damage repair using 3D printed concrete: (a) concrete patch produced for the experiment, (b) applying adhesive to the concrete patch, and (c) concrete patch seated in the damaged area [269].

2.10.4 Integrating 3D printing with smart technologies in road works

Cambridge University scientists have developed the first 3D-printed concrete headwall for culverts, installed on the A30 in Cornwall by National Highways. Equipped with sensors for temperature, strain, and pressure data, the headwall has a digital twin in the laboratory that provides live performance updates, enabling early fault detection and improving infrastructure efficiency and reliability. Figure 2-44 shows the 3D printed headwall.



Figure 2-44: 3D printed headwall by Cambridge researchers installed on a section of the A30 road in Cornwall¹⁹.

¹⁹ Credit: University of Cambridge research news:
<https://www.cam.ac.uk/research/news/cambridge-researchers-help-develop-smart-3d-printed-concrete-wall-for-national-highways-project>

2.10.5 Major challenges to 3D printing

It has been highlighted that 3D printing presents freedom of design and the ability to print complex structures with minimum waste. However, the technique is known to be expensive and exhibit anisotropic mechanical behaviour [240]. In addition, 3D printed layers are associated with void formations between adjoining layers and reduced interfacial bonding can result in poor mechanical performance [244].

2.11 4D Printing of Structures

Recently, the exploration of 3D printed structures that can change shape dynamically has emerged as a groundbreaking progression in additive manufacturing (AM) techniques. This notion of dynamic structures was initially conceptualised in 2013 by reference [270] proposing the term "4D printing" to describe the fabrication of 3D printed objects with the ability to modify their shape autonomously as time progresses. According to [270], 4D printing involves programmable materials that allow printed structures to transform over time, influenced by water, temperature, light, or other external triggers. This adaptability is achieved through the precise design of material composition and geometry at the microscale, enabling pre-programmed shape changes [271].

A critical aspect of 4D printing is the development of smart materials. Shape memory polymers (SMPs), hydrogels, and composite materials are commonly used due to their ability to undergo significant deformation and return to their original state under specific conditions [272]. The integration of these materials with advanced manufacturing techniques, such as selective laser sintering (SLS) and fused deposition modelling (FDM), enables the creation of complex, responsive structures [273].

The application of 4D printing is particularly promising in the field of structural engineering. Researchers have explored its use in self-assembling structures for space habitats [274], adaptive infrastructure capable of responding to environmental conditions, and smart building components, such as pipes and beams, that can adjust to load changes [275]. Despite its potential, 4D printing faces several challenges, including the limited range of materials with suitable properties, the complexity of programming shape transformations, and the scalability of printed structures [276]. [Figure 2-45](#) illustrates a 4D printed flower-shaped hydrogel architecture changing its shape over time through use of anisotropic swelling behaviours when exposed to water [277].

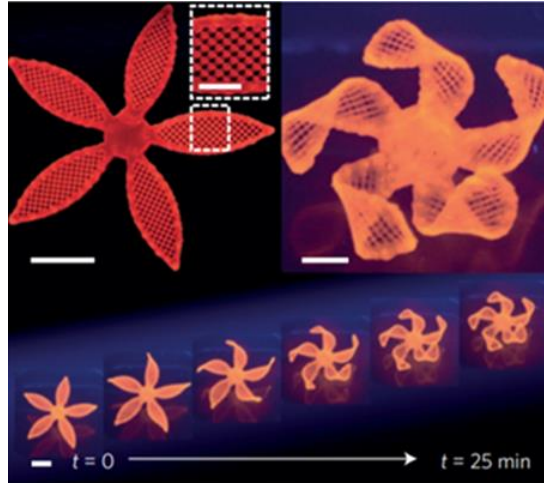


Figure 2-45: Illustration of the shape changing performance of the 4D printed flower over time [277].

2.12 Application of Physics Engine in Pavement Engineering

Physics engines are software tools that enable computers to approximate real-world physical phenomena, such as gravity, fluid dynamics, and collision forces, and apply them to 3D objects in computer graphics. These tools are commonly used in applications like video games, films, and architectural design, where they facilitate realistic simulations and 3D rendering of objects and environments. Commercially known physics engines include PhysX, Box2D, BeamNG, Bullet, PhysicsJS, and Matali Physics. For example, Box2D has been utilised to simulate polygonal particles with random shapes, as demonstrated in reference [278].

In structural engineering, physics engines have been adopted for structural analysis tasks. Reference [28], for instance, developed an algorithm capable of simulating the collapse of buildings. In the field of pavement engineering, physics engines have been successfully applied to simulate the motion of aggregates under compaction forces [26,30,31,142,144]. These simulations generated virtual aggregate skeletons that closely mimic aggregates in real asphalt mixtures. The method employed by [26], illustrated in Figure 2-46, demonstrates the ability of physics engines to replicate realistic aggregate behaviour in a virtual environment.

The advent of virtual simulation techniques using physics engines represents a significant advancement for pavement engineering. With the ability to estimate the volumetric properties and aggregate-mastic components of asphalt mixtures, these tools offer significant potential for the digital design of asphalt mixtures. This is grounded in the concept that the volumetrics and properties of

key components, such as aggregates and mastics, directly influence the mechanical behaviour of asphalt mixtures [279,280].

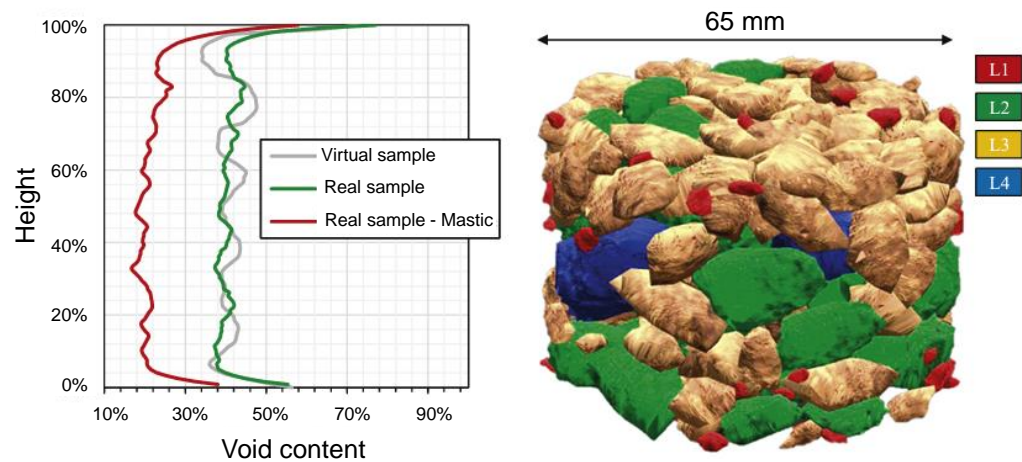


Figure 2-46: Example of a physics-engine-generated virtual aggregate²⁰ skeleton [26].

2.13 Literature Review Summary and Its Impact on the Methodology Adopted in the Research

Identified gaps in the state-of-the-art, a summary of useful information, and their impact on the methodology and approach used in the research are detailed as follows:

- i. Cracking is the most common distress in flexible pavements making up about 70% of all defects. Cracks could lead to a pothole if not repaired on time.
- ii. Crack and pothole repairs are mainly performed by labour forces, making the process costly, time-consuming, and risky due to traffic accidents. According to the Nebraska Department of Roads Pavement Maintenance Manual, labour costs account for approximately 66% of asphalt pavement crack repair expenses, with equipment and sealing materials representing 22% and 12% of costs, respectively. In the UK, the labour-intensive construction sector is notably the least productive compared to core industries such as production, manufacturing, and services.

Impact on research (IoR): The research will focus on automating crack and pothole repairs to minimise human involvement.

²⁰ The legend (L1 to L4) describes the limestone aggregate fractions utilised.

- iii. Repairing cracks in moderately cool temperatures, like in spring and autumn, is recommended.

IoR: Cracks simulated in the laboratory will be filled at room temperature.

- iv. Hot bitumen, both modified and unmodified, is commercially available for crack filling works. An important element of crack filling is ensuring adequate adhesion between the filled areas to provide resistance to shearing and fatigue. Additionally, the primary purpose of filling cracks is to prevent water from penetrating the inner layers of the pavement.

IoR: Commercially available hot bitumen will be used for the crack filling works. The air voids trapped in the fillers and between the bitumen and crack walls will be evaluated to assess the potential for water to permeate the filled cracks. X-ray CT scanning will be used for this assessment. Furthermore, to assess the adhesive and filling quality, shear bond tests, tensile bond tests, and flexural strength tests will be performed on filled cracks.

- v. A key quality requirement for pothole filling is stability. Similarly, reinstated trenches and openings in carriageways are expected to exhibit minimal settlements within tolerable limits. Air void content plays a crucial role in meeting these requirements.

IoR: The Marshall stability and flow tests ensure repaired asphalt mixtures meet industry standards for stability, flow, and air void content. Repair quality will be assessed by comparing these performance parameters between automated and manual repairs.

- vi. Current machines for crack filling and pothole repairs lack the autonomy to follow crack paths and pothole geometries during repair works. 3D printing technology appears promising in addressing this gap due to its capability to follow complex shapes and maintain steady temperature and printing speed when in use. Among available commercial printers, Cartesian 3D printers are superior in

terms of customisation, simplicity of use, cost, and, most importantly, payload capacity.

IoR: 3D printing technology will be applied to autonomously follow the geometry of defects during repairs. This is achieved by modifying a RepRap Cartesian 3D printer.

- vii. Current pumpable mixtures commonly used by commercial pothole repair machines are cold mix asphalt mixtures, which are associated with reduced durability. The biggest challenge in using HMA is that the mixtures are not workable and pose challenges in being satisfactorily extruded while meeting performance parameters like stability and flow.

IoR: A new asphalt mixture design method will be developed.

- viii. Practically, meeting all pavement performance requirements is nearly impossible. Asphalt mixtures are currently designed for optimal service and cost-effectiveness rather than maximum performance. A design approach that optimises the performance criteria of asphalt mixtures has been shown to effectively produce durable and high-quality mixtures.

IoR: The proposed new asphalt design method will be performance-based, aiming to meet specific industrial performance targets.

- ix. Distresses are influenced by the relative quantities of aggregate and asphalt binder in mixtures. Consequently, careful control over the characteristics and quantities of aggregates and bitumen in a mixture could lead to the development of mixtures with customised functionalities.

IoR: The morphology of aggregates will be incorporated into the newly developed design method to assist in optimising mixtures to meet specific functionalities, such as being workable and stable.

- x. There are no standardised methods of assessing the workability of asphalt mixtures. This is major barrier to evaluating how workable

new asphalt mixtures could perform whether laid directly on roadways or pumped through machines for repairs.

IoR: A new method for estimating the workability of asphalt mixtures will be developed using a simple and non-electric plunger penetration technique.

- xi. Physics engines, such as PhysX, Box2D, and Bullet, simulate real-world phenomena like gravity and fluid dynamics for 3D objects in video games and films, facilitating realistic interactions and design concepts. These engines can also be utilised to simulate the components of asphalt mixtures, such as aggregates and bitumen, accurately mirroring the properties of the real materials. This aids in understanding and predicting the behaviour of asphalt mixtures.

IoR: A physics engine software will be used to streamline and digitise the design of new asphalt mixtures suitable for automated pothole repair by machines.

- xii. Pothole and crack repairs have been manually performed for decades.

IoR: Hand filled cracks and potholes will be used as a control in the research.

- xiii. Extrusion-based 3D printing has been successfully adopted for printing concrete. The extrusion screw, barrel design, and operational parameters of the printing process must be optimised to enhance the quality of the material extruded. Similarly, the material for extrusion must be carefully formulated to acquire the required mechanical properties.

IoR: A mini paver machine based on screw-extrusion 3D printing will be developed for pothole repairs, with optimised operational parameters such as screw speed and motor power. The barrel and screw blades will be designed for the maximum aggregate size, and the extrusion ability of the machine will guide the formulation of asphalt cartridges used for repairs.

Chapter 3: Materials and Methods

3.1 Introduction

This chapter provides a detailed overview of the materials, equipment, and methodologies that form the foundation of this research, ensuring their alignment with the overarching objectives and their integration into a cohesive research framework. Firstly, the properties of aggregates, fillers, and bitumen used in asphalt mixtures are introduced, alongside the preparation of compacted asphalt specimens to simulate pavement cracks and potholes for targeted repair investigations ([Chapters 4 and 6](#)).

Objective 1 (addressed in [Chapter 4](#)) involved the modification of an Original Prusa MK3 3D printer to automate crack filling. Similarly, Objective 3 (discussed in [Chapter 6](#)) leveraged the printer for pothole filling applications. Quality assessments included advanced techniques such as X-ray CT scanning to evaluate crack fill integrity and wheel tracking tests to assess the quality of filled potholes. In addition, the methodologies used to achieve Objective 2 ([Chapter 5](#)) employed a physics engine to optimise digital asphalt designs, culminating in the development of virtual asphalt cartridges for automated repairs.

Additionally, this chapter provides details on the dominant design standards and statistical methods applied in the analysis of experimental results. It is worth noting that some statistical expressions, such as the Weibull equations, are not explicitly presented in this thesis, as they were computed using software tools like MATLAB, which are duly acknowledged. However, the equations are stated in the methodology to demonstrate the theoretical foundation used in the software. Furthermore, equations directly associated with the development of new models, such as rational regression equations, are fully detailed in the relevant chapters to ensure methodological clarity and reproducibility.

Furthermore, certain experimental procedures specific to later chapters are presented within those chapters. For instance, the methodology for simulating cracks in asphalt in the laboratory, which is exclusive to Objective 4, is detailed in [Chapter 6](#). This structured approach ensures a logical progression and enhances the readability of the thesis. Conversely, methodologies that are specific to certain chapters and hold exclusive novelty to the thesis, but are not extensive enough to justify standalone chapters, are detailed in this chapter. For

example, the development of a novel workability device for assessing asphalt mixtures is described in [Section 3.3.4](#).

Finally, [Figure 3-47](#) provides a visual summary, linking methodologies, research objectives, and corresponding chapters to clarify the systematic approach underpinning this research.

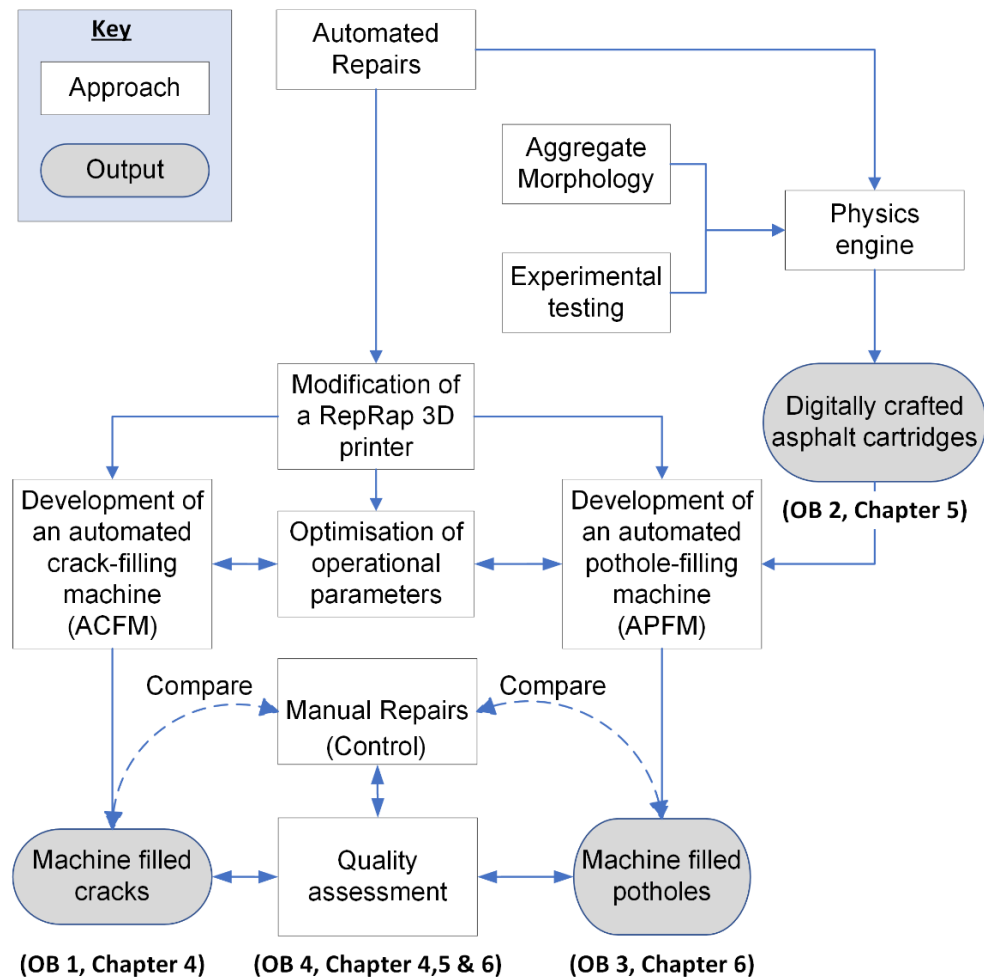


Figure 3-47: A flowchart linking the methodologies, chapters, and objectives of the research.

3.2 Methods

3.2.1 Aggregates and bitumen for the asphalt pavement

The asphalt mixture used in this research for creating surface course (see [Section 2.3.1](#)) was Stone Mastic Asphalt with maximum aggregate size 10 mm and paving grade (PG) bitumen 40/60. It had air void content of 4.5%, a density of 2,459.0 kg/m³, and a binder content of 5.6%. The aggregates used were crushed limestone with a density of 2.7 Mg/m³, and their gradation is shown in [Figure 3-48](#). The 40/60 pen-grade bitumen binder had penetration and softening

point of 43 mm and 51.0 °C, respectively. SMA was chosen because it is a typical surface course material in the UK, known for its high performance. The SMA 10 surf 40/60 was designed following BS EN 13108-5:2016 [281], and mixed and compacted following BS EN 12697-35:2016 [282] and BS EN 12697-33:2019 [283], respectively.

3.2.2 Asphalt manufacturing

The bitumen and aggregates were pre-heated to 155 °C for 4 hours and 12 hours, respectively. The batching moulds were equally heated at 155 °C for 4 hours. Aggregates were premixed for about 30 seconds, and then the heated bitumen was added to the premixed aggregates for a further 3 minutes mixing. The hot mixed asphalt was then placed into the hot moulds in an asphalt slab roller compactor for immediate compaction. The compacted slabs were allowed to cool down for about 48 hours and then sawn into the desired specimen sizes. The sawn specimens and how they are assembled to simulate cracks and potholes in the laboratory will be discussed in [Chapter 5](#) and [6](#). [Figure 3-48](#) shows the aggregate gradation curve used for the surface course slabs. In addition, [Figure 3-49](#) shows the batching, asphalt mixing and produced compacted asphalt SMA-10 asphalt slabs. Details of the properties of the 40/60 pen-grade bitumen used are also shown in [Table 3-7](#).

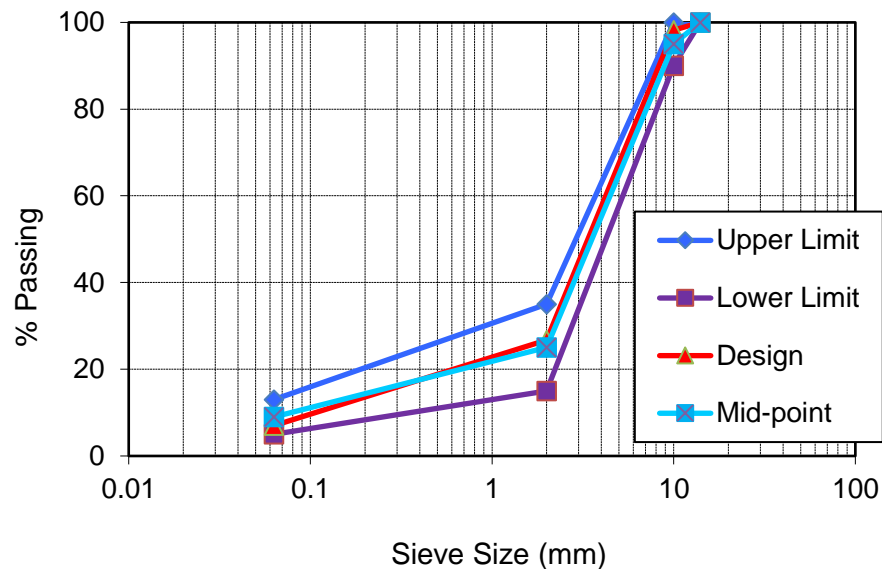


Figure 3-48: Aggregate grading curve for SMA-10.

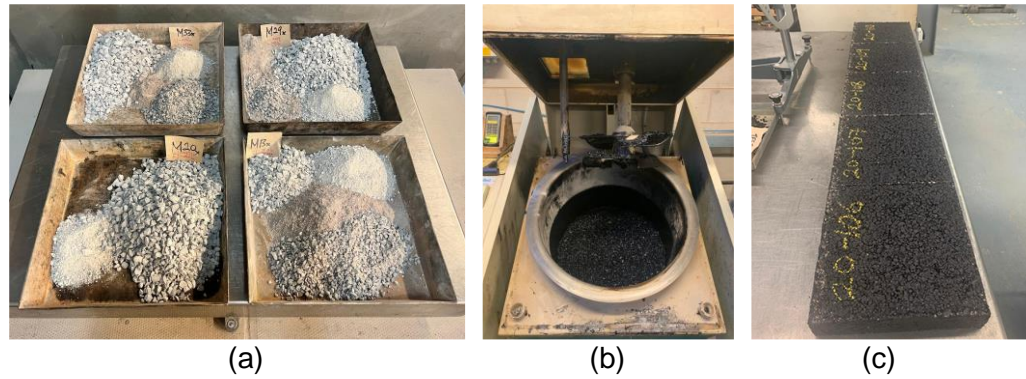


Figure 3-49: (a) batching of aggregates²¹, (b) asphalt mixing in accordance with BS EN 12697-35:2016, and (c) manufactured SMA-10 slabs.

Table 3-7: Properties of 40/60 pen-grade bitumen used for the asphalt specimen manufacturing.

Property	Test Method	Unit	Limits	Property
Penetration @ 25 °C	BS EN 1426:2026 [284]	0.1 mm	40 - 60	48
Softening point (Ring and Ball)	BS EN 1427:2015 [285]	°C	48 - 56	51.6
Kinematic viscosity at 135 °C	BS EN 12595:2023 [286]	mm ² /s	325 min.	455
Density	BS EN 15326:2007 [287]	Kg/m ³	-	1029
Safe heating temperature ²²	-	°C	200 max.	

3.2.3 The original Prusa MK3 3D printer

The Prusa MK3, the latest iteration in the Prusa i3 series, introduces significant improvements, including a refined extrusion mechanism that accommodates an extensive array of printing materials, from standard Polylactic Acid (PLA) [288] and Acrylonitrile Butadiene Styrene (ABS) [289] to sophisticated composite materials embedded with substances such as metals and wood. The Prusa MK3 is a cartesian 3D printer. [Section 2.10](#), outlines the selection of this printer based on its adeptness at tracking complex geometries, consistent temperature and speed control, along with its advantages in customisation, user-friendliness, affordability, and notably, its payload capacity. The same printer underwent modifications to serve both as a crack filling²³ and a pothole filling²⁴ machine.

²¹ This is for illustration. In the laboratory, aggregates were batched using buckets.

²² Reference to the Shell Bitumen Handbook, 6th edition.

²³ Bitumen for the crack filling, as well as the filling process, is described in [Chapter 4](#).

²⁴ Asphalt for the pothole filling, as well as the filling process, is described in [Chapter 6](#).

Figure 3-50 shows key components of the Original Prusa MK3 3D Printer prior to modifications.

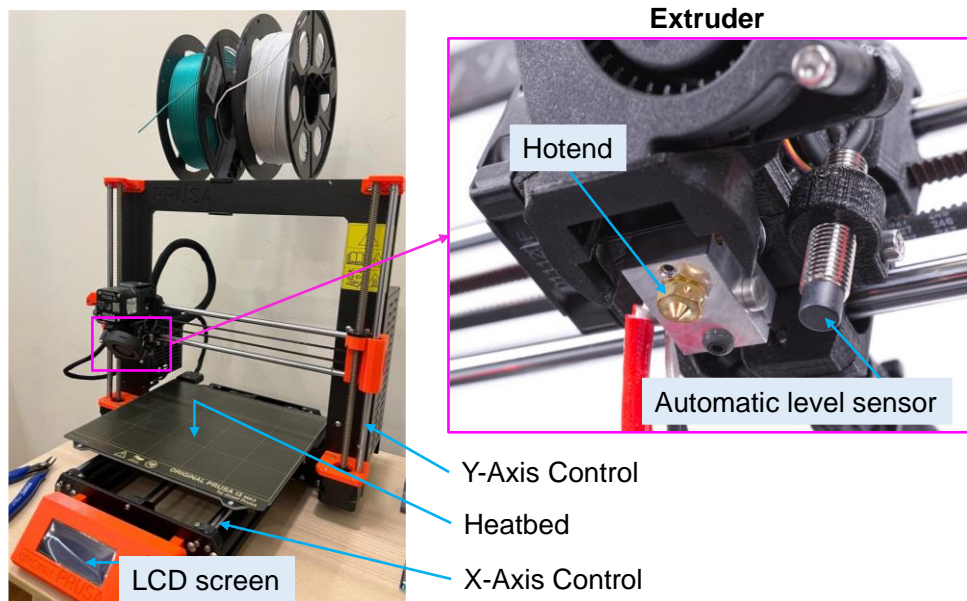


Figure 3-50: Essential parts of the original Prusa MK3 3D printer.

Key features of the Prusa MK3 include the following:

- Auto-calibration System: Automatically adjusts the print bed to simplify setup and ensure optimal print quality.
- Advanced Sensor Technology:
 - Filament Sensors: Detect the presence of filament and its movement, preventing failed prints due to runouts or jams. Also used for manually adjusting vertical height between nozzle and heatbed.
 - Thermal Runaway Protection: Monitors the temperature of the extruder and the heatbed to prevent overheating and potential damage.
- High-resolution Display and Interface: Features a user-friendly interface on a high-resolution display for easy control of print settings and progress monitoring.
- Generous Build Volume: Accommodates larger print projects or multiple small prints in one session, providing flexibility in print size and volume.
- Direct Drive Extruder: Directly feeds the filament to the nozzle, improving print quality and allowing for the use of flexible materials.
- Removable Magnetic Heatbed: Facilitates heating of the heatbed to maintain a steady temperature around the printing object.

3.3 Methods

3.3.1 X-ray CT scanning and data processing techniques

This methodology is relevant to Objective 1, as discussed in [Chapter 4](#). A Phoenix v|tome|x medium (M) @ 240 kV X-ray microCT scanner was utilised for scanning the beams. Operating conditions were set at 164 kV and 180 μ A for voltage and current, respectively. The scan involved rotating the specimen stage through 360° at 0.1° rotation step increments, acquiring a total of 3600 projection images. Each image resulted from integrating 1 frame with a detector exposure time of 500 ms, leading to a scan duration of 40 minutes and yielding a voxel resolution of 45 μ m. [Figure 3-51](#) shows the Phoenix v|tome|x medium scanner setup.

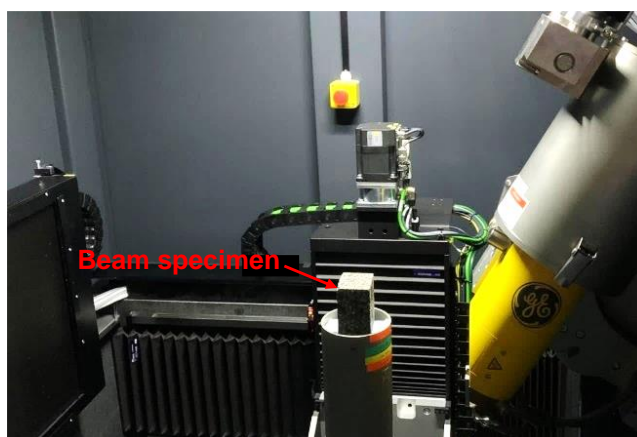


[Figure 3-51](#): The Phoenix v|tome|x medium (M) @ 240 kV X-ray microCT scanner scanning a beam specimen.

A Phoenix v|tome|x large (L) Custom @ 320 kV X-ray CT scanner was used to scan the blocks. Operating parameters were set to 290 kV and 2700 μ A for voltage and current, respectively. Similar to the beam scan, the specimen stage rotated through 360° at 0.1° increments, collecting 3600 projection images. Each projection image was integrated from 1 frame with a detector exposure time of 1000 ms. Each scan lasted approximately 68 minutes. Additionally, a 1 mm copper filter was applied to the X-ray tube's exit window to reduce beam hardening artefacts. The blocks were positioned at 45 °C to minimise the incidence of X-rays on flat surfaces, thereby reducing noise. This setup resulted in a voxel resolution of 90.583 μ m. [Figure 3-52](#) shows the Phoenix v|tome|x large scanner setup. Also, the operational parameters of the Phoenix v|tome|x scanners are detailed in [Table 3-8](#).

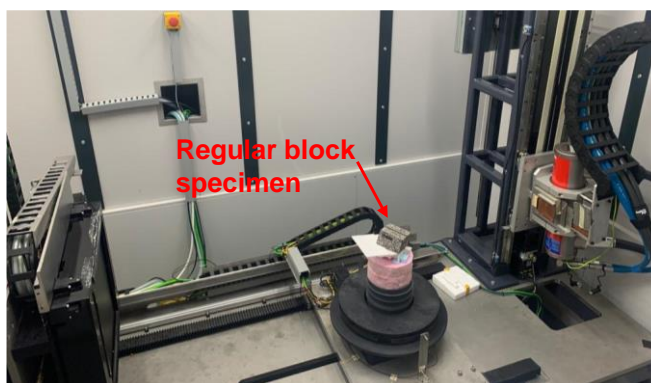


Figure 3-52: The Phoenix v|tome|x large (L) Custom @ 320 kV X-ray CT scanning a block specimen.

Table 3-8: Operational parameters²⁵ of the Phoenix v|tome|x scanners.

Scanner category	Specimens ²⁶	KV	μ A	MS	P	A/S	S	μ m	T (mins)	F
Medium	Beams	164	180	500	3500	1/0	2	45	30	Cu
Large	Block	290	2700	1000	3600	1/0	1	90.6	68	1 mm Cu

Post-scanning, the components of the asphalt specimens (aggregate, bitumen, and voids) were extracted and classified based on density variations using the surface determination and region growing tool in VG Studio MAX software (version 2.2.2; Volume Graphics GmbH, Heidelberg, Germany). Following component segmentation, a porosity analysis, detailed by [290], was conducted to examine void distribution and estimate void volumes. Visualising internal air voids involved rendering the bitumen regions transparent, as demonstrated in Figure 3-53.

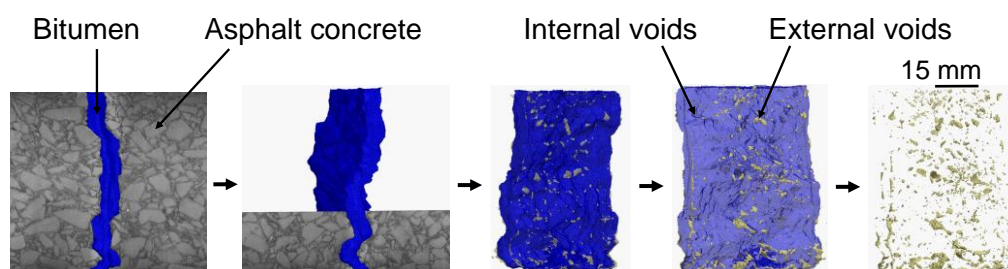


Figure 3-53: Illustration of porosity analysis for extracting voids from scanned bitumen in cracks.

²⁵ KV – Kilovolts, μ A – MicroAmps, MS – Milliseconds, P – Projections, A/S -Average in Skip, S - Detector Sensitivity, μ m – Resolution, T – Time, F – Filter, Cu - Copper.

²⁶ Details of block and beam specimens can be found under Section 4.2.

3.3.2 Extraction of crack path and pothole perimeter coordinates

This methodology is relevant to Objective 1 and Objective 3, as discussed in [Chapters 4](#) and [6](#), respectively. The usual practice in 3D printing is to develop a digital 3D model and slice it for a 3D printer to build objects layer-by-layer. In this research, the automated arms (3D printers for crack and pothole filling) had to fill several cracks, making it practically tedious to build a slice for each crack model.

To overcome this challenge, the 'G-code tools' extension features in Inkscape software [291], which is an open-source vector graphics editor software, was used to extract the G-code of all cracks and pothole perimeters from vector images of the shapes captured from the top view. The G-code extraction procedure is illustrated in [Figure 3-54](#) using irregular cracks as an example.

With this technique, the RepRap 3D printer was converted into a plotter capable of following defect geometries.

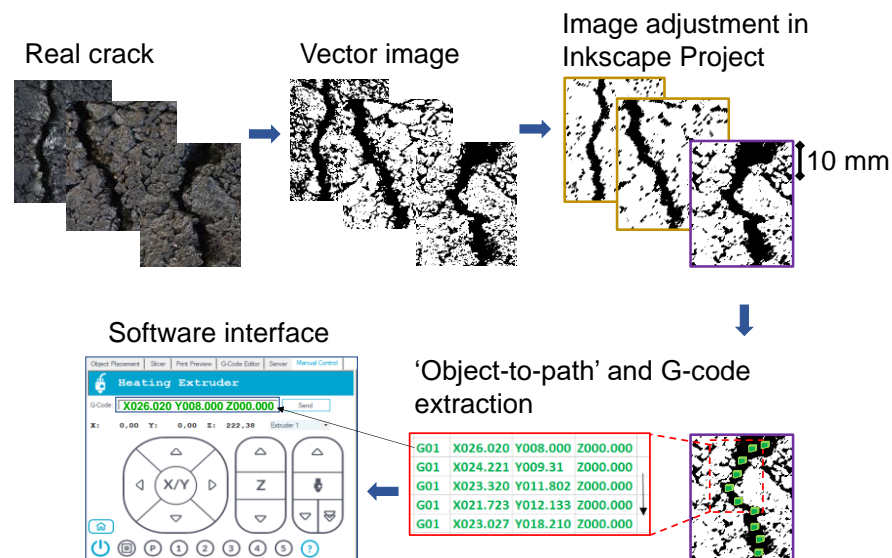


Figure 3-54: G-code extraction for crack paths.

3.3.3 3D printing process and commands

The 3D printing process was executed using Repetier-Host software [29]. The G-codes for the geometry of the cracks extracted in [Section 3.3.2](#) were inputted into the software interface in a command that enabled the printer to follow crack paths while adjusting to instructed printing parameters like printing speed. With its comprehensive features, Repetier-Host enables precise control over additive manufacturing, facilitating the realisation of intricate designs and innovative creations. The printer was commanded to move only when the nozzle had

heated to the preferred temperature. For example, 'M109 S160' commanded the extruder to wait for the nozzle to heat to 160°C before continuing any other command; and 'G1 X100 Y0 F50' commanded the extruder to move 100 mm on the positive x-axis, from left to right, at a speed of 50 mm per minute. A negative 'X' would mean moving in the reverse direction. The crack path coordinates followed the centre lines of the cracks. [Table 3-9](#) shows selected commands that were predominantly used in the research.

[Table 3-9: Common G-Code commands used for 3D Printing in this research.](#)

Command	Interpretation
G28	Home all axes (X, Y, and Z)
G28 X Y	Home X and Y axes
G28 Z	Home Z axis only
M104 S165 T0	Start heating the extruder temperature to 165 °C
G28 X0 Y0	Home X and Y axes at the same time
M140 S23	Start heating the bed temperature to 23 °C
G28 X0	Home the X axis while the extruder is still heating
M190 S23	Wait for the bed to reach 23 °C before continuing
M109 S165 T0	Wait for the extruder to reach 165 °C before continuing
G1 X0 Y0 F50	Move to the X=0 Y=0 position on the bed at a speed of 50 mm/min
G1 X100 Y0 F50	Move the extruder 100 mm to the X axis at a speed of 50 mm/min
G1 Z10 F50	Move the Z-axis to z = 10 mm at a speed of 50 mm/min

3.3.4 The newly developed workability device

A new non-standard penetrometer was designed and manufactured to measure the workability of different asphalt mixtures in this research. This device consisted of a stainless-steel rig support, a 4.3 kg plunger with a 30 mm diameter head, and a Marshall mould. During the test, the plunger was dropped into a filled mould to measure penetration depth. [Figure 3-55](#) shows the dimension and design of the device. Multiple measurements were taken, resulting in an average standard deviation of 2.4 mm. The test was conducted at compaction temperatures specific to the specimens, with preheated moulds and temperature monitoring.

with its free body diagram. The penetration test addresses fine material segregation and shear planing in asphalt mixes, which can cause significant deviations in workability data from paddle-torque devices [138]. Moreover, the non-electric penetrometer device is both simple to use and cost-effective.

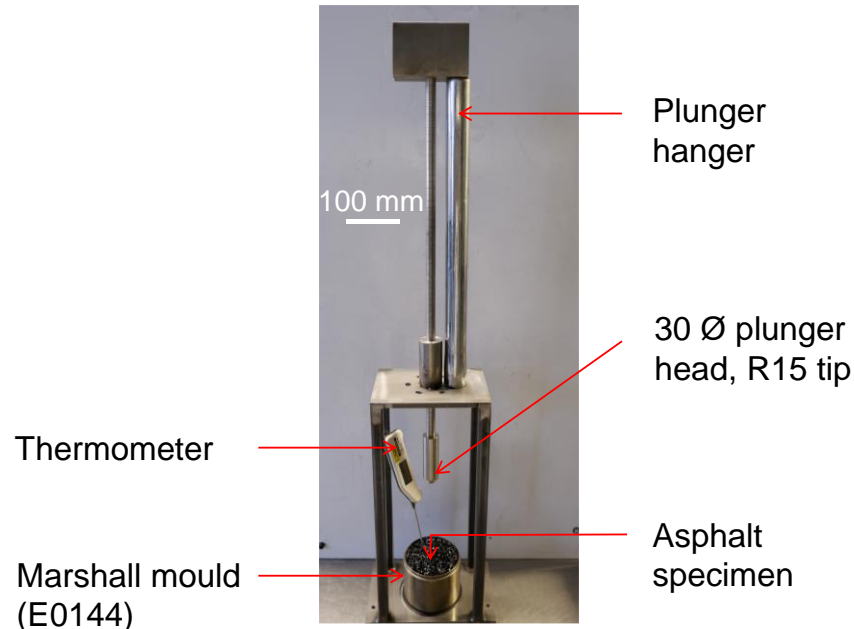


Figure 3-56: The asphalt penetrometer setup in the laboratory.

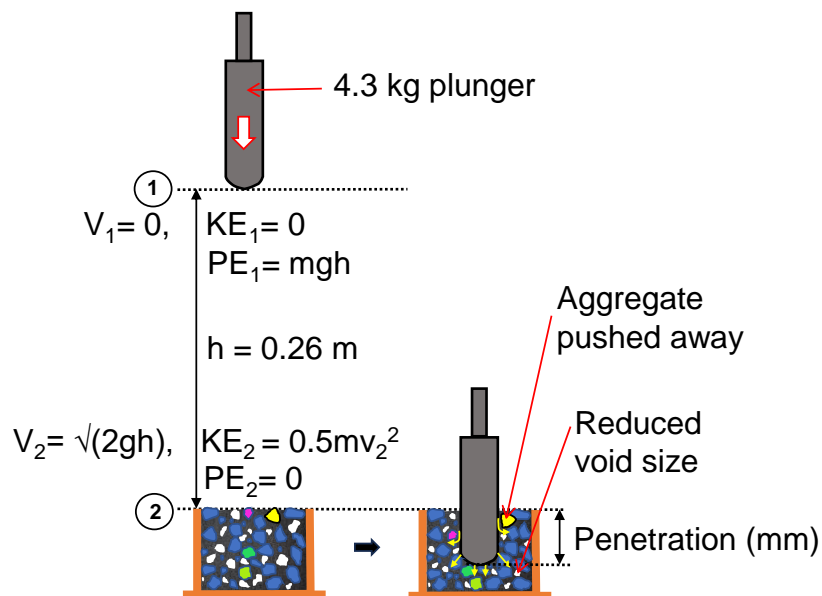


Figure 3-57: Free body diagram and schematic illustration of the asphalt penetration test.

The velocity just before impact (V_2) for a 4.3 kg object dropped from a height of 0.26 m was estimated to be 2.26 m/s. The kinetic energy just before impact is equal to the initial gravitational potential energy. Equation (3-5) describes this

relationship. By estimating the plunger's travel distance after impact to be approximately 34.3 mm (corresponding to penetrations in a standard SMA 8 surf 40/60 mixture) and using the work-energy principle (see Equation (3-6)), an average penetration force of 320 N was estimated. The reported workability for each mixture in the study is based on an average of three penetrations using identical specimens.

The penetrometer performance against other workability devices in literature [131,132] is shown in Figure 3-58. In those devices, a motor-connected paddle is utilised to measure the torque necessary to rotate a HMA. It is important to emphasise that the torque data shown in Figure 3-58 represents the extracted best fit from reference [132].

Precision and repeatability for the novel penetrometer relied on factors such as mixture homogeneity and accurate specimen handling.

$$PE_{gravity} = KE_{just\ before\ impact} = mgh = \frac{1}{2}mv_z^2 \quad (3-5)$$

$$\text{Average penetration force, } F = \frac{mgh}{d} \quad (3-6)$$

Interpretations of the variables in Equation (3-5) and Equation (3-6) are illustrated in Figure 3-57.

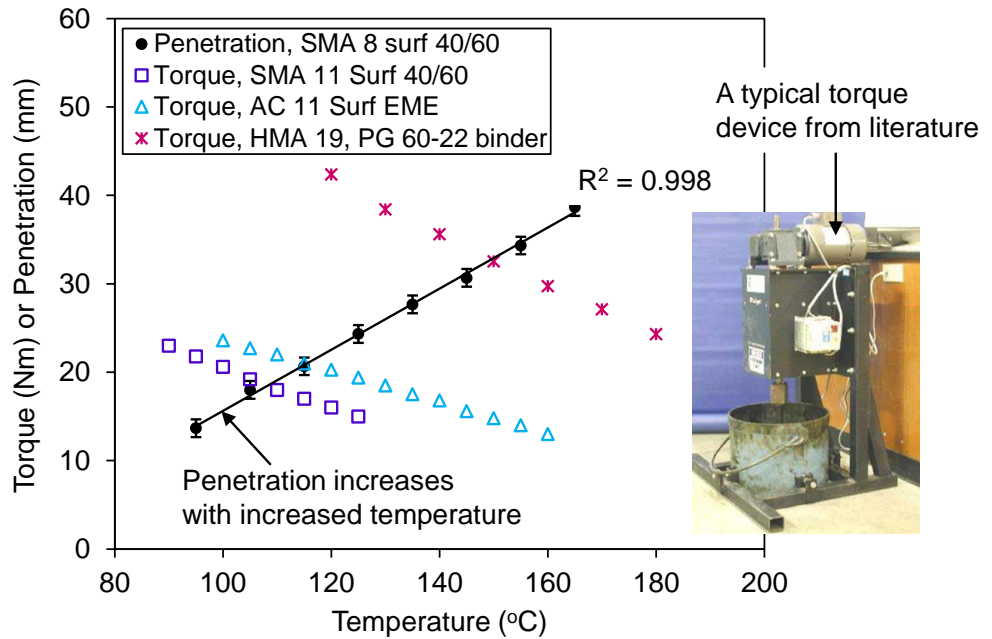


Figure 3-58: Comparison of plunger penetrations with mixing torque across various asphalt mixtures. Inserted device: Illustration of a conventional HMA workability apparatus developed over the years, sourced from [132].

3.3.5 Extraction of geometric properties from real aggregates using Image Processing Techniques

This technique is relevant to Objective 2, as discussed in Chapter 5, with its subsequent application in Chapter 6 contributing to Objective 3. Top and bottom images of at least 120 individual aggregates per batch were captured using the studio setup shown in Figure 3-59. The setup was adapted due to its affordability, ease of use, and the lack of readily available advanced particle and shape analysis systems like the CAMSIZER 3D [84]. It was designed to maintain as consistent an object distance²⁷ as possible for all aggregate specimens during image capturing. The cameras utilised were Sony Alpha A7R IV Mirrorless, chosen for their strong macro capabilities and high resolution, enabling accurate capture of the texture, size, and shape of aggregates.

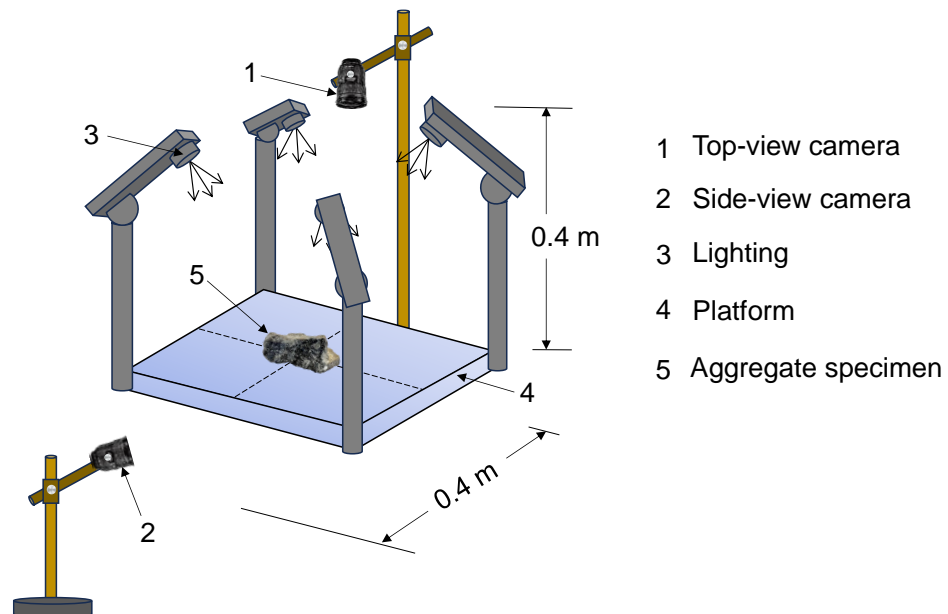


Figure 3-59: Setup for capturing images of aggregates.

Geometrical properties of the aggregates were analysed using ImageJ software²⁸, including area, minor and major Ferets, perimeter, and height. The sufficient number of aggregates measured allowed for fitting Weibull curves; aggregates were characterised using shape and scale parameters of minor Feret and aspect ratio, medians of the area and perimeter, and median height. MATLAB software was utilised to estimate the shape and scale parameters based on the Weibull equation presented in Section 3.3.9. More details on this process can be found in references [26,30]. Only aggregates with a minor Feret

²⁷ The distance between the camera lens and the subject being photographed.

²⁸ Open-source image processing and analysis in Java: <https://imagej.net/ij/>

greater than 2 mm were considered; those smaller than this value, as well as the bitumen and filler, were classified as mastic.

In this research, aspect ratio (AR) is defined as the ratio of the minor Feret's diameter to the major Feret's diameter. Feret's diameter, or Feret, represents the greatest distance between any two points along the outer boundary of the aggregate shape, also known as the maximum caliper.

The image processing technique in ImageJ involved converting images into vector images, grayscale images, binary images, and generating outlines with estimated morphologies. These stages are illustrated in Figure 3-60. These steps were repeated for both the top view and side view images, with the side view primarily used to obtain the aggregate height.

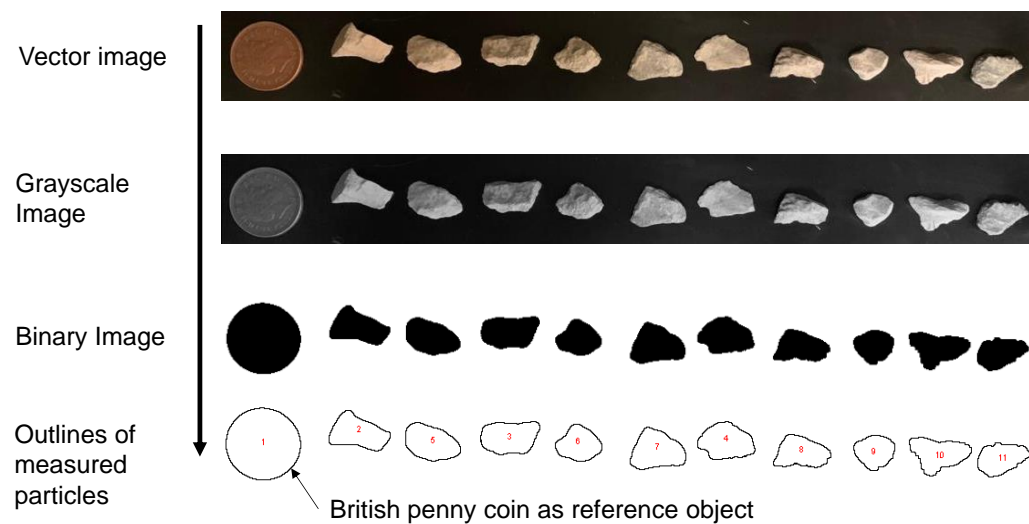


Figure 3-60: Illustration of the Image processing steps in ImageJ.

Also, Figure 3-61 illustrates some of the geometric features output by the ImageJ software from the generated outlines in Figure 3-60 for a typical 8 mm limestone aggregate.

3.3.6 Generation of virtual asphalt in physics engine and estimation of number of aggregates and volume of mastic²⁹

Virtual aggregates (using geometric properties from Section 3.3.5) and mastic were created using a physics engine in Unity 3D, similar to real asphalt mixtures.

²⁹ A full video on the creation of virtual asphalt can be found here:
https://youtu.be/hRFBX9CO_C8

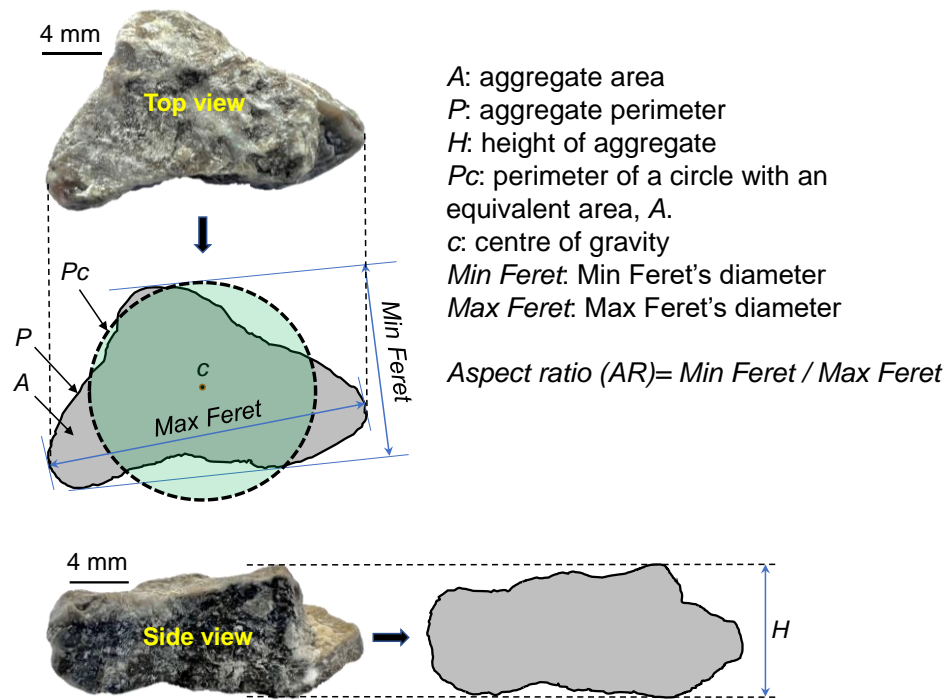


Figure 3-61: Geometric projections of typical 8 mm limestone aggregate examined in this research.

This engine calculates the number of aggregates and volume of mastic present in 250 g of the simulated asphalt mixture, based on input aggregate geometric features, Weibull characteristics, and fractions of aggregate sizes. The technique employs an impulse-based numerical model (iDEM) rather than data-based numerical models. iDEM prevents penetration between objects; an impulse is generated when they come within a certain distance, allowing for higher time steps than equivalent methods and reducing computer time.

A virtual mixture was created in a tube with dimensions of 3.77 cm in height, 3.25 cm in radius, 33.18 cm² of surface area, and 124.98 cm³ of volume. Mass percentages of aggregates, bitumen, and filler were weighed to make the mixtures. The Unity 3D algorithms start with a cuboid within certain dimensions, equivalent to the min and max Feret, and height, defined by the Weibull distributions. A number of points were seeded on the cuboid surface, then moved perpendicularly at varying distances, to create surfaces resembling those of real aggregates. The min Feret, max Feret, height, number of points, and distance from the cuboid surface define a virtual aggregate. Aggregates were compacted in two steps. To mix the aggregates, a 2 N force was applied to the centroid of each aggregate every 0.5 seconds. Initially, the piston moves until the air void content reaches 50 %. Then, as the force increases, the pistons move faster, causing the force to increase by 0.12 N/s.

The simulation resulted in a 3D model of the asphalt mixture and its volumetric properties such as porosity (%), virtual compaction force (N), aggregate mass (g), bitumen content (cm^3), and mastic (cm^3). The virtual compaction force simulates the force required to achieve the same level of air voids as in the equivalent experimental mixture through Marshall compaction. [Figure 3-62](#) shows a summary of the stages involved in the simulation of virtual aggregates, and [Figure 3-63](#) displays the compaction of generated aggregates to form virtual asphalt mixtures in the physics engine for specimen M8, as used in [Chapter 5](#).

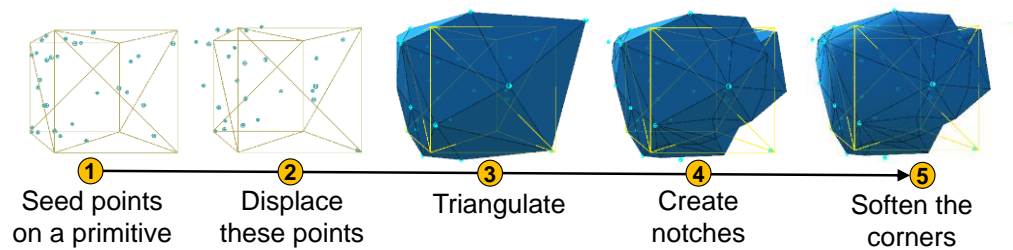


Figure 3-62: Illustration of the simulation stages used to create the virtual aggregates in the physics engine.

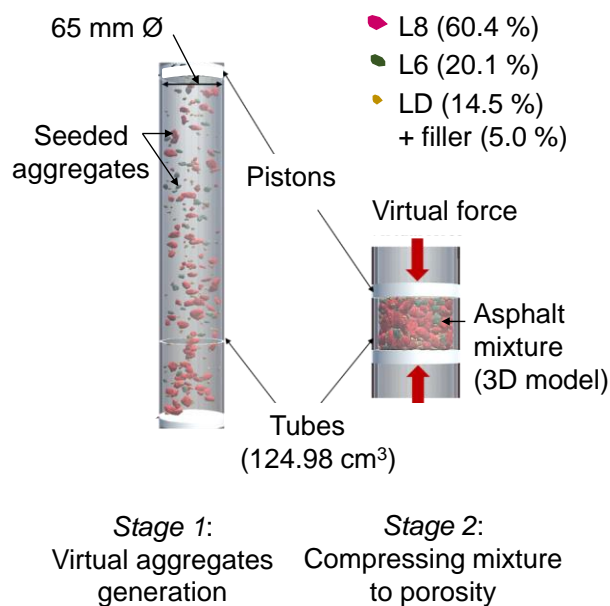


Figure 3-63: Illustration of the creation of virtual asphalt models in physics engine software (Unity 3D).

As mentioned earlier in this chapter, fine aggregates, typically those under 2 mm in size, along with fillers that are usually smaller than 0.063 mm, combine with bitumen to form a mastic. Consequently, the software calculates the mastic volume as the volume of all aggregates smaller than 2 mm present in the gradation, plus the volume of bitumen inputted. Note that the simulation does

not account for the rheology of different bitumen types; as such, only 40/60 pen bitumen, which was readily available at NTEC, was used in all simulations. This limitation needs to be addressed in future studies. In practice, the mastic fills the gaps between coarse aggregates, providing cohesion and binding them together.

The 2 mm aggregate limit was chosen because it is the sieve size that separates fines from coarse aggregates within European standards (EN). Typical EN sieve sizes include 10.0, 8.0, 6.3, 4.0, 2.8, 2.0, 1.0, 0.500, 0.250, 0.125, 0.063 mm, and pan. This range is part of a larger series starting from larger sizes, such as 40 mm. The application of this grading system can be found in the following EN standards, as an example:

- EN 933 series: tests for geometric properties of aggregates.
- EN 13108-5:2016 Bituminous mixtures - Material specifications Part 5: Stone Mastic Asphalt.
- EN 13043:2013: Aggregates for bituminous mixtures and surface treatments for roads, airfields, and other trafficked areas.

Specifically, in reference to BS EN 13108-5:2016 [281], both Table 1 (basic sieve set plus set 1) and Table 2 (basic sieve set plus set 2) of the general grading requirements for the target composition of SMA highlight the role of the 2 mm sieve as a key size.

3.3.7 Design standards

BSI standards, developed by the British Standards Institution (BSI), were the primary reference for standard tests in this research. They align with EN standards, developed by the European Committee for Standardisation (CEN), due to the UK's participation in CEN. "BS EN" in this research denotes "British Standard adopted as a European Norm," indicating recognition and use across European countries as a harmonised standard.

3.3.8 Standard tests to assess the volumetric and mechanical performance of asphalt and bitumen

Density of bitumen

The capillary-stoppered pycnometer method, as shown in [Figure 3-64](#), in accordance with BS EN 15326:2007+A1 (2009) [287], was used to determine the bitumen density at a test temperature of 25 °C. The bitumen density was

crucial for theoretically estimating the volume of bitumen poured into cracks, as discussed in [Chapter 4](#), to achieve Objective 1. Specifically, the volume was calculated as the product of the bitumen mass discharged into the cracks and its density. Furthermore, the mass of the bitumen was determined by measuring the difference in the mass of the crack specimen before and after filling.

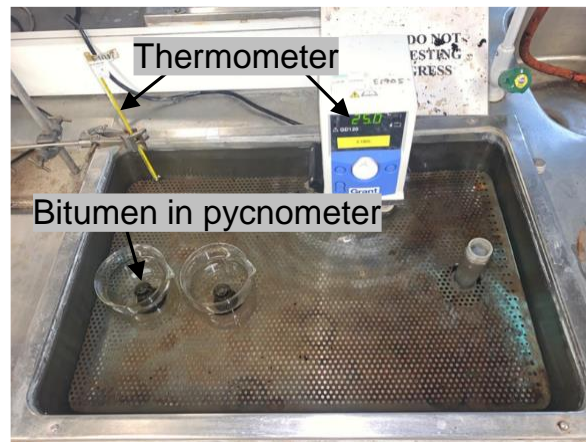


Figure 3-64: Bitumen density test with pycnometer.

Force ductility on bitumen

A force ductility method following BS EN 13589:2018 [292] was used to assess the tensile behaviour of 3D printed bitumen at a test temperature of 15°C. The test involved using a Force Ductility Testing Machine in determining the deformation energy required to stretch a bitumen sample to 400 mm at a rate of 50 mm/min. The test specimens were prepared by filling three parallel forced ductility moulds with bitumen from the bitumen crack filling machine. The moulds were filled layer by layer at 160 °C at a speed of 100 mm/min (100 mm/min selected to be the optimum filling speed for pen 40/60 grade bitumen as illustrated in [Section 4.7](#).

To serve as a control, the force ductility test was repeated for moulds filled manually by pouring hot bitumen at 160 °C with the hand in one direction, as recommended by BS EN 13589:2018 [292]. The brass mould surfaces were coated with a thin layer of glycerol and talc. The bitumen in the moulds was trimmed after cooling for 1 hour and then soaked in 15 °C testing water for 1 hour. The test time from pouring did not exceed 4 hours.

Modification: The recommended temperature for the force ductility test is 5 °C. However, this temperature is suitable for polymer-modified bitumen and will be too low to produce a 400 mm stretching length in 40/60 unmodified bitumen.

Therefore, a testing temperature of 15 °C was adopted for all bitumen, whether hand-filled or 3D printed. Figure 3-65 shows the force ductility test setup.

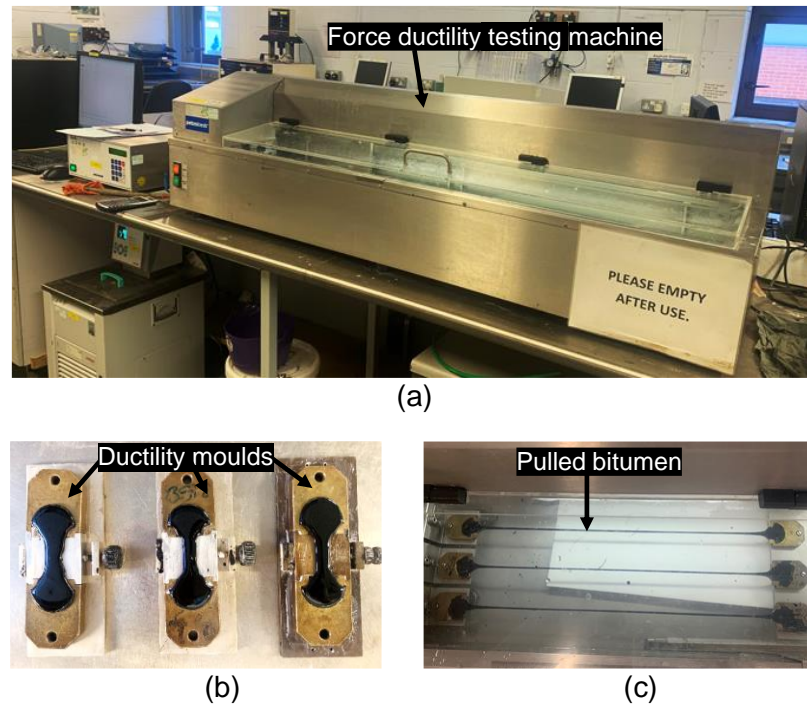


Figure 3-65: Force ductility test setup: (a) force ductility testing machine, (b) filled ductility moulds, and (c) extended bitumen specimen at 400 mm.

Shear bond test

The shear bond test was conducted to evaluate the resistance of filled cracks to deformation under vertical displacements. Although not standardised, the test was inspired by guidance from BS EN 12697-48:2021 [293] for asphalt interlayer bond testing. The procedure involved clamping one asphalt block in a metallic collar while a vertical plunger displaced the other block parallel to the crack length at 5°C, causing a fracture and splitting the blocks. The maximum load at fracture, recorded as the maximum shear force, was used to calculate shear stress by dividing it by the sectional area of the block. Figure 3-66 illustrates the experimental setup.

A Universal Testing Machine (INSTRON), was used for the shear testing with a 50 kN load limit applied over a 20 mm stroke at a rate of 83.335 $\mu\text{m/s}$. A slower stroke rate of 83.335 $\mu\text{m/s}$ was chosen to minimise dynamic effects and accurately capture the viscoelastic properties of bitumen, reflecting its behaviour under typical service loading conditions.

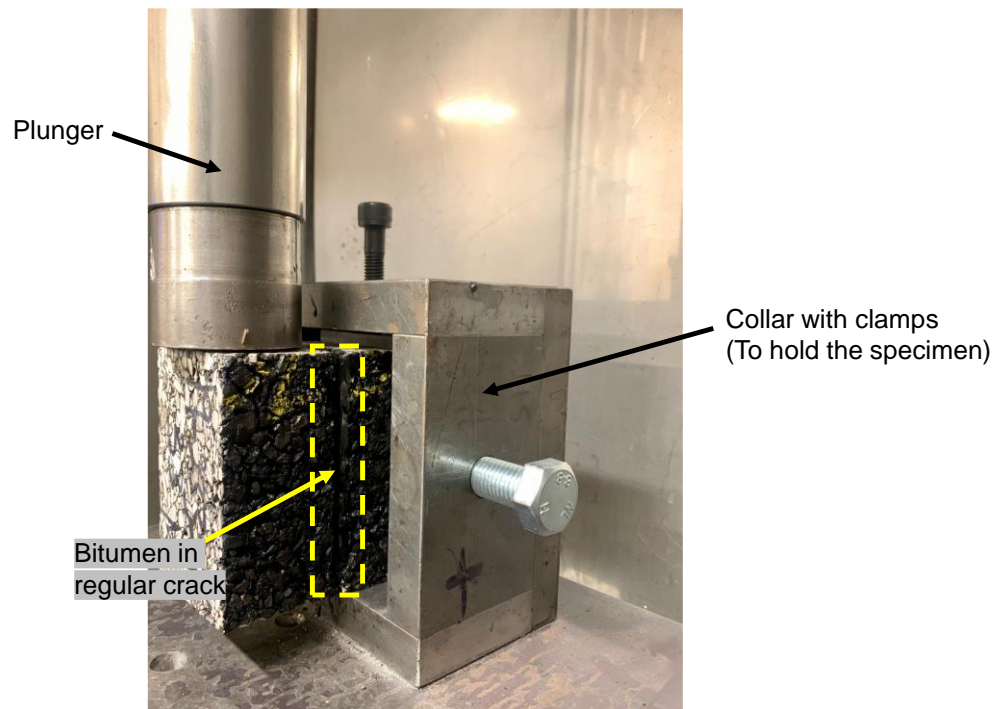


Figure 3-66: An experimental setup for the shear bond test.

Tensile bond test

The tensile bond test measured the adhesive capacity of the bitumen in the cracks to hold together the crack walls when the asphalt blocks were pulled apart. A Universal Testing Machine was used with the same loading and specimen conditions as for the shear bond test. The tensile bond test involved glueing the top and bottom of the block specimen with Araldite epoxy resins³⁰ onto stainless steel plates. The bottom plate was also anchored in a mould for block stability. The epoxy had a shear strength of 19 N/mm^2 , which exceeded the bitumen shear strength. The top plate on the specimen was locked into a steel fork with a rod and the opposite end of the fork was then screwed into the upper plunger of the INSTRON machine. Likewise, the base plate on which the specimen sat was bolted onto the lower plunger on the INTRON. The plungers were then pulled apart until the bitumen, which was sandwiched between the asphalt blocks, fractured. Failure was determined as the moment when the load started to decline from a peak. The tensile bond stress was calculated as a ratio of the maximum load applied to the surface area of the crack. Figure 3-67 illustrates the experimental setup and the free body diagram of the tensile bond test.

³⁰ Araldite: <https://www.go-araldite.com/en>

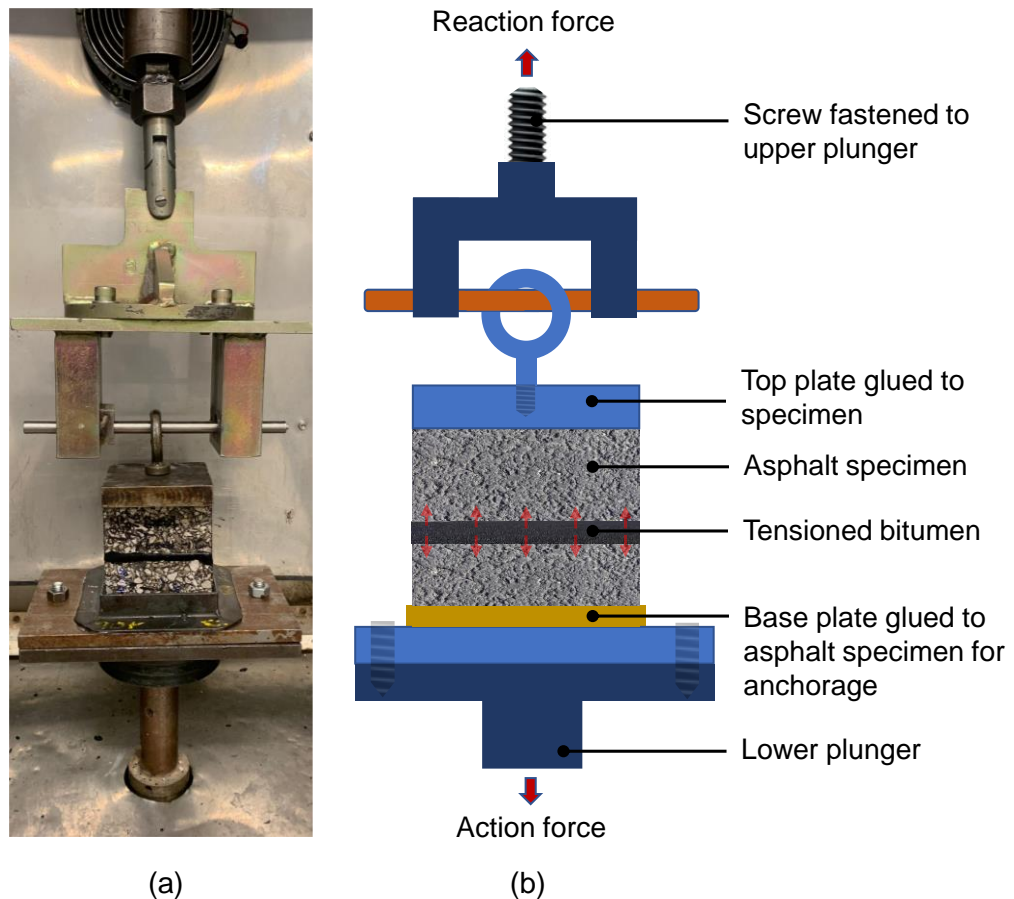


Figure 3-67: (a) Experimental setup and (b) free body diagram of the tensile bond test.

Flexural strength of filled cracks

The three-point bending test, inspired by guidance from BS EN 12697-24 [124], was used in this study to examine the ability of filled cracks to resist failure in bending. The beam specimens for this test measured 385 mm x 50 mm 60 mm. Supporting pins were placed at 220 mm span under the beam specimen, each at 82.5 mm offset from the beam ends. The top plunger (load) was applied at beam mid-span at a load application rate of 83.335 $\mu\text{m/s}$ over a 20 mm displacement. All specimens were preconditioned at a temperature of 5 °C.

Determination of Marshall stability and Marshall flow

To measure the Marshall stability and Marshall flow of asphalt mixtures, the Marshall test was performed in accordance with reference [123]. Additionally, Marshall compaction was used to produce core specimens for estimating air void content and density. The Marshall test was chosen due to its simplicity. Moreover, the standard testing temperature of 60 °C is thought to simulate the weakest HMA, which occurs in the summertime. Figure 3-68(a) depicts a

Marshall stability testing setup in the laboratory, while Figure 3-68 (b) illustrates a typical Marshall Stability Curve.

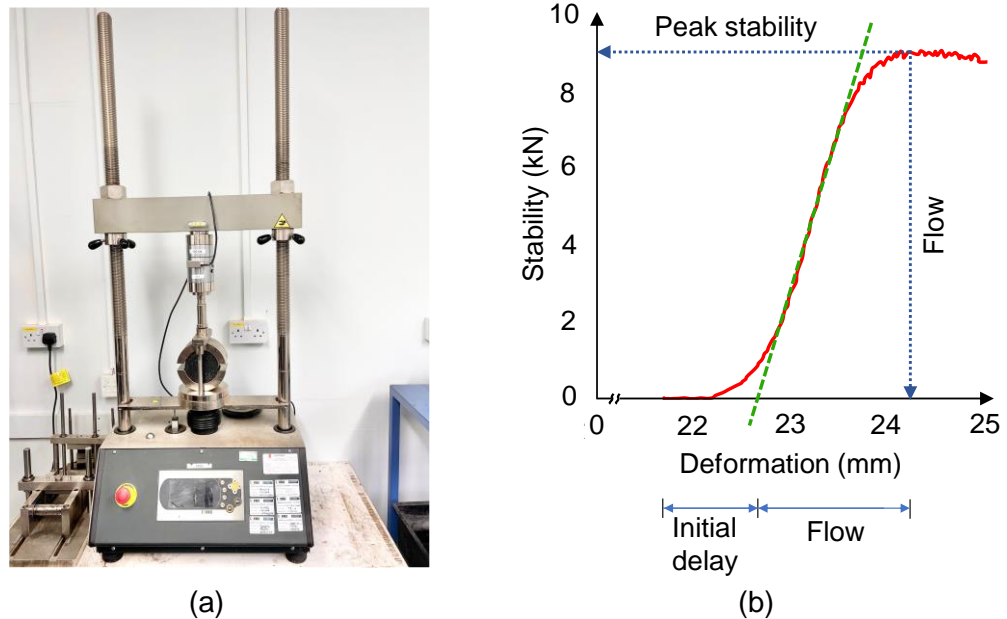


Figure 3-68: (a) Illustration of the Marshall Stability Tester and (b) a typical Marshall Stability curve.

Determination of the bulk density and air void content of asphalt

The bulk density and air void content of asphalt specimens were determined using the Saturated Surface Dry (SSD) method (Procedure B) and the sealed specimen method (Procedure C), as specified in BS EN 12697-6:2020 [125]. Specimens were obtained from Marshall cores or cores drilled from asphalt slabs. The SSD method is suitable for specimens with relatively closed surfaces and was selected for asphalts with targeted air void contents of less than approximately 8%. The procedure involved saturating the specimen with water, removing excess surface moisture using a damp chamois to achieve a saturated surface dry condition, and subsequently measuring its mass. The specimen's volume was determined through water displacement, which involved submerging the specimen in water and measuring the volume of water displaced.

For mixtures exhibiting high air void content, such as those exceeding 8%, the sealed specimen method was employed. This approach entailed coating the specimen with an impermeable film to seal surface voids prior to measuring its mass in water. This sealing prevented water ingress during measurement,

thereby ensuring accurate bulk density determination. Figure 3-69 shows a typical foil-sealed asphalt specimen used in this research.

In both the SSD and sealed specimen methods, the bulk density of asphalt specimens was calculated by dividing the specimen's mass by its volume. However, for the sealed specimen method, the densities of the asphalt specimens were adjusted by subtracting the mass and volume of the sealing film from the total mass and volume of the sealed specimen to determine the true bulk density.

The air void contents were calculated by comparing the bulk density of the asphalt mixtures to their theoretical maximum density, with the difference attributed to air voids.



Figure 3-69: Foil-sealed asphalt specimen prepared for bulk density and air void content determination using the sealed specimen method.

Wheel Tracking Test

Traffic simulation was conducted using a small-sized Wheel Tracking device (Cooper, Ripley, UK) following procedure B in accordance with BS EN 12697-22:2020 [115]. The goal was to assess the resistance of the filled potholes to permanent deformation under cyclic loading in soaked conditions. Asphalt samples, measuring 305 mm x 305 mm x 100 mm (including a 150 mm Ø x 40 mm deep filled pothole in the upper slab), were fully submerged in water at $30^{\circ}\text{C} \pm 1$.

The wheel, running at approximately 26.7 rpm with an applied load of 705 ± 4.5 N, tracked at 10,000 cycles per test. Each cycle consisted of two passes. A testing temperature of 30°C , a departure from the standard 60°C typically used

in rutting tests, was selected to minimise differential deformation between the pothole filling materials and the surrounding asphalt, which have varying densities and mechanical properties. This lower temperature setting was intended to reduce the likelihood of excessive rutting in the filling materials while also preventing the formation of rippling – a phenomenon that could introduce variability or noise into the rutting data – and mitigating potential strain or damage to the tracker wheels during the testing process. Test specimens were temperature-conditioned at 30 °C for 12 hours to ensure temperature equilibrium within the specimens. For each case scenario, two parallel specimens were tested to enhance the reliability of the results. The reported final rut depths represent the mean rut depths of the two parallel specimens. [Figure 3-70](#) shows the small-sized Wheel Tracking device used in this research.

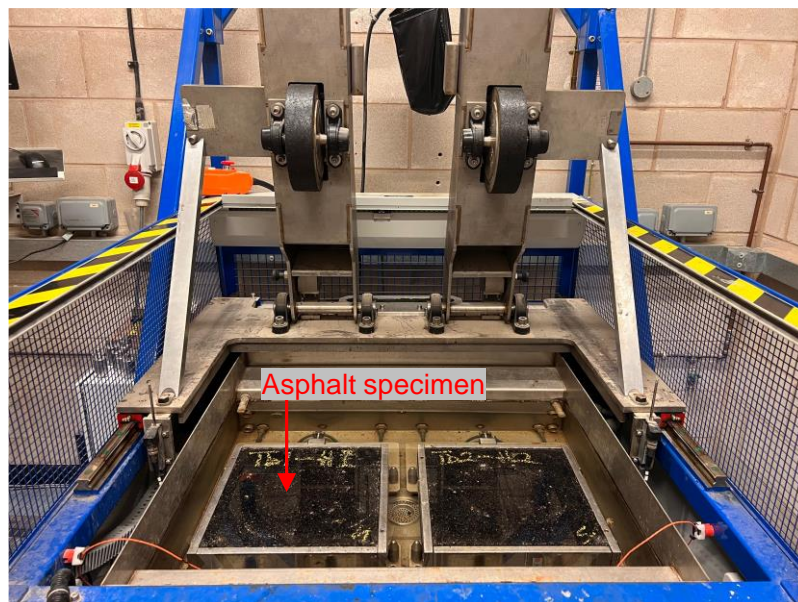


Figure 3-70: The Wheel Tracking device (Cooper, Ripley, UK) at NTEC.

3.3.9 Statistical derivatives

Basic data statistics

Basic data statistics used in this research are detailed in [Table 3-10](#).

Regression Analysis

In this research, regression analysis estimated the relationships between dependent and independent variables, using both linear and multiple regression models to evaluate and predict variable strengths.

Table 3-10: Description of basic data statistics used in the research.

Basic statistics	Standard formula ³¹	Description
Sample mean/Average	$\bar{x} = \frac{\sum x}{n}$	Measures the average value of a set of data.
Sample standard deviation	$s = \sqrt{\frac{\sum (x - \bar{x})^2}{n - 1}}$	Measures the spread of scores within a set of data.
Correlation coefficient (R)	$R = \frac{\sum (x_i - \bar{x})(y_i - \bar{y})}{\sqrt{\sum (x_i - \bar{x})^2 \sum (y_i - \bar{y})^2}}$	Indicates the strength and direction of the linear relationship between two variables.
Coefficient of determination, R-Squared (R ²)	$R^2 = \frac{\sum (y_i - \bar{y})^2}{\sum (y_i - \bar{y})^2}$	Provides information about the goodness of fit of a regression model.
Adjusted R ²	$Adj. R^2 = 1 - \left[\frac{(1 - R^2)(n - 1)}{(n - k - 1)} \right]$	Shows the proportion of variability in the dependent variable explained by the independent variables, adjusted for predictors.
Absolute error (E _a)	$E_a = m - p $	The error between predicted values and lab-measured values.
Mean Squared Error (MSE)	$MSE = \sum_{i=1}^n \frac{(m_i - p_i)^2}{n}$	Evaluates the mean squared error between observed and predicted values.
Root-mean-square error (RMSE)	$RMSE = \sqrt{\sum_{i=1}^n \frac{(m_i - p_i)^2}{n}}$	Sensitive to outliers and measures the accuracy of predictive models.

³¹ R - correlation coefficient, x_i - values of the x-variable in a sample, \bar{x} - mean of the values of the x-variable, y_i - values of the y-variable in a sample, \bar{y} - mean of the values of the y-variable, n - number of points in your data set, k - number of independent variables in the model, excluding the constant, m - measured value, p - predicted value.

Simple linear regression involved assessing the relationship between a dependent variable and an independent variable using equations in the form of Equation (3-7).

$$y = \beta_0 + \beta_1 x + \epsilon \quad (3-7)$$

Where y is the dependent variable (variable to predict), β_0 is the y-intercept, β_1 is the gradient of the regression, x is the independent or explanatory variable, and ϵ is the error term.

Multiple linear regression is similar to linear regressions but with multiple variable terms and combinations of coefficients (β) and independent variables (x) as illustrated in Equation (3-8).

$$y = \beta_0 + \beta_1 x_1 + \beta_2 x_2 + \dots + \beta_n x_n + \epsilon \quad (3-8)$$

Where x_n is the independent variable for each term, β_n is the regression coefficient for each independent variable and ϵ is the model's error term.

Rational function regression, which is simply a ratio of two polynomials, was developed to model the behaviour of asphalt mixtures. The selection of rational equation was informed by references [26,30] which have demonstrated its effectiveness in accurately modelling a range of emerging properties in asphalt attributed to aggregate gradation. These properties encompass hydraulic conductivity and the compaction force necessary for asphalt materials.

This regression enabled more than two properties of asphalt mixtures to be expressed in an equation. The equations composed of first-degree polynomials with denominators not equal to zero. Equation (3-9) shows the format of the rational regression used in the research for three variables, where $z = f(x, y)$.

$$z = \frac{\beta_0 + \beta_1 x_1 + \beta_2 y_1}{1 + \beta_3 x_1 + \beta_4 y_1} \quad (3-9)$$

Where z is the dependent variable, β_0 is a constant term, $\beta_1, \beta_2, \beta_3, \beta_4$ are rational coefficients, x and y are independent variables.

Confidence band

Confidence bands (typically 95% and 5%) were constructed around the estimated regression lines to indicate the level of uncertainty in the estimated

regression relationships. The bands were useful for assessing the reliability of regression estimates and for understanding the range of possible values for the dependent variable at different levels of the independent variable.

Independent samples t-test

The independent t-test, also known as an unpaired t-test, was used to assess whether there is a significant difference between the means of two distinct and unrelated groups of experimental results. This test is particularly useful when determining the significance of differences between the outcomes of two sets of experiments, especially when conclusions cannot be easily drawn from comparing their graph plots.

To conduct the analysis, a continuous variable that follows a normal distribution (referred to as the Test variable) and a categorical variable with two distinct groups (referred to as the Grouping variable) are required. The significance level is computed using the mean, standard deviation, and sample size for each group (Group 1 and Group 2). Initially, the equality of variances between the groups is assessed using Levene's test. If the result of Levene's test is nonsignificant ($P > 0.05$), indicating equal variances, the independent samples t-test is conducted with equal variances assumed. Conversely, if Levene's test is significant ($P < 0.05$), suggesting unequal variances, the independent samples t-test is performed with unequal variances [294,295].

Weibull equation

The Weibull distribution, which is dominant in reliability and survival modelling, was applied in this research to obtain two key parameters of aggregate geometries for the creation of virtual aggregates as demonstrated by [x]: the scale parameter (α) and the shape parameter (γ). The scale parameter (α) sets the distribution's characteristic life, while the shape parameter (γ) determines its skewness. A larger scale parameter signifies longer lifetimes, while different values of γ indicate varying degrees of skewness, from early to late failure. The maximum likelihood estimators of α and γ for the Weibull distribution are iteratively derived from the simultaneous equations (embedded in the MATLAB software) shown in Equation (3-10) and Equation (3-11).

$$\alpha = \left[\left(\frac{1}{n} \right) \sum_{i=1}^n x_i^{\gamma} \right]^{\frac{1}{\gamma}} \quad (3-10)$$

$$y = \frac{n}{\left(\frac{1}{\alpha}\right) \sum_{i=1}^n x_i^{\alpha} \log x_i - \sum_{i=1}^n \log x_i} \quad (3-11)$$

Where x_i represents the i -th value of the variable x ; and n represents the total number of data points.

Software for statistical analysis

MATLAB was the primary software used for basic data analysis, as well as regression analysis. The same software was used to generate the shape and scale parameters of aggregates. The Levenberg-Marquardt algorithm [296] was chosen for fitting nonlinear regression models due to its simplicity and efficiency in analysing laboratory experiments with small datasets. This algorithm is superior in terms of high accuracy, quick convergence (even with noisy or limited experimental data), and robustness against local minima. While the Gauss-Newton algorithm and gradient descent algorithm [297] are also commonly used for nonlinear regression, they require more careful tuning and handling to ensure convergence, especially with small and noisy datasets, as was the case in this research work.

3.4 Summary

The Materials and Methods chapter has provided an overview of the materials, laboratory simulation techniques, equipment, and statistical analyses utilised in the research. A summary of the overview includes:

Materials:

- SMA 10 Surf 40/60, with 40/60 penetration grade bitumen, was designed and manufactured in accordance with BS EN 13108-5:2016, BS EN 12697-35:2016, and BS EN 12697-33:2019 to simulate a typical UK surface course in the laboratory.
- The Original Prusa MK3 3D printer, a cartesian printer known for its precision, user-friendliness, and adaptability to a wide range of materials, was modified in this research to function as an automated crack- and pothole-filling machine.

Methods:

- X-ray CT scanning techniques were employed for analysing voids in filled cracks.

- A new, simple-to-use non-standard penetrometer device was developed to measure the workability of HMAs. The performance of this penetrometer has been compared with other workability devices reported in the literature.
- Standard tests, such as Marshall stability, wheel tracking, and shear bond tests, were performed in accordance with BSI standards.
- Statistical derivatives, such as basic data statistics and regression analysis, were utilised to analyse experimental results and assess relationships between variables.

Chapter 4: Machine Filling of Cracks in Asphalt Pavements

4.1 Introduction

This chapter presents the development of the ACFM (a modified RepRap 3D printer), the optimisation of its operational parameters to enhance the volume of cracks filled with bitumen, and an assessment of the quality of filled cracks. The volume and quality of cracks filled by the ACFM have been compared to those filled manually. A graphical illustration of the general overview of the automated crack filling investigation in this chapter is illustrated in [Figure 4-71](#).

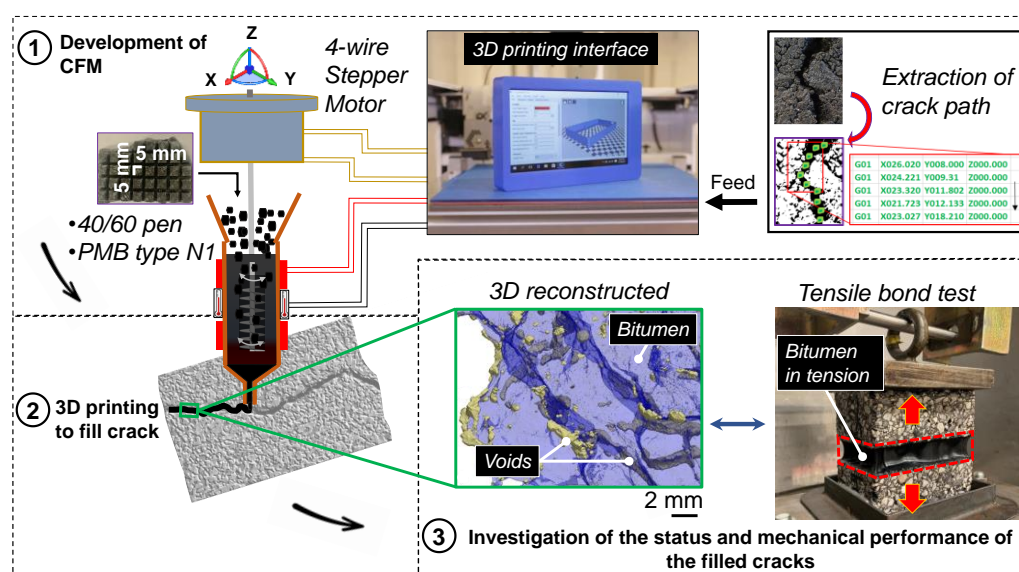


Figure 4-71: A graphical abstract of the automated crack filling investigation with the ACFM

Publication acknowledgement

This chapter includes techniques, results, and discussions that are part of earlier collaborative research efforts and have been previously published. Consequently, relevant portions of the content in this chapter are also detailed in the following publication: “Machine-filling of cracks in asphalt concrete,” published in *Automation in Construction*, Volume 141, 2024.

4.2 Laboratory Simulated Cracks in Asphalt Pavement

Asphalt blocks and beams were sectioned from larger slabs (see [Section 3.2.2](#) for the production of the asphalt slabs), with blocks measuring 100 mm x 50 mm x 60 mm and beams 380 mm x 50 mm x 60 mm. The block specimens were used for regular (straight) cracks, while the beams were utilised for irregular (curvy) cracks. Regular cracks were formed by aligning the two straight blocks

with a gap, while irregular cracks resulted from fracturing the beams at 5°C through a three-point bending test and rejoining the pieces with a gap. The beams were snapped at 5°C to make them brittle and reduce splintering of adjoining asphalt materials along the snapped surface. To simulate crack volume, the gaps in both the blocks and fractured beams were sealed on the bottom and sides with lead foil tape. Figure 4-72 illustrates the regular and irregular cracks utilised, all cracks being 5 mm wide, except for those in the experiments testing the influence of crack width on filling volume, which varied from 4 mm to 1 mm. For each parametric filling condition, four samples of both crack types were prepared to assess experimental variability.

The volume of the irregular cracks was quantified by filling them with glass powder, which has a bulk density of 1.51 g/cm³, resulting in an average volume of 16.9 cm³. A schematic illustration of a complete regular crack used in this research is shown in Figure 4-73.

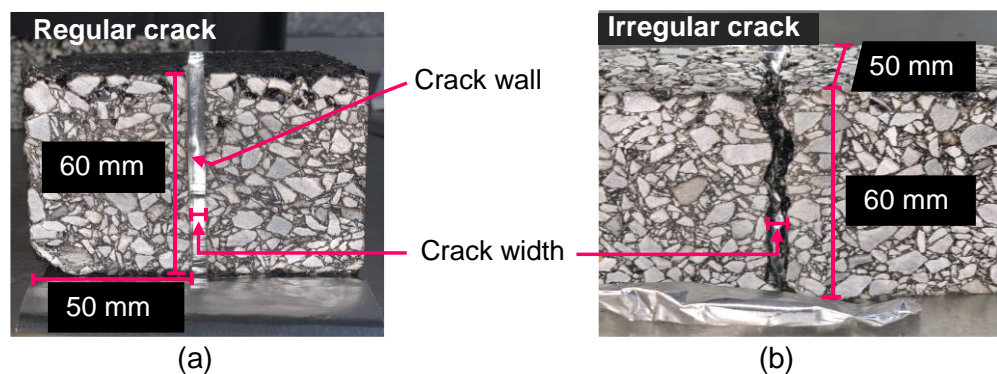


Figure 4-72: (a) regular crack in blocks and (b) irregular crack in snapped beam.

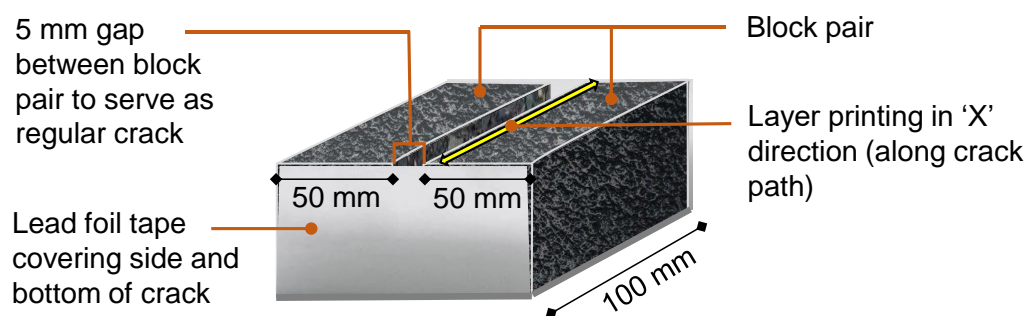


Figure 4-73: Schematic illustration of a regular crack between identical asphalt blocks.

4.3 Bitumen for Crack Filling

Two types of bitumen were used as fillers in this research:

- i. 40/60 paving grade bitumen (40/60 pen)
- ii. N1 Polymer Modified Bitumen (PMB N1)

The PMB N1 was supplied by Colas³² as Coljoint N1 hot applied joint sealant compound and the 40/60 pen was the same bitumen used in manufacturing the asphalt slabs presented in Section 3.2.1 which was readily available at NTEC. Bitumen pellets were made from bulk by cold casting at 90 °C for 40/60 pen and 120 °C for PMB N1. The pellets are shown in Figure 4-74. The properties of the 40/60 pen are presented in Table 3-7, and those of the PMB N1 are presented in Table 4-11.

Table 4-11: Performance of PMB N1 sealant as supplied by manufacturer.

Property	Specification
Penetration (25°C)	7-13 mm
Softening point (°C)	90-115 mm
Flow (60 °C, plate)	Less than 2mm
Extension test	Less than 50 mm ² debonding
Resilience (25°C)	60% minimum recovery
Determination of bitumen compatibility	No adhesion failure, no oily exudate
Density	1.002 g/cm ³
Safe pouring temperature	175/185°C
Safe heating temperature	185°C for 6 hours max.; 195°C max. temperature

5 mm x 5 mm pellet



Figure 4-74: 40/60 pen-grade bitumen pellets.

³² Colas: <https://www.colas.co.uk/>

4.4 Developing the ACFM

4.4.1 The hot-bitumen heating components

The hot-bitumen chamber consisted of a 1 mm thick aluminium cone (nozzle) with a 3 mm outlet, jacketed in a thick circular aluminium collar. Aluminium was chosen for its lightweight properties, reducing the payload of the extruder, and for its higher heating rate due to its higher specific heat capacity ($0.90 \text{ J/g } ^\circ\text{C}$) compared to copper ($0.385 \text{ J/g } ^\circ\text{C}$) and iron ($0.442 \text{ J/g } ^\circ\text{C}$) [298] which are common commercial conductors. Similarly, the aluminium cooled at a faster rate after heating.

The collar was fitted with a customised 38 mm internal diameter x 25 mm wide nozzle heater rated at 24 volts and 150 watts. The hot-end heater was secured with a simple bolted housing with insulation on the outer periphery to contain heat and ensure safe handling of the system. To agitate the bitumen regularly, an auger screw powered by a 4-wire stepper motor was suspended inside the cone. The motor and screw were supported by a 'C' shaped stand connected to the bolted hot end. Seated on top of the nozzle, a 100K thermistor was embedded in a dent in the inner wall of the nozzle to monitor the operational temperature of the setup. Figure 4-75 illustrates the components of the hot-end extruder, while Figure 4-76 shows the assembled 24 V-150 W heating chamber.

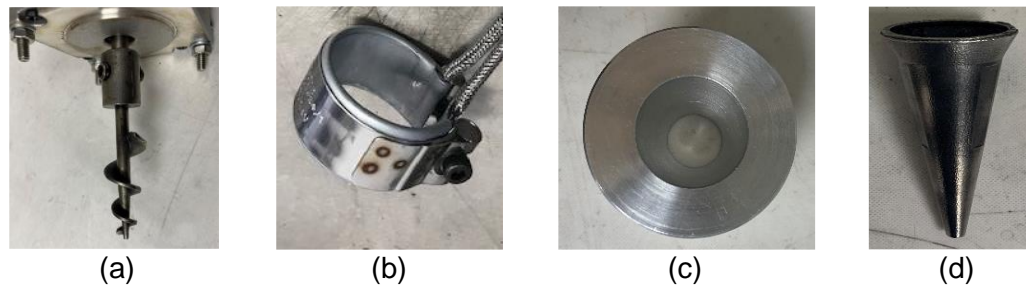


Figure 4-75: Images of extruder components: (a) auger screw attached to stepper motor, (b) band heater, (c) aluminium collar, and (d) funnel-shaped nozzle.

The UK standard single-phase 240V $\pm 6\%$ was supplied to the electrical heating system and stepper motor in the 3D printer through a 24 V DC output printed circuit board (PCB) as illustrated in Figure 4-77.



Figure 4-76: The assembled 24 V, 150 W heating chamber.

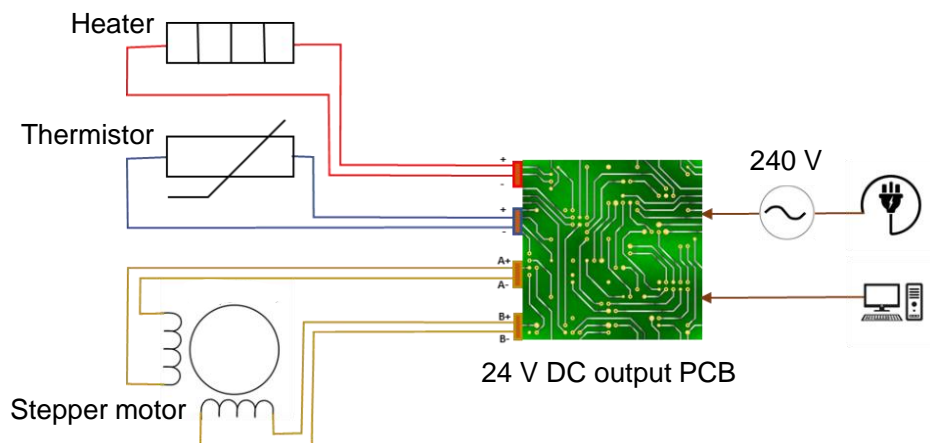


Figure 4-77: Schematic diagram of heating and control systems in the ACFM.

4.4.2 The assembled ACFM

The components under [Section 4.4.1](#) were assembled to form a heating chamber and then mounted to replace the original extruder illustrated under [Section 3.2.3](#). The original automatic bed levelling sensor (see [Figure 3-50](#) under [Section 3.2.3](#)) was clamped to the heating chamber and levelled to the nozzle. In this way, the sensor assisted in setting the nozzle outlet above the asphalt surfaces and halting horizontal movement to prevent the extruder from hitting obstacles should g-code commands go wrong. Practically, the extruder comprised the motor for screw rotation, a hopper to collect bitumen pellets, the heating chamber, and the nozzle outlet. This constitutes the system for heating and pouring the bitumen. The ACFM, on the other hand, comprised the extruder, electrical connections, gantry, and stepper motors. After complete setup, the heating capacity of the extruder and corresponding bitumen flow rate

were calibrated. As a control, a SPER Scientific 800115C thermometer³³ was regularly used to confirm the temperature of heated bitumen drained from the extruder nozzle. Practically, the APFM comprised the extruder, electrical connections, gantry, and stepper motors. Figure 4-78 shows the complete setup of the modified 3D printer (also known as the ACFM).

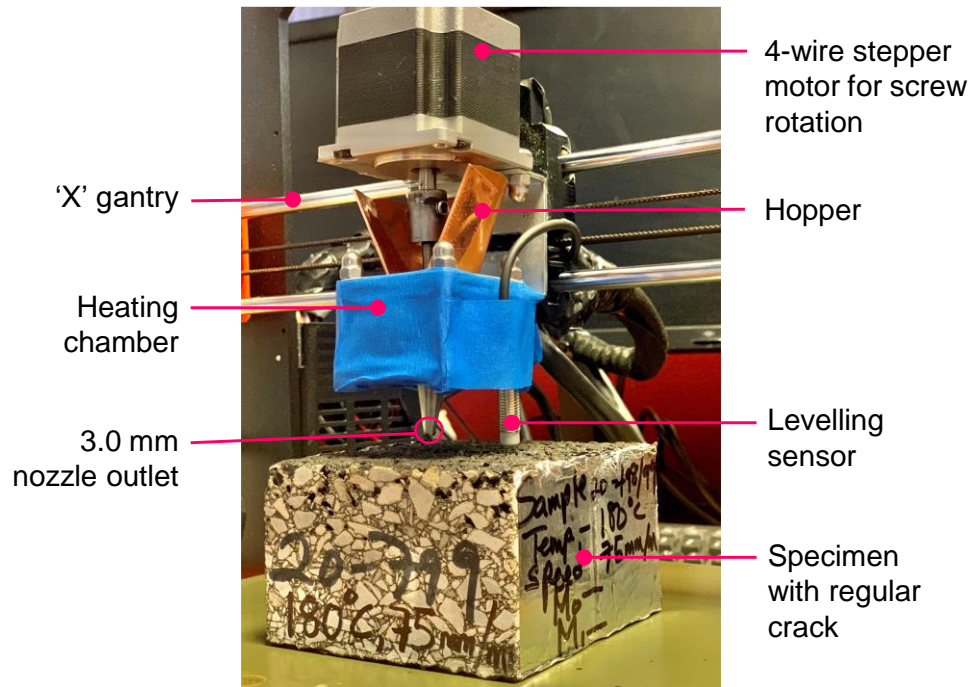


Figure 4-78: The ACFM setup.

4.5 The Crack Filling Process

4.5.1 Automated crack filling by 3D printing

Bitumen pellets for crack filling were loaded continuously into the hopper on the extruder. The 40/60 pen bitumen was heated to 100 °C, 140 °C, 160 °C and 180 °C. The polymer-modified bitumen was heated to 180°C. The printing speed ranges were 25 mm/min, 50 mm/min, 75 mm/min, 100 mm/min, 125 mm/min, 200 mm/min, 500 mm/min, 1000 mm/min and 5000 mm/min. Beyond 5000 mm/min, the hopper moved too fast to be fed with pellets, and operational errors in the crack filling increased. Using the 3D printer G-code command, the extruder was ordered to move only after reaching the specified heating temperature. By fixing the temperature reading thermistor close to the nozzle outlet, it was expected that the temperature recorded and communicated to the 3D printer would be the temperature of the extruded bitumen. As a control, the

³³ Sper Scientific: <https://sperdirect.com/en-ca/products/compact-infrared-food-safety-thermometer>

temperature of the extruded bitumen was measured manually with the SPER Scientific 800115C thermometer and found to be about 3% lower than the readings from the 3D printer's thermistor. This drop in temperature was due to cooling, as the thermometer took about a minute to register the peak reading. In addition, the flow rate of bitumen discharged from the nozzle outlet was quantified by measuring the volume of bitumen that drains out of the nozzle in 10 seconds. The nozzle outlet was opened and closed manually, and bitumen drained down from it under gravity. The distance between the top of the asphalt specimens and the nozzle outlet was 5 mm. During printing, the nozzle moved between the ends of the crack length discharging bitumen layer by layer until the crack was full to the brim. There were situations where bitumen was discharged beyond the brim of the crack due to the slow speed of the nozzle. In such situations, the bitumen poured could be more than the crack volume accounting for more than 100% volume filled. For fillings less than 100%, bitumen poured was certainly less than the crack volume. The layer-by-layer filling process with the extruder is illustrated in Figure 4-79. In addition, Figure 4-80 provides an example of the 3D printer filling cracks and the resulting filled crack.

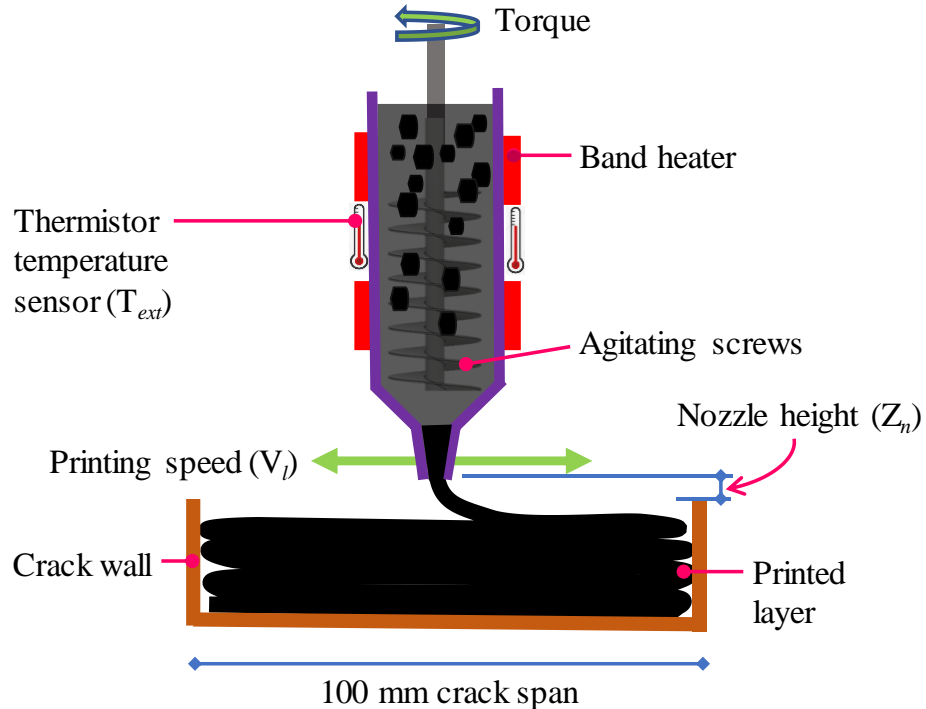


Figure 4-79: 3D printing crack filling process.

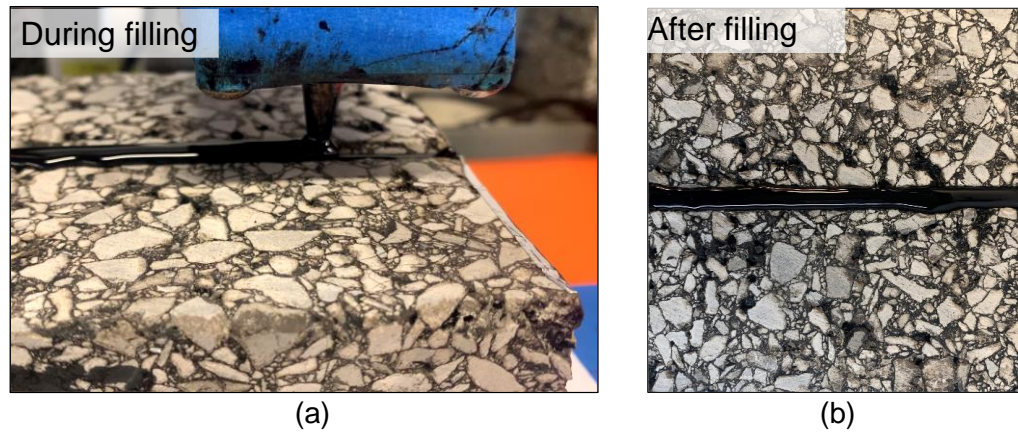


Figure 4-80: (a) 3D printing in progress to fill a regular crack³⁴ and (b) the filled crack.

4.5.2 Crack filling by hand

Control specimens were filled manually with hot bitumen at the same temperatures as in the 3D printing process. The heated bitumen was poured in bulk from a pre-heated galvanised tin with a narrow spout in one direction from one end of the crack to the other end. Filling cracks by hand did not follow a specific speed and stopped once the crack was filled to the brim. Figure 4-81 illustrates the crack filling process by hand.

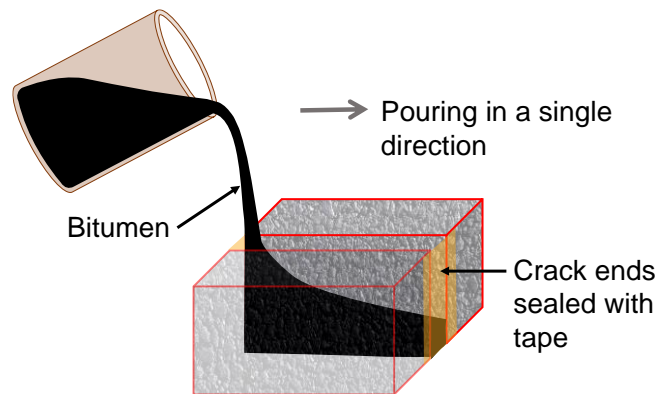


Figure 4-81: Crack filling by hand.

4.5.3 Determination of the volume of crack filled

The proportion of crack volume filled in the blocks was estimated as a percentage ratio of the practical volume to theoretical volume as shown in Equation (2-1).

$$\text{Crack volume filled} = \frac{\text{theoretical volume}}{\text{practical volume}} \times 100 \quad (4-12)$$

³⁴ A video showing 3D printing in progress for crack filling can be found here: <https://youtu.be/GWJq40IFUO4>

For example, with a 5 mm crack width, spanning 100 mm long and 60 mm deep, a theoretical volume of 30,000 mm³ was estimated. To determine the practical volume filled, the mass of filled bitumen was obtained as a difference between the mass of block specimen before and after filling. The practical volume was estimated as a product of the bitumen mass and the bitumen density.

Applying Equation (2-1), the estimated crack volume filled with bitumen could be greater or less than 100%. Fillings greater than 100% were considered as overfills which means top-printed layers had exceeded the crack brim whilst those less than 100% were considered as underfills. Cracks filled to the brim at 100 % volume capacity were considered a precise fill.

4.6 Preliminary Assessment of the Flow Rate and Ductility of Extruded Bitumen

Figure 4-82 illustrates the rate at which bitumen drained from the extruder nozzle when the extruder was heated at different temperatures. Generally, increasing the heating level enhanced the bitumen flow rate which implies cracks are likely to be filled faster at higher temperatures. This flow rate pattern mirrors the temperature-viscosity patterns observed in bitumen, as documented in the literature [299].

Figure 4-83 compares the ductility of 40/60 bitumen 3D printed at 25 mm/min to those filled by hand from a forced ductility test. A lower 25 mm/min printing speed was chosen to ensure that cracks were filled in a steadier state closer to hand fills.

An independent-sample t-test comparing the two filling methods revealed no significant difference between them: $t(6) = 0.35$, $p = 0.75$. The mean square for manual fill was 5.8, while for 3D printing, it was 5.6. It is important to note that a small t-score, such as 0.35 (less than 0.5), suggests similarity between the ductility behaviour for both filling methods.

The conclusion drawn from this observation is that the newly developed bitumen extruder does not alter the ductility or cohesive characteristics of bitumen.

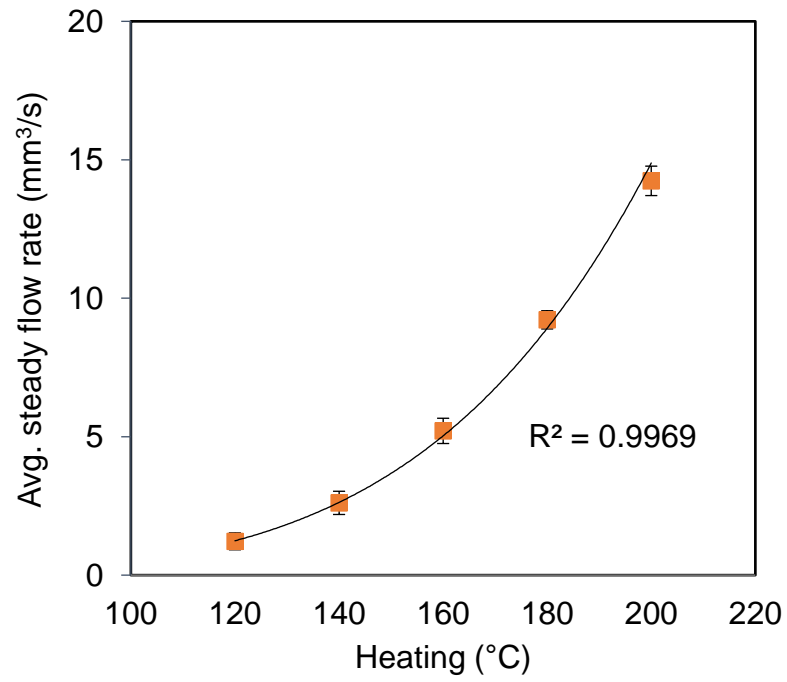


Figure 4-82: The steady flow rate of 40/60 pen bitumen from the extruder nozzle outlet.

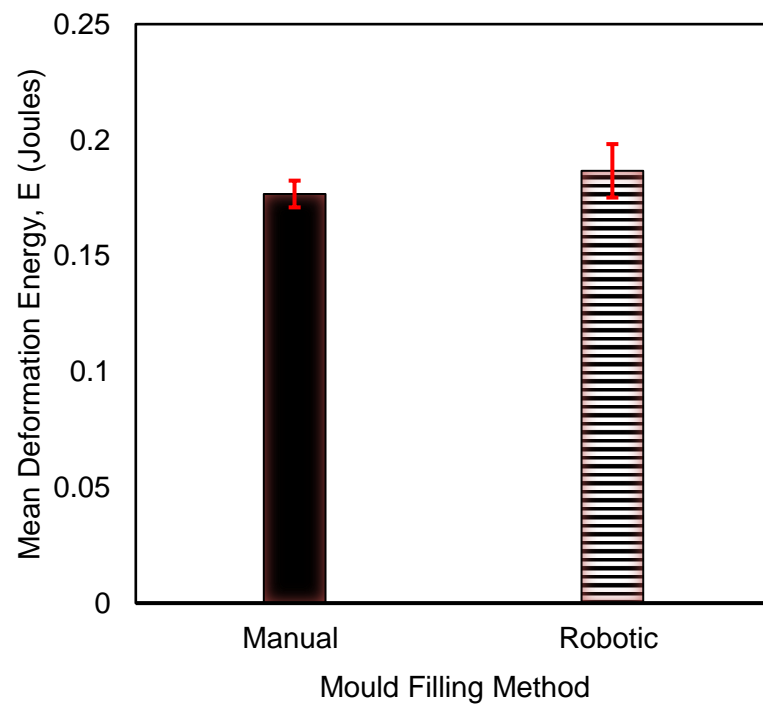


Figure 4-83: Comparison between the deformation energy for 3D-printed fills and manual fills.

4.7 Effect of Temperature and Printing Speed on the Volume of Crack Filled with 40/60 Pen-grade Bitumen

Figure 4-84 shows the relationship between printing speed, temperature and the volume of cracks filled with 40/60 pen bitumen. The figure reveals that crack volumes are not fully filled at lower temperatures. For example, at 100 °C, the highest volume filled is observed at a speed of 25 mm/min, reaching 92.3% of the total crack volume. At a filling rate of 25 mm/min, temperatures of 140 °C, 160 °C, and 180 °C result in filling volumes exceeding 100%, indicating that cracks were filled beyond the brim of asphalt specimens, particularly at lower printing speeds. These findings align with results from manually filled cracks at similar temperatures, where the average volumes filled were close to 100%.

A CT scan of the specimens revealed that at lower temperatures, the bitumen was viscous and could not fully drain to occupy the entire crack volume. This observation is illustrated in Figure 4-85, which compares regular blocks filled at 100 °C and 160 °C, both filled at a printing speed of 100 mm/min³⁵.

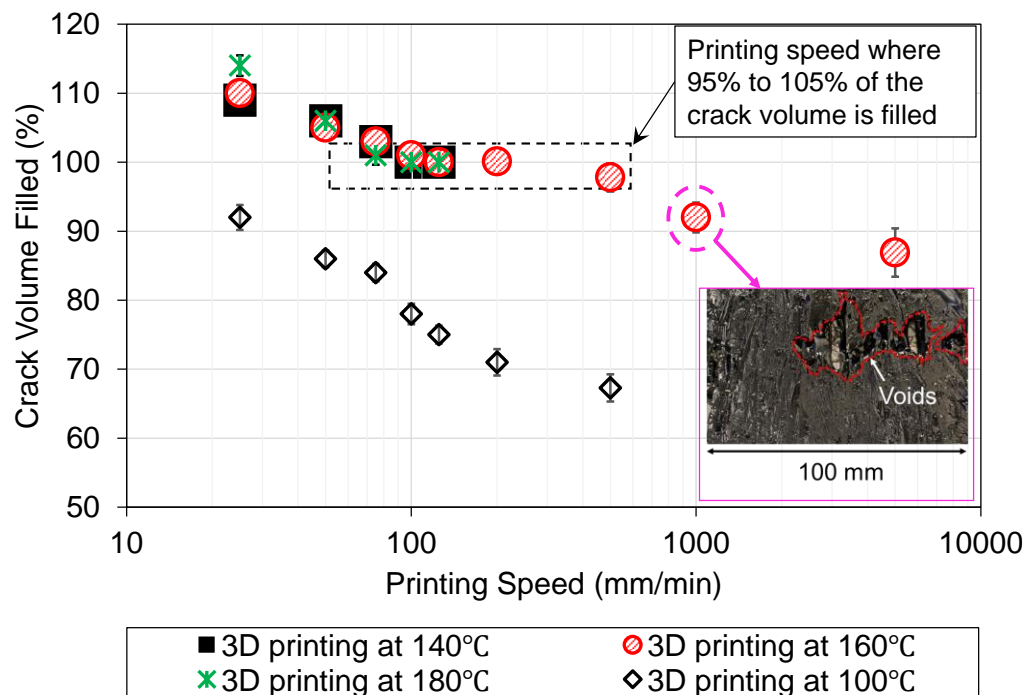


Figure 4-84: Volume of regular cracks filled with 40/60 pen-grade bitumen at different extrusion temperatures and layer printing speeds. The inserted image shows voids trapped in bitumen printed at 160 °C at 1000 mm/min.

³⁵ With 40/60 pen bitumen, cracks were fully filled at 160 °C and printing speed of 100 mm/min. These parameters were applied in subsequent investigations.

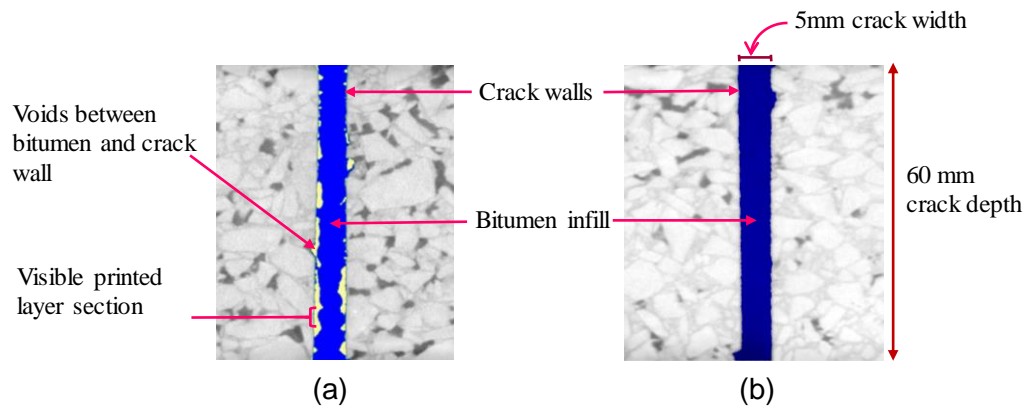


Figure 4-85: A section of 40/60 pen-grade bitumen in regular cracks printed at 100 mm/min: (a) at 100 °C and (b) at 160 °C.

One interesting observation was the decline in crack volume filled at printing speeds beyond 500 mm/min. Specimens filled at such high speeds were visually examined during a shear test where the filled cracks were split with the bitumen close to solid states. Upon visual examination, it was observed that cracks filled at temperatures of 160 °C and 180 °C at speeds exceeding 500 mm/min contained air bubbles trapped within the bitumen. This implies that higher printing speeds whisk air bubbles into the bitumen and reduces the volume of bitumen within the crack. An example of a 3D printed fill with trapped voids at 1000 mm/min and 160 °C is inserted in [Figure 4-84](#) and fully illustrated in [Figure 4-86](#).

The formation of large voids in the bitumen is believed to be similar to cavitation, where high relative motion traps vapour-filled bubbles within the bitumen [300,301]. As the printed bitumen cools and its pressure decreases, the vapour escapes, leading to the formation of partial vacuums in the solidified bitumen. This phenomenon could be mitigated by lowering the printing temperature or decreasing the printing speed. Since bitumen is sensitive to temperature, which directly affects flow rate and filling quality, a reduction in printing speed is considered a feasible option. Subsequent research could explore methods to diminish cavitation in bitumen at high-speed printing.

Based on the analysis of [Figure 4-84](#), [Figure 4-85](#), and [Figure 4-86](#), a printing speed range of 50 mm/ min to 500 mm/min, with temperatures ranging between 140 °C and 180 °C are considered for further investigations.

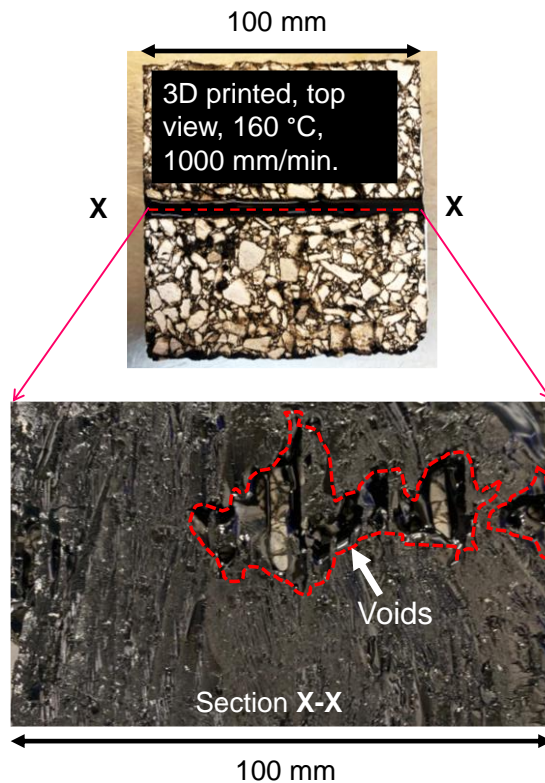


Figure 4-86: Sections through a 3D printed fill at 1000 mm/min and 160 °C for 40/60 pen bitumen in a regular crack after shear-splitting at 5 °C.

4.8 Shear Strength of Filled Regular Cracks

Figure 4-87(a) shows the maximum shear forces resisted by 3D printed fills at 140 °C, 160 °C and 180 °C at a speed of 100 mm/min compared to cracks filled by hand at the same temperatures. 100 mm/min printing speed was selected as a representation from the feasible filling speed ranges discussed in Section 4.7 as it produced volume fills closest to 100%. This figure shows that 160 °C has the highest shearing resistance for both 3D printed (5.607 kN) and manual fills (5.792 kN).

It is believed that the lowest shear force at 140 °C could mean the bitumen rapidly loses its temperature when in contact with the crack surfaces and has reduced adhesion. Also, lower shear values at 180 °C could result from thermal degradation that damages the bitumen's viscoelastic properties [302]. Consequently, 160 °C produced the highest shearing performance. Furthermore, at the 160 °C filling temperature, Figure 4-87 shows how a reduction in printing speed impacted the samples' shearing resistance. Hence, low printing speeds and higher filling volumes have higher resistance to shear deformation.

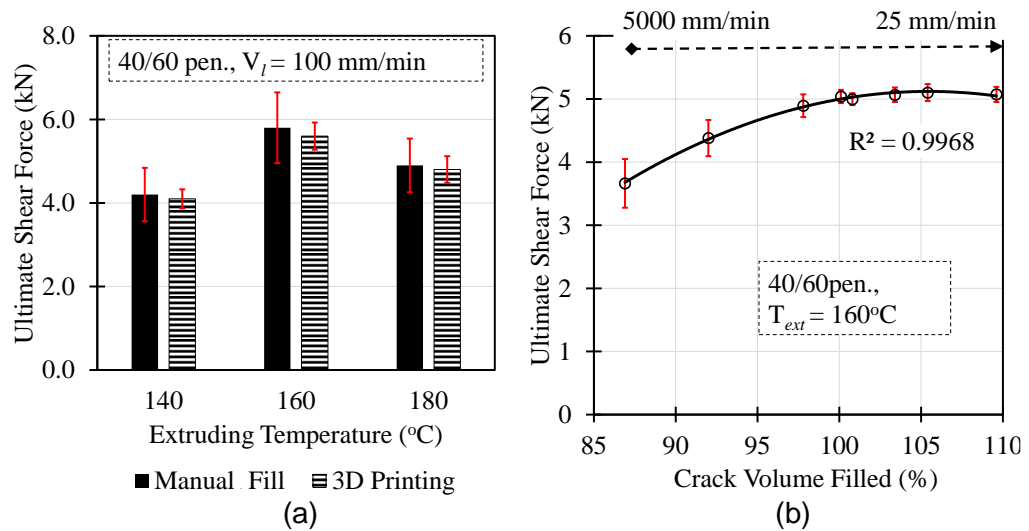


Figure 4-87: Resistance of filled cracks to shear failure for 40/60 pen-grade bitumen: (a) ultimate shear force for filled cracks at 140 °C, 160 °C, and 180 °C at 100 mm/min, and (b) impact of crack volume filled on shear resistance.

4.9 Tensile Strength in Filled Regular Cracks

Figure 4-88(a) compares the tensile bond strength of regular cracks filled at the optimised temperature and speed, 160 °C and 100 mm/min, to manually filled cracks. The figure shows that manually filled cracks exhibit higher bonding strength than 3D printed fills.

Consequently, from the volume of cracks filled and their mechanical performance examined so far, 160 °C at 100 mm/min were adopted as the optimal temperature and printing speed, respectively, for 3D printing for crack filling for the 40/60 pen-grade bitumen. Note that 160 °C is within the recommended target laboratory mixing temperature per BS EN 12697-35:2016 [303]. The conclusion here is that cracks can be filled fully using 3D printing technology at an optimised temperature and printing speed. The filled cracks, however, exhibit weaker mechanical performance compared to hand fills.

4.10 Impact of Crack Widths on Proportions of Crack Volume Filled

At the optimised temperature and printing speed in this study, Figure 4-88(b) shows how changes in crack width influence a crack's filling capacity. It was observed that those crack widths smaller than the nozzle size, 3.0 mm, were not fully filled (67% maximum fill at 3.0 mm crack width). For 1 mm cracks of about one-third of the nozzle width, only 22.3% of the crack volumes were filled. On the other side, cracks bigger than 3.0 mm were completely filled.

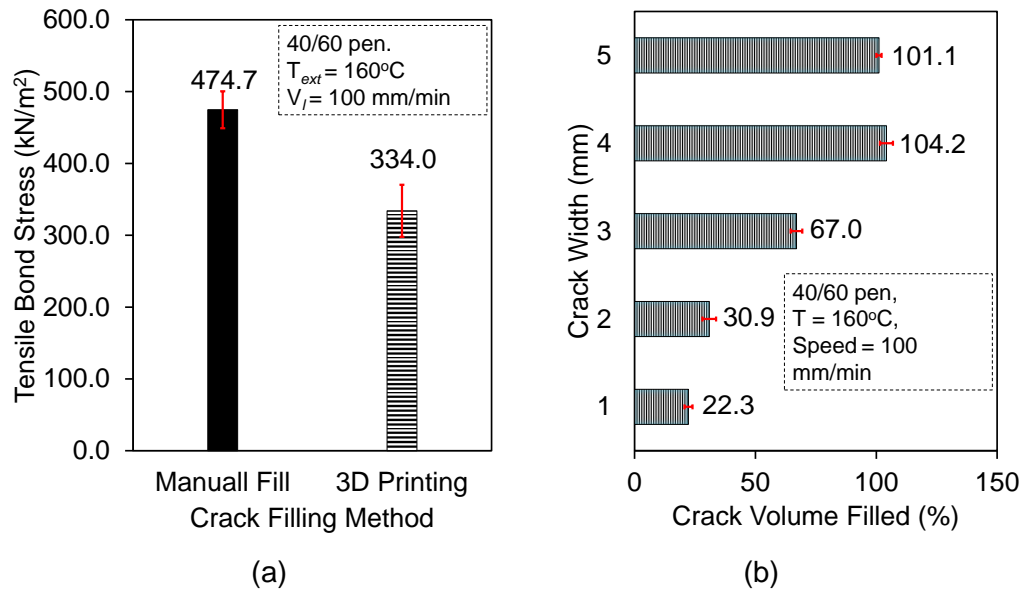


Figure 4-88: (a) Tensile bond stress for regular cracks filled with 40/60 pen-grade bitumen, and (b) crack-filling volumes for cracks of various widths.

The conclusion is that different nozzle sizes are required to fill cracks of different widths at a given optimised printing speed and temperature. Therefore, it is recommended that the nozzle's outlet diameter be dynamically adapted to the width of cracks rather than being fixed at a constant diameter.

4.11 Filling in Irregular Cracks with 40/60 Pen-Grade Bitumen

Table 4-12 shows the percentage of crack volumes filled by the 3D printer with 40/60 pen bitumen at 160 °C and 100 mm/min. The crack volume filled reduced to 95.5% from the 100.8% in regular cracks. Thus, a drop of about 5.55% in bitumen volume. A similar observation is made in the manual fill with a drop from 102% volume fill in regular cracks to 97.3% in irregular cracks. Irregularities in the cracks reduced the crack filling efficiency. Moreover, in Table 4-12 it is shown that irregular cracks filled by hand have higher flexural strength than 3D printed fills. However, these results make it challenging to conclude which type of crack filling, manual or 3D printing, produces better results since differences may be due to the variability of crack morphologies.

Furthermore, Figure 4-89 shows irregular cracks filled with 40/60 bitumen for both manual and 3D printed fills. In both fills, more voids were observed near the outer part of the cracks, which may be due to faster cooling, causing the bitumen to harden before occupying every spot. Also, it is visually observed that 3D printed fills have higher voids, which could cause weaker mechanical behaviour. The higher voids in 3D printed fills resulted from the layer-by-layer

filling approach. As a result, the manual filling could show improved mechanical behaviour since all the bitumen is poured at once. Hence, a layer-by-layer approach is not appropriate to fill cracks.

Table 4-12: Crack volume filled with 40/60 pen-grade bitumen and flexural behaviour in irregular cracks.

	Manual filling	3D printing
Filling conditions	40/60 pen. Temp. ³⁶ . = 160 °C	40/60 pen. Temp. = 160 °C Speed = 100 mm/min
Number of specimens	4	4
Filling Volume		
Avg. crack volume filled (%)	97.3	95.5
Standard deviation	1.506	2.236
Flexure		
Avg. ultimate flexural strength (kN)	0.925	0.650
Standard deviation	0.029	0.033

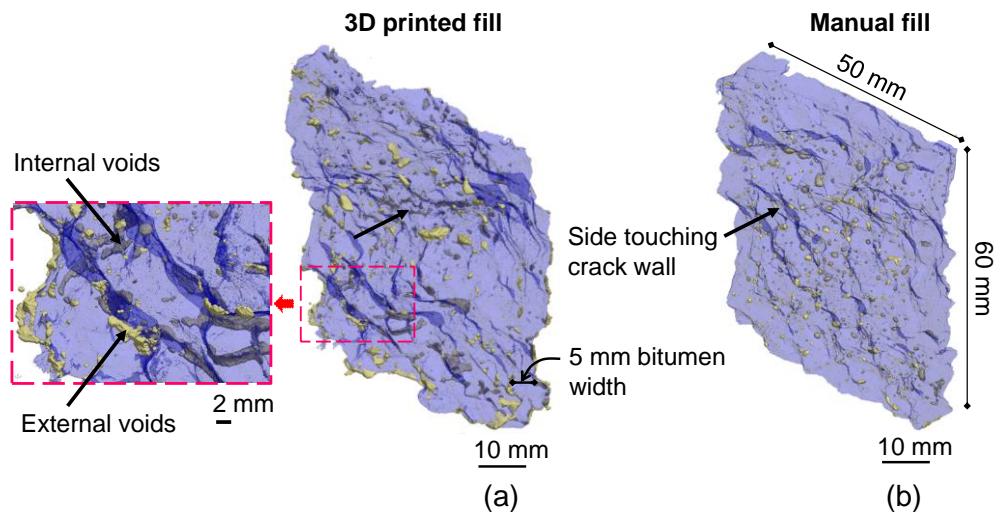


Figure 4-89: Isometric view of 3D reconstructed images of 40/60 pen-grade bitumen infill in irregular cracks: (a) 3D printed fill and (b) manual fill.

From these observations, it is believed that routing crack surfaces to reduce their irregularity and pouring all the bitumen at once could help improve the durability of the filled cracks. Crack pre-heating [158], which is a well-known technique, is also encouraged to reduce bitumen cooling at crack walls.

³⁶ Temp. = Temperature

Notwithstanding the higher voids in the 3D printed fills, it is worth noting that the voids created are localised and not connected. Given the disconnected nature of the voids in the bitumen, it is considered that water cannot permeate through the filled cracks, fulfilling the primary objective of crack filling.

4.12 Crack Filling with Polymer-Modified Bitumen

The polymer-modified bitumen (PMB type N1) exhibited an average steady flow rate of $109.78 \text{ mm}^3/\text{s}$ at 180°C , which is lower than the $507.50 \text{ mm}^3/\text{s}$ at 160°C observed with the 40/60 penetration bitumen. Consequently, a recommended average heating and pouring temperature of 180°C was adopted based on the bitumen provider's suggestion. Figure 4-90 illustrates the percentage of crack volumes filled in regular cracks using PMB type N1 for both manual and 3D printing methods.

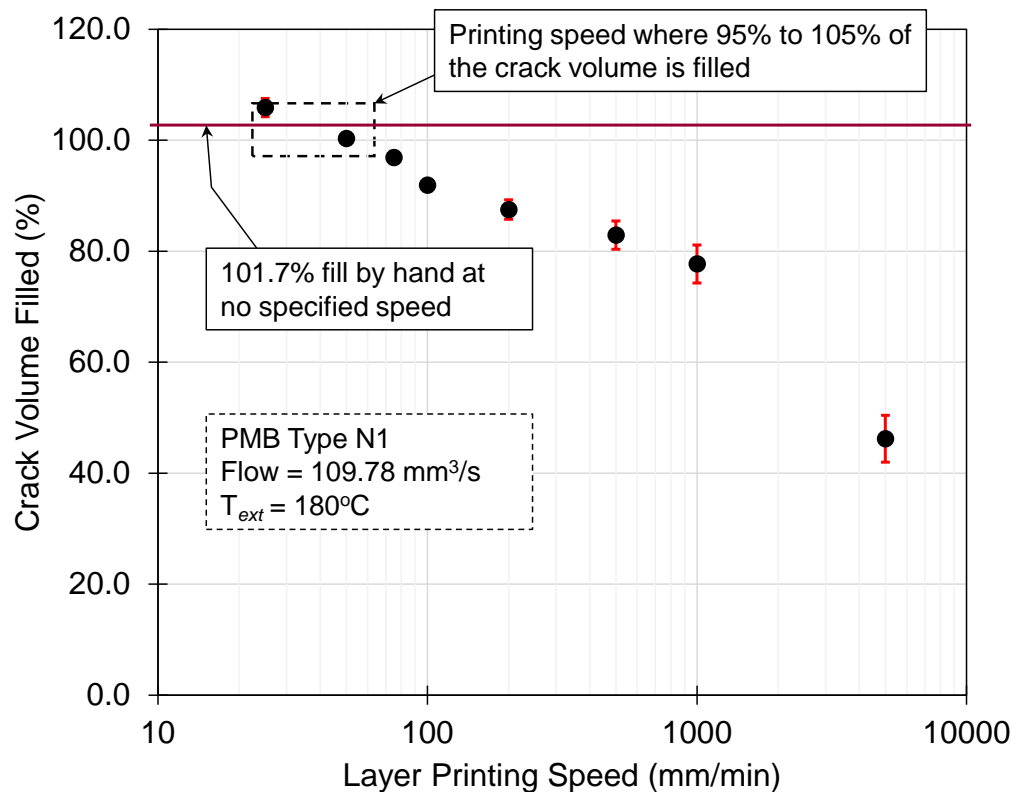


Figure 4-90: Volume of cracks filled with PMB type N1 at a temperature of 180°C at varying printing speeds.

These findings align with those presented in Figure 4-84. However, PMB type N1 demonstrated complete and accurate crack filling at lower printing speeds compared to the 40/60 penetration bitumen. Specifically, regular cracks were effectively filled at a speed of 50 mm/min with PMB type N1, in contrast to 100 mm/min with the 40/60 penetration bitumen. This decrease in filling rate can be

attributed to the lower flow rate of PMB type N1. For instance, a filling rate of 5000 mm/min achieved a 46.2% volume fill with PMB type N1, whereas an 80% volume fill was attained with the 40/60 penetration bitumen. Given that PMB type N1 has a higher softening point of 96 °C compared to 51 °C for the 40/60 penetration bitumen, it is expected to harden more quickly upon contact with the crack walls.

Additionally, in PMB type N1, the tensile bond shear stresses were higher in manual fills, similar to those in 40/60 penetration bitumen fills. As illustrated in [Figure 4-91](#), 3D-printed layer boundaries acted as weak planes where tensile failures initiated. Consequently, it is crucial to minimise or entirely avoid layering bitumen during machine filling in the future.

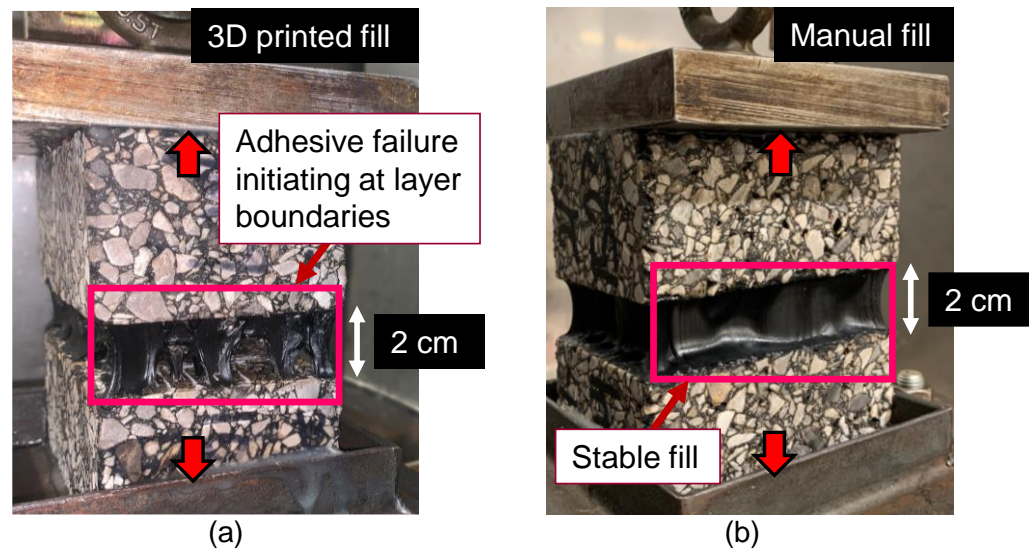


Figure 4-91: Tensile bond failure modes in regular cracks filled with PMB type N1 and pulled apart at 5 °C: (a) 3D printing and (b) manual filling.

In irregular cracks, 3D printing with the optimised temperature and printing speed for PMB type N1, 180 °C and 50 mm/min respectively, resulted in smaller volume fills (100.3% in regular compared to 83.6% in irregular). This reduction was also observed when using 40/60 penetration bitumen. This observation supports the earlier conclusion in [Section 4.11](#) that irregularities diminish the effectiveness of crack filling, as they contribute to the formation of voids within the bitumen infill. Additionally, similar to the 40/60 pen. bitumen fills, 3D printed fills with PMB type N1 were weaker in flexure (see [Table 4-13](#)). Again, the comparatively weaker mechanical performance with PMB type N1 may be attributed to higher voids entrapped in the printed bitumen, especially at layer boundaries.

Therefore, it can be concluded that 3D printing polymer-modified bitumen and other stiffer crack sealants to fill cracks is feasible. However, lower printing speeds are necessary for effective filling, and similar to unmodified bitumen, 3D-printed fills exhibit comparatively weaker mechanical performance.

Table 4-13: Crack filling performance of PMB type N1.

Filling conditions	Manual filling	3D printing
	PMB type N1	PMB type N1
	Temp. = 180 °C	Temp. = 180 °C Printing speed = 50 mm/min
Regular cracks³⁷		
Number of specimens	4	4
Average ultimate shear force (kN)	0.343	0.330
Standard deviation	0.031	0.010
Average tensile bond shear stress (kN/m ²)	112.333	72.000
Standard deviation	2.082	2.646
Irregular cracks		
Number of specimens	4	4
Crack volume filled (%)	88.167	83.633
Standard deviation	2.108	1.779
Average flexural strength (kN)	0.067	0.043
Standard deviation	0.0060	0.0042

4.13 Summary

In this chapter, the feasibility of machine-filling cracks with hot bitumen in asphalt using 3D printing technology has been demonstrated. The operational parameters affecting the volume, quality (in terms of trapped voids), and the mechanical properties of the filled cracks have been examined. For simplicity, a 3D printer was employed to fill the cracks in the laboratory. It is recognised that identifying automated crack filling parameters at the laboratory scale is a step towards developing a fully functional robotic device for sealing cracks and joints in the field. It has been shown that the bitumen flow, filling speed, and the width and depth of cracks are critical in determining the quality of the fill and must be carefully managed in any future automated filling operation. The following more specific conclusions can be drawn from the findings of this chapter:

³⁷ Refer to Figure 4-84 for proportions of volume filled.

- The speed and temperature of the bitumen during crack filling are critical factors that influence the filling volume of cracks and their resistance to mechanical deformation.
- There is a minimum temperature below which cracks cannot be fully filled and a maximum temperature above which bitumen thermally degrades, in addition to an optimum crack filling speed.
- Understanding the complex interactions between the filling speed, crack width, depth, and tortuosity, as well as the temperatures of the bitumen, the environment, and the cracked pavement, is crucial to producing crack fillings of the highest quality.
- Increasing the printing speed beyond the optimum speed leads to the formation of large air bubbles in the bitumen, which reduce the mechanical strength of the filled cracks.
- The layer-by-layer filling approach of 3D printing increases the porosity in the filled cracks. The layer boundaries also act as weak planes where tensile failures begin. As a result, future machine-filling applications should minimise or, if possible, avoid creating bitumen layers.
- The crack filling speed needs to be adjusted according to the temperature and dimensions of the crack. Thus, it is important to develop accurate models to predict crack geometries and calculate the required filling rate for each specific location.
- Machine crack filling is more effective for filling straight cracks, such as those in pavement joints. Therefore, it is recommended that this application be developed first, while the complex interaction between the identified parameters and irregularities in crack paths should be thoroughly investigated in future research.

The findings from using a 3D printer to fill cracks provide critical insights for advancing extrusion techniques for pothole repairs. The next chapters address two major challenges: designing extrusion-friendly asphalt mixes while maintaining performance, and developing an automated machine, the APFA, to enhance the effectiveness and consistency of pothole filling.

Chapter 5: Digital Design of Asphalt Mixtures

5.1 Introduction

This chapter presents a novel performance-based method for designing a hot mix asphalt based on the air voids content, workability, Marshall stability, and Marshall flow that considers aggregate geometry. This method is based on the idea that the aggregate geometry, gradation, and other elements in asphalt, e.g. filler, dust, and bitumen volumes, impact the compacted topology and structural performance of an asphalt mixture [26,31,143]. The asphalt design method is data driven. First, the geometric characteristics of the aggregates in asphalts are extracted from pictures using image processing techniques. Second, software is used to estimate the number of aggregates and volume of mastic (bitumen, filler, and aggregates smaller than 2 mm) in a fixed 250 g of asphalt. Third, the number of aggregates and volume of mastic that meet the desired properties are obtained based on correlations between the air voids content, Marshall stability, Marshall flow, and workability, and the number of aggregates and volume of mastic. The correlations are based on the number of aggregates in a certain mass of asphalt; hence, they can be used to design asphalts with any aggregates. A graphical illustration of the concept investigated in this chapter is shown in Figure 5-92.

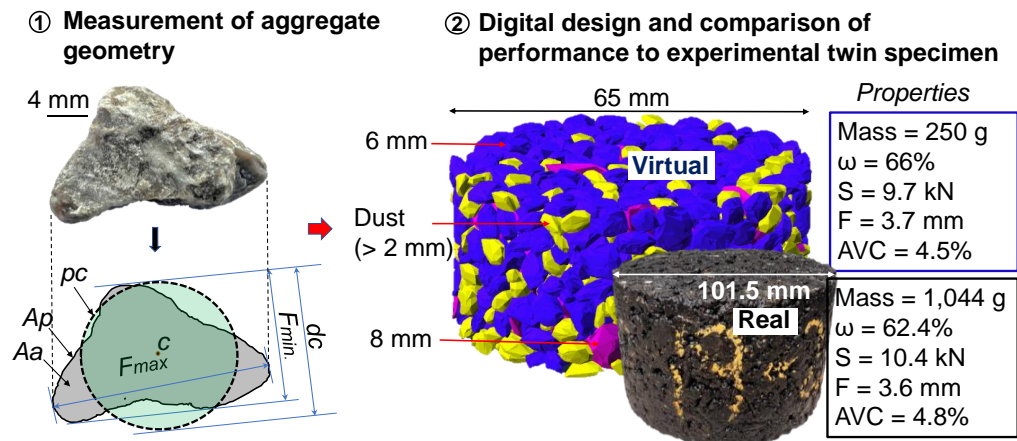


Figure 5-92: An illustration of the asphalt digital design concept using aggregate geometry as a key input.

Publication acknowledgement

This chapter includes techniques, results, and discussions from earlier collaborative research efforts that have been previously published. Consequently, relevant portions of the content in this chapter are also detailed

in the following publication: “A digital design method for asphalt mixtures that incorporates aggregate geometry,” published in Construction and Building Materials, Volume 416, 2024.

5.2 Aggregates, Bitumen and Asphalt Mixtures

This chapter utilises a diverse range of aggregates, including limestone, hornblende, basalt, granite, granodiorite and greywacke. The geometric features of these aggregates' samples were obtained using the method outlined in [Section 3.3.5](#). Additional samples from the same batch were used in the design and production of corresponding asphalt mixtures.

The aggregates and mixtures in this study were divided into two categories: Category A (Cat A) and Category B (Cat B), based on their application. Cat A aggregates, limestone from the Tunstead Quarry in the UK, were utilised to prepare asphalt mixtures (Cat A mixtures) for predictive modelling. These aggregates had an average density of 2.7 Mg/cm³ and an average water absorption rate of 0.6%, as determined in accordance with BS EN 1097-6:2022 [304]. Their gradations typically featured a nominal maximum aggregate size of 8 mm and a maximum size of 10 mm. To achieve the desired final gradations, four aggregate batches of different sizes (8 mm, 6 mm, dust [0 - 4 mm], and filler) were mixed in various proportions. The gradations selected for the mixtures were intentionally chosen to cover a broad range of asphalt types, including dense, semi-porous, and porous, to avoid overfitting in the predictive models. [Figure 5-93](#) showcases selected Marshall cores of manufactured asphalt for the Cat A mixtures, while [Figure 5-94](#) displays the gradation curves of the 25 aggregates in Cat A mixtures for predictive modelling, along with the upper and lower limits of Stone Mastic Asphalt (SMA) as specified in reference [281].



[Figure 5-93](#): Exhibit of selected Marshall specimens for Cat A mixtures.

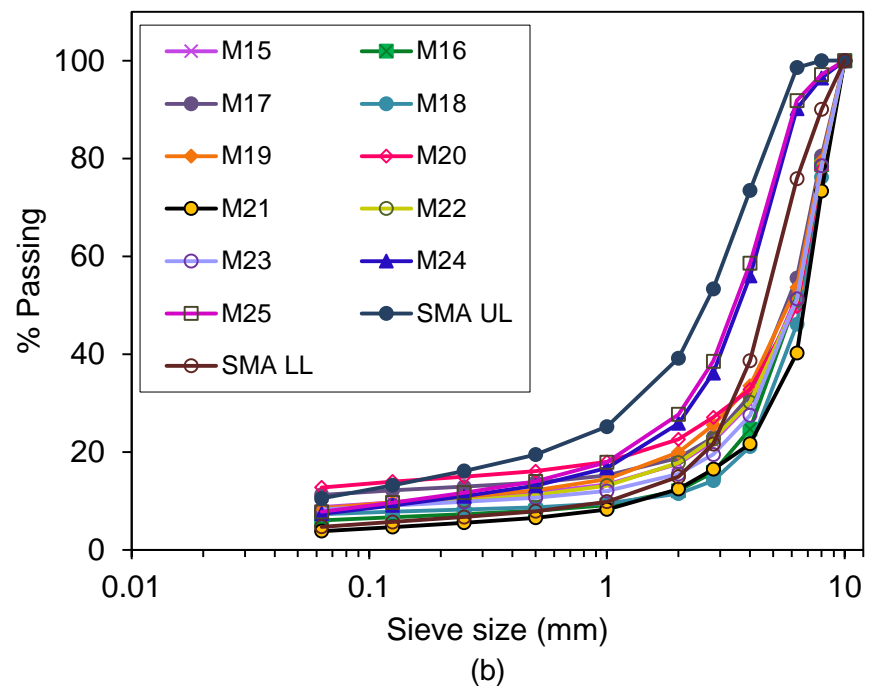
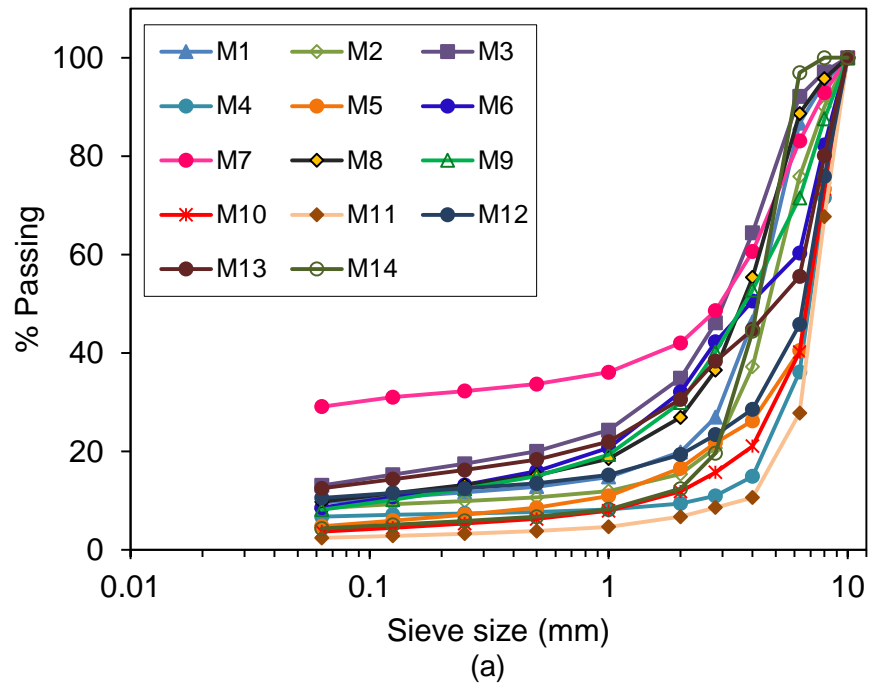


Figure 5-94: Aggregate gradations for predictive modelling specimens: (a) specimen M1 to M14, and (b) specimen M15 to M25 and SMA limits.

Neat bitumen with a penetration grade of 40/60 (43 mm penetration and 51.0 °C softening point) was used for all Cat A mixtures, which were compacted with uniform energy levels (50 blows on each side) at approximately 150 °C. The properties of these mixtures, also referred to as mixture performance, are detailed in [Table 5-14](#).

Table 5-14: Asphalt mix properties for predictive modelling specimens.

Mixture ID	Bitumen type	Compaction temperature (°C)	No. of blows	BC (%)	AVC (%)	Max. density (Mg/m ³)
M1	PG 40/60	150.0	2 x 50	6.0	5.4	2.477
M2	PG 40/60	150.0	2 x 50	6.0	6.3	2.483
M3	PG 40/60	150.0	2 x 50	6.0	7.8	2.473
M4	PG 40/60	150.0	2 x 50	6.0	22.9	2.505
M5	PG 40/60	150.0	2 x 50	5.0	16.0	2.533
M6	PG 40/60	150.0	2 x 50	6.0	10.5	2.488
M7	PG 40/60	150.0	2 x 50	8.0	3.4	2.419
M8	PG 40/60	150.0	2 x 50	6.0	3.5	2.475
M9	PG 40/60	150.0	2 x 50	5.5	2.4	2.499
M10	PG 40/60	150.0	2 x 50	5.5	22.2	2.518
M11	PG 40/60	150.0	2 x 50	4.5	29.3	2.56
M12	PG 40/60	150.0	2 x 50	5.5	12.4	2.516
M13	PG 40/60	150.0	2 x 50	6.0	5.9	2.56
M14	PG 40/60	150.0	2 x 50	5.2	5.2	2.498
M15	PG 40/60	150.0	2 x 50	6.0	16.7	2.496
M16	PG 40/60	150.0	2 x 50	5.5	15.6	2.513
M17	PG 40/60	150.0	2 x 50	6.6	10.4	2.474
M18	PG 40/60	150.0	2 x 50	5.4	15.3	2.511
M19	PG 40/60	150.0	2 x 50	5.5	9.1	2.481
M20	PG 40/60	150.0	2 x 50	6.5	8.3	2.473
M21	PG 40/60	150.0	2 x 50	4.0	20.4	2.513
M22	PG 40/60	150.0	2 x 50	5.5	13.3	2.513
M23	PG 40/60	150.0	2 x 50	5.4	15.6	2.516
M24	PG 40/60	150.0	2 x 50	5.0	3.7	2.477
M25	PG 40/60	150.0	2 x 50	5.0	3.4	2.472

Cat B aggregates and their corresponding mixtures were utilised for a sensitivity analysis of the design method proposed in this study. This analysis evaluated the impact of changes in aggregate size, asphalt volumetrics, and other performance variables on the developed predictive model. The aggregates were sourced from the Belice, Zbraslav, Chornice, Chvaletice, and Zarubka quarries in the Czech Republic, and comprised limestone (L), hornblende (H), basalt (B), granite (G), granodiorite (D), greywacke (W), and some undisclosed (U) aggregates. These aggregates typically featured a nominal maximum aggregate size of 16 mm and an absolute maximum size of 31.5 mm, differing from the 10 mm maximum size of Cat A aggregates. Their densities ranged from

2.26 to 2.97 Mg/m³, with water absorption rates between 0.2% and 0.8%. The volumetric and performance properties of Cat B mixtures were independently evaluated at the Department of Road Structures, Czech Technical University, Prague. Figure 5-95 and Table 5-15 details the aggregate gradation curves and asphalt mix properties of the Cat B mixtures, respectively.

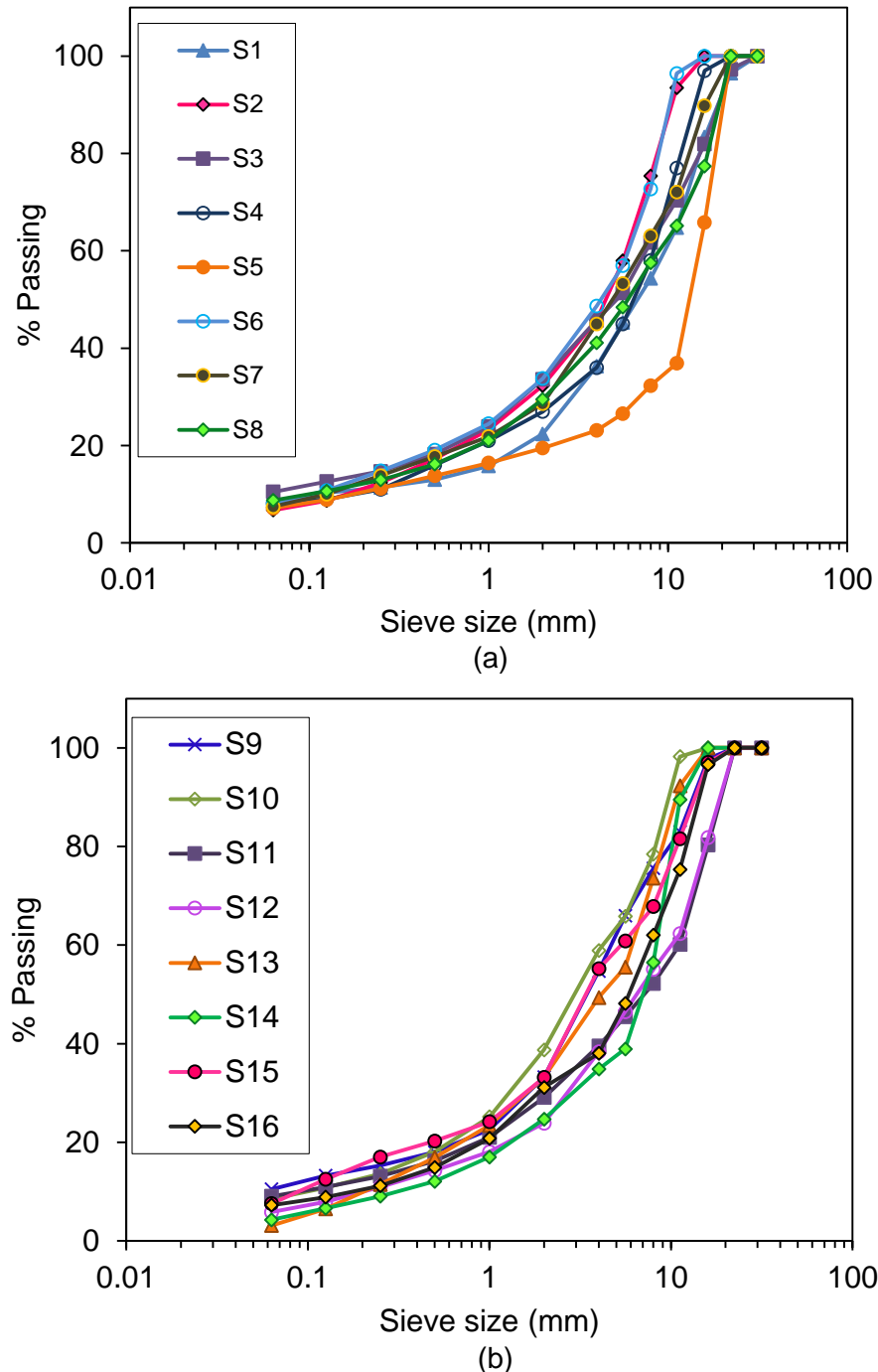


Figure 5-95: Aggregate gradation for sensitivity analysis specimens: (a) specimen S1 to S8 and (b) specimen S9 to S16.

Table 5-15: Asphalt mix properties for sensitivity analysis specimens.

Mixture ID	Bitumen type	Compaction temperature (°C)	No. of blows	BC (%)	AVC (%)	Max. density (Mg/m ³)
S1	PG 50/70	150.0	2 x 50	4.0	5.3	2.556
S2	PMB 40/85-65	160.0	2 x 75	5.8	4.0	2.448
S3	PMB 10/40-65	160.0	2 x 75	3.7	4.1	2.748
S4	PG 50/70	150.0	2 x 50	4.3	6.0	2.524
S5	PMB 25/55-65	160.0	2 x 75	3.5	7.1	2.514
S6	PMB 40/85-65	160.0	2 x 75	5.9	1.2	2.421
S7	PG 50/70	155.0	2 x 50	4.4	5.5	2.617
S8	PMB 10/40-65	160.0	2 x 75	4.7	4.2	2.635
S9	PG 50/70	150.0	2 x 50	4.7	4.8	2.518
S10	PG 50/70	150.0	2 x 50	5.6	5.8	2.462
S11	PMB 10/40-65	160.0	2 x 75	4.4	5.4	2.679
S12	PMB 25/55-60	160.0	2 x 75	5.0	3.0	2.488
S13	PMB 40/85-65	160.0	2 x 75	5.7	1.2	2.421
S14	PMB 40/85-65	160.0	2 x 75	5.0	4.6	2.504
S15	PG 50/70	150.0	2 x 50	3.7	8.4	2.877

The physically measured properties were compared to those estimated using the model developed in this study, with the difference in performance expressed through the Mean Absolute Percentage Error (MAPE). The mixtures comprised both neat and modified bitumen and represented various types of pavements, including binder courses, wearing courses, and reclaimed asphalt mixtures

Figure 5-96 showcases the physical aggregates for specimens S1, S2, and S3, which were randomly selected for illustration.



Figure 5-96: A showcase of selected Cat B aggregates.

5.3 Extracted Geometric Properties from Real Aggregates

Table 5-16 displays the geometric and Weibull characteristics of both Cat A and Cat B aggregates extracted following the method in Chapter 3.3.5. Only three aggregates (S1 to S3) from the extensive list of Cat B mixtures are presented here for illustration. A complete list of all the broad ranges of Cat B aggregates used is presented in Table A-34 in Appendix A.

5.4 Illustration of Virtually Generated Aggregates and Mastic

Figure 5-97 shows an example of a virtually generated aggregate for Specimen M8 in Cat A mixtures. The physics engine software counts the number of aggregates from this generation. Additionally, a comparison between real and virtual aggregates, using Specimen M2 as an example, is illustrated in Figure 5-98. Figure 5-99 shows a complete 3D model of virtual asphalt, specifically, the generated coarse aggregates blended with bitumen, fines, and filler.

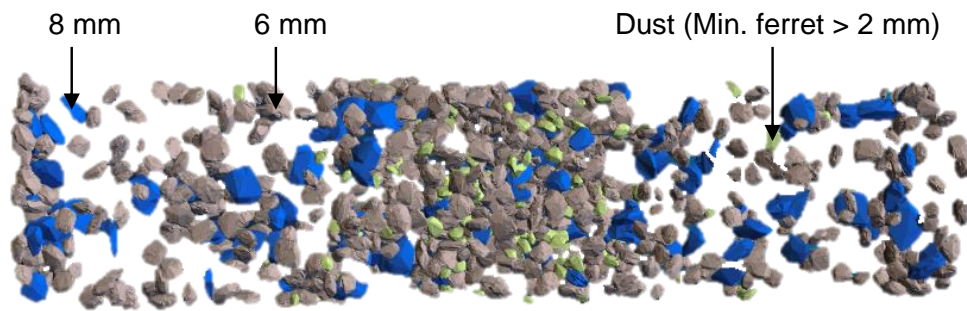


Figure 5-97: Virtual aggregate gradation example (specimen M8).

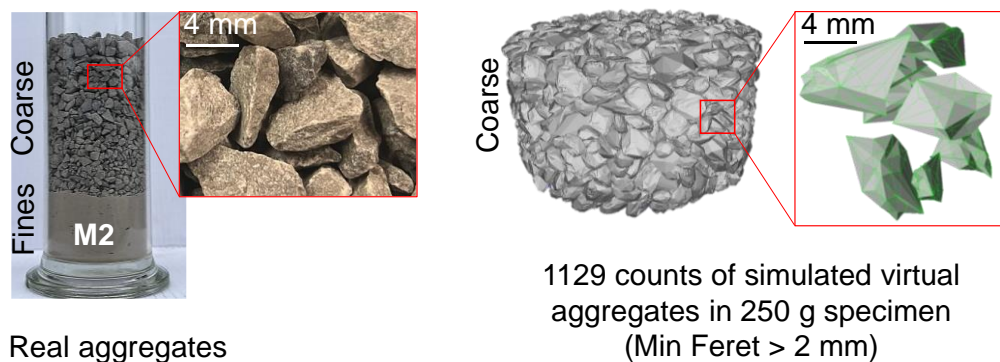


Figure 5-98: A comparison of real and virtual limestone aggregates for specimen M2.

Table 5-16: Geometric and Weibull characteristics of aggregates.

Mixture category	ID	Aggregate fractions	Min Feret ₅₀ (mm)	WSc ³⁸ Min Feret (mm)	WSh ³⁹ Min Feret	AR ₅₀	WSc AR	WSh AR	A ₅₀ (cm ²)	P ₅₀ (cm)	H	% mass < 2 mm
Fractions for Cat A aggregates	LD	Dust	3.17	3.66	5.21	0.69	0.73	6.70	0.12	1.31	0.74	62.98
	L6	6 mm (passing 8.0 mm)	8.72	5.30	3.90	0.68	0.77	7.37	0.23	1.81	0.61	3.48
	L8	8 mm (Passing 10mm)	10.81	8.61	4.17	0.75	0.75	6.54	0.69	3.21	0.61	1.15
Cat B combined aggregates (S1 – S3)	S1	Coarse (> 4 mm)	13.03	16.39	2.17	0.76	0.73	7.53	2.10	5.78	0.63	
		Fines (4-2 mm)	3.34	3.67	8.78	0.75	0.78	14.47	0.11	1.26	0.64	19.0
	S2	Coarse	8.66	9.50	3.12	0.66	0.73	7.29	0.83	3.50	0.75	
		Fines	2.84	3.28	4.92	0.73	0.77	8.38	0.08	1.12	0.74	22.1
	S3	Coarse	3.34	3.67	8.78	0.75	0.78	14.47	0.11	1.26	0.64	
		Fines	2.84	3.28	4.92	0.73	0.77	8.38	0.08	1.12	0.74	21.1

³⁸ WSc – Weibull Scale³⁹ WSh – Weibull Shape



Figure 5-99: An illustration of loose coarse aggregates (> 2 mm) coated with mastic (fines, filler and bitumen mixed) from the physics engine simulation.

5.5 Properties⁴⁰ of the Asphalt Mixtures

Table 5-17 and Table 5-18 present the experimental results for workability, Marshall stability, and Marshall flow, directly measured alongside the software-simulated number of aggregates and volume of mastic for all mixtures in this study. The mixtures varied significantly, spanning porous to dense asphalt compositions.

As a result, the workability, Marshall stability, and Marshall flow showed a broad range of outcomes. This method was chosen to avoid making the predictive models overly specific to certain mixtures, thereby preventing overfitting. Due to a limited number of specimens, the sensitivity analysis of workability was confined to mixtures S1, S2, S6, S9, S12, and S14.

5.6 Relationships Between Aggregate Geometric Properties, Performance Parameters, Number of Aggregates, and Volume of Mastic

Figure 5-100 illustrates the relationship between aggregate Aspect Ratio (AR) and the number of aggregates in HMAs. AR represents the weighted average of all aggregates in the mixture, based on data from predictive specimens (Cat A mixtures). The figure includes 21 randomly generated gradations (mock data) to evaluate extrapolation. It demonstrates that a decrease in AR leads to an increase in the number of aggregates.

Both experimental and mock values fall within the 95% confidence limits, yielding an overall R^2 value of 0.98. AR was chosen for this study to examine its

⁴⁰ M - mastic, in cm^3 ; NA - number of aggregates; ω is the workability, in %; S - Marshall stability, in kN; F - Marshall flow, in mm.

influence on the number of aggregates, as it is a well-established geometric parameter for optimising the performance of granular materials, according to literature [74,305–307]. Future research may explore the effects of other geometric characteristics, such as aggregate height and perimeter, on the number of aggregates in HMAs.

Table 5-17: Simulated and experimental characteristics of Cat A asphalt mixtures for the predictive modelling⁴¹.

Mixture ID	M (cm ³)	NA	ω (%)	S (kN)	F (mm)
M1	31.8	1268.0	85.5	7.7	1.7
M2	27.8	1129.0	101.1	6.8	1.4
M3	44.9	1283.0	57.9	11.7	7.1
M4	22.6	522.0	160.6	7.1	1.2
M5	26.7	655.0	90.7	8.3	1.8
M6	42.4	874.0	64.3	10.9	5.8
M7	55.1	869.0	48.9	14.5	9.3
M8	37.9	1272.0	70.9	10.1	3.0
M9	39.5	1087.0	71.1	9.1	4.0
M10	23.6	664.0	144.8	7.7	1.8
M11	17.3	510.0	213.8	6.6	1.0
M12	30.2	614.0	79.2	9.3	1.8
M13	41.1	750.0	82.4	9.2	3.2
M14	23.4	1537.0	141.1	7.5	1.4
M15	23.8	722.0	153.7	8.6	1.5
M16	23.8	802.0	162.7	7.6	1.4
M17	32.2	753.0	97.2	9.1	2.1
M18	27.0	681.0	103.7	8.0	1.1
M19	30.7	775.0	96.4	9.7	1.7
M20	35.2	647.0	69.2	8.5	3.4
M21	20.7	710.0	152.6	7.7	1.2
M22	28.8	693.0	87.5	7.4	2.0
M23	26.6	676.0	85.1	7.5	1.7
M24	34.8	1342.0	67.0	10.2	3.0
M25	36.5	1357.0	63.0	10.5	3.5

⁴¹ AVC is one of the key performance parameters for the predictive modelling, alongside ω , S, and F. However, it is not duplicated in this table, as it is already included in Table 5-14, which lists the fundamental asphalt characteristics, such as density and bitumen content. This approach is consistently applied across all subsequent tables.

Table 5-18: Simulated and experimental characteristics of Cat B asphalt mixtures for the sensitivity analysis.

Mixture ID	M (cm ³)	NA	ω (%)	S (kN)	F (mm)
S1	15.6	1099.0	67.1	11.7	4.2
S2	22.8	1827.3	142.9	17.3	5.1
S3	16.7	2407.3	-	23.2	8.8
S4	16.9	1207.0	-	15.2	3.7
S5	12.5	868.3	-	14.0	5.1
S6	23.3	1329.3	90.4	17.4	5.3
S7	18.1	1042.3	-	16.1	3.8
S8	18.5	1439.0	-	22.5	9.5
S9	19.8	1079.0	84.5	15.6	3.4
S10	25.1	1225.0	-	11.8	3.6
S11	19.4	1695.0	-	19.6	6.4
S12	18.8	1430.0	67.1	14.8	5.7
S13	23.9	2044.0	-	17.4	5.3
S14	19.0	1028.7	102.0	11.5	6.2
S15	17.7	1905.0	-	18.4	2.9
S16	18.7	1252.0	-	9.5	4.4

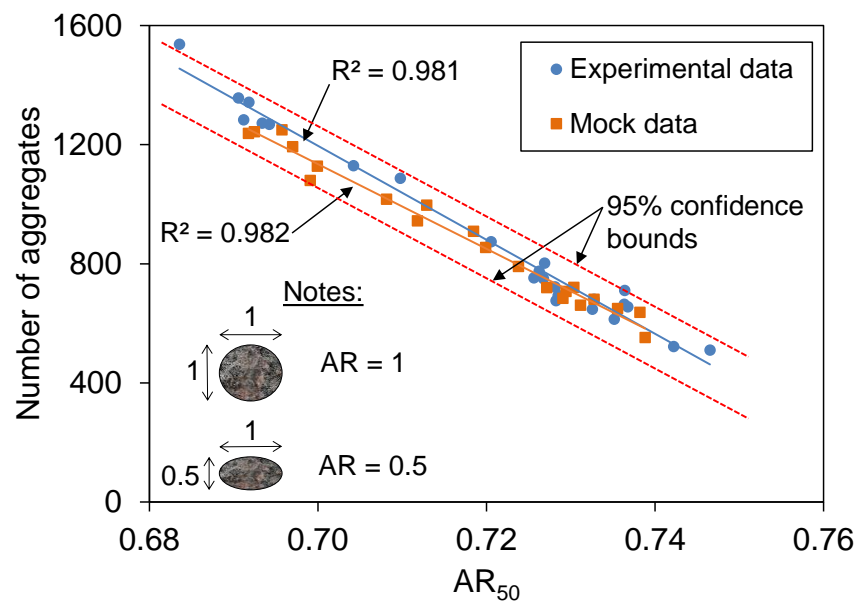


Figure 5-100: Impact of aspect ratio on asphalt aggregate content.

Equation (5-13) has been used to predict the performance parameters under study. As indicated in Section 3.3.9, this rational equation was selected based on references [144] and [305], which demonstrated its ability to accurately

model various emerging properties in asphalt resulting from aggregate gradation.

$$\phi = \frac{\beta_0 + \beta_1 M + \beta_2 NA}{1 + \beta_3 M + \beta_4 NA} \quad (5-13)$$

Where ϕ = asphalt property, β_0 is a constant term, $\beta_1, \beta_2, \beta_3$ and β_4 are rational coefficients, M is volume of mastic (cm^3) and NA is number of aggregates.

Table 5-19 shows the fitting parameters of Equation (5-13) for AVC, workability, Marshall stability, and Marshall flow, also indicating the goodness of fit for these parameters. In all four cases, the R^2 values exceed 0.80, suggesting that the number of aggregates and the volume of mastic account for over 80% of the input variations. Furthermore, the close alignment between R^2 and adjusted R^2 values implies that the prediction of the asphalt mix properties is significant and not due to chance. As detailed in Equation (5-13), $\phi = f(M, NA)$.

Table 5-19: Parameters for the fitting equations and goodness of fit.

	AVC	ω	S	F
β_0	4.36E+08	1.70E+09	6.25	2.62E-01
β_1	-2.62E+06	1.07E+07	-1.50E-03	3.97E-02
β_2	-2.00E+05	-9.90E+05	-1.92E-03	-5.13E-04
β_3	5.62E+05	5.90E+05	-9.52E-03	-1.00E-02
β_4	2.13E+02	-6.86E+03	-2.51E-04	-2.62E-04
R^2	0.99	0.87	0.79	0.94
Adjusted R^2	0.99	0.87	0.79	0.94
RMSE	0.77	15.34	0.77	0.48

Figure 5-101 illustrates the visual relationship between the asphalt mix properties, the number of aggregates, and the volume of mastic. Both the figure and the statistical analysis presented indicate that HMA properties are significantly influenced by the number of aggregates and the volume of mastic in the mixture. The impact of these factors in the proposed design method has been evaluated through a sensitivity analysis in Section 5.9. It is important to note that these results do not account for various factors, such as variations in bitumen characteristics and compaction energies, which also affect the performance of HMAs.

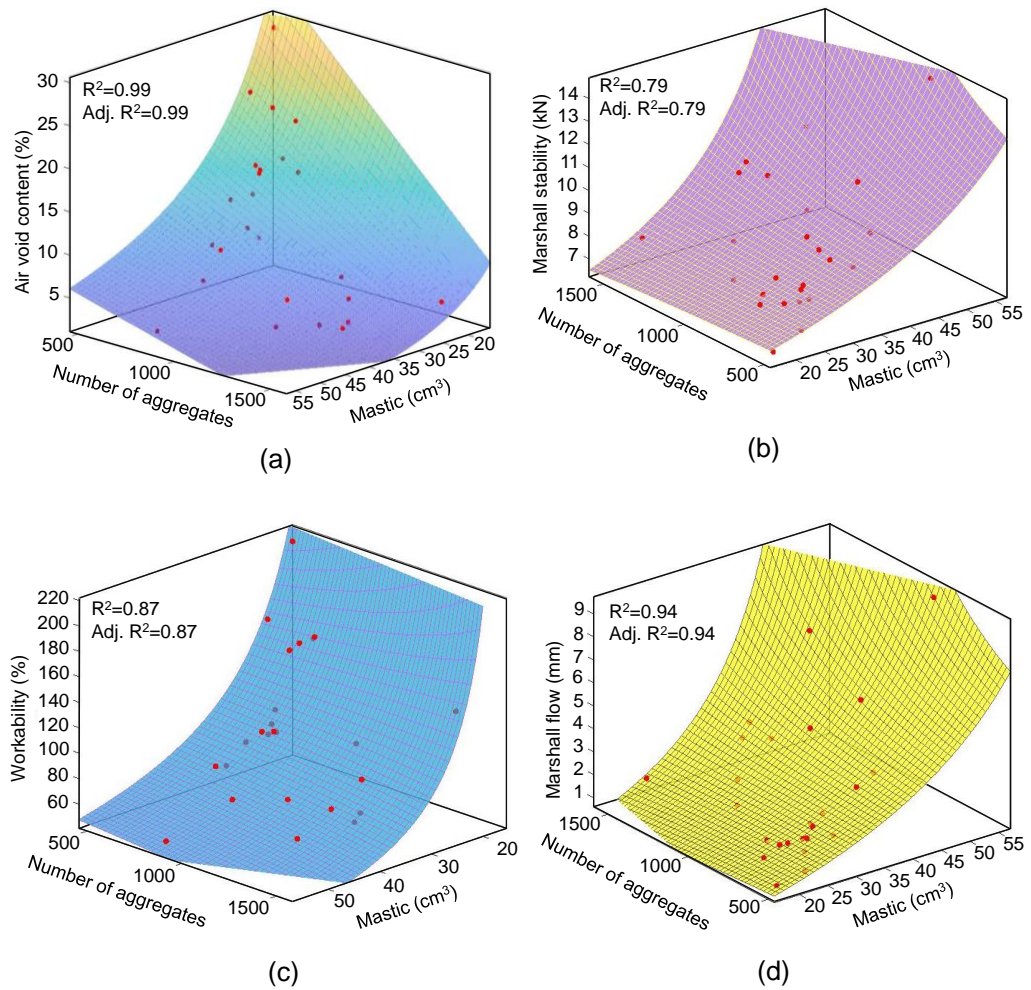


Figure 5-101: Relationship between asphalt performance parameters, number of aggregates and volume of mastic.

5.7 Nomograph for the Design of Asphalt Mixtures

The established performance limits for the properties of the asphalt mixtures used in this research have been used to define a region of interest for the design of targeted HMAs. These established limits are listed in Table 5-20. The limit for workability was determined based on experience, while the limits for Marshall stability, Marshall flow, and air void content were derived from references [121,122].

Table 5-20: Performance limits for the design of asphalt mixtures [121,122].

Asphalt property	Performance limits	
	Min.	Max.
ω , %	50	80
S, kN	> 6.7	—
F, mm	2	4
AVC, %	3	5

All limits are represented on the nomograph in Figure 5-102 to visualise the region of interest common to all selected asphalt properties. This nomograph is used in conjunction with gradation limits defined by specifications to select the number of aggregates and volume of mastic acceptable for designing asphalts that meet the criteria in Table 5-20. The upper and lower limit gradations for an SMA 8 asphalt were adopted for this research. For designing the asphalts, a fixed bitumen content of 5% in a 250 g portion of asphalt was considered.

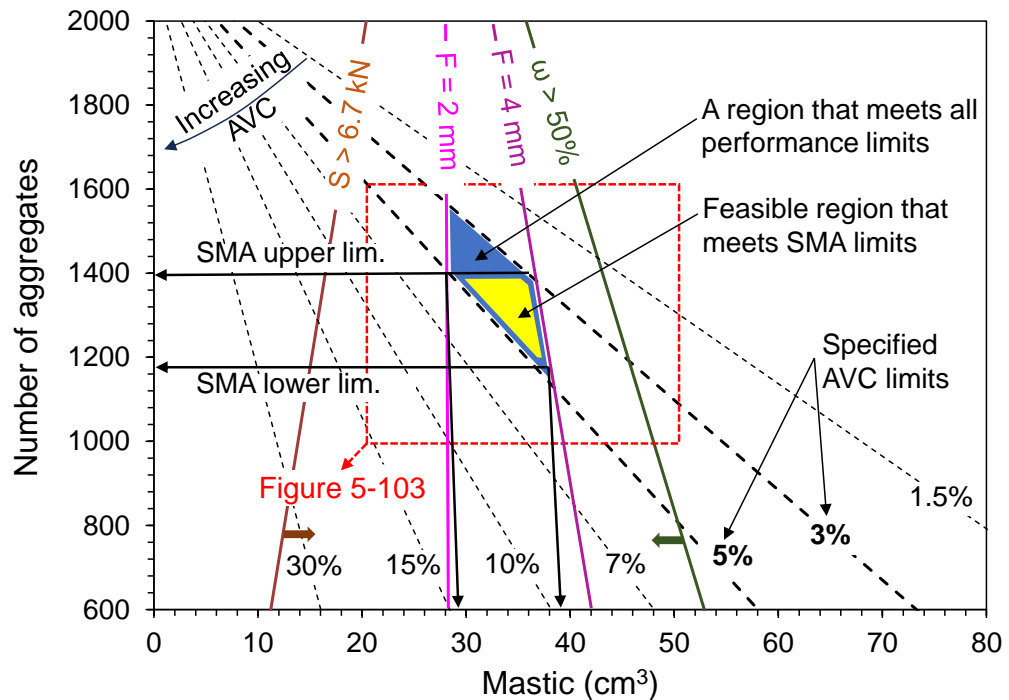


Figure 5-102: Nomograph for the design of asphalt: feasible region defined by performance and SMA limits.

Figure 5-102 and Figure 5-103 illustrate the interplay among the properties of asphalt mixes, the number of aggregates, and the volume of mastic. These figures highlight that reducing the volume of mastic increases porosity, while volumes over 10 cm³ are necessary for achieving a minimum Marshall stability of 6.7 kN. It is noteworthy that this Marshall stability is compromised when the volume of mastic is insufficient to coat and stabilise the aggregate skeleton, resulting in porous mixtures. On the contrary, increasing the volume of mastic enhances aggregate bonding but simultaneously reduces the mixture's workability, as mastic-filled voids hinder aggregate mobility. Thus, the graphic encapsulates the delicate balance needed in an ideal mixture: an optimised volume of mastic that supports both Marshall stability and workability.

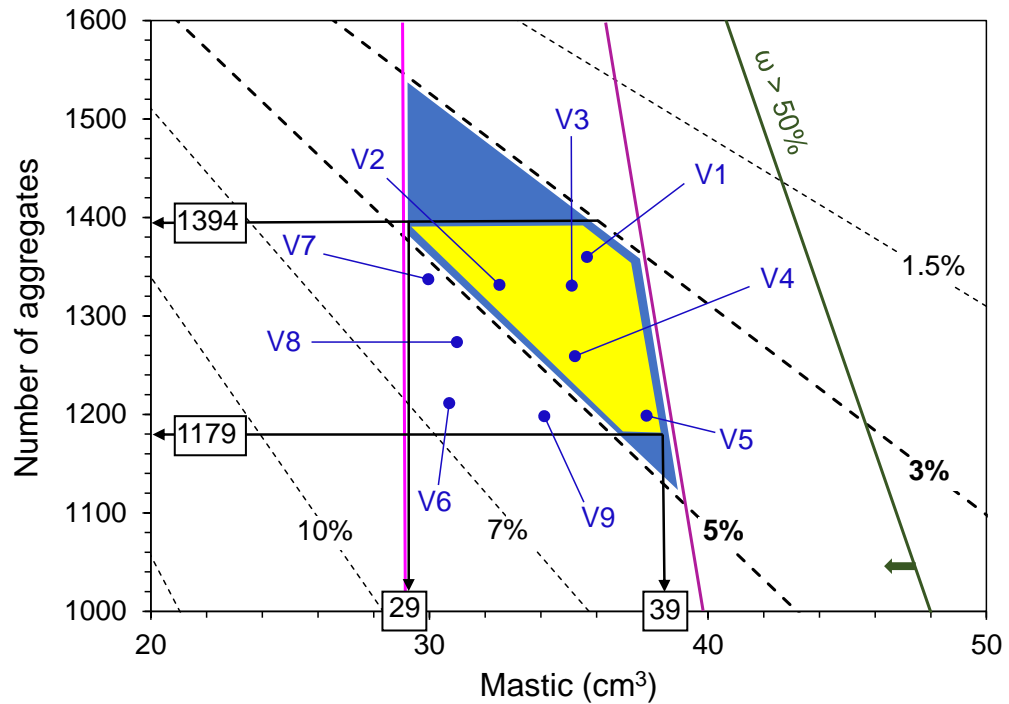


Figure 5-103: Nomograph for the design of asphalt: selected coordinates for validation of the nomograph.

Additionally, as illustrated in Figure 5-101, the volume of mastic influences the Marshall flow. An optimal intersection of volume of mastic, satisfying stability, workability, and flow (2 mm to 4 mm), designates the region meeting all specified performance limits. Within this region, the number of aggregates dictates the AVC in the mixture, with fewer aggregates in the same specimen mass increasing mixture porosity. This result emphasises how adjusting aggregate geometry and gradation can control asphalt mix porosity.

Future research could adapt this methodology to manage the topological properties of connective pores - pore area, pore circularity, equivalent pore diameter, and pore network - potentially enabling the prediction of the hydraulic conductivity of porous asphalt mixtures. Moreover, the flow zone is categorised based on the desired asphalt mixture type, such as dense asphalt, open graded, SMA, etc. This categorisation involves using the number of aggregates within the upper and lower limits for a desired mixture, for example, a standard SMA (refer to Figure 5-94(b) for the limits), to create a subregion within the performance boundary. This subregion represents a feasible region consisting of SMA mixtures that adhere to all design rules specified in Table 5-20. Within this feasible region, any combination of volume of mastic (x-axis) and number of aggregates (y-axis) can be selected to generate aggregate gradation and a recipe for producing an SMA mixture. These choices are expected to

accurately reflect the performance of the corresponding SMA mixtures based on Equation (5-13). Examples of the aggregate gradation generation process are provided in the nomograph validation process in Section 5.8.

5.8 Nomograph validation

The research utilised Figure 5-103 to randomly deduce aggregate gradations for mixtures V1 to V9. The corresponding number of aggregates and volume of mastic for these coordinates are detailed in Table 5-21. Four of the gradations (V6, V7, V8, and V9) were selected outside the specified 3% to 5% AVC range to test the predictive ability of the nomograph beyond the limits specified in Table 5-20.

Table 5-21: Number of aggregates and volume of mastic for selected coordinates on the nomograph.

Mixture ID	M (cm ³)	NA
V1	35.91	1348
V2	33.36	1295
V3	35.74	1316
V4	35.78	1251
V5	37.26	1196
V6	31.64	1202
V7	30.52	1303
V8	31.80	1285
V9	34.40	1206

The aggregate fractions available in the laboratory for manufacturing asphalt mixtures (L₈, L₆, and L_D) were individually analysed to determine the number of aggregates and volume of mastic within an assumed 5% bitumen content. It is noted that the AVC of a mixture does not influence its aggregate content. Moreover, when keeping the bitumen volume constant and using the same aggregate fraction, the volume of mastic in a specified mass of specimen remains unchanged. Table 5-22 presents the values for each aggregate fraction, which can be combined with Equation (5-14) and Equation (5-15) to design new asphalt mixtures. For instance, in a mixture containing solely filler aggregates (Min Feret < 0.063 mm), a zero number of aggregates (Min Feret > 2 mm) will be registered, resulting in a 100% volume of mastic (bitumen and aggregates with Min Feret < 2 mm). Table 5-22 shows the number of aggregates and volume of mastic for 250 g of each aggregate fraction. The limit

range for the number of aggregates (1179 to 1394) and volume of mastic (29 cm³ to 39 cm³) is defined by the SMA limits as illustrated in Figure 5-103.

An optimisation algorithm was developed in Microsoft Excel to calculate the proportions of aggregates (α_{L8} , α_{L6} , α_{LD} , α_{Lf}) by minimising squared errors, as illustrated in Equation (5-16). For complex iterations in future studies, machine learning applications may be employed. Equation (5-14) and Equation (5-15) estimated a 100% number of aggregates and volume of mastic compared to quantities generated with the software. Details of this comparison can be found in Table A-38 in the appendix. With the number of aggregates and volume of mastic estimated, the corresponding properties of the asphalt mixtures were predicted using Equation (5-13).

Table 5-22: Number of aggregates and volume of mastic for different fractions of aggregates, SMA limits and feasible region bounds.

ID	Proportion of aggregate (α)	M (cm ³)	NA
L ₈	α_{L8}	13.01	375
L ₆	α_{L6}	15.08	1582
L _D	α_{LD}	67.62	1269
L _f	α_{Lf}	100	0
SMA (upper)		46.6	1394
SMA (lower)		25.2	1179
Feasible region		29-39	1179-1394

Equation for the volume of mastic:

$$13.01\alpha_{L8} + 15.08\alpha_{L6} + 67.62\alpha_{LD} + 100\alpha_{Lf} = (29 - 39) \text{ cm}^3 \quad (5-14)$$

Equation for the number of aggregates:

$$375\alpha_{L8} + 1582\alpha_{L6} + 1269\alpha_{LD} + 100\alpha_{Lf} = (1179 - 1394) \quad (5-15)$$

$$\text{NA optimisation output} = (\text{NA}_{\text{estimated}} - \text{NA}_{\text{targeted}})^2 \quad (5-16)$$

Where α_{L8} , α_{L6} , α_{LD} , and α_{Lf} are the proportions (in percentage) of 8 mm aggregates, 6 mm aggregates, limestone dust, and limestone filler, respectively, in the final gradation. Note that NA in $100\alpha_{Lf}$ is zero, as all aggregates will have a Min Feret < 2 mm.

Table 5-23 details the aggregates generated for the validation specimens V1 to V9. The subsequent step entailed manufacturing laboratory asphalt specimens

(V1 to V9) using the generated aggregate gradations and 5% bitumen content. The properties of these asphalt mixtures were then experimentally measured. Table 5-24 presents a comparison between the predicted values obtained from the nomograph and the experimentally measured values. Predictivity is expressed as the percentage of the relative error between the predicted and measured values. On average, the nomograph exhibited an error rate of 5.7%, corresponding to a prediction accuracy of 94.3%. The air void content prediction was the most accurate, with an average error of 3.7%. Marshall stability and workability demonstrated lower accuracies, with errors of 8.7% and 5.7%, respectively.

From these results, it is concluded that when the geometric properties of aggregates, such as aspect ratio, perimeter, height, and area, are known, it is possible to estimate the number of aggregates and the volume of mastic in asphalt mixtures. Also, these parameters significantly influence the performance of asphalt mixtures. Most importantly, understanding aggregate geometry is crucial for creating 3D digital models of asphalt mixtures that accurately exhibit structural properties such as stability and flow.

Figure 5-104 visually illustrates and compares the properties of specimen V5. As indicated, the predicted properties were derived from the nomograph, whereas the measured properties came from physically manufactured laboratory specimens.

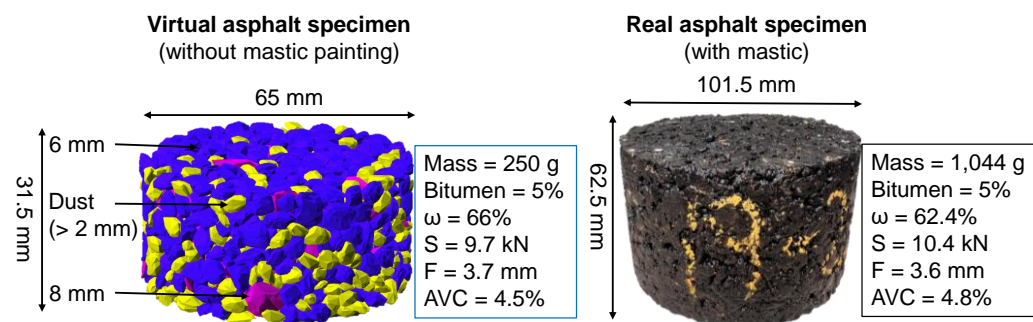


Figure 5-104: Comparison of virtual and physically manufactured asphalt for specimen V5.

Table 5-23: Generated gradations for validation specimens.

Gradation																
Mixture ID	Aggregate proportion (α)				Cumulative percentages of aggregates passing sieves (BS EN 13043:2013)											
	8mm	6mm	Dust	Filler	Sieve size (mm)	10	8	6.3	4	2.8	2	1	0.5	0.25	0.125	0.063
V1	9	51	40	0	% passing	100.0	96.8	91.0	57.6	37.7	27.1	17.5	13.7	11.4	9.5	7.7
V2	11	55	32	2		100.0	96.1	89.3	53.1	33.4	24.2	16.4	13.4	11.5	10.0	8.4
V3	8.5	54	34	3.5		100.0	97.0	91.3	56.2	36.5	26.9	18.7	15.4	13.5	11.8	10.2
V4	16	44	40	0		100.0	94.3	85.7	55.3	37.2	26.9	17.4	13.6	11.3	9.4	7.6
V5	18	40	40.5	1.5		100.0	93.6	84.3	55.9	38.8	28.6	19.1	15.2	12.9	10.9	9.0
V6	19	51.5	25	4.5		100.0	93.3	83.1	47.6	29.9	22.3	16.1	13.7	12.3	11.0	9.7
V7	12	60	25	3		100.0	95.7	88.3	48.9	29.0	21.0	14.7	12.3	10.9	9.7	8.4
V8	15.5	53	30	1.5		100.0	94.5	85.8	50.0	31.1	22.4	15.1	12.2	10.5	9.1	7.6
V9	19.2	45	33	2.8		100.0	93.2	83.1	51.6	34.3	25.4	17.5	14.3	12.4	10.8	9.2

Table 5-24: Predictivity of asphalt mixtures' properties designed with the monograph.

Mixture ID	Asphalt property	Predicted (p)	Measured (m)	Absolute error (m-p)	% error [(m - p)/m] x 100
V1	ω, %	67.0	65.7	1.3	2.1
	S, kN	9.6	10.2	0.6	5.9
	F, mm	3.5	3.3	0.2	6.1
	AVC, %	3.5	3.6	0.1	2.8
V2	ω, %	76.0	72.8	3.2	4.4
	S, kN	9.0	9.7	0.7	7.2
	F, mm	2.9	3.1	0.2	6.5
	AVC, %	4.5	4.7	0.2	4.3
V3	ω, %	68.0	74.2	6.2	8.4
	S, kN	9.5	9.9	0.4	4.0
	F, mm	3.5	3.6	0.1	2.8
	AVC, %	3.8	4.1	0.3	7.3
V4	ω, %	69.0	64.0	5.0	7.8
	S, kN	9.5	10.1	0.6	5.9
	F, mm	3.4	3.6	0.2	5.6
	AVC, %	4.4	4.5	0.1	2.2
V5	ω, %	66.0	62.4	3.6	5.8
	S, kN	9.7	10.4	0.7	6.7
	F, mm	3.7	3.6	0.1	2.8
	AVC, %	4.5	4.8	0.3	6.3
V6	ω, %	85.0	82.0	3.0	3.7
	S, kN	8.7	9.8	1.1	11.2
	F, mm	2.5	2.6	0.1	3.8
	AVC, %	6.2	6.3	0.1	1.6
V7	ω, %	88.0	82.0	6.0	7.3
	S, kN	8.5	9.6	1.1	11.5
	F, mm	2.3	2.4	0.1	4.2
	AVC, %	5.4	5.6	0.2	3.6
V8	ω, %	83.0	79.0	4.0	5.1
	S, kN	8.7	9.8	1.1	11.2
	F, mm	2.5	2.4	0.1	4.2
	AVC, %	5.4	5.5	0.1	1.8
V9	ω, %	75.0	70.0	5.0	7.1
	S, kN	9.1	10.6	1.5	14.2
	F, mm	2.9	3.1	0.2	6.5
	AVC, %	5.4	5.6	0.2	3.6
Average % error	ω, %			4.2	5.7
	S, kN			0.9	8.7
	F, mm			0.1	4.7
	AVC, %			0.2	3.7
Mean % error					5.7

5.9 Sensitivity Analysis of the Developed Asphalt Design Model

Figure 5-105 compares the properties of physically measured HMA properties with digitally predicted properties for Cat B mixtures.

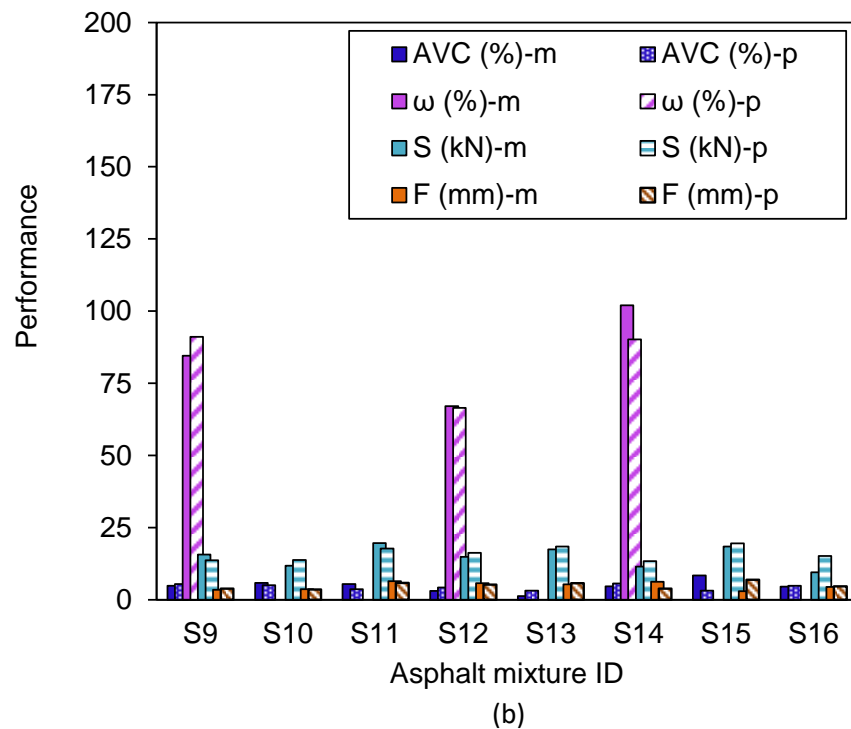
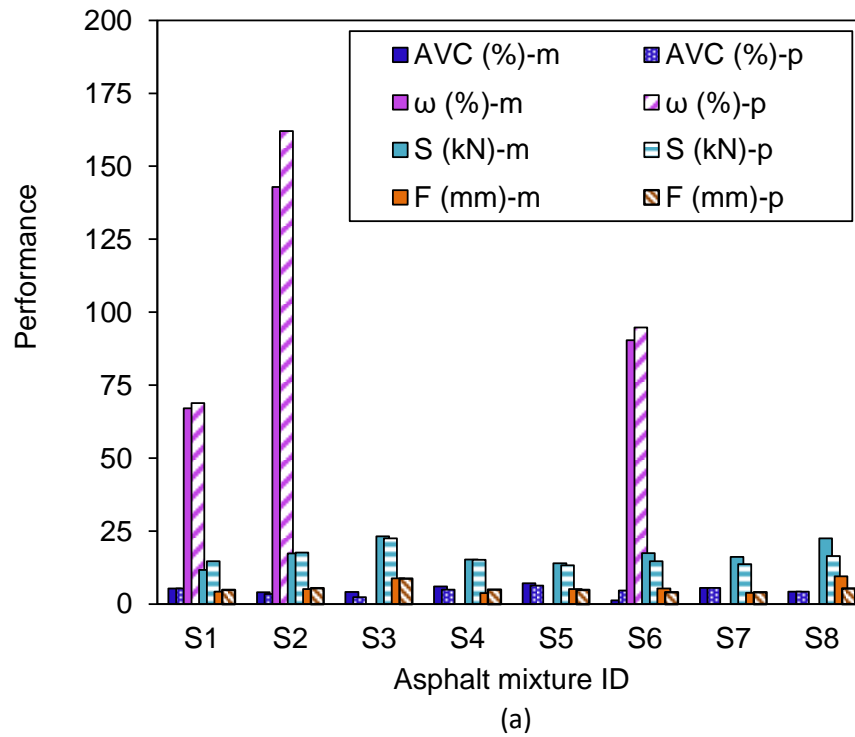


Figure 5-105: A comparison between physically measured properties (m) and predicted properties (p) for Cat B mixtures using the developed model.

In addition, Table 5-25 displays the average Mean Absolute Percentage Error (MAPE) for the studied properties - workability, Marshall stability, Marshall flow, and AVC. The developed model showed an average MAPE of 22.3% (a reduction from an average error of 5.7% in Table 5-24), indicating a predictivity of 77.7%. AVC exhibited the highest error at 45.3%, while the minimum error

was observed in workability (6.9%). This indicates that the developed model has weaker predictive accuracy for HMAs with diverse aggregate and bitumen characteristics.

The causes of these deviations remain unclear; however, one possible factor could be the findings from reference [308], which suggest that mastic, with its varying air void contents, can significantly impact the overall AVC of HMAs. Therefore, further research is needed to characterise and quantify air voids in HMA mastic based on bitumen modifications and the nature of other mastic-composite materials like fillers. Furthermore, it is proposed that the presence of larger aggregate sizes and reclaimed asphalt (50%) in Cat B asphalt mixtures may lead to decreased predictivity across all properties.

Table 5-25: MAPE for physically measured properties compared with digitally predicted properties of Cat B HMA mixtures.

Asphalt mix property	MAPE (%)
ω , %	6.9%
S, kN	14.3%
F, mm	22.5%
AVC, %	45.3%
Average	22.3%

Additionally, variations in compaction energy levels and methods can greatly affect the size and distribution of AVC [309]; future studies should consider these factors. The low predictivity for Cat B mixtures may also suggest that the geometric parameters used in this study, such as aspect ratio, and the estimated volumetric quantities like the volume of mastic, do not fully capture the properties of all HMAs. This calls for further investigation, with a valuable suggestion being incorporating performance parameters into Equation (5-13). Future studies should also consider the impact of lithology and surface texture of aggregates on the performance of HMAs.

5.10 Summary

In this chapter, a new digital approach to design hot mix asphalt (HMA) in a rapid and resource-efficient manner has been developed that minimises the need for time-consuming and laborious physical and mechanical tests to determine the properties of new asphalt mixtures. The method makes it possible for mixtures that are both workable and yet meet other mechanical

performances like stability under traffic loading to be formulated with ease. The method estimates these asphalt properties based on established performance rules using the number of aggregates and the volume of mastic in the mixtures. Some specific conclusions of this chapter are:

- Statistical analysis indicates that the fundamental properties of HMAs, such as air voids content, workability, Marshall stability, and Marshall flow, are significantly influenced by the number of aggregates and the volume of mastic contained in the mixes.
- The number of aggregates in HMAs is influenced by the aspect ratio of the aggregates ($R^2 = 0.98$). When the aspect ratio decreases, the number of aggregates increases. Therefore, an understanding of the geometric properties of aggregates and the ability to control them is necessary for the design of future HMAs with tailored functionalities.
- The digitally generated aggregates and mastic were used to develop 3D models of the designed HMAs. These virtual representations allowed for the observation of aggregate distributions in the HMA before they were physically manufactured.
- Through an iterative process, the authors digitally designed nine different HMAs using identical bitumen and aggregate sources that fulfilled 94% of the properties of their physical counterparts. However, the predictive accuracy of the model decreased to 78% for HMAs that contained diverse aggregate and bitumen characteristics.

With the optimisation-centred and performance-based approach of this new design method, there is high potential for its adoption to overcome the challenges associated with the current use of HMA in pothole repair machines, which are predominantly limited by extrusion performance, as highlighted in [Section 2.5.2](#). This is the focus of [Chapter 6](#), which investigates a miniaturised paver, simulates a pothole in the laboratory, and evaluates the feasibility of using real asphalt mixtures from the digital design method for pothole repairs.

Chapter 6: Machine Filling of Potholes in Asphalt Pavements

6.1 Introduction

This chapter presents the development of an automated pothole filling machine (APFM), optimises its operational parameters, and utilises cartridges of asphalt designed through the application of the digital concept introduced in [Chapter 5](#). To ascertain the quality of automated fills, parallel potholes are filled manually, and the quality of both automated and manually filled potholes has been compared using rutting depth.

A graphical illustration providing a general overview of the automated pothole filling investigation in this chapter is shown in [Figure 6-106](#).

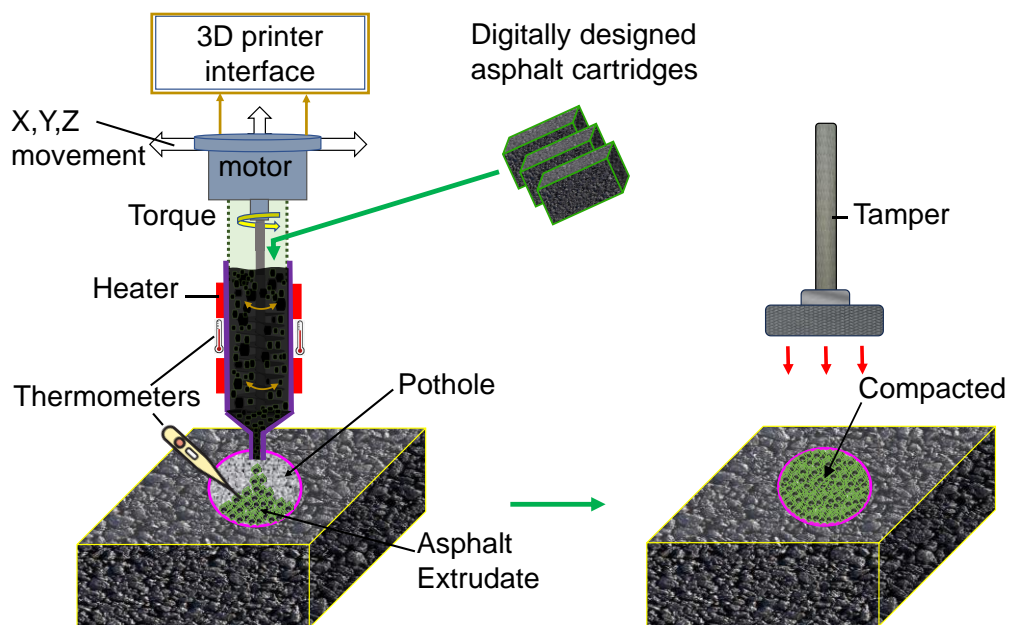


Figure 6-106: A graphical abstract of the automated pothole filling investigation with the APFM.

Publication acknowledgement

This chapter includes techniques, results, and discussions that are part of earlier collaborative research efforts and have been previously published. Consequently, relevant portions of the content in this chapter are also detailed in the following publication: “Automating the repair of potholes using machine techniques and digitally crafted asphalt cartridges,” published in *Construction Robotics*, Volume 8, 2024.

6.2 Development of the Hot-End Screw-Extrusion-Based Asphalt 3D Printer (APFM)

A modified 3-axis screw extrusion 3D printer served as the APFM. The APFM featured an extruder with a 90 mm outer diameter × 100 mm long aluminium heating collar and a nozzle outlet with a nominal 30 mm through bore. The nozzle outlet included a 316 stainless steel lever with an adjustable outlet gate valve. A 90 mm × 90 mm mica band heater, rated at 24 V DC and 250 watts, was housed within the collar. An integral type K temperature sensor, situated close to the nozzle outlet, monitored the system's temperature, cross-validated regularly with an SPER Scientific 800115C thermometer.

A removable 200 mm diameter extension funnel, made of stainless steel, was positioned atop the collar to store surplus asphalt cartridges for seamless continuous extrusion. A spiral feed screw inside the collar, with a 60 mm pitch and diameter, facilitated the extrusion process. A 3 mm diameter and 20 mm tall circular peg, affixed to the centre screw blade, induced lateral stirring of mixtures during extrusion, ensuring even heating and minimising stripping. The feed screw connected to a McLennan 1308-12-100 geared 100:1 DC motor, capable of a maximum torque of 0.4 Nm and a no-load speed of 35 rpm. For safety, the heating collar was encased in an insulating jacket. This extruder setup was integrated with the RepRap original Prusa i3 MK3S 3D printer in [Figure 3-50](#), chosen for its substantial payload capacity. A connected computer, supported by 3D printing software, controlled the extruder movement in the X, Y, and Z directions, heating management, and asphalt extrusion at screw speeds ranging from 1 to 36 rpm.

[Figure 6-107](#) displays the components of the extruder, [Figure 6-108](#) shows the setup of the extruder assembly in progress, [Figure 6-109](#) showcases the extruder mounted onto the 3D printer frame, and [Figure 6-110](#) illustrates the complete APFM setup during the pothole filling process.

6.3 Optimisation of the Operational Parameters of the APFM

The critical operational parameters of the printer involve DC power, extrusion rate, and extrusion temperature. The optimisation of maximum power involved a trade-off between torque and extrusion speed, as depicted in [Figure 6-111\(a\)](#). The DC motor had a maximum torque of 0.4 Nm and a no-load speed of 35 rpm.

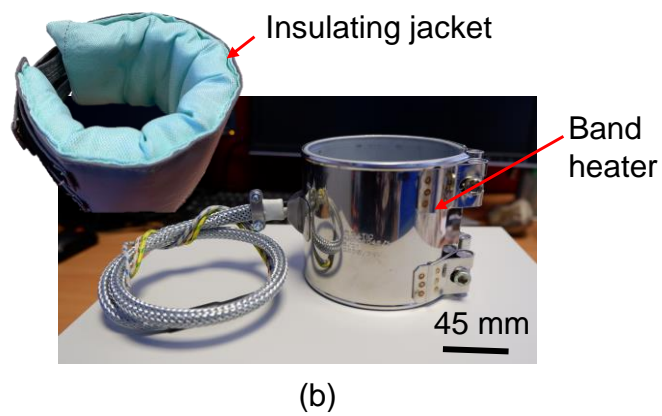
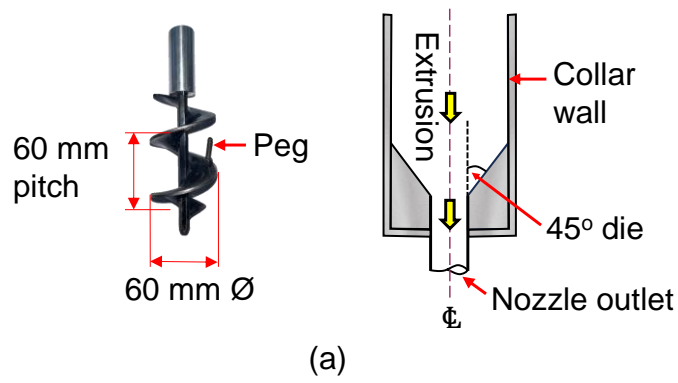


Figure 6-107: Illustration of the (a) spiral feed screw and die angle, and (b) band heater and insulating jacket.

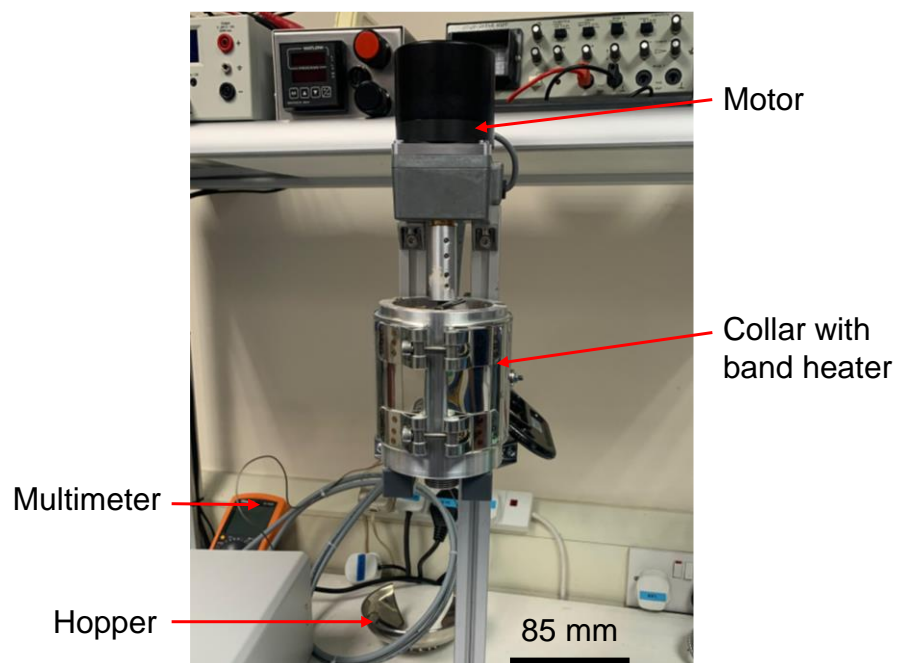


Figure 6-108: Assembling the heating system and extruder.

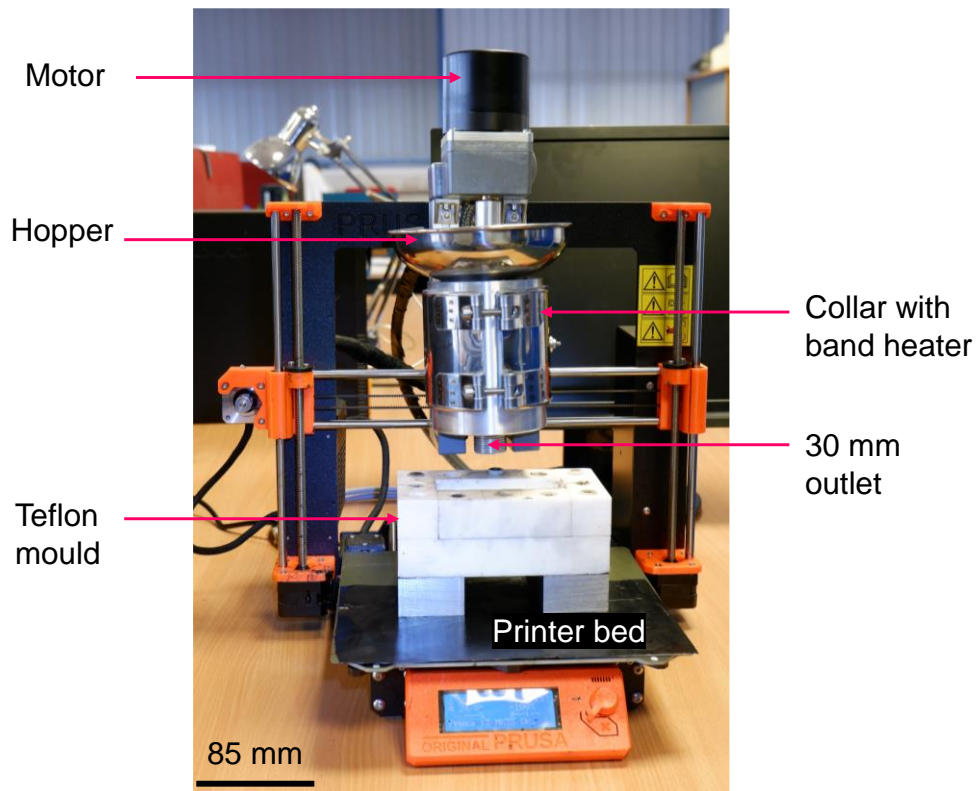
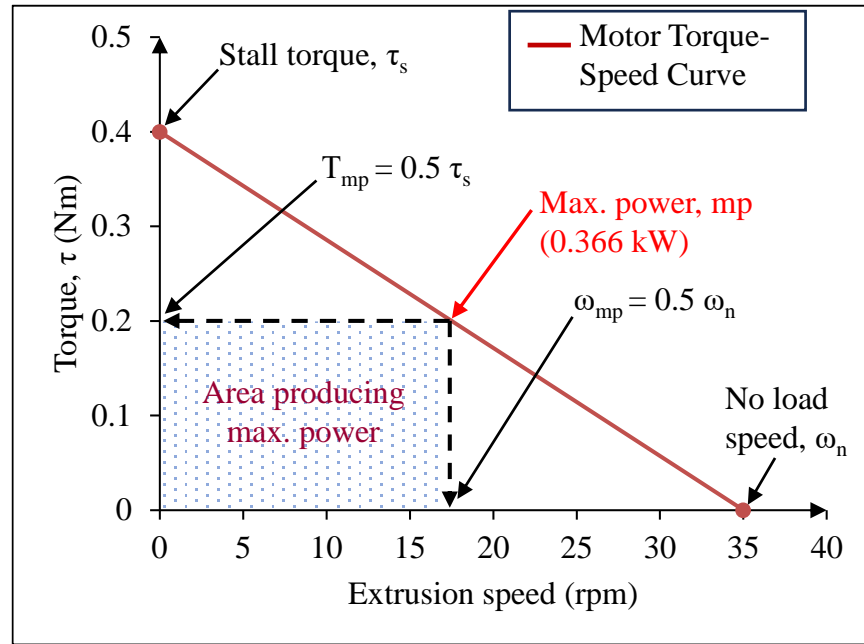


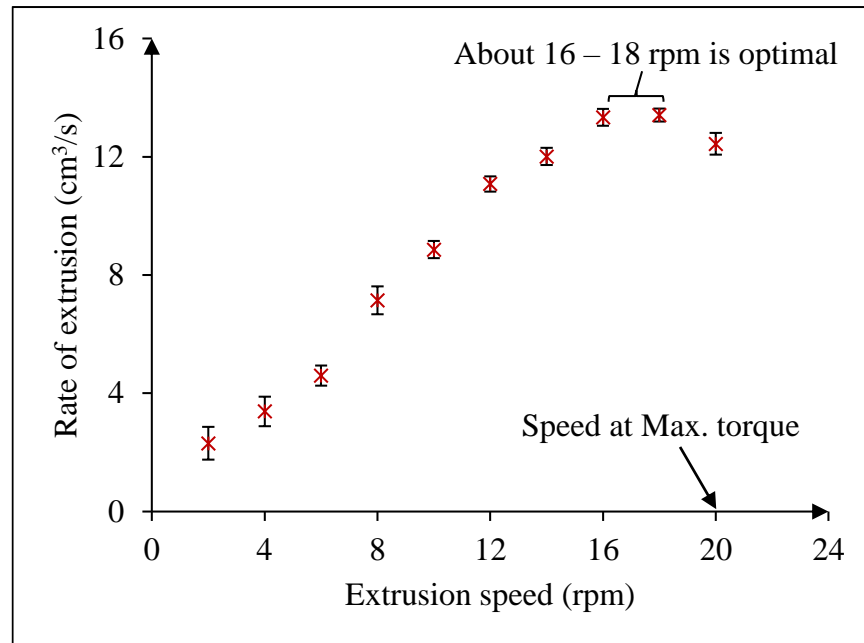
Figure 6-109: Illustration of the asphalt extruder mounted onto the 3D printer frame shown in Figure 3-50.



Figure 6-110: The complete APFM setup at NTEC during the pothole filling process. Electric motor torque represents the rotational force generated by the motor. The maximum power was approximated through a speed-torque optimisation, resulting in the largest area beneath the speed-torque curve.



(a)



(b)

Figure 6-111: Optimisation of the operational parameters of a DC motor: (a) maximising operating power, and (b) optimising extrusion speed using mixture P8.

From the graphical representation in Figure 6-111(a), the optimised coordinates intersected at the midpoint of speed and torque, specifically at $0.5 \tau_s$ and $0.5 \omega_n$. Using this relationship, a maximum power of approximately 0.366 kW was achieved using Equation (6-17), with a torque of 0.2 Nm and a speed of 17.5 rpm.

$$P = \frac{2\pi\tau\omega}{60} \quad (6-17)$$

Here, P represents power in kW, τ denotes torque in Nm, and ω signifies speed (angular velocity) in rpm.

The extrusion die angle was also a crucial consideration in the extrusion process, as it significantly influenced the flow of asphalt material. This angle affected not only the extrusion force but also the occurrence of defects in the extrudates due to friction and uneven material flow. A lower die angle, for instance, introduced more friction at the asphalt-die interface. Consequently, an optimised die angle of 45° was adopted to enhance the efficiency and effectiveness of the extrusion process, while mitigating issues such as material flow resistance, clogging, and excessive wear [310,311].

Additionally, it was observed that the extrudates were approximately 6°C cooler than the programmed band heating. This temperature drop was anticipated due to heat losses to the surroundings as the extrudate exited the nozzle outlets. Importantly, since the asphalt mixtures were extruded at 165°C with a targeted compaction temperature of 150°C , the variance was not a significant concern.

Lastly, a circular outlet shape was selected for its simplicity. It is important to note that as the cross-section becomes more intricate, higher pressure and greater extrusion force would be required.

6.4 Measurement of the Extrusion Rate of Mixtures by the APFM

Extrusion rate measurements involved feeding asphalt cartridges into the collar while rotating the screw at 2 rpm, opening the outlet until a consistent dropping rate indicated sufficient collar filling, and then closing the outlet. A 10-second screw rotation eliminated voids near the nozzle tip after removing the caps. The volume of extruded asphalt (extrudate) in 10 seconds was recorded at the optimised extrusion rate of 18 rpm. Rates, averaged over three tests, were expressed in cm^3/s to quantify the asphalt required for a specific pothole volume. Density variations had negligible impact on rate estimation due to similar asphalt densities.

6.5 Aggregates and Asphalt Specimens

In this chapter, limestone aggregates were utilised in four distinct fractions: filler (0-0.125 mm), dust (0-4 mm), L6 (0-6.3 mm), and L8 (0-8.0 mm). The gradations for these fractions are detailed in [Table A-32](#) in the appendix. These fractions were combined to create aggregate gradations for both slab and pothole filling mixtures. [Figure 6-112](#) displays the combined gradations for each specimen,

while Table A-39 in Appendix A provides detailed information on the asphalt mixture properties for the 34 blends used.

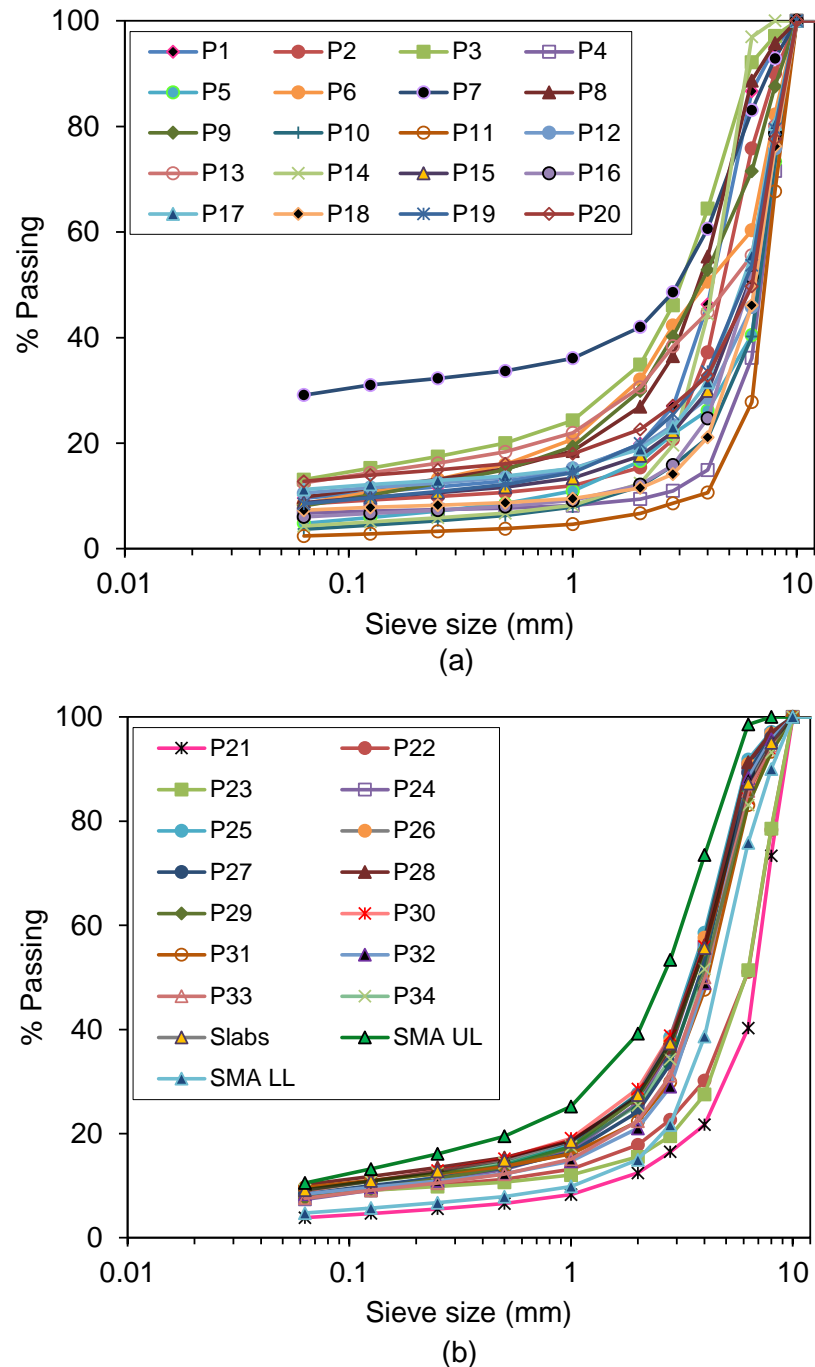


Figure 6-112: Aggregate gradation for asphalt specimens, including SMA limits and pothole slabs: (a) P1 to P20, and (b) P21 to P34

6.6 Laboratory Simulation of Potholes

A simulated pothole was created by merging two asphalt slabs, each measuring 305 mm × 305 mm, and manufactured according to the process described in Section 3.2.2. The upper slab, serving as the surface course, was 40 mm thick, replicating the depth of a standard medium-sized pothole [180] and the typical

thickness of a surface course in the UK. A 60 mm thickness for the bottom slab was selected to maintain the specimen's total thickness at 100 mm, meeting the wheel tracking device's specifications. A 150 mm diameter hole was carved out from the centre of the upper slab using a core drilling machine⁴² (as shown in Figure 6-113(c)).

Subsequently, this top slab, with the created void, was tack coated to the bottom slab using a bitumen emulsion adhesive. This method produced a pothole model with a 40 mm depth. The process was finalised by tack coating the cut vertical surfaces of the pothole walls to improve the adhesion of the filling asphalt to the pothole walls. Figure 6-113 illustrates the stages of the pothole simulation, while Figure 6-114 compares a fully lab-simulated pothole to an actual field pothole. It is important to note that, for durable in-situ pothole repairs such as the semi-permanent techniques discussed in Section 2.5.2, rough and weak pothole edges are trimmed to create clean, vertical walls similar to the prepared walls in lab-simulated specimens.

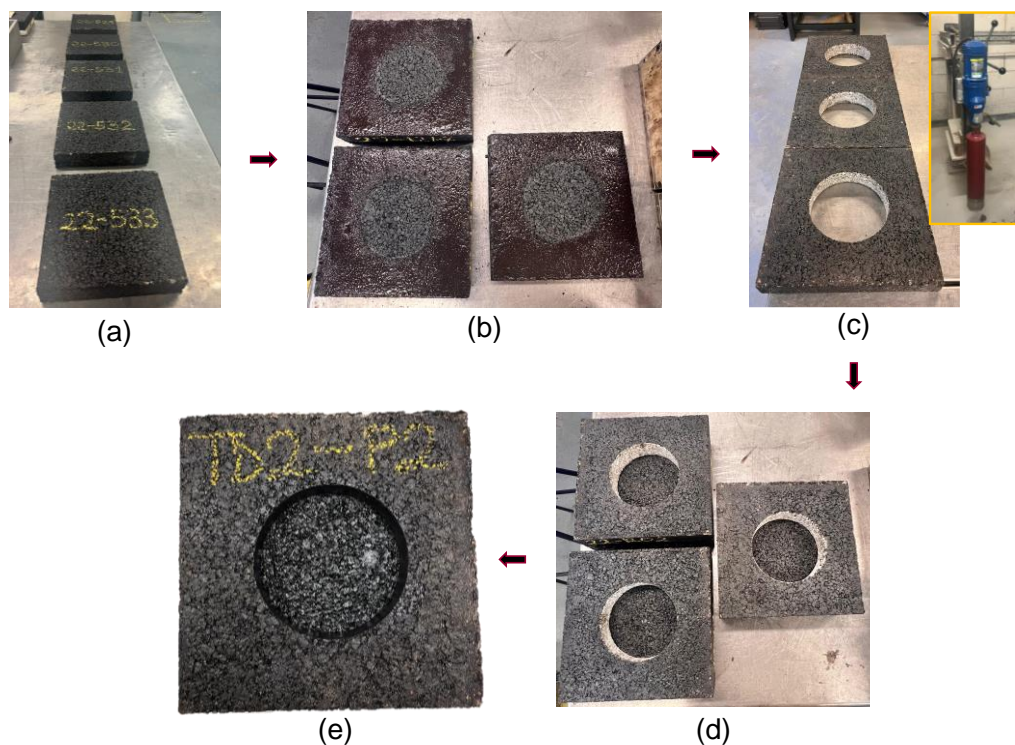


Figure 6-113: (a) Manufactured slabs, (b) tack-coated base surface, (c) hollow upper slab (core drilling machine inserted), (d) hollow upper slab laid on the base slab, and (e) fully assembled pothole with tack-coated pothole walls.

⁴² An example can be found here: <https://www.diamondtoolstore.com/collections/core-drilling-equipment/products/manta-iii-core-drill-rigs>.

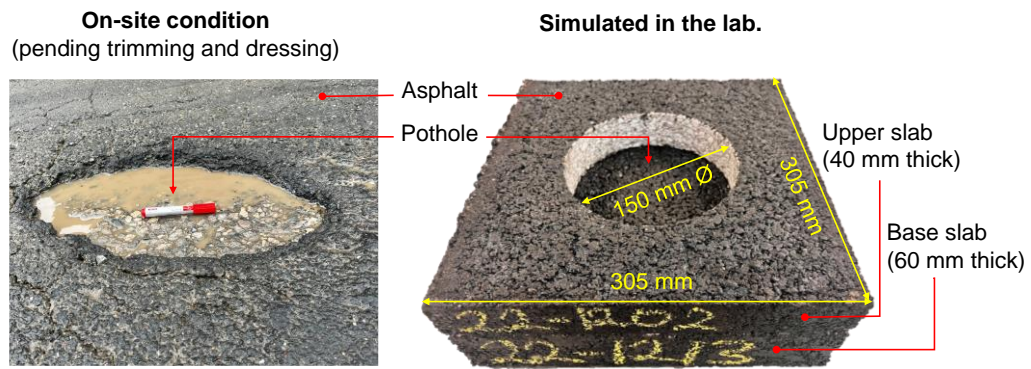


Figure 6-114: Illustration of a pothole: (a) on-site condition and (b) lab simulated.

6.7 Development of a Design Model for the Formulation of Suitable Filling Mixtures

6.7.1 Creation of virtual aggregates and asphalt mixtures

Virtual aggregates and asphalt mixtures were generated using the procedure outlined in [Section 3.3.5](#) and [Section 3.3.6](#) in [Chapter 3](#). Examples of generated aggregates and asphalt mixtures are also illustrated in [Section 5.3](#). Additionally, the geometric and Weibull characteristics of the aggregates (sourced identically to Cat A mixtures in [Chapter 5](#)) are displayed in [Table 5-16](#).

6.7.2 Performance properties of the asphalt mixtures for pothole filling

[Table A-40](#) in [Appendix A](#) details the experimental outcomes and the computed numbers of aggregates and volumes of mastic for the 34 mixtures used in this chapter (P1 - P34). Each value reflects the results from three experiments or numerical simulations. These mixtures showed significant variation, ranging from porous to dense asphalt compositions. As a result, Extrudability (E), Marshall Stability (S), and Marshall Flow (F) exhibited a broad spectrum of results. Once again, this approach was adopted to ensure that the models do not become excessively tailored to specific mixtures, thereby avoiding overfitting.

The data in [Table A-40](#) are used for further statistical analysis to identify any potential relationships between these parameters more precisely. These statistical correlations will facilitate the determination of optimal mixture compositions tailored extrusion and mechanical performance.

6.7.3 Assessment of the relationships between asphalt performance parameters, volume of mastic and number of aggregates

Equation (6-18) serves as the predictive model for assessing the performance parameters of mixtures and follows a similar pattern to Equation (5-13). Slight variations in variables, such as using MV to represent volumes of mastic instead of M as used in Chapter 5, are intended to differentiate the same parameters for different applications.

$$\text{Performance parameter} = \frac{a + bMV + cNA}{1 + dMV + eNA} \quad (6-18)$$

Where a, b, c, d, and e are constants; MV is the volume of mastic (cm³), and NA is number of aggregates.

Table 6-26 presents the fitting parameters for Equation (6-18) in relation to Extrudability, Marshall Stability, Marshall Flow, and AVC. The table also evaluates the goodness of fit for these parameters. Once again, across all four instances, the R² values either meet or surpass 0.80, signifying that the NA and MV jointly account for more than 80% of the input variations in each scenario. Furthermore, the close concurrence between R² and adjusted R² values further reinforces the notion that the prediction of performance parameters is not a random occurrence but rather a robust and reliable outcome.

The relationships in Table 6-26 can be graphically illustrated to visualise the trends. Figure 6-115 provides an example illustration for Extrudability and Marshall Stability. Both Table 6-26 and the graphical illustrations indicate that NA and MV strongly influence the Extrudability, Marshall Stability, Marshall Flow, and AVC of asphalt mixtures. However, it is important to note that the analysis is based on only 34 results, which is insufficient to draw definitive conclusions regarding the use of this relationship for predicting asphalt performance. Nonetheless, these findings provide valuable insights for future studies, highlighting the potential inputs that need to be considered. It is also important to acknowledge that these results do not account for various factors, including different types of bitumen, variations in compaction temperatures, and differences in compaction energies.

Table 6-26: Parameters for the fitting equations, goodness of fit and design limits.

Performance	Fitting Equation	R ²	Adj. R ²	RMSE	Design limits
E (cm ³ /s)	$E = \frac{-4.344 + 4.206 \times 10^{-1} MV - 2.669 \times 10^{-3} NA}{1 + 3.042 \times 10^{-3} MV - 4.211 \times 10^{-4} NA}$	0.89	0.89	1.53	> 10
S (kN)	$S = \frac{5.865 - 2.031 \times 10^{-3} MV - 1.140 \times 10^{-3} NA}{1 - 9.176 \times 10^{-3} MV - 6.831 \times 10^{-5} NA}$	0.78	0.78	0.75	> 6.7
F (mm)	$F = \frac{0.157 + 4.234 \times 10^{-2} MV - 5.330 \times 10^{-4} NA}{1 - 1.000 \times 10^{-2} MV - 1.096 \times 10^{-4} NA}$	0.99	0.99	0.12	2 - 4
AVC (%)	$AVC = \frac{1.127 \times 10^9 - 6.767 \times 10^6 MV - 5.161 \times 10^5 NA}{1 + 1.454 \times 10^6 MV + 205 NA}$	0.94	0.94	1.73	3 - 5

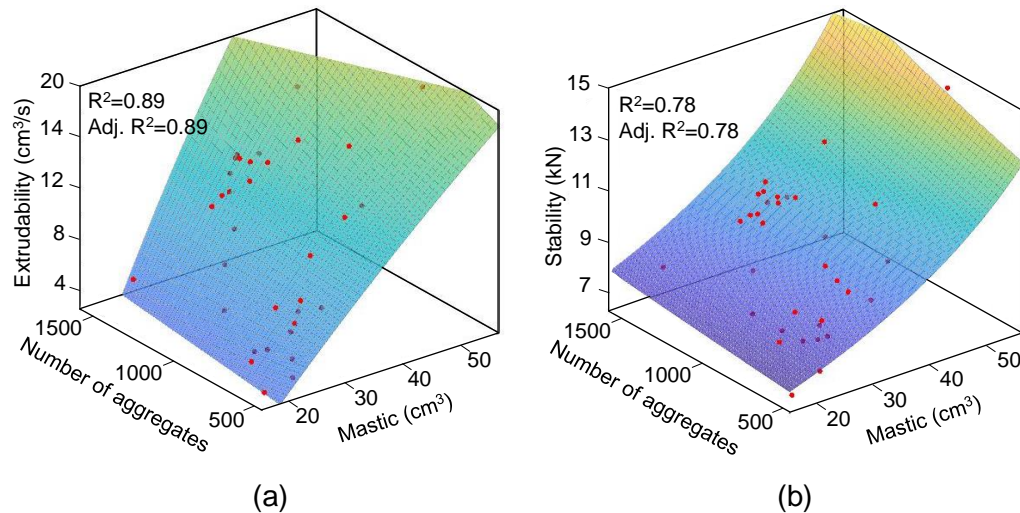


Figure 6-115: Relationship between number of aggregates, volume of mastic, and (a) extrudability, and (b) stability.

6.7.4 Creating a nomograph for asphalt design

The performance parameter boundaries, established in this chapter and detailed in Table A-39, delineate the focal area for the asphalt design. These thresholds, grounded in experimental knowledge and corroborated by references [121,122], are visualised in Figure 6-116's nomograph, which assists in selecting appropriate NA and MV values that comply with the limits set out in Table A-39.

Figure 6-116 illustrates the relationship between the performance metrics of asphalt mixtures, NA and MV. It highlights that a reduction in MV increases the porosity of the mixtures, while maintaining an MV above 34 cm³ is essential to achieve a minimum extrusion rate of 10 cm³/s with the APFM. Additionally, a higher quantity of mastic tends to enhance the flow in the asphalt mixtures.

In the spiral feed screw extrusion process, an increased amount of mastic helps to raise the extrusion rate by effectively lubricating the interaction between the larger asphalt aggregates and the collar-screw walls. The mastic also potentially enhances the moldability along the extrusion path. Conversely, mixtures containing a higher proportion of NA tend to exhibit increased internal friction and stresses, thereby reducing the extrusion rate. Once again, it should be noted that this research used the same bitumen type in all mixtures and did not examine the influence of fluctuating temperatures on the extrudability of the mixtures.

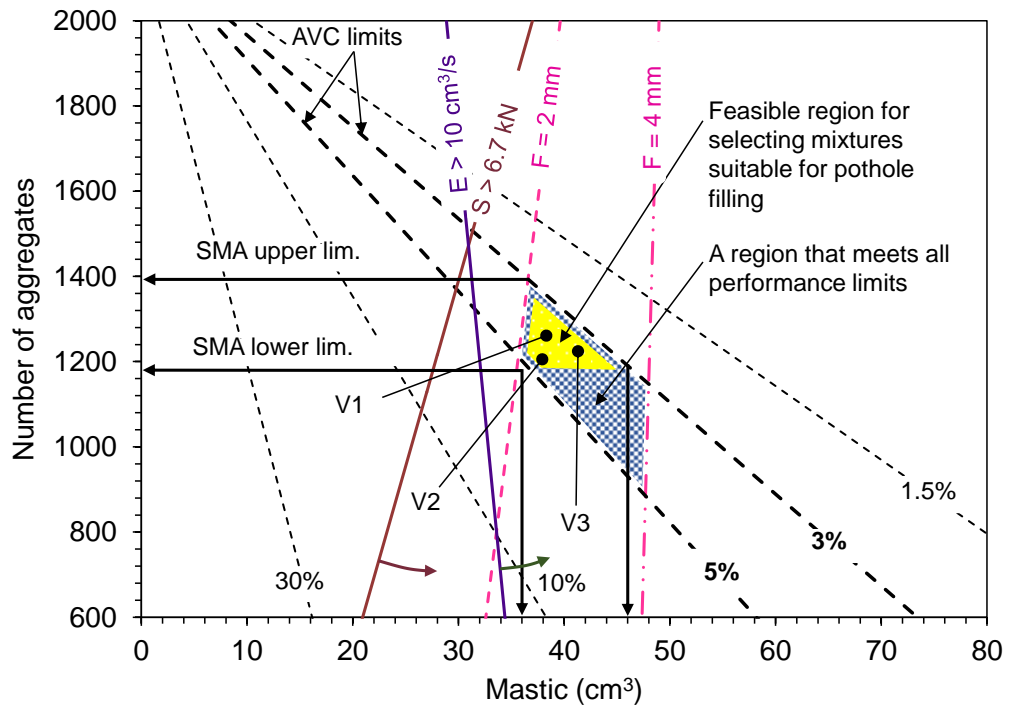


Figure 6-116: Nomograph for the design of performance-satisfactory asphalt mixtures for pothole filling.

Figure 6-116 delineates "a region that meets all performance limits," highlighting the intersection of NA and MV within which asphalt is expected to adhere to the design rules. Moving forward, the delineated performance boundary could be further refined based on specific mixture classifications, including dense asphalt, open-graded, and SMA, among others. This categorisation involves using the NA and MV within the upper and lower limits of the desired mixture. The limits for an SMA have been adopted in this chapter and used to create a subregion within the performance boundary. This subregion represents a feasible region consisting of SMA mixtures that conform to all design rules specified in Table 6-26. Within this viable realm, selecting any MV-NA coordinate pair (along the x and y axes) will guide the selection of suitable aggregate gradation for the creation of an extrudable yet durable SMA mixture. The selections made are anticipated to precisely represent the performance of the corresponding SMA mixtures as per Equation (6-18).

A detailed iteration process for selecting aggregate gradations for manufacturing extrudable and fit-for-purpose mixtures, based on the estimated MV-NA values from the feasible region in Figure 6-116, is demonstrated in the subsequent sections.

6.7.5 Iterations for the generation of aggregate gradations from the nomograph

The aggregate fractions available in the laboratory for manufacturing asphalts (filler (L_f), dust (L_D), L_6 and L_8) were individually analysed to determine the NA and MV with an assumed 5% bitumen content. It should be noted that the AVC of a mixture does not influence its aggregate count. Additionally, when keeping the bitumen volume constant and using the same aggregate fraction, the MV in a specified mass of specimen remains unchanged. Table 6-27 presents the values for each aggregate fraction, which can be combined with Equation (6-19) and Equation (6-20) to design new asphalt mixtures for the pothole filling. In a mixture with only filler aggregates, for example, no NA will be recorded making the entire composition 100% mastic. Table 6-27 also shows the number of aggregates and volume of mastic for the 250 g of each aggregate fraction.

Table 6-27: Number of aggregates and volume of mastic for different fractions of aggregates, SMA limits, and feasible region bounds.

ID	Proportion of aggregate (ϕ)	MV (cm ³)	NA
L_8	ϕ_{L8}	13.01	375
L_6	ϕ_{L6}	15.08	1582
L_D	ϕ_{LD}	67.62	1269
L_f	ϕ_{Lf}	100	0
SMA (upper)		46.6	1394
SMA (lower)		25.2	1179
Feasible region ⁴³		38-46	1179-1394

The limit range for the NA (1179 to 1394) and mastic volume (38 cm³ to 46 cm³) were obtained from the nomograph in Figure 6-116. More specifically, three mixtures have been selected randomly for the aggregate generation, mixtures V1, V2 and V3. The corresponding MV and NA coordinates for these mixtures have been shown in Figure 6-116 and detailed in Table 6-28. Further, an optimisation algorithm was developed in Microsoft Excel to calculate the proportions of aggregates (ϕ) required to produce values of the aggregate

⁴³ The feasible region in Table 6-27 differs from that in Table 5-22 primarily due to differences in the extrudability and workability performance parameters, which use distinct predictive models. Additionally, Table 6-27 is based on 34 specimens (see Table A-40), while Table 5-22 is based on 25 specimens (see Table 5-17). It should also be noted that identical mixes with the same performance limits may exhibit slight differences in NA and MV, leading to marginally different performance outputs. These variations are evident in the monograph orientations (Figure 5-102(a) and Figure 6-116) and the parameter-NA-MV relationships (Figure 5-101(c) and Figure 6-115(a)).

fractions (ϕ_{L8} , ϕ_{L6} , ϕ_{LD} , ϕ_{Lf}) that meet the NA and MV based on minimising squared errors. An example of this is shown in Equation (6-19) and Equation (6-20) for illustration of mixture V1's optimisation.

Table 6-28: Number of aggregates and volume of mastic for selected coordinates on the nomograph.

Mixture ID	MV (cm ³)	NA
V1	39.05	1284
V2	38.07	1213
V3	41.71	1231

Equation for the volume of mastic for specimen V1:

$$13.01\phi_{L8} + 15.08\phi_{L6} + 67.62\phi_{LD} + 100\phi_{Lf} = 39.05 \text{ cm}^3 \quad (6-19)$$

Equation for the number of aggregates for specimen V1:

$$375\phi_{L8} + 1582\phi_{L6} + 1269\phi_{LD} + 100\phi_{Lf} = 1284 \quad (6-20)$$

Where ϕ_{L8} , ϕ_{L6} , ϕ_{LD} , and ϕ_{Lf} represent the respective proportions (in percentage) of 8 mm aggregates, 6 mm aggregates, limestone dust, and limestone filler in the final gradation.

The required proportions of aggregate fractions, determined through iterations to yield the specified NA and MV quantities, are detailed in Table 6-29. Additionally, Figure 6-117 displays the combined gradations of these fractions used to create various mixtures (V1, V2, and V3). The boundaries of the SMA specifications are indicated to illustrate the position of the generated gradations for the validation mixtures (V1, V2, and V3) within the SMA envelope.

Table 6-29: Generated gradations for validation of nomographs.

Mixture ID	Aggregate proportion (ϕ)			
	L ₈	L ₆	L _D	L _f
V1	10.5	45	42	2.5
V2	17	40	40.7	2.3
V3	14	36	48	2.0

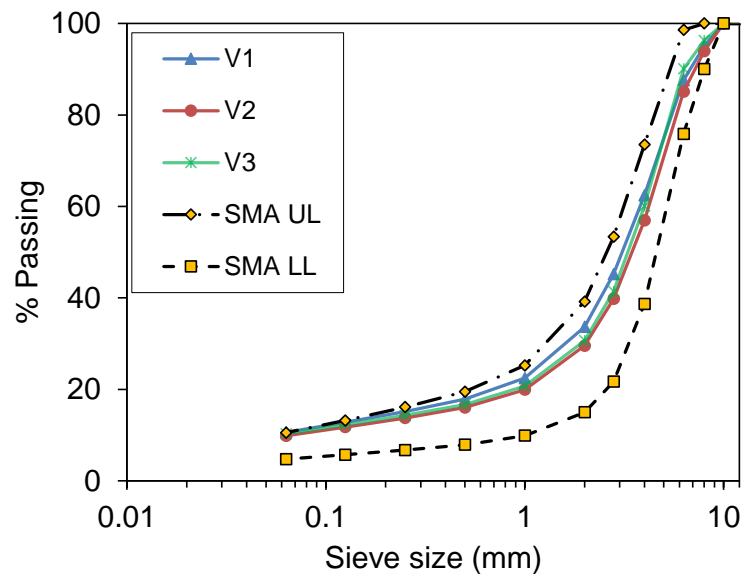


Figure 6-117: Cumulative gradations for generated aggregates compliant with BS EN 13108-5:2016 [281].

6.7.6 Validation of digitally designed pothole filling mixtures: comparing nomograph-generated and experimentally tested performances

The subsequent procedure involved producing laboratory asphalt samples V1, V2, and V3, utilising the simulated aggregate gradations presented in Table 6-29 with the 5% bitumen content. The targeted porosity was determined based on the nomograph AVC estimates. The maximum densities achieved for V1, V2, and V3 were 2.438 Mg/m³, 2.471 Mg/m³, and 2.522 Mg/m³, respectively. The Extrudability, Marshall stability, and Marshall Flow of these mixtures were also experimentally measured. Table 6-30 presents a comparison between the predicted values obtained from the nomograph approach proposed in this chapter and the experimentally measured values. Predictivity is expressed as a percentage of the relative error between the predicted and experimentally measured values. On average, the nomograph demonstrated an error rate of 8.0%, corresponding to a prediction rate of 92.0%.

6.8 Creation of Asphalt Cartridges

The manufactured hot loose asphalt mixtures (V1, V2, and V3) were separated using a riffle technique before being placed within a Teflon mould. Following this, the upper surfaces of the specimens were levelled using a scraper. After a cooling period of 30 minutes, the specimens were removed from the mould, resulting in cartridges with dimensions of 50 mm to 60 mm in length, 35 mm in width, and 16 mm in thickness.

Table 6-30: Predictivity of performance of asphalt designed with the monograph.

Mixture ID	Parameter	Nomograph (p)	Experimental (m)	Absolute error (m-p)	% error $[(m - p)/m] \times 100$
V1	E, cm ³ /s	15.0	15.8	0.8	5.3
	S, kN	7.8	7.2	0.6	8.4
	F, mm	2.4	2.6	0.2	7.6
	AVC, %	3.5	3.9	0.4	10.1
V2	E, cm ³ /s	13.9	14.5	0.6	3.9
	S, kN	7.8	8.6	0.8	9.8
	F, mm	2.3	2.5	0.2	7.7
	AVC, %	4.4	4.8	0.4	8.8
V3	E, cm ³ /s	16.3	15.7	0.6	3.8
	S, kN	8.2	8.7	0.5	5.6
	F, mm	2.8	3.1	0.3	8.8
	AVC, %	3.4	4.1	0.7	16.1
Average error	E, cm ³ /s			0.7	4.3
	S, kN			0.6	7.9
	F, mm			0.2	8.0
	AVC, %			0.6	13.5
Mean % error					8.0

These cartridges had a mass ranging approximately between 67.0 g and 70.0 g. The volume of an individual cartridge was assessed by multiplying its mass by the target density of the asphalt. This estimation approach was then applied to determine the total number of cartridges required to effectively fill a pothole with specified dimensions. Samples of the fabricated cartridges are shown in Figure 6-118.

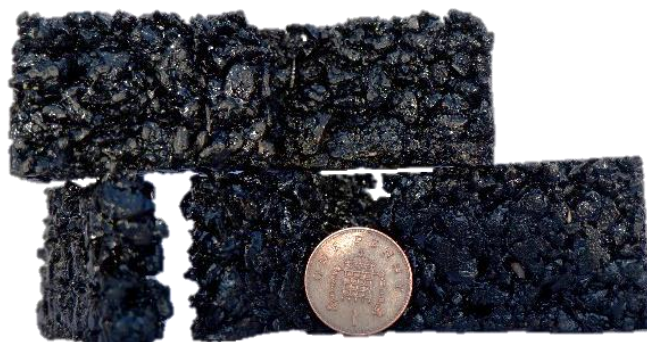


Figure 6-118: The asphalt cartridges.

6.9 The Extrusion and Pothole Filling Process

Mixtures V1 and V2 were randomly chosen for the purpose of filling the potholes. In automated fills, cartridges made from these mixtures were fed by hand into the APFM's hopper (illustrated in [Figure 6-109](#)), heated in the collar, and extruded into the lab-simulated potholes using the spiral feed screw. In future upscaled machines, cartridges could be automatically deposited using conveyor systems.

During filling, movement of the APFM's extruder nozzle followed specified pothole coordinates. These coordinates were obtained following the method in [Section 3.3.2](#). The designated filling path was set 30 mm from the pothole's edges, initiating a circular route until the brim was reached, after which the centre was filled. This strategy ensured a consistent distribution of materials, making it easier to achieve comprehensive coverage during the compaction process.

Prior to extrusion, asphalt cartridges were preheated at 60 °C for 30 minutes, and the extrusion collar system was preheated at 171 °C for 10 minutes to ensure a uniform temperature.

6.10 Densification of Asphalt Extrudate in Potholes

Following the extrusion of the required asphalt volume into potholes with tack-coated walls, a free-falling 2.5 kg compaction tamper was used to smooth the filling, ensuring that the extrudates levelled with the surface of the adjoining asphalt slab and that the targeted densities of the filled potholes were achieved. Due to the mechanical complexities of integrating it with a simple lab-scaled 3D printer, the tamper compaction was separate from the APFM filling machine. In future upscaled studies, the two systems could be programmed to function as a single component, and other more efficient methods of achieving the required densities of asphalt extrudates could be explored, as suggested in [Section 7.2](#).

Initially, a 150 mm diameter iron plate, heated to 150 °C, was placed on top of the mixture to be compacted, creating a level surface. Given that the targeted density was estimated based on a pothole volume of 515 cm³, compacting the asphalt to a depth of 40 mm was necessary to achieve the desired density.

6.11 Pothole Filling by Hand

In the laboratory, parallel potholes were manually filled to replicate on-site pothole patching methods for comparison with automated fills. This involved producing asphalt with identical gradations and recipes as those used for the autonomous fills. The primary distinction was that loose hot asphalt mixtures were poured directly into the potholes in one go. Similar to the automated fills, the poured asphalt was compacted using a tamper to align with the surrounding asphalt.

6.12 Evaluation of Filled Pothole Quality

The effect of traffic loading on filled potholes, and to an extent their stability, was assessed by comparing the rut depth. Rutting was evaluated through the wheel tracking test detailed in [Section 3.3.8](#).

In addition to stability assessment, AVC values were evaluated by comparing the experimentally measured AVC of 100 mm cores extracted from the filled potholes to the theoretically targeted AVC values. Samples of the pothole-extracted cores are shown in [Figure 6-119](#).



Figure 6-119: Cores drilled from filled potholes for the estimation of AVC.

[Figure 6-120](#) presents the rutting deformation profiles of the potholes repaired with these materials, offering a comparison between the quality of both automated and manual filling techniques. [Table 6-31](#) provides data on final rut depths and corresponding AVC values. Notably, V1 fills exhibit lower rutting resistance due to their lower stability and higher flow characteristics (as indicated in [Table 6-30](#)). With a mean rut depth error percentage of 14.4% as indicated in [Table 6-31](#), automated fills achieved 85.6% of the rutting resistance observed in manual fills.

The enhanced rutting resistance in manual fills was observed to stem from more effective compaction and lower air void content deviations. Manual fills were poured in bulk and compacted at once, unlike automated fills, which were applied in thinner layers, cooled faster due to their higher surface-to-volume ratio, and reached thermal equilibrium with their surroundings more rapidly [312].

Positively, automated-filled potholes demonstrated about 86% of the traffic endurance seen in manual fills, indicating a promising future for the automated technique. Improving compaction and extrudate cooling could enhance future automated repairs, and subsequent studies could explore extrudable self-compacting asphalt mixtures for better performance.

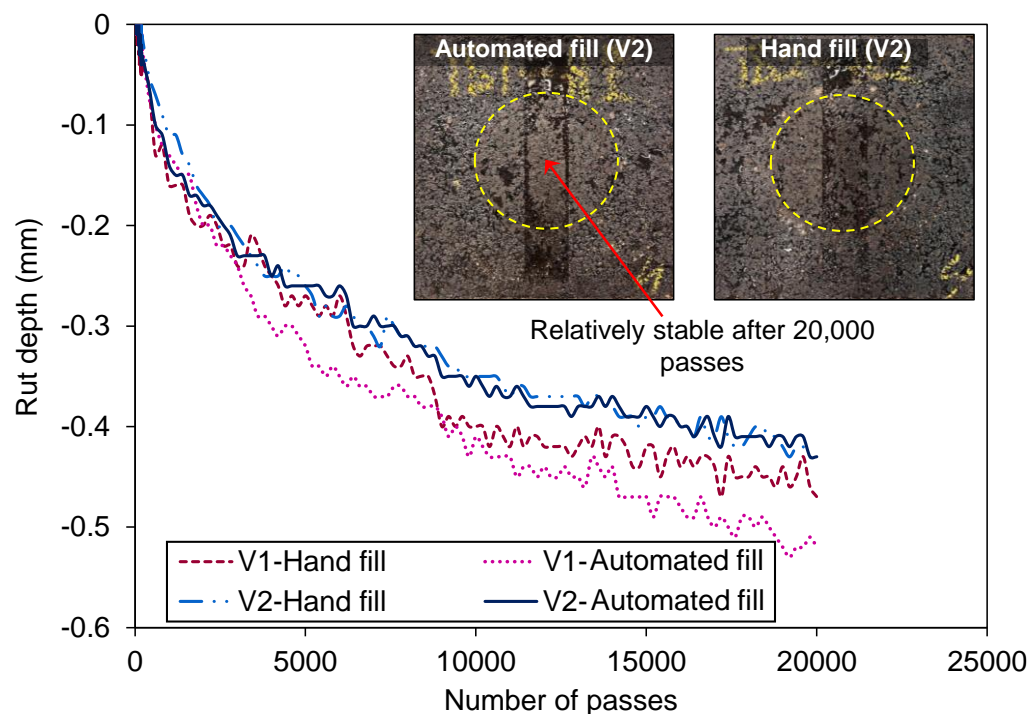


Figure 6-120: Comparative rutting resistance of filled pothole specimens: automated versus hand filling.

Table 6-31: Wheel tracking test results comparing the rutting resistance of automated and hand filled pothole specimens.

Specimen ID	AVC (%)		Final rut depth (mm)		Absolute error (h-a)	% error $[(h-a)/h] \times 100$
	Automated	Hand	Automated (a)	Hand (h)		
V1	4.3	3.8	0.39	0.33	0.06	18.2
V2	5.1	4.6	0.52	0.47	0.05	10.6
Rut depth mean % error						14.4

6.13 Summary

This chapter introduced a new, less labour-intensive method for filling potholes using a modified 3D printer as an automated filling machine. The machine's parameters, such as extrusion speed, were optimised to enhance the extrusion of asphalt mixtures and improve filling efficiency. A digital design from [Chapter 5](#) enabled the rapid selection of aggregate-bitumen proportions for extrudable hot-mix asphalt repair cartridges, meeting performance standards such as Marshall stability, flow, and air void content. The chapter also compared the quality of automated and manual pothole filling. The following conclusions can be drawn:

- The application of the newly developed digital design method for hot-mix asphalt mixtures, presented in [Chapter 5](#), for developing mixes adaptable for machine applications in pothole repairs has been demonstrated. The method exhibited 92% accuracy in developing repair mixtures that meet specified extrusion rates while achieving standard Marshall stability, Marshall flow, and air void content performances. Comparing this accuracy to the 94% design accuracy established in [Chapter 5](#) further reinforces the accuracy of this new design method and, most importantly, highlights the broad applicability of the method.
- In the laboratory setting, a simple-to-use 3-axis screw-extrusion 3D printer served as the machine. This machine could navigate pothole contours while extruding asphalt into lab-simulated potholes at the required temperature and speed.
- Asphalt extrusion rates (expressed in cm^3/s) were enhanced with maximised motor power (0.366 kW) achieved by operating at an optimised extrusion speed of 18 rpm and a motor torque of 0.2 Nm. These findings underscore the need to carefully optimise in order to customise extrusion speeds in future automated pothole filling machines to achieve the highest asphalt extrusion rate values.
- Comparing manual and automated pothole filling techniques revealed that manual fills exhibited superior rutting resistance due to more effective compaction. Nevertheless, automated filling demonstrated promising potential, achieving 86% of the rutting resistance observed in manual fills. This underscores the feasibility of automation as a viable alternative to current manual methods.

Chapter 7: Conclusions, Future Work and Outlook

The primary aim of this research was to assess the feasibility of automating crack and pothole repairs in bituminous pavements using hot bitumen and hot-mix asphalt in a laboratory setting. Achieving this required the development of machines capable of operating with minimal human intervention and the formulation of compatible asphalt mixtures. [Chapter 2](#) identified 3D printing as the most feasible, cost-effective approach for developing simple laboratory-scale repair machines. Based on this, a RepRap 3D printer was adapted for both crack and pothole filling tasks, with operational parameters, such as filling speed and extrusion temperature, optimised to enhance repair efficiency and quality.

Hot bitumen for crack filling was readily available on the market, but the formulation of extrudable hot-mix asphalt mixtures posed a significant challenge for pothole repair. Existing pothole filling machines primarily use cold-mix asphalt, which lacks durability. This is due to the difficulty of producing hot-mix asphalt mixtures that are both extrudable at practical rates and meet standard performance requirements on site. Furthermore, conventional design methods rely heavily on manual trial and error, limiting their compatibility with automated processes. To address these gaps, a new digital design method for asphalt mixtures was developed in [Chapter 5](#). This method demonstrated its ability to accurately predict the properties of 16 mixtures through independent validation tests conducted at the Czech Technical University in Prague. Unlike traditional methods, this streamlined approach reduces the need for time-intensive physical and mechanical tests while leveraging data-driven techniques to optimise performance.

In [Chapter 6](#), the validated digital method was applied to produce asphalt repair cartridges for an automated pothole filling machine. This machine demonstrated its ability to navigate pothole contours and fill lab-simulated potholes with extrudable asphalt at optimised speeds and temperatures. To ensure robustness, automated repairs were benchmarked against manual fills, which served as controls.

The conclusions below summarise the key findings and outcomes of this research across crack filling, asphalt design, and pothole filling. The Future Work section outlines potential extensions of this research and discusses strategies to overcome highlighted limitations. Finally, the Outlook section offers

a broader perspective on the research implications, drawing from findings, expert opinions, and ongoing studies. This speculative vision seeks to bridge the gap between laboratory advancements and real-world applications.

7.1 Conclusions

The following conclusions can be drawn:

Automated filling of cracks

- The crack filling speed and temperature of the bitumen are critical factors influencing the filling volume of cracks and their resistance to mechanical deformation.
- There is a minimum temperature below which cracks cannot be fully filled, and a maximum temperature above which bitumen thermally degrades.
- Understanding the complex interactions between the filling speed, crack width, depth, and tortuosity (the degree to which a crack is straight or curved), along with the temperatures of the bitumen, the environment, and the cracked pavement, is crucial for producing high-quality crack fillings.
- There is also an optimum crack filling speed. As the printing speed increases beyond this optimum, large air bubbles form in the bitumen, which reduces the mechanical strength of the filled cracks.
- The layer-by-layer filling approach of 3D printing increases the porosity in filled cracks. The layer boundaries also act as weak planes where tensile failures begin. Therefore, it is advisable to avoid using bitumen layers in future machine-filling applications as much as practicable.
- The crack filling speed needs to be adjusted according to the temperature and crack dimensions. Therefore, it is crucial to develop precise models that can predict the geometries of the cracks and calculate the necessary filling rates for each crack that needs to be filled on site.
- Machine crack filling is more effective for straight cracks, such as those in pavement joints. Therefore, it is recommended that this be the first application to be developed.

Digital design of asphalt

- A physics engine software was used to create and characterise the aggregates and bitumen in different HMAs. Insights derived from the physics engine were systematically integrated to develop models that quantify the number of aggregates (based on their shapes) and the volume of mastic in asphalt mixtures. Statistical analysis indicates that the fundamental properties of HMAs, such as air void content, workability, Marshall stability, and Marshall flow, are significantly influenced by the number of aggregates and the volume of mastic contained in the mixes.
- The number of aggregates in HMAs is influenced by the aspect ratio of the aggregates ($R^2 = 0.98$). When the aspect ratio decreases, the number of aggregates increases. Therefore, an understanding of the geometric properties of aggregates and the ability to control them is essential for designing future HMAs with tailored functionalities.
- Digitally generated aggregates and mastic can be used to develop 3D models of HMAs. These virtual representations allow the observation of aggregate distributions in the HMA before they are physically manufactured.
- Through an iterative process, nine different HMAs were designed using identical bitumen and aggregate sources that fulfilled about 94% of the properties of their physical counterparts. However, the predictive accuracy of the model decreased to 78% for HMAs that contained diverse aggregate and bitumen characteristics.

Automated filling of potholes

- The new digital performance-based method developed in this research was applied to formulate HMA cartridges that are extrudable by automated repair machines while also meeting standard structural performance requirements such as Marshall stability, Marshall flow, and air void content. The digital method once again exhibited high accuracy (92% accuracy in this case) in developing HMAs and further demonstrated its versatility for use in creating HMAs with specific characteristics and functional requirements.
- In the laboratory setting, a simple-to-use 3-axis screw-extrusion 3D printer served as the machine. This machine could navigate pothole

contours while extruding asphalt into lab-simulated potholes at the required temperature and speed.

- Asphalt extrusion rates (expressed in cm^3/s) were enhanced with maximised motor power (0.366 kW) achieved by operating at an optimised extrusion speed of 18 rpm and a motor torque of 0.2 Nm. These findings underscore the need to carefully optimise in order to customise extrusion speeds in future automated pothole filling machines to achieve the highest asphalt extrusion rate values.
- Comparing manual and automated pothole filling techniques revealed that manual fills exhibited superior rutting resistance due to more effective compaction. Nevertheless, automated filling demonstrated promising potential, achieving 86% of the rutting resistance observed in manual fills. This underscores the feasibility of automation as a viable alternative to current manual methods.

7.2 Future Works

Automated filling of cracks

As demonstrated in this research, the bitumen flow, filling speed, and the width and depth of cracks determine the quality of the filling and will need to be carefully controlled in future automated crack filling devices. The complex interaction between these parameters should be researched further in future studies.

In addition, it has been shown that large void formations occur in the bitumen in cracks when filling beyond optimal printing speeds (or filling speeds). The air void entrapment could be likened to cavitation, where high relative motion allows small vapour bubbles to be entrapped in the bitumen. This air entrapment restricts high filling speeds, hence affecting the productivity of using automated filling machines. This is certainly a limitation from an economic perspective. Future research could therefore investigate techniques to reduce voids in bitumen at high printing speeds. Modifying the rheology of bitumen for crack filling to overcome this challenge could be a good starting point.

Furthermore, the capability of robotic devices to precisely estimate in-situ crack volumes and thereby calculate the exact amount of bitumen required remains an area for further exploration. In this research, level sensors were utilised, suggesting potential for more accurate measurements with further investigation. Notably, recent research at the University of Cambridge [313], building on this

research in reference [314], suggests using position-based fluid simulation to improve the precision of automated crack sealing. This research, along with several others, is still at preliminary stages, and further is recommended.

Digital design of asphalt

The research findings underscore the significance of aggregate geometries in accurately designing future asphalt mixtures, especially in creating realistic digital HMA representations. However, due to the current input limitations of the physics engine software, not all aggregate morphologies have been considered in detail. In a sensitivity analysis with diverse asphalt mixtures (varied aggregate and bitumen characteristics and asphalt formulations), the digital method exhibited reduced accuracy in predicting HMA properties. For example, AVC exhibited the highest error at 45.3% in prediction. The observed low AVC prediction in the sensitivity analysis could mean that the geometric parameters used in this research, such as the aspect ratio and height, do not comprehensively capture the properties of all HMA aggregates. As such, it is suggested that future studies should investigate the impact of other aggregate morphologies such as lithology and surface texture on the performance of HMAs and their possible inclusion in future digital design methods.

Additionally, as one can imagine, 34 HMAs (limited by resources and time in this research) are insufficient to produce definitive conclusions in the prediction of broad ranges of asphalt performance. However, these results are a good indicator of the inputs that future studies may require to explore. Consequently, future research could involve creating a more extensive asphalt database for model fitting and validation. For such complex iterations in future studies, machine learning applications may be utilised.

Furthermore, the nomograph used in this research presents a potential to be used in manipulating aggregate geometry and gradation to regulate asphalt mix porosities. Future research could adapt this nomograph methodology to manage the topological properties of connective pores⁴⁴ of such as pore area, pore circularity, equivalent pore diameter, and pore network, thereby accurately designing the hydraulic conductivity of porous asphalt mixtures.

⁴⁴ In the context of porous composite materials, "connective pores" refer to the pores within the material that are interconnected, forming a network that allows for the passage of water. These connective pores are critical for determining many of the physical properties of the asphalt mixture, such as permeability, porosity, and mechanical strength.

Automated filling of pothole

A Nominal Maximum Aggregate Size (NMAS) of 8 mm was used to downsize the extruder on the APFM, thereby constraining its usability. A larger NMAS should be considered in future applications. Moreover, the research did not address automation of the compaction process due to its complexity in integrating with a laboratory-based APFM, and the asphalt extrudate in the potholes was compacted with an isolated tamper as illustrated in [Figure 6-106](#). Further research is required, particularly on the upscaling of the APFM, to explore more efficient methods of achieving the required densities of asphalt extrudates in potholes. The use of self-compacting asphalt mixtures, which is currently in the early stages of research, could be a promising starting point to potentially avoid this challenge.

7.3 Outlook

Digital design of asphalt mixtures

As we move forward, the development of digital design methods for asphalt mixtures that incorporate aggregate geometry is poised to revolutionise the field of pavement engineering. The integration of detailed aggregate geometry into asphalt mixture design, as explored in this research, highlights the potential for more precise and optimised workable pavement materials that cater specifically to varying traffic and environmental conditions.

Future directions

Future developments should focus on refining computational models that can simulate the real-world behaviour of asphalt mixtures under various loading and weather conditions. This includes the use of machine learning and artificial intelligence to predict mixture performance with greater accuracy.

Also, as environmental considerations become increasingly critical, future research will need to integrate sustainable practices into digital asphalt design. This includes using recycled materials and developing new, eco-friendly aggregate compositions that maintain or enhance pavement performance. In addition, the cost of asphalt development could be factored into the optimisation process.

In addition, leveraging real-time traffic and environmental data to dynamically adjust the properties of asphalt mixtures could enable smarter, more adaptive

infrastructure. Implementing Internet of Things sensors within pavements could feed back into digital design systems, creating a continuously improving loop of data, design, and deployment.

For these innovations to be effectively integrated into mainstream practice, considerable effort will need to be focused on standardising digital design methodologies and gaining regulatory acceptance. This involves rigorous validation of the models and collaboration with industry stakeholders to update codes and standards.

Also, aside from minimising the need for physical laboratories in designing future asphalt mixtures, the use of physics engines shows promising potential to address current physicochemical challenges in digital representations, including addressing the lack of physics in current asphalt digital twin models.

Challenges

Understanding and predicting how complex material interactions (particularly bitumen) affect the longevity and resilience of asphalt mixtures remains a significant challenge. Continued research into the micromechanics of materials and their behaviour under stress will be essential.

The outlook for digital design methods in asphalt mixture development is robust and filled with potential. As the field evolves, it will undoubtedly bring forth innovations that not only enhance the performance and durability of roadways but also align with global sustainability goals. This will require a multidisciplinary approach, bringing together engineers, data scientists, and environmental experts to forge the future of pavement technology.

Robotic repair of roads

The finding from this research suggests the future of pothole repair is heading towards greater automation and precision, leveraging advancements in digital and machine techniques to enhance the efficiency and effectiveness of road maintenance. The integration of digitally crafted asphalt cartridges with automated machinery represents a promising frontier in this domain. As explored in this research, several key developments are expected to shape this field.

Future Directions

There is likely to be an increased emphasis on incorporating recycled materials and environmentally friendly additives into asphalt cartridges, driven by sustainability goals and regulatory pressures.

In addition, AI algorithms have the potential to improve the ability of automated repair systems to make on-the-fly adjustments to their operations, enhancing their efficiency and effectiveness under varying operational conditions.

Lastly, as automated systems become more common, specific standards and regulations will need to be developed to ensure safety, reliability, and compatibility with existing infrastructure.

Challenges and Considerations

The high cost of advanced technologies and the inertia of existing maintenance protocols may slow down the adoption of fully automated systems. To facilitate the implementation of automated robotic repair processes, a phased transition is necessary, involving full input from key stakeholders such as robotic manufacturing companies, road management authorities, and asphalt design and construction experts.

Upscaling the automated repair machines and field trials

The transition from small-scale prototypes to full-scale deployment involves scaling up the machinery developed in this research to handle real-world conditions, which are often more complex and variable than those simulated in the laboratory environment. During the upscaling process, field trials will be essential to provide invaluable data on how these machines perform under actual operational stresses and environmental conditions not apparent in laboratory settings.

Looking ahead, the upscaling and field trials of automated repair machines will need to focus on enhancing machine adaptability, reducing costs, and improving user interfaces to ensure that the technology can be easily integrated into existing road maintenance regimes. Collaboration between industry, academia, and government agencies will be vital in driving these developments forward, ensuring that the benefits of automation in road repair are fully realised in the coming years.

Presently, there are various concepts from researchers regarding how defect repair machines should be constructed. For example, researchers at the University of Leeds (see Figure 7-121, a) suggest that drones equipped with 3D printers could be ideal for use as autonomous repair machines. Conversely, researchers at Robotiz3d⁴⁵ and the University of Liverpool (see Figure 7-121, b) propose a machine similar to a Land Rover with an attached roller compactor. These designs are at the conceptual stage, and the mechanics and operational parameters of these machines have yet to be finalised.

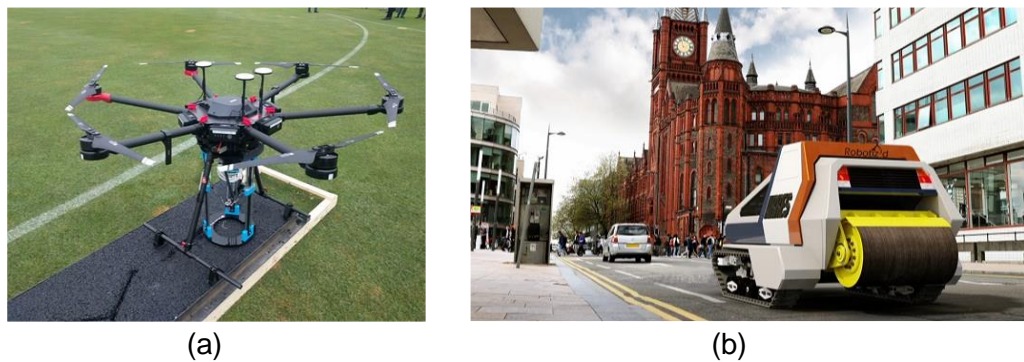


Figure 7-121: (a) A 3D printing drone prototype developed by Leeds University under the Self-Repairing Cities Project, and (b) an artistic impression of the Robotiz3d road repair robot by the University of Liverpool.

With the experience gathered from this research, the drone options appear to have practical limitations in terms of payload (quantity of repair materials that can be delivered at a time) and safety. It is worth noting that there were attempts to collaborate with Leeds to attach the extruder used in this research to Leeds' drone for field testing. One major challenge encountered was that the drone could not carry sufficient bitumen to fly at one time. Additionally, there were Civil Aviation Authority regulation hurdles related to flying a drone that, when loaded with repair bitumen, exceeded 25 kg and was categorised as high-risk or complex flying⁴⁶.

On the other hand, the Robotiz3d concept obviously promises to accommodate more payload; nonetheless, as mentioned earlier, the idea is conceptual, and it is not clear how the asphalt extrusion and compaction would be achieved on site. Moreso, in the time where driverless vehicles appear to have operational challenges, it is not certain how this perceived concept will operate in the short term as indicated by the researchers.

⁴⁵ Robotiz3d: <https://www.robotiz3d.com/>

⁴⁶ Civil Aviation Authority: <https://register-drones.caa.co.uk/drone-code/getting-what-you-need-to-fly#:~:text=This%20allows%20you%20to%20fly,that%20weighs%2025kg%20or%20more.>

Looking into all these challenges, this research's verdict is that the robotic repair technology should be rolled out in phases along transition levels. In the medium term (2 - 5 years), it is proposed that the upscaled robotic arm (which contains the extruder) should be attached to manual repair vehicles to be driven to site. Upon reaching site, technicians could then park the trucks and release the arms to autonomously locate and repair nearby defects (the robotic arm here just replaces human arms on site). This concept for crack filling, for example, is illustrated in [Figure 7-122](#). In essence, the research suggests adopting a semi-automated process, as opposed to a fully robotic or drone-delivered repair in the short to medium term. Consequently, it is recommended that future research in the short-term should focus on the application of techniques such as Augmented Reality to optimise cooperation between humans and robots [315].

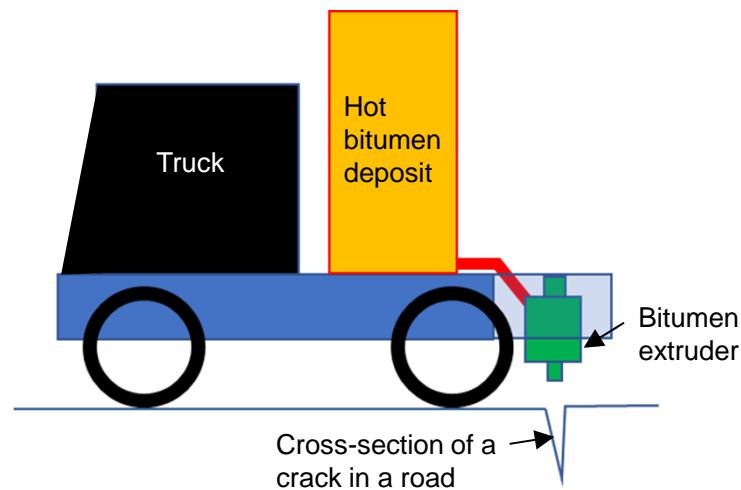


Figure 7-122: Illustration of how a bitumen extruder attached to a repair vehicle for field applications could look in the medium term.

Certainly, as technology rapidly evolves, with the development of flying taxis and other unmanned vehicles, a complete robotic application could be implemented after this transition period. Even with these advancements in technologies, perhaps a more feasible option would be using drones to capture crack and pothole geometry and location and feeding the data to the repair machines. This futuristic concept is illustrated in [Figure 7-123](#).

Lastly, in the era of fully robotic repairs, it is foreseen that as autonomous car technology advances and digitalisation of roads and vehicles improves, there is an opportunity to link future repair robots to travelling vehicles to pre-inform vehicles of roadblocks and safety precautions as they approach the robotic repair zones.



Figure 7-123: A futuristic highway scene featuring a robot actively repairing a pothole, with real-time pothole and traffic data provided by a drone. Image generated using GPT-4 by OpenAI.

From interactions with investors at conferences, it is evident that they are highly enthusiastic about the futuristic concept of land rovers equipped with extruders and robotic repair systems. The U.S Department of Transportation had started collaboration with the researcher to implement the findings of this research with much focus on exploring the application of 3D printing in other road infrastructure management. One challenge to the fully robotised platform is the payload limitations and the development of a precise control and navigation system which falls outside the scope of this research. It is fair to say that these challenges are comparable to those faced by driverless vehicles and advanced autonomous space system suitable for single or collaborative space robotic missions. In the UK, GMV NSL Limited, for example, have started developing precise and robust autonomous robotic platforms with adaptable levels of autonomy. See [Figure 7-124](#) for a photograph taken during one of the platform trials in front of NTEC at the University of Nottingham. It is only when these autonomous robotic platforms are precise, reliable and fully operational that full robotic repair of roads can be realised.

Drawing on the comprehensive discussions presented, it is unequivocally clear that the realisation of fully autonomous robotic repair systems for asphalt roads demands robust multidisciplinary collaboration. Crucially, it is projected that the robotic repair of cracks and potholes could be operational within the next decade. This prospective advancement underscores the substantial value of further investments in collaborative research, regulatory frameworks, and strategic implementation to harness this innovative technology effectively.

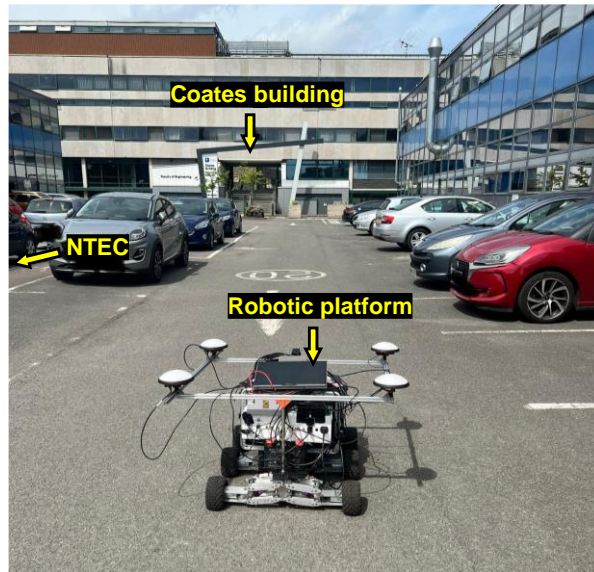


Figure 7-124: Field trial of an autonomous robotic platform in front of NTEC at University Park, University of Nottingham. Research led by GMV NSL Limited.

References

- [1] Office for National Statistics, Labour productivity, (2022). <https://www.ons.gov.uk/employmentandlabourmarket/peopleinwork/labourproductivity>.
- [2] P. Lavin, Pavement maintenance, 2003. <https://doi.org/10.1201/9781482267716-18>.
- [3] M. Hoeft, S. Kronsell, S. Manzoor, F. Johansson, A. Gustafson, T. Von Haslingen, K. Eriksson, Construction Automation and Robotics in Infrastructure, 2022. <https://www.diva-portal.org/smash/get/diva2:1694999/FULLTEXT01.pdf>.
- [4] P. Wu, J. Wang, X. Wang, A critical review of the use of 3-D printing in the construction industry, Autom Constr 68 (2016) 21–31. <https://doi.org/10.1016/j.autcon.2016.04.005>.
- [5] S.H. Ghaffar, J. Corker, M. Fan, Additive manufacturing technology and its implementation in construction as an eco-innovative solution, Autom Constr 93 (2018) 1–11. <https://doi.org/10.1016/j.autcon.2018.05.005>.
- [6] B. Khoshnevis, Automated construction by contour crafting - Related robotics and information technologies, Autom Constr 13 (2004) 5–19. <https://doi.org/10.1016/j.autcon.2003.08.012>.
- [7] B. Xiao, C. Chen, X. Yin, Recent advancements of robotics in construction, Autom Constr 144 (2022). <https://doi.org/10.1016/j.autcon.2022.104591>.
- [8] B. García de Soto, I. Agustí-Juan, J. Hunhevicz, S. Joss, K. Graser, G. Habert, B.T. Adey, Productivity of digital fabrication in construction: Cost and time analysis of a robotically built wall, Autom Constr 92 (2018) 297–311. <https://doi.org/10.1016/j.autcon.2018.04.004>.
- [9] LetsBuild, UK could save £15 billion every year by lifting construction productivity, (2023). <https://www.letsbuild.com/blog/uk-could-save-15-billion-by-lifting-construction-productivity>.
- [10] Highways England, The Road to Growth Our strategic economic growth plan, 2017. https://assets.publishing.service.gov.uk/media/5a823f7c40f0b62305b93463/m160503_the_road_to_growth_Our_strategic_economic_growth_plan.pdf.
- [11] Department of Transport, Transport Statistics Great Britain: 2022 Summary, (2023). <https://www.gov.uk/government/statistics/transport-statistics-great-britain-2023/transport-statistics-great-britain-2022-summary>.
- [12] C.A. O'Flaherty, D. Hughes, Highways: the location, design, construction and maintenance of road pavements, ICE Publishing, London, 2016. <https://typeset.io/pdf/highways-the-location-design-construction-and-maintenance-of-4g7i8ctbvt.pdf>.
- [13] Highways Maintenance Efficiency Programme, Prevention and a better cure: potholes review., 2012.

<https://assets.publishing.service.gov.uk/media/5a78a10b40f0b63247698e7c/pothole-review.pdf>.

- [14] J.E. Ponniah, G.J. Kennepohl, Crack sealing in flexible pavements: A life-cycle cost analysis, *Transp Res Rec* (1996) 86–94.
<https://doi.org/10.3141/1529-11>.
- [15] Y. Yildirim, Field performance comparison of asphalt crack-filling materials: hot pour versus cold pour, *Canadian Journal of Civil Engineering* 34 (2007) 505–512. <https://doi.org/10.1139/I06-143>.
- [16] F. Bian, H. Cai, Choice of crack repairing material for asphalt pavement based on AHP, *J Test Eval* 40 (2012) 1144–1147.
<https://doi.org/10.1520/JTE20120154>.
- [17] D. Bennett, S. A. Velinsky, Development of the Sealzall Machine - Upgrade to the TTLS (Pavement Crack Sealer), (2009).
<https://rosap.ntl.bts.gov/view/dot/25270/Share>.
- [18] JCB, JCB Pothole Pro - Efficient & Safe Road Pothole & Street Repairs, (2023). <https://www.jcbcea.com.au/2023/06/revolutionising-roadworks-unveiling-the-jcb-pothole-pro-the-ultimate-solution-for-efficient-and-safe-pothole-repairs/>.
- [19] Velocity, Spray Injection Patching, (2023).
<https://velocityroads.co.uk/spray-injection-patching/>.
- [20] B.J. Kwon, D. Kim, S.K. Rhee, Y.R. Kim, Spray injection patching for pothole repair using 100 percent reclaimed asphalt pavement, *Constr Build Mater* 166 (2018) 445–451.
<https://doi.org/10.1016/j.conbuildmat.2018.01.145>.
- [21] T. Wang, Y.A.S.S. Dra, X. Cai, Z. Cheng, D. Zhang, Y. Lin, H. Yu, Advanced cold patching materials (CPMs) for asphalt pavement pothole rehabilitation: State of the art, *J Clean Prod* 366 (2022).
<https://doi.org/10.1016/j.jclepro.2022.133001>.
- [22] A. Ipavec, POTHOLE: Study of existing standards, techniques, materials and experience with them on the European market, 2012.
https://www.cedr.eu/download/other_public_files/research_programme/eranet_road/call_2011/design/pothole/03_pothole_d3-techniques-and-materials-study.pdf.
- [23] A. Changra, E.G. Singh, Comparison of Marshall Stability values of the different bitumen mixes with crumb rubber, in: *IOP Conf Ser Earth Environ Sci*, Institute of Physics, 2023. <https://doi.org/10.1088/1755-1315/1110/1/012034>.
- [24] M.A. Gul, M.K. Islam, H.H. Awan, M. Sohail, A.F. Al Fuhaid, M. Arifuzzaman, H.J. Qureshi, Prediction of Marshall Stability and Marshall Flow of Asphalt Pavements Using Supervised Machine Learning Algorithms, *Symmetry (Basel)* 14 (2022).
<https://doi.org/10.3390/sym14112324>.
- [25] UNITY, Physics solutions for game development, (2024).
<https://unity.com/solutions/programming-physics>.
- [26] A. Garcia-Hernandez, L. Wan, S. Dopazo-Hilario, A. Chiarelli, A. Dawson, Generation of virtual asphalt concrete in a physics engine,

Constr Build Mater 286 (2021).
<https://doi.org/10.1016/j.conbuildmat.2021.122972>.

- [27] P. Cao, F. Jin, D. Feng, C. Zhou, W. Hu, Prediction on dynamic modulus of asphalt concrete with random aggregate modeling methods and virtual physics engine, *Constr Build Mater* 125 (2016) 987–997.
<https://doi.org/10.1016/j.conbuildmat.2016.08.121>.
- [28] Z. Xu, X. Lu, H. Guan, B. Han, A. Ren, Seismic damage simulation in urban areas based on a high-fidelity structural model and a physics engine, *Natural Hazards* 71 (2014) 1679–1693.
<https://doi.org/10.1007/s11069-013-0972-8>.
- [29] Repetier Software, (2024). <https://www.repetier.com/>.
- [30] A. Garcia-Hernandez, S. Michot-Roberto, S. Dopazo-Hilario, A. Chiarelli, A. Dawson, Creation of realistic virtual aggregate avatars, *Powder Technol* 378 (2021) 760–771.
<https://doi.org/10.1016/j.powtec.2020.10.036>.
- [31] A. Chiarelli, A.R. Dawson, A. García, Generation of virtual asphalt mixture porosity for computational modelling, *Powder Technol* 275 (2015) 351–360. <https://doi.org/10.1016/j.powtec.2015.01.070>.
- [32] Welsh Assembly Government, Economic Effects of Road Infrastructure Improvements: Stage 3 Report, 2004.
<https://www.gov.wales/sites/default/files/statistics-and-research/2018-12/060524-economic-effects-transport-infrastructure-improvements-en.pdf>.
- [33] National Highways, Connecting the Country - Planning for the long term, 2017.
https://assets.publishing.service.gov.uk/media/5a81ff88ed915d74e62353d3/Connecting_the_country_Planning_for_the_long_term.pdf.
- [34] National Highways, Shaping the future of England's strategic roads, (2023). <https://www.gov.uk/government/consultations/shaping-the-future-of-englands-strategic-roads/shaping-the-future-of-englands-strategic-roads>.
- [35] National statistics, Road lengths in Great Britain: 2021, (2022).
<https://www.gov.uk/government/statistics/road-lengths-in-great-britain-2021#:~:text=In%202021%2C%20the%20total%20length,%25%20trunk%2C%2082%25%20principal>.
- [36] National statistics, Road lengths in Great Britain: 2022, (2023).
<https://www.gov.uk/government/statistics/road-lengths-in-great-britain-2022/road-lengths-in-great-britain-2022>.
- [37] Asphalt Industry Alliance, Annual Local Authority Road Maintenance Survey Report 2024, 2024. <https://www.asphaltuk.org/wp-content/uploads/ALARM-survey-report-2024-FINAL.pdf>.
- [38] Asphalt Industry Alliance, Annual Local Authority Road Maintenance Survey Report 2023, 2023. <https://www.asphaltuk.org/wp-content/uploads/ALARM-survey-2023-FINAL-with-links.pdf>.
- [39] A. Das, Structural Design of Asphalt Pavements: Principles and Practices in Various Design Guidelines, *Transportation in Developing Economies* 1 (2015) 25–32. <https://doi.org/10.1007/s40890-015-0004-3>.

- [40] Alberta Transportation and Utilities, Pavement Design Manual Edition 1, 1997.
<https://www.transportation.alberta.ca/Content/docType233/Production/pavedm2.pdf>.
- [41] FDOT, Flexible Pavement Design Manual, 2020.
https://fdotwww.blob.core.windows.net/sitefinity/docs/default-source/roadway/pm/publications/2023fpdm.pdf?sfvrsn=22f4536c_2.
- [42] D.N. Little, D.H. Allen, A. Bhasin, Modeling and design of flexible pavements and materials, Cham : Springer, Cham, 2018.
<https://doi.org/https://doi.org/10.1007/978-3-319-58443-0>.
- [43] J.G. Speight, Asphalt Materials Science and Technology, 1st ed., San Diego: Elsevier Science, San Diego, 2015.
<https://www.sciencedirect.com/book/9780128002735/asphalt-materials-science-and-technology>.
- [44] American Concrete Pavement Association (ACPA), Design of concrete pavement for streets and roads, 2006.
<https://cf.specifyconcrete.org/doc/Design-of-Concrete-Pavement-for-Streets.pdf>.
- [45] K. Smith, J. Signore, D. Tompkins, P. Ram, Implementation of Composite Pavement Systems-FHWA-HIF-19-014, 2019.
<https://www.fhwa.dot.gov/pavement/pubs/hif19014.pdf>.
- [46] TRB, Composite Pavement Systems, 2014.
https://onlinepubs.trb.org/onlinepubs/shrp2/shrp2_pb_r21_2014-05.pdf.
- [47] British Standards Institution, BS EN 13108, Bituminous mixtures. Material specifications, (2016).
<https://landingpage.bsigroup.com/LandingPage/Series?UPI=BS%20EN%2013108>.
- [48] British Standard Institution, BS EN 13043:2013, Aggregates for bituminous mixtures and surface treatments for roads, airfields and other trafficked areas, (2013).
<https://bsol.bsigroup.com/PdfViewer/Viewer?pid=000000000030292049>
- [49] F. Shang, K.X. Li, X.Y. Zhang, Y. Gao, Effect of Fine Aggregate on Properties of Asphalt Mixture, Key Eng Mater 599 (2014) 115–119.
<https://doi.org/https://doi.org/10.4028/www.scientific.net/KEM.599.115>.
- [50] B.D. Prowell, J. Zhang, E.R. Brown, Aggregate Properties and the Performance of Superpave- Designed Hot Mix Asphalt, Transportation Research Board, 2005. <https://doi.org/10.17226/13844>.
- [51] A.M. Alnadish, N.S.S. Singh, A.M. Alawag, Applications of Synthetic, Natural, and Waste Fibers in Asphalt Mixtures: A Citation-Based Review, Polymers (Basel) 15 (2023).
<https://doi.org/10.3390/polym15041004>.
- [52] L.G. Picado-Santos, S.D. Capitão, J.M.C. Neves, Crumb rubber asphalt mixtures: A literature review, Constr Build Mater 247 (2020).
<https://doi.org/10.1016/j.conbuildmat.2020.118577>.
- [53] E. Turbay, G. Martinez-Arguelles, T. Navarro-Donado, E. Sánchez-Cotte, R. Polo-Mendoza, E. Covilla-Valera, Rheological Behaviour of

WMA-Modified Asphalt Binders with Crumb Rubber, Polymers (Basel) 14 (2022). <https://doi.org/10.3390/polym14194148>.

- [54] D. Lo Presti, Recycled Tyre Rubber Modified Bitumens for road asphalt mixtures: A literature review, *Constr Build Mater* 49 (2013) 863–881. <https://doi.org/10.1016/j.conbuildmat.2013.09.007>.
- [55] Q. Liu, S. Varamini, S. Tighe, Field evaluation of red-coloured Hot Mix Asphalt pavements for bus rapid transit lanes in Ontario, Canada, *Coatings* 7 (2017). <https://doi.org/10.3390/coatings7050058>.
- [56] M. Pasetto, A. Baliello, G. Giacomello, E. Pasquini, Aesthetic and Mechanical Suitability of a Clear Synthetic Resin as a Unconventional Binder for Road Pavements, *Advances in Materials Science and Engineering* 2019 (2019). <https://doi.org/10.1155/2019/8643608>.
- [57] K. Kawther, Colored asphalt and street print are decorating paving in public spaces, in: *MATEC Web of Conferences*, EDP Sciences, 2018. <https://doi.org/10.1051/mateconf/201816205027>.
- [58] P. Cui, Y. Xiao, B. Yan, M. Li, S. Wu, Morphological characteristics of aggregates and their influence on the performance of asphalt mixture, *Constr Build Mater* 186 (2018) 303–312. <https://doi.org/10.1016/j.conbuildmat.2018.07.124>.
- [59] I.S. Bessa, V.T.F.C. Branco, J.B. Soares, J.A.N. Neto, Aggregate shape properties and their influence on the behavior of Hot-Mix Asphalt, *Journal of Materials in Civil Engineering* 27 (2015). [https://doi.org/10.1061/\(asce\)mt.1943-5533.0001181](https://doi.org/10.1061/(asce)mt.1943-5533.0001181).
- [60] Y. Kim, L.T. Souza, Effects of Aggregate Angularity on Mix Design Characteristics and Pavement Performance, 2009. <https://rosap.ntl.bts.gov/view/dot/25454>.
- [61] B.I. Siswosoebrotho, K. Ginting, T.L. Soedirdjo, Workability and resilient modulus of asphalt concrete mixtures containing flaky aggregates shape, *Eastern Asia Studies Transportation Society* 6 (2005) 1302–1312. <https://doi.org/10.11175/EASTS.6.1302>.
- [62] P. Polaczyk, X. Shu, H. Gong, B. Huang, Influence of aggregates angularity on the locking point of asphalt mixtures, *Road Materials and Pavement Design* 20 (2019) S183–S195. <https://doi.org/10.1080/14680629.2019.1588151>.
- [63] British Standards Institution, PD 6691:2022, Guidance on the use of BS EN 13108, Bituminous mixtures, (2022). <https://knowledge.bsigroup.com/products/guidance-on-the-use-of-bs-en-13108-bituminous-mixtures-1?version=standard>.
- [64] F.C.G. Martinho, L.G. Picado-Santos, S.D. Capitão, Feasibility assessment of the use of recycled aggregates for asphalt mixtures, *Sustainability* (Switzerland) 10 (2018). <https://doi.org/10.3390/su10061737>.
- [65] ASTM International, ASTM C136 / C136M - 19: Standard Test Method for Sieve Analysis of Fine and Coarse Aggregates, (2019). <https://cdn.standards.iteh.ai/samples/105288/cc00c2991f694b6f9ef2c7006d7e79df/ASTM-C136-C136M-19.pdf>.

- [66] The Concrete Countertop Institute, The Role of Aggregate in Concrete Countertop Mix Designs, (2024). <https://concretecountertopinstitute.com/free-training/the-role-of-aggregate-in-concrete-countertop-mix-designs/>.
- [67] K.D. Hall, S.G. Williams, Superpave Mix Designs for Arkansas - Final Report (TRC9604), Arkansas, 1998. https://www.ardot.gov/wp-content/uploads/2021/01/TRC9604_Superpave_Mix_Designs_for_Arkansas.pdf.
- [68] R.J. Cominsky, G.A. Huber, T.W. Kennedy, Michael. Anderson, University of Texas at Austin., Heritage Research Group., Asphalt Institute., Strategic Highway Research Program (U.S.), The Superpave mix design manual for new construction and overlays, Strategic Highway Research Program, 1994. <https://trid.trb.org/view/404930>.
- [69] F.L. Roberts, P.S. Kandhal, E.R. Brown, D.-Y. Lee, T.W. Kennedy, Hot mix asphalt materials, mixture design, and construction. Second edition, Lanham, Md : NAPA Educational Foundation, Lanham, Md, 1991. <https://trid.trb.org/View/473852>.
- [70] H. Liu, P. Hao, J. Xu, Effects of nominal maximum aggregate size on the performance of stone matrix asphalt, Applied Sciences (Switzerland) 7 (2017). <https://doi.org/10.3390/app7020126>.
- [71] H. Al-Mosawe, N. Thom, G. Airey, A. Ai-Bayati, Effect of aggregate gradation on the stiffness of asphalt mixtures, (2015). <https://doi.org/10.1515/ijpeat-2015-0008>.
- [72] Z. Wei, K. Hou, Y. Jia, S. Wang, Y. Li, Z. Chen, Z. Zhou, Y. Gao, Impact of aggregate gradation and asphalt-aggregate ratio on pavement performance during construction using back propagation neural network, Autom Constr 165 (2024). <https://doi.org/10.1016/j.autcon.2024.105569>.
- [73] E. Kearsley, Aggregates in concrete, South African Institution Of Civil Engineering (SAICE) 2006 (2006) 28. <https://www.proquest.com/trade-journals/aggregates-concrete/docview/221158270/se-2>.
- [74] D.M. Kusumawardani, Y.D. Wong, The influence of aggregate shape properties on aggregate packing in porous asphalt mixture, Constr Build Mater 255 (2020). <https://doi.org/10.1016/j.conbuildmat.2020.119379>.
- [75] D. Little, B. Joe, J. Priyantha, S. Mansour, H. Barry, Quantify shape, angularity and surface texture of aggregates using image analysis and study their effect on performance, Texas, 2003. <https://static.tti.tamu.edu/tti.tamu.edu/documents/0-1707-4.pdf?referer=www.clickfind.com.au>.
- [76] B. Sengoz, A. Onori, A. Topal, Effect of aggregate shape on the surface properties of flexible pavement, KSCE Journal of Civil Engineering 18 (2014) 1364–1371. <https://doi.org/10.1007/s12205-014-0516-0>.
- [77] H.M.Z. Hassan, K. Wu, W. Huang, S. Chen, Q. Zhang, J. Xie, X. Cai, Study on the influence of aggregate strength and shape on the performance of asphalt mixture, Constr Build Mater 294 (2021). <https://doi.org/10.1016/j.conbuildmat.2021.123599>.

- [78] S. Arasan, E. Yenera, F. Hattatoglu, S. Hınıslioglu, S. Akbuluta, Correlation between shape of aggregate and mechanical properties of asphalt concrete: Digital image processing approach, *Road Materials and Pavement Design* 12 (2011) 239–262. <https://doi.org/10.3166/rmpd.12.239-262>.
- [79] T. Ferreira, W. Rasband, ImageJ User Guide – IJ1.46r, (2012). <https://imagej.net/ij/docs/guide/user-guide.pdf>.
- [80] The Constructor, Classification of aggregates as per size and shape - coarse and fine aggregates, (2009). <https://theconstructor.org/building/classification-of-aggregates-size-shape/12339/>.
- [81] S. Tafesse, J.M. Robison Fernlund, W. Sun, F. Bergholm, Evaluation of image analysis methods used for quantification of particle angularity, *Sedimentology* 60 (2013) 1100–1110. <https://doi.org/10.1111/j.1365-3091.2012.01367.x>.
- [82] British Standard Institution, BS EN 933-3:2012, Tests for geometrical properties of aggregates - Determination of particle shape. Flakiness index, (2012). <https://knowledge.bsigroup.com/products/tests-for-geometrical-properties-of-aggregates-determination-of-particle-shape-flakiness-index-1?version=standard>.
- [83] C.F. Mora, A.K.H. Kwan, Sphericity, shape factor, and convexity measurement of coarse aggregate for concrete using digital image processing, *Cem Concr Res* 30 (2000) 351–358. [https://doi.org/10.1016/S0008-8846\(99\)00259-8](https://doi.org/10.1016/S0008-8846(99)00259-8).
- [84] Microtrac Retsch GmbH, CAMSIZER 3D - Particle size and shape analyzer, (2013). <https://www.microtrac.com/products/particle-size-shape-analysis/dynamic-image-analysis/camsizer-3d/downloads/>.
- [85] M. Moaveni, E. Mahmoud, E.M. Ortiz, E. Tutumluer, S. Beshears, Use of advanced aggregate imaging systems to evaluate aggregate resistance to breakage, abrasion, and polishing, *Transp Res Rec* (2014) 1–10. <https://doi.org/10.3141/2401-01>.
- [86] E.J. Garboczi, J.W. Bullard, 3D analytical mathematical models of random star-shape particles via a combination of X-ray computed microtomography and spherical harmonic analysis, *Advanced Powder Technology* 28 (2017) 325–339. <https://doi.org/10.1016/j.appt.2016.10.014>.
- [87] D. Asahina, M.A. Taylor, Geometry of irregular particles: Direct surface measurements by 3-D laser scanner, *Powder Technol* 213 (2011) 70–78. <https://doi.org/10.1016/j.powtec.2011.07.008>.
- [88] J. Brocher, Mutterer, biovoxxel/BioVoxxel-Figure-Tools: BioVoxxel Figure Tools - v4.0.0 (bvft-4.0.0). Zenodo, (2024). <https://doi.org/10.5281/zenodo.14284229>.
- [89] E.A. Masad, Aggregate Imaging Systems (AIMS): Basics and Applications (FHWA/TX-05/5-1707-01-1), 2004. <https://static.tti.tamu.edu/tti.tamu.edu/documents/5-1707-01-1.pdf>.
- [90] C. Rao, E. Tutumluer, J.A. Stefanski, Coarse Aggregate Shape and Size Properties Using a New Image Analyzer, 29 (2001) 461–471.

<https://experts.illinois.edu/en/publications/coarse-aggregate-shape-and-size-properties-using-a-new-image-anal>.

- [91] E. Tutumluer, T. Pan, Imaging based size, gradation and shape characterizations of aggregate particles used in road pavements, (2006). <https://experts.illinois.edu/en/publications/imaging-based-size-gradation-and-shape-characterizations-of-aggre>.
- [92] H. Qi Vue, I. Morin, Digital image processing for aggregate orientation in asphalt concrete mixtures, 1996. <http://laws.justice.gc.ca/en/showtdm/cs/C-42><http://lois.justice.gc.ca/fr/showtdm/cs/C-42>.
- [93] Y. Descantes, Y. Fosse, G. Ehret, Automated measurement of aggregate properties: Part 1 - Crushed and broken surfaces in coarse aggregate particles, Materials and Structures/Materiaux et Constructions 39 (2006) 3–12. <https://doi.org/10.1617/s11527-005-9001-z>.
- [94] W.S.tyler, What is a Computerized Particle Analyzer?, (2019). <https://blog.wstyler.com/cpa/what-is-a-computerized-particle-analyzer>.
- [95] British Standard Institution, BS ISO 13322-2:2021. Particle size analysis. Image analysis methods - Dynamic image analysis methods, (2022). <https://knowledge.bsigroup.com/products/particle-size-analysis-image-analysis-methods-dynamic-image-analysis-methods-1?version=standard>.
- [96] R.N. Hunter, A. Self, J. Read, Shell Bitumen Handbook (6th Edition), in: ICE Publishing, 2015. <https://app.knovel.com/hotlink/pdf/id:kt00UBCM81/shell-bitumen-handbook/introduction>.
- [97] M. Ronald, F.P. Luis, Asphalt emulsions formulation: State-of-the-art and dependency of formulation on emulsions properties, Constr Build Mater 123 (2016) 162–173. <https://doi.org/10.1016/j.conbuildmat.2016.06.129>.
- [98] A. Al-mohammedawi, K. Mollenhauer, Current Research and Challenges in Bitumen Emulsion Manufacturing and Its Properties, Materials 15 (2022). <https://doi.org/10.3390/ma15062026>.
- [99] J. Zhu, B. Birgisson, N. Kringos, Polymer modification of bitumen: Advances and challenges, Eur Polym J 54 (2014) 18–38. <https://doi.org/10.1016/j.eurpolymj.2014.02.005>.
- [100] M. Enieb, L. Shbeeb, I. Asi, X. Yang, A. Diab, Effect of Asphalt Grade and Polymer Type (SBS and EE-2) on Produced PMB and Asphalt Concrete Mix Properties, Journal of Materials in Civil Engineering 32 (2020). [https://doi.org/10.1061/\(asce\)mt.1943-5533.0003479](https://doi.org/10.1061/(asce)mt.1943-5533.0003479).
- [101] J. Pais, C.R. Santos, M. Cabette, L. Hilliou, J. Ribeiro, H. Wang, M.R. Mohd Hasan, Feasibility of using bio-oil from biodiesel production for bio-bitumen creation, Road Materials and Pavement Design 24 (2023) 209–228. <https://doi.org/10.1080/14680629.2023.2180305>.
- [102] Z. Sun, J. Yi, D. Feng, C. Kasbergen, A. Scarpas, Y. Zhu, Preparation of bio-bitumen by bio-oil based on free radical polymerization and

production process optimization, *J Clean Prod* 189 (2018) 21–29.
<https://doi.org/10.1016/j.jclepro.2018.04.060>.

- [103] R. Penki, S.K. Rout, Next-generation bitumen: a review on challenges and recent developments in bio-bitumen preparation and usage, *Biomass Convers Biorefin* 13 (2023) 9583–9600.
<https://doi.org/10.1007/s13399-021-01803-4>.
- [104] G.G. Al-Khateeb, S.A. Alattieh, W. Zeiada, C. Castorena, State-of-the-Art Review on the Behavior of Bio-Asphalt Binders and Mixtures, *Molecules* 29 (2024). <https://doi.org/10.3390/molecules29163835>.
- [105] J. Zhu, A. Ahmed, Y. Dinegdae, X. Lu, P. Witkiewicz, E. Gardner, K. Olsson, R. Nilsson, Durability assessment of bio-extended bituminous binders by rheological characterisation after long-term ageing, *Molecules* 29 (2024).
<https://doi.org/10.3390/molecules29163835AcademicEditors:Pietro>.
- [106] A. Vaitkus, D. Čygas, A. Laurinavičius, Z. Perveneckas, Analysis and evaluation of possibilities for the use of warm mix asphalt in lithuania, *Baltic Journal of Road and Bridge Engineering* 4 (2009) 80–86.
<https://doi.org/10.3846/1822-427X.2009.4.80-86>.
- [107] J. Chehovits, L. Galehouse, Energy Usage and Greenhouse Gas Emissions of Pavement Preservation Processes for Asphalt Concrete Pavements, *Compendium of Papers from the First International Conference on Pavement Preservation* (2010).
<https://trid.trb.org/View/919015>.
- [108] P. Dorchies, *Environmental Road of the Future: Analysis of Energy Consumption and Greenhouse Gas Emissions*, 2005.
<https://api.semanticscholar.org/CorpusID:106987869>.
- [109] M.M.E. Zumrawi, S.A.S. Edrees, Comparison of Marshall and Superpave asphalt design methods for Sudan pavement mixes, *International Journal of Scientific and Technical Advancements* 2 (2016) 29–35. <https://www.ijsta.com/papers/ijstav2n1y16/IJSTA-V2N1R14Y16.pdf>.
- [110] F.N. Hveem, Pavement Deflections and Fatigue Failures, *Highway Research Board Bulletin* 114 (1995) 43–87.
<https://onlinepubs.trb.org/Onlinepubs/hrbbulletin/114/114-004.pdf>.
- [111] M. Bulevičius, K. Petkevičius, S. Čirba, The influence of geometric parameters on strength properties of the aggregates used to produce asphalt mixtures, *Journal of Civil Engineering and Management* 19 (2013) 894–902. <https://doi.org/10.3846/13923730.2013.858645>.
- [112] B.D. Prowell, J. Zhang, E.R. Brown, Aggregate Properties and the Performance of Superpave- Designed Hot Mix Asphalt, *Transportation Research Board*, 2005. <https://doi.org/10.17226/13844>.
- [113] J.S. Lee, S.Y. Lee, T.H.M. Le, Developing Performance-Based Mix Design Framework Using Asphalt Mixture Performance Tester and Mechanistic Models, *Polymers (Basel)* 15 (2023).
<https://doi.org/10.3390/polym15071692>.
- [114] W. Li, W. Cao, X. Ren, S. Lou, S. Liu, J. Zhang, Impacts of aggregate gradation on the volumetric parameters and rutting performance of

asphalt concrete mixtures, *Materials* 15 (2022).
<https://doi.org/10.3390/ma15144866>.

- [115] British Standards Institution, BS EN 12697-22:2020, Bituminous mixtures - Test methods - Part 22: Wheel tracking, (2020).
<https://bsol.bsigroup.com/PdfViewer/Viewer?pid=000000000030371556>
- [116] T. Bennert, Dynamic Modulus of Hot Mix Asphalt, 2009.
https://rosap.ntl.bts.gov/view/dot/17674/dot_17674_DS1.pdf.
- [117] M. Saghafi, S. Nazarian, I. Abdallah, C. Tirado, D. Rodriguez, Harmonizing Flexible Pavement Rutting Design with Balanced Mix Design, in: *Transp Res Rec*, SAGE Publications Ltd, 2022: pp. 823–836. <https://doi.org/10.1177/03611981221082557>.
- [118] British Standards Institution, BS EN 12697-23:2017. Bituminous mixtures. Test methods - Determination of the indirect tensile strength of bituminous specimens, 2017.
<https://knowledge.bsigroup.com/products/bituminous-mixtures-test-methods-determination-of-the-indirect-tensile-strength-of-bituminous-specimens?version=tracked&tab=overview>.
- [119] P. Pereira, J. Pais, Main flexible pavement and mix design methods in Europe and challenges for the development of an European method, *Journal of Traffic and Transportation Engineering (English Edition)* 4 (2017) 316–346. <https://doi.org/10.1016/j.jtte.2017.06.001>.
- [120] J.F. Corte, J.P. Serfass, The French Approach to Asphalt Mixture Design: A Performance-Related System of Specifications, *Transp Res Rec* 69 (2000) 794–834. <https://trid.trb.org/View/1160128>.
- [121] British Standards Institution, BS EN 13108-1:2016, Bituminous mixtures - Material specifications - Part 1: Asphalt Concrete, (2020).
<https://bsol.bsigroup.com/PdfViewer/Viewer?pid=000000000030410633>
- [122] Main Roads Western Australia, Specification 504: Asphalt Wearing Course, 2022.
<https://www.mainroads.wa.gov.au/globalassets/technical-commercial/technical-library/specifications/500-series-pavements/specification-504-asphalt-wearing-course.pdf>.
- [123] British Standards Institution, BS EN 12697-34:2020, Bituminous mixtures - Test methods, Part 34: Marshall test, (2020).
<https://bsol.bsigroup.com/PdfViewer/Viewer?pid=000000000030382720>
- [124] British Standard Institution, BS EN 12697-24, Bituminous mixtures, Test methods, Resistance to fatigue, 2018.
<https://doi.org/10.3403/30330768U>.
- [125] British Standard Institution, BS EN 12697-6:2020, Bituminous mixtures - Test methods, Determination of bulk density of bituminous specimens, (2020).
<https://bsol.bsigroup.com/PdfViewer/Viewer?pid=000000000030382726>
- [126] M.J. McHale, A. Ferguson, M. Gordon, Use of digital technology to improve the way asphalt roads are constructed, *Proceedings of the Institution of Civil Engineers: Municipal Engineer* 176 (2023) 189–195.
<https://doi.org/10.1680/jmuen.23.00005>.

- [127] M.A. Talaghat, A. Golroo, A. Kharbouch, M. Rasti, R. Heikkilä, R. Jurva, Digital twin technology for road pavement, *Autom Constr* 168 (2024). <https://doi.org/10.1016/j.autcon.2024.105826>.
- [128] M. Uaissova, B. Zharlykassov, Application of AI Techniques for Asphalt Concrete Mix Production Optimization, *Journal European Des Systemes Automatisees* 57 (2024) 353–361. <https://doi.org/10.18280/jesa.570205>.
- [129] J. Liu, F. Liu, L. Wang, Automated, economical, and environmentally-friendly asphalt mix design based on machine learning and multi-objective grey wolf optimization, *Journal of Traffic and Transportation Engineering (English Edition)* 11 (2024) 381–405. <https://doi.org/10.1016/j.jtte.2023.10.002>.
- [130] R. Botella, Sustainable Pavement Materials and Technology, *Sustainability (Switzerland)* 14 (2022). <https://doi.org/10.3390/su14116605>.
- [131] N. Poeran, B. Sluer, Workability of asphalt mixtures, in: 6th Eurasphalt & Eurobitume Congress, Prague, 2016. <https://doi.org/10.14311/ee.2016.057>.
- [132] M.J. Gudimettla, L.A.Jr. Cooley, E.R. Brown, Workability of Hot Mix Asphalt, Auburn, 2003. <https://rosap.nhl.bts.gov/view/dot/16069/Share>.
- [133] B.I. Siswosoebrotho, K. Ginting, T.L. Soedirdjo, Workability and resilient modulus of asphalt concrete, *Eastern Asia Studies Transportation Society* 6 (2005) 1302–1312. <https://doi.org/10.11175/EASTS.6.1302>.
- [134] S. Dessouky, A. Pothuganti, L.F. Walubita, D. Rand, Laboratory Evaluation of the Workability and Compactability of Asphaltic Materials prior to Road Construction, *Journal of Materials in Civil Engineering* 25 (2013) 810–818. [https://doi.org/10.1061/\(asce\)mt.1943-5533.0000551](https://doi.org/10.1061/(asce)mt.1943-5533.0000551).
- [135] J. Huang, G.S. Kumar, Y. Sun, Evaluation of workability and mechanical properties of asphalt binder and mixture modified with waste toner, *Constr Build Mater* 276 (2021) 122230. <https://doi.org/10.1016/j.conbuildmat.2020.122230>.
- [136] M. Wróbel, A. Woszek, W. Franus, Laboratory methods for assessing the influence of improper asphalt mix compaction on its performance, *Materials* 13 (2020). <https://doi.org/10.3390/ma13112476>.
- [137] R.N. Dongre, E. Morari, Development of a simple test to determine workability and field compaction temperatures of asphalt concrete, in: TRB 2013 Annual Meeting Compendium of Papers, 2013. <https://trid.trb.org/view/1242664>.
- [138] M. Sukhija, V.P. Wagh, N. Saboo, Development of workability based approach for assessment of production temperatures of warm mix asphalt mixtures, *Constr Build Mater* 305 (2021) 124808. <https://doi.org/10.1016/j.conbuildmat.2021.124808>.
- [139] H. Yu, Z. Leng, Z. Dong, Z. Tan, F. Guo, J. Yan, Workability and mechanical property characterization of asphalt rubber mixtures modified with various warm mix asphalt additives, *Constr Build Mater* 175 (2018) 392–401. <https://doi.org/10.1016/j.conbuildmat.2018.04.218>.

- [140] C. Wang, P. Hao, F. Ruan, X. Zhang, S. Adhikari, Determination of the production temperature of warm mix asphalt by workability test, *Constr Build Mater* 48 (2013) 1165–1170.
<https://doi.org/10.1016/j.conbuildmat.2013.07.097>.
- [141] A. Diab, Z. You, A bitumen-based prototype to predict the workability of asphalt concrete mixtures, in: *International Congress and Exhibition "Sustainable Civil Infrastructures: Innovative Infrastructure Geotechnology*, 2018. https://doi.org/10.1007/978-3-319-61908-8_2.
- [142] M. Haft-Javaherian, Virtual Microstructure Generation of Asphaltic Mixtures, (2011) 1–52.
<https://api.semanticscholar.org/CorpusID:17026240>.
- [143] A. Chiarelli, A.R. Dawson, A. García, Stochastic generation of virtual air pores in granular materials, *Granul Matter* 17 (2015) 617–627.
<https://doi.org/10.1007/s10035-015-0585-x>.
- [144] M. Aboufoul, A. Chiarelli, I. Triguero, A. Garcia, Virtual porous materials to predict the air void topology and hydraulic conductivity of asphalt roads, *Powder Technol* 352 (2019) 294–304.
<https://doi.org/10.1016/j.powtec.2019.04.072>.
- [145] J. Wimmer, B. Stier, J.W. Simon, S. Reese, Computational homogenisation from a 3D finite element model of asphalt concrete - Linear elastic computations, *Finite Elements in Analysis and Design* 110 (2016) 43–57. <https://doi.org/10.1016/j.finel.2015.10.005>.
- [146] R. Bayat, S. Talatahari, A.H. Gandomi, M. Habibi, B. Aminnejad, Artificial Neural Networks for Flexible Pavement, *Information (Switzerland)* 14 (2023). <https://doi.org/10.3390/info14020062>.
- [147] M. Miani, M. Dunnhofer, F. Rondinella, E. Manthos, J. Valentin, C. Micheloni, N. Baldo, Bituminous mixtures experimental data modeling using a hyperparameters-optimized machine learning approach, *Applied Sciences (Switzerland)* 11 (2021).
<https://doi.org/10.3390/app112411710>.
- [148] S. Busang, J. Maina, Influence of aggregates properties on microstructural properties and mechanical performance of asphalt mixtures, *Constr Build Mater* 318 (2022).
<https://doi.org/10.1016/j.conbuildmat.2021.126002>.
- [149] AASHTO, Guide for Design of Pavement Structures, (1993).
https://www.academia.edu/8963834/AASHTO_Guide_for_Design_of_Pavement_Structures_1993.
- [150] Federal Highway Administration, Mechanistic Empirical Pavement Design Guide, Highway Materials Engineering Course, 2004.
https://www.fhwa.dot.gov/pavement/materials/hmec/pubs/module_e/participant_workbook.pdf.
- [151] L. Ziliute, A. Laurinavicius, A. Vaitkus, The defects of asphalt pavements and their impact to driving quality in Vilnius city streets, 7th International Conference on Environmental Engineering, ICEE 2008 - Conference Proceedings (2008) 1247–1252.
<https://doi.org/000257946100189>.

- [152] J.B. Odoki, H.G.R. Kerali, Analytical Framework and Model Descriptions: Highway Development and Management, 4th ed., 2000. <https://library.ctr.utexas.edu/Presto/content/Detail.aspx?ctlID=UHVibGljYXRpb25fMTE2MTA%3D&rlID=MTI1ODU%3D&ssid=c2NyZWVuSURfMTQ2MDk%3D&bmdc=MQ==>.
- [153] G. Morosiuk, Mike J Riley, J.B. Odoki, Modelling road deterioration and works effects in HDM-4, in: The Highway Development and Management Series Vol.6, Version 2, World Road Association (PIARC), Paris, France, 2000. <http://worldcat.org/isbn/2840601036>.
- [154] C.R. Bennett, W.D.O. Paterson, Guidelines on Calibration and Adaptation of HDM-4, 2019. <http://lpcb.org/index.php/document-library/hdm-4/calibration/2000-guidelines-on-calibration-and-adaptation-of-hdm-4>.
- [155] Q. Yang, Y. Deng, Evaluation of cracking in asphalt pavement with stabilized base course based on statistical pattern recognition, International Journal of Pavement Engineering 20 (2019) 417–424. <https://doi.org/10.1080/10298436.2017.1299528>.
- [156] H.J. Park, M. Eslaminia, Y.R. Kim, Mechanistic evaluation of cracking in in-service asphalt pavements, Materials and Structures/Materiaux et Constructions 47 (2014) 1339–1358. <https://doi.org/10.1617/s11527-014-0307-6>.
- [157] Y. Miao, T.G. He, Q. Yang, J.J. Zheng, Multi-domain hybrid boundary node method for evaluating top-down crack in Asphalt pavements, Eng Anal Bound Elem 34 (2010) 755–760. <https://doi.org/10.1016/j.enganabound.2010.04.002>.
- [158] S. Reay, M. Appleyard, T. Van Dam, L. Sandberg, Sealing and filling of cracks for bituminous concrete pavements selection and installation procedures, 1999. <https://trid.trb.org/View/1211216>.
- [159] D.S. Decker, Best practices for crack treatments in asphalt pavements, in: 6th Eurasphalt & Eurobitume Congress, Prague, Czech Republic, 2016. <https://doi.org/dx.doi.org/10.14311/EE.2016.045>.
- [160] Y. Hou, L. Wang, P. Yue, W. Sun, Fracture failure in crack interaction of asphalt binder by using a phase field approach, Materials and Structures/Materiaux et Constructions 48 (2015) 2997–3008. <https://doi.org/10.1617/s11527-014-0372-x>.
- [161] J. Zhang, G.D. Airey, J.R.A. Grenfell, Experimental evaluation of cohesive and adhesive bond strength and fracture energy of bitumen-aggregate systems, Materials and Structures/Materiaux et Constructions 49 (2016) 2653–2667. <https://doi.org/10.1617/s11527-015-0674-7>.
- [162] M. Mubarak, Highway subsurface assessment using pavement surface distress and roughness data, International Journal of Pavement Research and Technology 9 (2016) 393–402. <https://doi.org/10.1016/j.ijprt.2016.10.001>.
- [163] K. Smith, D. Peshkin, Pavement Preservation on High-Traffic-Volume Roadways, Transportation Research Record: Journal of the Transportation Research Board 2235 (2011) 54–65. <https://doi.org/10.3141/2235-07>.

- [164] G. Rohde, F. Jooste, E. Sadzik, T. Henning, The calibration and use of HDM-IV performance models in a pavement management system, (2020). <https://trid.trb.org/View/659194>.
- [165] H.U. Bahia, D.I. Hanson, M. Zeng, H. Zhai, M.A. Khatri, R.M. Anderson, L.A. Cooley, K.L. Williams, M. Buncher, M. Anderson, MS-2 7 th Edition Asphalt Mix Design Methods, 2009. <http://www.asfaltotecnica.cl/documentos/MANUEL>.
- [166] D. Beer, C. Fisher, F.J. Jooste, Determination of Pneumatic Tyre-Pavement Interface Contact Stresses under Moving Loads and some Effects on Pavements with Thin Asphalt Surfacing Layers, 8th International Conference on Asphalt Pavements 1 (1997) 179–227. <https://trid.trb.org/view/501629>.
- [167] L.B. Wang, L.A. Myers, L.N. Mohammad, Y.R. Fu, Micromechanics Study on Top-Down Cracking, Transp Res Rec (2003) 121–133. <https://doi.org/10.3141/1853-14>.
- [168] E. Freitas, P. Pereira, Assessment of Top-Down Cracking Causes in Asphalt Pavements, 3rd International Symposium on Maintenance and Rehabilitation of Pavements and Technological Control (2003) 555–564. <https://trid.trb.org/view/684856>.
- [169] S.M.J.G. Erkens, J. Moraal, Cracking in asphalt concrete, Heron 41 (1996) 53–70. <https://heronjournal.nl/41-1/4.pdf>.
- [170] N. Sudarsanan, R. Karpurapu, Reflection Cracking: A Review on the Potential of Interlayer System with reference to Natural Fibres, (2014). <https://doi.org/10.13140/2.1.2020.2245>.
- [171] M. Halle, T. Rukavina, J. Domitrovic, Influence of temperature on asphalt stiffness modulus, 5th Eurasphalt & Eurobitume Congress, 13-15th June 2012, Istanbul (2012) 13–15. <https://www.h-a-d.hr/pubfile.php?id=553>.
- [172] AASHTO, Flexible Pavement Materials Program - crack sealing, crack filling & joint sealing of flexible & rigid pavements, 2003. <https://transportation.org/technical-training-solutions/wp-content/uploads/sites/64/2023/02/AT-TC3PP005-16-T1-JA011.pdf>.
- [173] S. Yin, H. Peng, G.A. Interlayers, Effect of interlayer bonding quality of asphalt layers on pavement performance Effect of interlayer bonding quality of asphalt layers on pavement performance, (2017). <https://doi.org/10.1088/1757-899X/236/1/012005>.
- [174] G. Elnashar, R.B. Bhat, R. Sedaghati, Modeling pavement damage and predicting fatigue cracking of flexible pavements based on a combination of deterministic method with stochastic approach using Miner's hypothesis, SN Appl Sci 1 (2019) 1–9. <https://doi.org/10.1007/s42452-019-0238-5>.
- [175] N. Attoh-Okine, O. Adarkwa, Pavement Condition Surveys-Overview of Current Practices, 2013. <https://cpb-us-w2.wpmucdn.com/sites.udel.edu/dist/1/1139/files/2013/10/Rpt-245-Pavement-Condition-Okine-DCTR422232-1pzk0uz.pdf>.

- [176] S. Chambon, J.M. Moliard, Automatic road pavement assessment with image processing: Review and comparison, *International Journal of Geophysics* 2011 (2011). <https://doi.org/10.1155/2011/989354>.
- [177] Y. Zhou, X. Guo, F. Hou, J. Wu, Review of Intelligent Road Defects Detection Technology, *Sustainability (Switzerland)* 14 (2022). <https://doi.org/10.3390/su14106306>.
- [178] K. Jeyapalan, J.K. Cable, R. Welper, Iowa DOT Evaluation of the PASCO Road Survey System, 1987. <https://publications.iowa.gov/id/eprint/19733>.
- [179] FHWA, Distress Identification Manual for the Long-Term Pavement Performance Program, 2014. <https://highways.dot.gov/media/4421>.
- [180] J.S. Miller, W.Y. Bellinger, FHWA, Distress Identification manual for the Long-Term Pavement Performance Program. Report FHWA-HRT-13-092, Federal Highway Administration (2014) 142. <https://highways.dot.gov/media/4421>.
- [181] Federal Highway Administration, Pavement distress identification manual for the NPS Road Inventory, (2009). <https://docplayer.net/38333950-Pavement-distress-identification-manual.html>.
- [182] F. Li, J. Feng, Y. Li, S. Zhou, Crack Filling and Crack Seal Band, in: F. Li, J. Feng, Y. Li, S. Zhou (Eds.), *Preventive Maintenance Technology for Asphalt Pavement*, Springer Singapore, Singapore, 2021: pp. 55–71. https://doi.org/10.1007/978-981-15-6206-8_3.
- [183] D. Ghosh, M. Turos, M. Hartman, R. Milavitz, J.-L. Le, M. Marasteanu, Pothole Prevention and Innovative Repair, Final Report CTS #2016007, Minnesota Local Road Research Board, Minnesota Department of Transportation, St-Paul, Minnesota (2018). <https://api.semanticscholar.org/CorpusID:186266108>.
- [184] S.R. White, N.R. Sottos, P.H. Geubelle, J.S. Moore, M.R. Kessler, S.R. Sriram, E.N. Brown, S. Viswanathan, Autonomic healing of polymer composites, *Nature* 409 (2001) 794–797. <https://doi.org/10.1038/35057232>.
- [185] K.L. Smith, R.A. Romine, Materials and Procedures for Sealing and Filling Cracks in Asphalt-Surfaced Pavements (FHWA-RD-99-147), (2001) 85 p. <http://www.fhwa.dot.gov/publications/research/infrastructure/pavements/ltp/99168/99168.pdf>.
- [186] F. Li, T. Li, Field investigation and laboratory evaluation of asphalt pavement crack seal band, *J Test Eval* 43 (2015) 123–132. <https://doi.org/10.1520/JTE20130196>.
- [187] Á. García, Self-healing of open cracks in asphalt mastic, *Fuel* 93 (2012) 264–272. <https://doi.org/10.1016/j.fuel.2011.09.009>.
- [188] M. Riara, P. Tang, L. Mo, M. Chen, J. Zhang, S. Wu, Experimental assessment of the long-time crack healing in asphalt mixtures using healing agents, *Constr Build Mater* 191 (2018) 411–422. <https://doi.org/10.1016/j.conbuildmat.2018.10.001>.

- [189] D. Grossegger, B. Gomez-Meijide, S. Vansteenkiste, A. Garcia, Influence of rheological and physical bitumen properties on heat-induced self-healing of asphalt mastic beams, *Constr Build Mater* 182 (2018) 298–308. <https://doi.org/10.1016/j.conbuildmat.2018.06.148>.
- [190] J. Norambuena-Contreras, A. Garcia, Self-healing of asphalt mixture by microwave and induction heating, *Mater Des* 106 (2016) 404–414. <https://doi.org/https://doi.org/10.1016/j.matdes.2016.05.095>.
- [191] A. García, M. Bueno, J. Norambuena-Contreras, M.N. Partl, Induction healing of dense asphalt concrete, *Constr Build Mater* 49 (2013) 1–7. <https://doi.org/10.1016/j.conbuildmat.2013.07.105>.
- [192] Q. Liu, Á. García, E. Schlangen, M. Van De Ven, Induction healing of asphalt mastic and porous asphalt concrete, *Constr Build Mater* 25 (2011) 3746–3752. <https://doi.org/10.1016/j.conbuildmat.2011.04.016>.
- [193] A. Menozzi, A. Garcia, M.N. Partl, G. Tebaldi, P. Schuetz, Induction healing of fatigue damage in asphalt test samples, *Constr Build Mater* 74 (2015) 162–168. <https://doi.org/10.1016/j.conbuildmat.2014.10.034>.
- [194] B. Gómez-Meijide, H. Ajam, A. Garcia, S. Vansteenkiste, Effect of bitumen properties in the induction healing capacity of asphalt mixes, *Constr Build Mater* 190 (2018) 131–139. <https://doi.org/10.1016/j.conbuildmat.2018.09.102>.
- [195] N.A.M. Radzi, K.A. Masri, P.J. Ramadhansyah, N.E. Jasni, A.K. Arshad, J. Ahmad, N. Mashros, H. Yaacob, Stability and Resilient Modulus of Porous Asphalt Incorporating Steel Fiber, in: *IOP Conf Ser Mater Sci Eng*, Institute of Physics Publishing, 2020. <https://doi.org/10.1088/1757-899X/712/1/012027>.
- [196] H. Fang, Y. Sun, Q. Liu, B. Li, S. Wu, J. Tang, Ice melting properties of steel fiber modified asphalt mixtures with induction heating, *IOP Conf. Ser.: Mater. Sci. Eng.* 182 (2017). <https://doi.org/10.1088/1757-899X/182/1/012042>.
- [197] A. Garcia, C.J. Austin, J. Jelfs, Mechanical properties of asphalt mixture containing sunflower oil capsules, *J Clean Prod* 118 (2016) 124–132. <https://doi.org/10.1016/j.jclepro.2016.01.072>.
- [198] T. Al-Mansoori, J. Norambuena-Contreras, A. Garcia, Effect of capsule addition and healing temperature on the self-healing potential of asphalt mixtures, *Materials and Structures/Materiaux et Constructions* 51 (2018) 1–12. <https://doi.org/10.1617/s11527-018-1172-5>.
- [199] Á. García, E. Schlangen, M. Van De Ven, Properties of capsules containing rejuvenators for their use in asphalt concrete, *Fuel* 90 (2011) 583–591. <https://doi.org/10.1016/j.fuel.2010.09.033>.
- [200] T. Al-Mansoori, J. Norambuena-Contreras, R. Micaelo, A. Garcia, Self-healing of asphalt mastic by the action of polymeric capsules containing rejuvenators, *Constr Build Mater* 161 (2018) 330–339. <https://doi.org/10.1016/j.conbuildmat.2017.11.125>.
- [201] R. Micaelo, T. Al-Mansoori, A. Garcia, Study of the mechanical properties and self-healing ability of asphalt mixture containing calcium-alginate capsules, *Constr Build Mater* 123 (2016) 734–744. <https://doi.org/10.1016/j.conbuildmat.2016.07.095>.

- [202] E. Bakir, E. Yalcin, ; Mehmet Yilmaz, ; Baha, V. Kok, A. Garcia Hernandez, Effect of Using Capsules with Waste Mineral Oil on Self-Healing of Long-Term Aged Hot-Mix Asphalt, *American Society of Civil Engineers* 35 (2023). <https://doi.org/10.1061/JMCEE7.MTENG>.
- [203] S. Xu, A. García, J. Su, Q. Liu, A. Tabaković, E. Schlangen, Self-Healing Asphalt Review: From Idea to Practice, *Adv Mater Interfaces* 5 (2018) 1–21. <https://doi.org/10.1002/admi.201800536>.
- [204] M. Vila-Cortavitarte, D. Jato-Espino, D. Castro-Fresno, M. Calzada-Pérez, Self-healing capacity of asphalt mixtures including by-products both as aggregates and heating inductors, *Materials* 11 (2018). <https://doi.org/10.3390/ma11050800>.
- [205] C. Yin, H. Zhang, Y. Pan, Cracking mechanism and repair techniques of epoxy asphalt on steel bridge deck pavement, *Transp Res Rec* 2550 (2016) 123–130. <https://doi.org/10.3141/2550-16>.
- [206] Y. Huang, R.N. Bird, O. Heidrich, A review of the use of recycled solid waste materials in asphalt pavements, *Resour Conserv Recycl* 52 (2007) 58–73. <https://doi.org/10.1016/j.resconrec.2007.02.002>.
- [207] G. Winterbottom, F. Goodwin, Concrete cracks: Causes, correcting, and coating, (2019). <https://trid.trb.org/View/750168>.
- [208] V. Doychinov, M. Abdellatif, B. Kaddouh, B. Malik, G. Jackson-Mills, R. Fuentes, A. Cohn, R. Richardson, N. Chudpooti, I.D. Robertson, N. Somjit, Infrastructure Robotics Research at the University of Leeds, Research, Invention, and Innovation Congress (2019). <https://eprints.whiterose.ac.uk/152078/>.
- [209] R.J. Jackson, A. Wojcik, M. Miodownik, 3D printing of asphalt and its effect on mechanical properties, *Mater Des* 160 (2018) 468–474. <https://doi.org/10.1016/j.matdes.2018.09.030>.
- [210] J. Zhu, B. Birgisson, N. Kringos, Polymer modification of bitumen: Advances and challenges, *Eur Polym J* 54 (2014) 18–38. <https://doi.org/10.1016/j.eurpolymj.2014.02.005>.
- [211] F. Zhang, C. Hu, The research for SBS and SBR compound modified asphalts with polyphosphoric acid and sulfur, *Constr Build Mater* 43 (2013) 461–468. <https://doi.org/10.1016/j.conbuildmat.2013.03.001>.
- [212] G.D. Airey, Styrene butadiene styrene polymer modification of road bitumens, *Journal of Material Science* 39 (2004) 951–959. <https://link-springer-com.nottingham.idm.oclc.org/content/pdf/10.1023/B%3AJMSC.0000012927.00747.83.pdf>.
- [213] A. Ali, Y. Mehta, G. Shackil, Laboratory Performance Evaluation of Pavement Preservation Alternatives, 2020. <https://cait.rutgers.edu/wp-content/uploads/2019/02/cait-utc-reg-12-final.pdf>.
- [214] I. Katsamenis, M. Bimpas, E. Protopapadakis, C. Zafeiropoulos, D. Kalogeras, A. Doulamis, N. Doulamis, C.M.-P. Montoliu, Y. Handanos, F. Schmidt, L. Ott, M. Cantero, R. Lopez, Robotic Maintenance of Road Infrastructures: The HERON Project, (2022). <http://arxiv.org/abs/2205.04164>.

- [215] M.J. Mchale, J.C. Nicholls, I. Carswell, I. Carswell, TRL RN44: Best Practice guide for the selection of pothole repair options, 2016. <https://www.transport.gov.scot/media/4706/rn44-best-practice-guide-for-the-selection-of-pothole-repair-options.pdf>.
- [216] CSIR, Potholes: Technical guide to their causes, identification and repair, 2005. <https://doi.org/10.1080/17533170500406104>.
- [217] A. Abed, M. Rahman, N. Thom, D. Hargreaves, L. Li, G. Airey, Analysis and Prediction of Pothole Formation Rate Using Spatial Density Measurements and Pavement Condition Indicators, *Transp Res Rec* 2677 (2023) 651–664. <https://doi.org/10.1177/03611981231166684>.
- [218] B.P. Watson, D. Hoffmann, D.P. Roberts, Investigation of stress in a pothole in the Bushveld Complex: A case study, *The Journal of the Southern African Institute of Mining and Metallurgy* 121 (2021). <https://doi.org/10.17159/2411>.
- [219] C. Djabatey, Experimenting and modelling the role of road surface detritus in the formation of potholes, (2023). <https://eprints.nottingham.ac.uk/73466/1/ID%20-%2014343216.pdf>
- [220] LINCOLN, Pothole Fact Sheet, (2024). <https://www.lincoln.ne.gov/files/sharedassets/public/v/7/ltu/transportation/maintenance-operations/ltu-pothole-fact-sheet.pdf>.
- [221] WeatherWorks, Potholes: Everyone's Favorite in Spring, (2019). <https://weatherworksinc.com/news/why-do-potholes-form-in-spring>.
- [222] Northamptonshire County Council, Northamptonshire Highways - Categorisation of Potholes, 2013. <https://www.astonlewallsparrishcouncil.gov.uk/uploads/potholes0001.pdf>
- [223] A.K. Sarma, D. Singh, Cold Mix Asphalt Pothole Patching Material: A Review, (2019). <https://doi.org/10.13140/RG.2.2.34249.42080>.
- [224] A. Maher, N. Gucunski, W. Yanko, F. Petsi, Evaluation of Pothole Patching Materials, 2001. <https://cait.rutgers.edu/wp-content/uploads/2018/05/fhwa-nj-2001-002.pdf>.
- [225] M. Sainz, Pothole Patching: A Review on Materials and Methods, 2016. https://www.il-asphalt.org/files/2814/5589/1847/Matthew_Sainz_IAPA_Research_2016_Bradley_University.pdf.
- [226] M.Y. Karelina, A. V. Vasiliev, V. V. Guly, A. V. Podgorny, V.A. Erpulev, Robotic Systems in Road Construction, in: 2022 Systems of Signals Generating and Processing in the Field of on Board Communications, SOSG 2022 - Conference Proceedings, Institute of Electrical and Electronics Engineers Inc., 2022. <https://doi.org/10.1109/IEEECONF53456.2022.9744273>.
- [227] M.E. Torbaghan, B. Kaddouh, M. Abdellatif, N. Metje, J. Liu, R. Jackson, C.D.F. Rogers, D.N. Chapman, R. Fuentes, M. Miodownik, R. Richardson, P. Purnell, Robotic and autonomous systems for road asset management : a position paper, in: *ICE Smart Infrastructure and Construction*, ICE, 2020: pp. 83–93. <https://doi.org/https://doi.org/10.1680/jsmic.19.00008>.

- [228] Specification for the Reinstatement of Openings in Highways - Fourth edition, 2020. www.gov.uk/dftGeneralenquiries:https://forms.dft.gov.uk.
- [229] H.H. Awan, A. Hussain, M.F. Javed, Y. Qiu, R. Alrowais, A.M. Mohamed, D. Fathi, A.M. Alzahrani, Predicting Marshall Flow and Marshall Stability of Asphalt Pavements Using Multi Expression Programming, *Buildings* 12 (2022). <https://doi.org/10.3390/buildings12030314>.
- [230] M. Eskandari Torbaghan, B. Kaddouh, M. Abdellatif, N. Metje, J. Liu, R. Jackson, C.D.F. Rogers, D.N. Chapman, R. Fuentes, M. Miodownik, R. Richardson, P. Purnell, Robotic and autonomous systems for road asset management: a position paper, *Proceedings of the Institution of Civil Engineers - Smart Infrastructure and Construction* 172 (2019) 83–93. <https://doi.org/10.1680/jsmic.19.00008>.
- [231] PlanRadar, Constructing a safer future: How construction robotics can improve site safety, (2023). <https://www.planradar.com/au/construction-robotics-site-safety/>.
- [232] N. Obinnaya Chikezie Victor, Optimizing Construction Productivity Through Automation and Artificial Intelligence, *International Journal of Artificial Intelligence and Machine Learning* 3 (2023) 28–44. <https://doi.org/10.51483/ijaiml.3.2.2023.28-44>.
- [233] X. Chen, A.Y. Chang-Richards, A. Pelosi, Y. Jia, X. Shen, M.K. Siddiqui, N. Yang, Implementation of technologies in the construction industry: a systematic review, *Engineering, Construction and Architectural Management* 29 (2022) 3181–3209. <https://doi.org/10.1108/ECAM-02-2021-0172>.
- [234] A.E. Oke, J. Aliu, P. Fadamiro, P.S.J. Singh, M.S. Samsurijan, M. Yahaya, Robotics and automation for sustainable construction: microscoping the barriers to implementation, *Smart and Sustainable Built Environment* 13 (2023) 625–643. <https://doi.org/10.1108/SASBE-12-2022-0275>.
- [235] FBR, Annual Report 2024, (2024). <https://www.listcorp.com/asx/fbr/fbr-limited/news/fbr-annual-report-2024-3101629.html>.
- [236] Wienerberger, Automatization in construction, (2021). <https://www.wienerberger-building-solutions.com/Products/Wall/prefabrication-and-robotics.html>.
- [237] ROMDAS, ROMDAS guidelines: customizing a system & common configurations, (2016). <https://romdas.com/downloads/documents/How%20to%20Design%20a%20ROMDAS%20System.pdf>.
- [238] P. Vähä, T. Heikkilä, P. Kilpeläinen, M. Järviluoma, E. Gambao, Extending automation of building construction - Survey on potential sensor technologies and robotic applications, *Autom Constr* 36 (2013) 168–178. <https://doi.org/10.1016/j.autcon.2013.08.002>.
- [239] E.M. Sachs, J.S. Haggerty, M.J. Cima, P.A. Williams, Three-dimensional printing techniques, Google Patents, 1993. <https://patents.google.com/patent/US5204055A/en>.

- [240] T.D. Ngo, A. Kashani, G. Imbalzano, K.T.Q. Nguyen, D. Hui, Additive manufacturing (3D printing): A review of materials, methods, applications and challenges, *Compos B Eng* 143 (2018) 172–196. <https://doi.org/10.1016/j.compositesb.2018.02.012>.
- [241] Z. Malaeb, F. AlSakka, F. Hamzeh, 3D Concrete Printing: Machine Design, Mix Proportioning, and Mix Comparison Between Different Machine Setups, in: J.G. Sanjayan, A. Nazari, B. Nematollahi (Eds.), *3D Concrete Printing Technology*, Butterworth-Heinemann, 2019: pp. 115–136. <https://doi.org/https://doi.org/10.1016/B978-0-12-815481-6.00006-3>.
- [242] T. Salet, Z. Ahmed, F. Bos, H. Laagland, Design of a 3D printed concrete bridge by testing, *Virtual Phys Prototyp* (2018) 1–15. <https://doi.org/10.1080/17452759.2018.1476064>.
- [243] I. Hager, A. Golonka, R. Putanowicz, 3D printing of buildings and building components as the future of sustainable construction?, *Procedia Eng* 151 (2016) 292–299. <https://doi.org/10.1016/j.proeng.2016.07.357>.
- [244] X. Wang, M. Jiang, Z. Zhou, J. Gou, D. Hui, 3D printing of polymer matrix composites: A review and prospective, *Compos B Eng* 110 (2017) 442–458. <https://doi.org/10.1016/j.compositesb.2016.11.034>.
- [245] K.G. Swift, J. D. Booker, *Manufacturing Process Selection Handbook: From design to manufacture*, 1st ed., Oxford: Elsevier Science & Technology, 2013. <https://doi.org/10.1016/C2011-0-07343-X>.
- [246] I. (Ian) Gibson, *Additive manufacturing technologies* / Ian Gibson, David Rosen, Brent Stucker, Mahyar Khorasani., Third edit, Cham, Switzerland: Springer, 2021. https://ris.utwente.nl/ws/files/302088833/978_3_030_56127_7.pdf.
- [247] A. Kazemian, X. Yuan, E. Cochran, B. Khoshnevis, Cementitious materials for construction-scale 3D printing: Laboratory testing of fresh printing mixture, *Constr Build Mater* 145 (2017) 639–647. <https://doi.org/10.1016/j.conbuildmat.2017.04.015>.
- [248] A. Kampker, J. Triebs, S. Kawollek, P. Ayvaz, S. Hohenstein, Review on machine designs of material extrusion based additive manufacturing (AM) systems - Status-Quo and potential analysis for future AM systems, in: *Procedia CIRP*, Elsevier B.V., 2019: pp. 815–819. <https://doi.org/10.1016/j.procir.2019.03.205>.
- [249] J. Gonzalez-Gutierrez, S. Cano, S. Schuschnigg, C. Kukla, J. Sapkota, C. Holzer, Additive manufacturing of metallic and ceramic components by the material extrusion of highly-filled polymers: A review and future perspectives, *Materials* 11 (2018). <https://doi.org/10.3390/ma11050840>.
- [250] Y. Lyu, H. Zhao, X. Wen, L. Lin, A.K. Schlarb, X. Shi, Optimization of 3D printing parameters for high-performance biodegradable materials, *J Appl Polym Sci* 138 (2021). <https://doi.org/10.1002/app.50782>.
- [251] R. Velu, N. Vaheed, M.K. Ramachandran, F. Raspall, Experimental investigation of robotic 3D printing of high-performance thermoplastics (PEEK): a critical perspective to support automated fibre placement process, *International Journal of Advanced Manufacturing Technology* 108 (2020) 1007–1025. <https://doi.org/10.1007/s00170-019-04623-z>.

- [252] T.A. Dutra, C. Costa, J.R. Matos, B.F. Oliveira, L.M. Oliveira, C.P. Coutinho, Effects of Printing Parameters on Geometrical and Mechanical Properties of 3D-Printed High-Performance Thermoplastics, Toward the Digitalization of Power Transformers, in: American Society of Mechanical Engineers, 2022. <https://doi.org/10.1115/IAM2022-91989>.
- [253] K. Yang, J.C. Grant, P. Lamey, A. Joshi-Imre, B.R. Lund, R.A. Smaldone, W. Voit, Diels–Alder Reversible Thermoset 3D Printing: Isotropic Thermoset Polymers via Fused Filament Fabrication, *Adv Funct Mater* 27 (2017). <https://doi.org/10.1002/adfm.201700318>.
- [254] M. Gupta, 3D Printing of Metals, MDPI - Multidisciplinary Digital Publishing Institute, 2019. <https://doi.org/10.3390/books978-3-03921-342-9>.
- [255] S.M.H. Hojjatzadeh, N.D. Parab, W. Yan, Q. Guo, L. Xiong, C. Zhao, M. Qu, L.I. Escano, X. Xiao, K. Fezzaa, W. Everhart, T. Sun, L. Chen, Pore elimination mechanisms during 3D printing of metals, *Nat Commun* 10 (2019). <https://doi.org/10.1038/s41467-019-10973-9>.
- [256] H. Chen, D. Zhang, P. Chen, N. Li, A. Perrot, A Review of the Extruder System Design for Large-Scale Extrusion-Based 3D Concrete Printing, *Materials* 16 (2023). <https://doi.org/10.3390/ma16072661>.
- [257] Z. Liu, M. Zhang, B. Bhandari, C. Yang, Impact of rheological properties of mashed potatoes on 3D printing, *J Food Eng* 220 (2018) 76–82. <https://doi.org/10.1016/j.jfoodeng.2017.04.017>.
- [258] A.I. Portoacă, R.G. Ripeanu, A. Diniță, M. Tănase, Optimization of 3D Printing Parameters for Enhanced Surface Quality and Wear Resistance, *Polymers (Basel)* 15 (2023). <https://doi.org/10.3390/polym15163419>.
- [259] Z. Liu, M. Li, Y. Weng, T.N. Wong, M.J. Tan, Mixture Design Approach to optimize the rheological properties of the material used in 3D cementitious material printing, *Constr Build Mater* 198 (2019) 245–255. <https://doi.org/10.1016/j.conbuildmat.2018.11.252>.
- [260] F.D.C. Siacor, Q. Chen, J.Y. Zhao, L. Han, A.D. Valino, E.B. Taboada, E.B. Caldona, R.C. Advincula, On the additive manufacturing (3D printing) of viscoelastic materials and flow behavior: From composites to food manufacturing, *Addit Manuf* 45 (2021). <https://doi.org/10.1016/j.addma.2021.102043>.
- [261] R. O'Neill, H.O. McCarthy, E. Cunningham, E. Montufar, M.P. Ginebra, D.I. Wilson, A. Lennon, N. Dunne, Extent and mechanism of phase separation during the extrusion of calcium phosphate pastes, *J Mater Sci Mater Med* 27 (2016) 1–13. <https://doi.org/10.1007/s10856-015-5615-z>.
- [262] R.A. Basterfield, C.J. Lawrence, M.J. Adams, On the interpretation of orifice extrusion data for viscoplastic materials, *Chem Eng Sci* 60 (2005) 2599–2607. <https://doi.org/10.1016/j.ces.2004.12.019>.
- [263] S. Syahrullail, C.S.N. Azwadi, Y.M. Najib, The Influences of the Die Half Angle of Taper Die During Cold Extrusion Process, *Arab J Sci Eng* 38 (2013) 1201–1207. <https://doi.org/10.1007/s13369-012-0531-8>.

- [264] A.M.S. Zuan, S.Y. Yong, M.A. Nurul, S. Syahrullail, E.A. Rahim, The effects of the die half angle of taper die on plane strain extrusion, in: 2016. <https://doi.org/10.11113/JT.V78.9654>.
- [265] V. Nienhaus, K. Smith, D. Spiehl, E. Dörsam, Investigations on nozzle geometry in fused filament fabrication, *Addit Manuf* 28 (2019) 711–718. <https://doi.org/10.1016/j.addma.2019.06.019>.
- [266] H.A. Colorado, E.I.G. Velásquez, S.N. Monteiro, Sustainability of additive manufacturing: the circular economy of materials and environmental perspectives, *Journal of Materials Research and Technology* 9 (2020) 8221–8234. <https://doi.org/10.1016/j.jmrt.2020.04.062>.
- [267] A. Al Rashid, M. Koç, Additive manufacturing for sustainability and circular economy: needs, challenges, and opportunities for 3D printing of recycled polymeric waste, *Materials Today Sustainability* 24 (2023). <https://doi.org/10.1016/j.mtsust.2023.100529>.
- [268] B.D. Hettiarachchi, J.I. Sudusinghe, S. Seuring, M. Brandenburg, Challenges and Opportunities for Implementing Additive Manufacturing Supply Chains in Circular Economy, in: *IFAC-PapersOnLine*, Elsevier B.V., 2022: pp. 1153–1158. <https://doi.org/10.1016/j.ifacol.2022.09.545>.
- [269] J. Yeon, J. Kang, W. Yan, Spall damage repair using 3D printing technology, *Autom Constr* 89 (2018) 266–274. <https://doi.org/10.1016/j.autcon.2018.02.003>.
- [270] S. Tibbits, The emergence of “4D printing,” in: TED Conference, 2013. https://www.ted.com/talks/skylar_tibbits_the_emergence_of_4d_printing?language=en.
- [271] Z.X. Khoo, J.E.M. Teoh, Y. Liu, C.K. Chua, S. Yang, J. An, K.F. Leong, W.Y. Yeong, 3D printing of smart materials: A review on recent progresses in 4D printing, *Virtual Phys Prototyp* 10 (2015) 103–122. <https://doi.org/10.1080/17452759.2015.1097054>.
- [272] W. Zhou, Z. Qiao, E. Nazarzadeh Zare, J. Huang, X. Zheng, X. Sun, M. Shao, H. Wang, X. Wang, D. Chen, J. Zheng, S. Fang, Y.M. Li, X. Zhang, L. Yang, P. Makvandi, A. Wu, 4D-Printed Dynamic Materials in Biomedical Applications: Chemistry, Challenges, and Their Future Perspectives in the Clinical Sector, *J Med Chem* 63 (2020) 8003–8024. <https://doi.org/10.1021/acs.jmedchem.9b02115>.
- [273] J.J. Wu, L.M. Huang, Q. Zhao, T. Xie, 4D Printing: History and Recent Progress, *Chinese Journal of Polymer Science (English Edition)* 36 (2018) 563–575. <https://doi.org/10.1007/s10118-018-2089-8>.
- [274] A. Sydney Gladman, E.A. Matsumoto, R.G. Nuzzo, L. Mahadevan, J.A. Lewis, Biomimetic 4D printing, *Nat Mater* 15 (2016) 413–418. <https://doi.org/10.1038/nmat4544>.
- [275] R. Rael, V.S. Fratello, Clay bodies: Crafting the future with 3D printing, *Architectural Design* 87 (2017) 92–97. <https://doi.org/10.1002/ad.2243>.
- [276] A. Mitchell, U. Lafont, M. Hołyńska, C. Semprimoschnig, Additive manufacturing — A review of 4D printing and future applications, *Addit Manuf* 24 (2018) 606–626. <https://doi.org/10.1016/j.addma.2018.10.038>

- [277] K. McLellan, Y.C. Sun, H.E. Naguib, A review of 4D printing: Materials, structures, and designs towards the printing of biomedical wearable devices, *Bioprinting* 27 (2022).
<https://doi.org/10.1016/j.bprint.2022.e00217>.
- [278] M. Pytlos, M. Gilbert, C.C. Smith, Modelling granular soil behaviour using a physics engine, *Geotechnique Letters* 5 (2015) 243–249.
<https://doi.org/10.1680/jgele.15.00067>.
- [279] British Standards Institution, BS EN 13108-5:2016, Bituminous mixtures – Material specification, Part 5: Stone Mastic Asphalt., (2016).
<https://bsol.bsigroup.com/PdfViewer/Viewer?pid=000000000030278718>
- [280] British Standards Institution, Bituminous mixtures – Test methods, Part 35: Laboratory mixing (BS EN 12697-35:2016), (2016).
<https://bsol.bsigroup.com/PdfViewer/Viewer?pid=000000000030310362>
- [281] British Standards Institution, BS EN 12697-33:2019, Bituminous mixtures - Test methods - Part 33: Specimen prepared by roller compactor, (2019).
<https://bsol.bsigroup.com/PdfViewer/Viewer?pid=000000000030407454>
- [282] British Standards Institution, BS EN 1426:2024, Bitumens and bituminous binders, Determination of needle penetration, 2024.
<https://knowledge.bsigroup.com/products/bitumens-and-bituminous-binders-determination-of-needle-penetration?version=tracked>.
- [283] British Standards Institution, BS EN 1427:2015, Bitumen and bituminous binders, Determination of the softening point, Ring and Ball method, (2015). <https://knowledge.bsigroup.com/products/bitumen-and-bituminous-binders-determination-of-the-softening-point-ring-and-ball-method?version=tracked>.
- [284] British Standards Institution, BS EN 12595:2023, Bitumen and bituminous binders, Determination of kinematic viscosity, British Standards Institution, 2023.
<https://knowledge.bsigroup.com/products/bitumen-and-bituminous-binders-determination-of-kinematic-viscosity-2?version=tracked>.
- [285] British Standards Institution, BS EN 15326:2007+A:2009, Bitumen and bituminous binders, Measurement of density and specific gravity, Capillary-stopped pyknometer method, (2009).
<https://bsol.bsigroup.com/PdfViewer/Viewer?pid=000000000030189588>
- [286] Y. Xia, W. Xu, H. Zhang, X. Wu, H. Dai, 3D-printing polylactic acid/hydroxyapatite fracture internal fixation plates for bone repair, *J Appl Polym Sci* 139 (2022). <https://doi.org/10.1002/app.53147>.
- [287] L. Han, L. Shen, H. Lin, Z. Huang, Y. Xu, R. Li, B. Li, C. Chen, W. Yu, J. Teng, 3D printing titanium dioxide-acrylonitrile-butadiene-styrene (TiO₂-ABS) composite membrane for efficient oil/water separation, *Chemosphere* 315 (2023).
<https://doi.org/10.1016/j.chemosphere.2023.137791>.
- [288] A. du Plessis, W.P. Boshoff, A review of X-ray computed tomography of concrete and asphalt construction materials, *Constr Build Mater* 199 (2019) 637–651. <https://doi.org/10.1016/j.conbuildmat.2018.12.049>.

- [289] T. Bah, Inkscape Guide to a Vector Drawing Program - Fourth Edition (2011).
<https://ptgmedia.pearsoncmg.com/images/9780132764148/samplepages/0132764148.pdf>.
- [290] British Standard Institution, BS EN 13589:2018, Bitumen and bituminous binders. Determination of the tensile properties of modified bitumen by the force ductility method, British Standard Institution (2018). <https://knowledge.bsigroup.com/products/bitumen-and-bituminous-binders-determination-of-the-tensile-properties-of-modified-bitumen-by-the-force-ductility-method?version=standard&tab=preview>.
- [291] British Standards Institution, BS EN 12697-48:2021. Bituminous mixtures. Test methods - Interlayer Bonding, 2021.
<https://knowledge.bsigroup.com/products/bituminous-mixtures-test-methods-interlayer-bonding?version=standard>.
- [292] J.J. Shuster, Student t-tests for potentially abnormal data, Stat Med 28 (2009) 2170–2184. <https://doi.org/https://doi.org/10.1002/sim.3581>.
- [293] H. Arora, Statistics for Research with a guide to SPSS, Abhigyan (New Delhi) 31 (2013) 77. <https://www.semanticscholar.org/paper/Statistics-for-Research-with-a-Guide-to-SPSS-for-a-Argyrous/08a89db750441dd24802d08afaedb09556ef3df2>.
- [294] H.P. Gavin, The Levenberg-Marquardt algorithm for nonlinear least squares curve-fitting problems, in: 2019.
<https://api.semanticscholar.org/CorpusID:113404737>.
- [295] X.-S. Yang, Optimization Techniques and Applications with Examples., 1st ed., Newark : John Wiley & Sons, Incorporated, 2018.
<https://www.wiley.com/en-us/Optimization+Techniques+and+Applications+with+Examples-p-9781119490623>.
- [296] CRC Handbook of Chemistry and Physics, 2009–2010, 90th ed, J Am Chem Soc 131 (2009) 12862. <https://doi.org/10.1021/ja906434c>.
- [297] M.J. Martín-Alfonso, F.J. Martínez-Boza, F.J. Navarro, M. Fernández, C. Gallegos, Pressure-temperature-viscosity relationship for heavy petroleum fractions, Fuel 86 (2007) 227–233.
<https://doi.org/10.1016/j.fuel.2006.05.006>.
- [298] F.G. Hammitt, Cavitation and multiphase flow phenomena / Frederick G. Hammitt., New York : McGraw-Hill, New York, 1980.
https://books.google.co.uk/books/about/Cavitation_and_Multiphase_Flow_Phenomena.html?id=92AYAQAIAAJ&redir_esc=y.
- [299] I.S. Pearsall, Cavitation, 1974.
https://books.google.co.uk/books/about/Cavitation.html?id=e2UYAQAIAAJ&redir_esc=y.
- [300] M. Sarnowski, K.J. Kowalski, J.B. Król, P. Radziszewski, Influence of overheating phenomenon on bitumen and asphalt mixture properties, Materials 12 (2019). <https://doi.org/10.3390/ma12040610>.
- [301] British Standards Institution, BS EN 12697-35:2016, Bituminous mixtures - Test methods - Part 35: Laboratory mixing, (2020).
<https://bsol.bsigroup.com/PdfViewer/Viewer?pid=000000000030409670>

- [302] British Standards Institution, BS EN 1097-6:2022, Tests for mechanical and physical properties of aggregates. Determination of particle density and water absorption, 2022. <https://doi.org/10.3403/30392581>.
- [303] A. Garcia-Hernandez, L. Wan, S. Dopazo-Hilario, In-silico manufacturing of asphalt concrete, *Powder Technol* 386 (2021) 399–410. <https://doi.org/10.1016/j.powtec.2021.03.065>.
- [304] V.C. Sanchez, P. Weston, A. Yan, R.H. Hurt, A.B. Kane, A 3-dimensional in vitro model of epithelioid granulomas induced by high aspect ratio nanomaterials, *Part Fibre Toxicol* 8 (2011). <https://doi.org/10.1186/1743-8977-8-17>.
- [305] P.A. Sivanantham, G.G. Prabhu, G.G. Vimal Arokiaraj, K. Sunil, Effect of fibre aspect-ratio on the fresh and strength properties of steel fibre reinforced self-compacting concrete, *Advances in Materials Science and Engineering* 2022 (2022). <https://doi.org/10.1155/2022/1207273>.
- [306] L.H. Shu, F.J. Ni, J.W. Jiang, Z.L. Zhao, Z.Y. Guo, Calculation and characterization of air void in mortar of the Hot Mix Asphalt (HMA) based on CT Scanning and Image Analysis Methods, *Applied Sciences* (Switzerland) 13 (2023). <https://doi.org/10.3390/app13010652>.
- [307] E. Masad, V.K. Jandhyala, N. Dasgupta, N. Somadevan, N. Shashidhar, Characterization of Air Void Distribution in Asphalt Mixes using X-ray Computed Tomography, *Journal of Materials in Civil Engineering* 14 (2002) 122–129. <https://doi.org/10.1061/ASCE0899-1561200214:2122>.
- [308] N. Lebaal, F. Schmidt, S. Puissant, D. Schlaefli, D. Schläfli, Design of Optimal Extrusion Die for a Range of Different Materials, *Polym Eng Sci* 49 (2009) 432–440. <https://doi.org/10.1002/pen.21298i>.
- [309] O.P. Gbenebor, O.S.I. Fayomi, A.P.I. Popoola, A.O. Inegbenebor, F. Oyawale, Extrusion die geometry effects on the energy absorbing properties and deformation response of 6063-type Al-Mg-Si aluminum alloy, *Results Phys* 3 (2013) 1–6. <https://doi.org/10.1016/j.rinp.2013.01.002>.
- [310] Y.A. Çengel, Heat and mass transfer: a practical approach / Yunus A. Çengel., 3rd ed., Boston, Mass. : McGraw-Hill, Boston, Mass., 2007. <https://www.scribd.com/doc/64565428/cen29305-ch00-fm>.
- [311] S.D. Schaefer, J. Xu, D. Palin, A. Al-Tabbaa, F. Iida, Position-based fluid simulation for robotic injection sealing of pavement cracks, *J Field Robot* (2024). <https://doi.org/10.1002/rob.22339>.
- [312] F.K.A. Awuah, A. Garcia-Hernández, Machine-filling of cracks in asphalt concrete, *Autom Constr* 141 (2022). <https://doi.org/10.1016/j.autcon.2022.104463>.
- [313] G. Michalos, P. Karagiannis, S. Makris, Ö. Tokçalar, G. Chryssolouris, Augmented Reality (AR) Applications for Supporting Human-robot Interactive Cooperation, in: *Procedia CIRP*, Elsevier B.V., 2016: pp. 370–375. <https://doi.org/10.1016/j.procir.2015.12.005>.
- [314] I. Hafeez, M.A. Kamal, M.W. Mirza, Barkatullah, S. Bilal, Laboratory fatigue performance evaluation of different field laid asphalt mixtures,

Constr Build Mater 44 (2013) 792–797.
<https://doi.org/10.1016/j.conbuildmat.2013.03.083>.

- [315] Y.R. Kim, D. Ph, F. Asce, H.J. Park, D. Ph, Investigation of primary causes of fatigue cracking in asphalt pavement in North Carolina, (2015). <https://connect.ncdot.gov/projects/research/RNAProjDocs/2010-01FinalReport.pdf>.
- [316] Transportation Research Board, Relationship between laboratory cracking tests and field performance of asphalt mixtures, (2019). <https://onlinepubs.trb.org/onlinepubs/circulars/ec251.pdf>.

Appendices

Appendix A

Gradation and Characteristics of Aggregates Used in the Research

Table A-32: Gradation of aggregate fractions predominantly used in this research at NTEC.

Sieve size (mm)		10	8	6.3	4	2.8	2	1	0.5	0.25	0.125	0.063
L8	% Passing	100	64.48	20.64	1.85	1.21	1.15	1.14	1.13	1.12	1.1	1.07
L6		100	100	96.41	34.73	8.39	3.48	2.55	2.48	2.46	2.39	2.27
Dust		100	100	100	99.31	83.33	62.98	40.32	30.83	25.21	20.4	16.03
Filler		100	100	100	100	100	100	100	100	100	100	96.79

Table A-33: Geometric and Weibull characteristics of fractions of aggregates⁴⁷ at NTEC.

Mixture ID	Aggregate fractions	Min Feret ₅₀ (mm)	WSc ⁴⁸ Min Feret (mm)	WSh ⁴⁹ Min Feret	AR ₅₀	WSc AR	WSh AR	A ₅₀ (cm ²)	P ₅₀ (cm)	H	% mass < 2 mm
LD	Dust	3.17	3.66	5.21	0.69	0.73	6.70	0.12	1.31	0.74	62.98
L6	6 mm (passing 8.0 mm)	8.72	5.30	3.90	0.68	0.77	7.37	0.23	1.81	0.61	3.48
L8	8 mm (Passing 10mm)	10.81	8.61	4.17	0.75	0.75	6.54	0.69	3.21	0.61	1.15

⁴⁷ Same aggregates were used as Cat A aggregates in Table 5-16.

⁴⁸ WSc – Weibull Scale

⁴⁹ WSh – Weibull Shape

Table A-34: Geometric and Weibull characteristics of aggregate fractions provided by the Department of Road Structures, Czech Technical University, Prague.

Mixture ID	Aggregate fractions	Min Feret ₅₀ (mm)	WSc Min Feret (mm)	WSh Min Feret	AR ₅₀	WSc AR	WSh AR	A ₅₀ (cm ²)	P ₅₀ (cm)	H	% mass < 2 mm
S1	Coarse (> 4 mm)	13.63	17.14	2.17	0.76	0.77	7.53	2.10	5.78	0.61	
	Fines (4-2 mm)	3.34	3.67	8.78	0.75	0.78	14.47	0.11	1.26	0.64	19.0
S2	Coarse	8.66	9.50	3.12	0.66	0.73	7.29	0.83	3.50	0.75	
	Fines	2.84	3.28	4.92	0.73	0.77	8.38	0.08	1.12	0.74	22.1
S3	Coarse	3.34	3.67	8.78	0.75	0.78	14.47	0.11	1.26	0.64	
	Fines	2.84	3.28	4.92	0.73	0.77	8.38	0.08	1.12	0.74	21.1
S4	Coarse	12.48	12.78	2.37	0.73	1.38	6.12	0.98	3.20	0.58	
	Fines	3.10	3.47	7.81	0.73	0.74	8.22	0.11	1.27	0.61	21.1
S5	Coarse	11.84	12.62	2.43	0.76	1.12	7.46	0.93	3.46	0.63	
	Fines	4.10	4.07	10.50	0.65	0.75	5.44	0.16	1.47	0.58	19.5
S6	Coarse	7.69	9.70	2.82	0.74	0.81	11.47	0.51	2.72	0.69	
	Fines	3.45	3.48	13.60	0.68	0.71	9.76	0.13	1.35	0.74	21.2
S7	Coarse	8.21	10.70	2.28	0.82	1.06	7.22	0.64	2.82	0.83	
	Fines	3.81	4.06	6.95	0.65	0.74	6.45	0.15	1.53	0.62	19.8
S8	Coarse	13.00	12.55	2.61	0.69	1.34	5.90	1.04	3.29	0.94	
	Fines	3.81	3.90	4.78	0.75	0.75	8.94	0.14	1.47	0.47	21.0

Table A-34 (continued)

Mixture ID	Aggregate fractions	Min Feret ₅₀ (mm)	WSc Min Feret (mm)	WSh Min Feret	AR ₅₀	WSc AR	WSh AR	A ₅₀ (cm ²)	P ₅₀ (cm)	H	% mass < 2 mm
S9	Coarse	11.57	14.00	2.13	0.65	1.15	4.67	1.29	3.96	0.56	
	Fines	3.70	4.12	7.65	0.67	0.69	5.41	0.20	1.70	0.59	19.8
S10	Coarse	14.49	18.59	2.15	0.78	1.05	8.21	1.99	4.77	0.40	
	Fines	3.96	3.97	14.72	0.72	0.72	5.71	0.17	1.54	0.58	22.3
S11	Coarse	11.61	14.71	2.10	0.65	1.23	5.08	1.02	3.47	0.82	
	Fines	3.80	3.76	5.13	0.70	0.72	9.78	0.15	1.57	0.53	20.9
S12	Coarse	10.49	12.39	2.40	0.86	1.25	10.63	0.61	2.72	0.88	
	Fines	3.80	3.76	5.13	0.70	0.72	9.78	0.15	1.57	0.53	20.0
S13	Coarse	8.88	9.38	3.32	0.68	0.73	11.60	0.76	3.42	0.83	
	Fines	3.16	3.50	5.31	0.74	0.77	5.66	0.11	1.21	0.57	23.0
S14	Coarse	9.56	10.76	3.38	0.78	0.79	23.05	0.96	3.84	0.60	
	Fines	3.50	3.87	4.96	0.59	0.67	6.87	0.14	1.47	0.59	22.7
S15	Coarse	12.84	15.21	2.39	0.73	1.40	8.47	1.00	3.51	0.58	
	Fines	3.25	3.73	5.25	0.73	0.77	10.46	0.11	1.20	0.56	19.5
S16	Coarse	17.10	19.94	3.01	0.76	1.26	8.07	2.01	4.86	0.43	
	Fines	3.86	4.01	6.66	0.71	0.74	11.22	0.17	1.54	0.41	23.6

Table A-35: Characteristics of aggregates for mixtures (Cat A) used in developing the digital design model in Chapter 5. The gradations are also graphically shown in Figure 5-94.

Mixture ID	Type of rock	Average density (Mg/m ³)	Water absorption (%)	Gradation													
				Sieve size (mm)	14	12.5	10	8	6.3	4	2.8	2	1	0.5	0.25	0.125	0.063
M1	L*	2.70	0.6	% passing	100.0	100.0	100.0	95.0	86.7	46.3	27.0	19.9	14.8	12.8	11.7	10.7	9.6
M2	L	2.70	0.6		100.0	100.0	100.0	90.1	75.8	37.2	20.7	15.4	11.9	10.7	9.9	9.2	8.4
M3	L	2.70	0.6		100.0	100.0	100.0	97.2	92.1	64.4	46.1	34.9	24.3	20.0	17.5	15.3	13.1
M4	L	2.70	0.6		100.0	100.0	100.0	71.6	36.2	14.9	11.0	9.4	8.2	7.7	7.4	7.1	6.7
M5	L	2.70	0.6		100.0	100.0	100.0	73.4	40.5	26.2	21.7	16.6	10.9	8.6	7.1	5.9	4.8
M6	L	2.70	0.6		100.0	100.0	100.0	82.2	60.3	50.6	42.3	32.1	20.7	16.0	13.2	10.8	8.5
M7	L	2.70	0.6		100.0	100.0	100.0	92.9	83.1	60.6	48.6	42.0	36.1	33.7	32.3	31.0	29.1
M8	L	2.70	0.6		100.0	100.0	100.0	95.7	88.7	55.3	36.5	26.9	18.5	15.2	13.2	11.5	9.8
M9	L	2.70	0.6		100.0	100.0	100.0	87.6	71.5	52.8	40.2	29.9	19.4	15.0	12.4	10.2	8.2
M10	L	2.70	0.6		100.0	100.0	100.0	73.4	40.2	21.0	15.7	11.8	7.9	6.3	5.3	4.5	3.7
M11	L	2.70	0.6		100.0	100.0	100.0	67.7	27.8	10.6	8.6	6.7	4.7	3.8	3.3	2.8	2.4
M12	L	2.70	0.6		100.0	100.0	100.0	75.8	45.8	28.6	23.4	19.4	15.2	13.5	12.5	11.6	10.5
M13	L	2.70	0.6		100.0	100.0	100.0	80.1	55.6	44.8	38.3	30.6	22.0	18.3	16.2	14.4	12.5
M14	L	2.70	0.6		100.0	100.0	100.0	100.0	96.9	44.4	19.6	12.4	8.2	6.7	5.9	5.1	4.3

Table A-35 (continued)

Mixture ID	Type of rock	Average density (Mg/m³)	Water absorption (%)	Gradation													
				Sieve size (mm)	14	12.5	10	8	6.3	4	2.8	2	1	0.5	0.25	0.125	0.063
M15	L	2.70	0.6	% passing	100.0	100.0	100.0	78.7	51.8	29.9	22.2	17.6	13.4	11.6	10.6	9.7	8.8
M16	L	2.70	0.6		100.0	100.0	100.0	78.7	51.5	24.7	15.8	12.1	9.2	8.0	7.3	6.7	6.0
M17	L	2.70	0.6		100.0	100.0	100.0	80.5	55.6	31.6	23.0	18.8	15.2	13.8	12.9	12.2	11.2
M18	L	2.70	0.6		100.0	100.0	100.0	76.2	46.1	21.1	14.2	11.5	9.5	8.7	8.3	7.8	7.3
M19	L	2.70	0.6		100.0	100.0	100.0	79.5	53.7	33.5	25.5	19.9	14.5	12.2	10.9	9.7	8.5
M20	L	2.70	0.6		100.0	100.0	100.0	77.6	49.7	32.8	27.1	22.6	18.0	16.1	14.9	14.0	12.8
M21	L	2.70	0.6		100.0	100.0	100.0	73.4	40.2	21.7	16.5	12.4	8.3	6.6	5.6	4.7	3.8
M22	L	2.70	0.6		100.0	100.0	100.0	78.3	51.1	30.2	22.7	17.8	13.1	11.2	10.1	9.1	8.1
M23	L	2.70	0.6		100.0	100.0	100.0	78.5	51.3	27.5	19.5	15.5	12.0	10.7	9.8	9.1	8.3
M24	L	2.70	0.6		100.0	100.0	100.0	96.4	90.2	56.0	36.1	25.9	16.8	13.1	11.0	9.1	7.4
M25	L	2.70	0.6		100.0	100.0	100.0	97.2	91.8	58.6	38.5	27.7	17.9	14.0	11.7	9.7	7.8
SMA UL	L	2.70	0.6		100.0	100.0	100.0	100.0	98.6	73.5	53.4	39.2	25.2	19.5	16.1	13.2	10.5
SMA LL	L	2.70	0.6		100.0	100.0	100.0	90.0	75.9	38.7	21.7	15.0	9.9	7.9	6.7	5.7	4.7

*L is limestone.

Table A-36: Characteristics of aggregates for Cat B mixtures used in validating the digital design model in Chapter 5. The gradations are also graphically shown in Figure 5-95.

Mixture ID	Type of rock*	Average density (Mg/m ³)	Water absorption (%)	Gradation													
				Sieve size (mm)	31.5	22.4	16	11.2	8	5.6	4	2	1	0.5	0.25	0.125	0.063
S1	H	2.77	0.2	% passing	100.0	96.5	83.4	64.8	54.3	45.3	36.3	22.4	15.8	13.0	11.4	10.3	8.6
S2	U	2.70	0.5		100.0	100.0	100.0	93.5	75.4	57.9	45.8	32.3	23.3	17.2	12.4	8.7	6.8
S3	B	2.97	0.3		100.0	97.3	81.9	70.4	61.7	51.3	45.7	33.6	23.9	18.3	14.7	12.6	10.5
S4	G	2.76	0.3		100.0	100.0	97.0	77.0	58.0	45.0	36.0	27.0	21.0	16.0	11.0	9.0	8.2
S5	D	2.68	0.2		100.0	100.0	65.8	36.9	32.3	26.6	23.1	19.5	16.4	13.8	11.2	8.9	7.2
S6	W	2.66	0.7		100.0	100.0	100.0	96.4	72.7	57.0	48.7	33.8	24.5	19.1	14.8	10.8	8.0
S7	G	2.84	0.3		100.0	100.0	89.8	72.1	63.1	53.3	45.0	28.6	21.9	17.7	13.8	10.0	7.5
S8	U	2.87	0.2		100.0	100.0	77.4	65.1	57.5	48.4	41.1	29.5	21.1	16.2	12.9	10.7	8.8
S9	H	2.77	0.1		100.0	100.0	97.8	82.9	75.6	66.0	54.7	33.2	22.6	18.0	15.3	13.3	10.5
S10	G	2.66	0.7		100.0	100.0	100.0	98.2	78.5	65.8	58.9	38.7	25.2	18.1	13.6	10.8	8.5
S11	L	2.25	0.8		100.0	100.0	80.3	60.2	52.2	45.5	39.6	29.1	21.0	16.2	13.1	10.9	9.1
S12	D	2.95	0.4		100.0	100.0	81.8	62.3	55.1	46.5	38.3	23.9	18.1	14.3	11.0	7.9	5.9

* Aggregates sourced from various quarries in the Czech Republic, including Belice, Zbraslav, Chornice, Chvaletice, and Zarubka quarries. Aggregates included limestone (L), hornblende (H), basalt (B), granite (G), granodiorite (D), greywacke (W), and some undisclosed (U) aggregates.

Table A-36 (continued)

Mixture ID	Type of rock	Average density (Mg/m³)	Water absorption (%)	Gradation													
				Sieve size (mm)	31.5	22.4	16	11.2	8	5.6	4	2	1	0.5	0.25	0.125	0.063
S13	U	2.69	0.7		100.0	100.0	100.0	92.3	73.6	55.5	49.4	33.2	23.5	16.9	11.5	6.5	3.1
S14	G	2.68	0.5		100.0	100.0	100.0	89.5	56.5	38.9	34.9	24.7	17.0	12.1	9.1	6.6	4.3
S15	B	2.94	0.4		100.0	100.0	97.1	81.6	67.8	60.9	55.2	33.2	24.2	20.3	17.0	12.5	7.6
S16	B	2.97	0.7		100.0	100.0	96.6	75.3	62.0	48.2	38.0	31.1	20.8	14.9	11.2	8.9	7.3

Table A-37: Characteristics of aggregates for mixtures used in developing the digital design model in Chapter 6. The gradations are also graphically shown in Figure 6-112.

Mixture ID	Type of rock	Average density (Mg/m ³)	Water absorption (%)	Gradation													
				Sieve size (mm)	14	12.5	10	8	6.3	4	2.8	2	1	0.5	0.25	0.125	0.063
P1	L	2.70	0.6	% passing	100.0	100.0	100.0	95.0	86.7	46.3	27.0	19.9	14.8	12.8	11.7	10.7	9.6
P2	L	2.70	0.6		100.0	100.0	100.0	90.1	75.8	37.2	20.7	15.4	11.9	10.7	9.9	9.2	8.4
P3	L	2.70	0.6		100.0	100.0	100.0	97.2	92.1	64.4	46.1	34.9	24.3	20.0	17.5	15.3	13.1
P4	L	2.70	0.6		100.0	100.0	100.0	71.6	36.2	14.9	11.0	9.4	8.2	7.7	7.4	7.1	6.7
P5	L	2.70	0.6		100.0	100.0	100.0	73.4	40.5	26.2	21.7	16.6	10.9	8.6	7.1	5.9	4.8
P6	L	2.70	0.6		100.0	100.0	100.0	82.2	60.3	50.6	42.3	32.1	20.7	16.0	13.2	10.8	8.5
P7	L	2.70	0.6		100.0	100.0	100.0	92.9	83.1	60.6	48.6	42.0	36.1	33.7	32.3	31.0	29.1
P8	L	2.70	0.6		100.0	100.0	100.0	95.7	88.7	55.3	36.5	26.9	18.5	15.2	13.2	11.5	9.8
P9	L	2.70	0.6		100.0	100.0	100.0	87.6	71.5	52.8	40.2	29.9	19.4	15.0	12.4	10.2	8.2
P10	L	2.70	0.6		100.0	100.0	100.0	73.4	40.2	21.0	15.7	11.8	7.9	6.3	5.3	4.5	3.7
P11	L	2.70	0.6		100.0	100.0	100.0	67.7	27.8	10.6	8.6	6.7	4.7	3.8	3.3	2.8	2.4
P12	L	2.70	0.6		100.0	100.0	100.0	75.8	45.8	28.6	23.4	19.4	15.2	13.5	12.5	11.6	10.5
P13	L	2.70	0.6		100.0	100.0	100.0	80.1	55.6	44.8	38.3	30.6	22.0	18.3	16.2	14.4	12.5
P14	L	2.70	0.6		100.0	100.0	100.0	100.0	96.9	44.4	19.6	12.4	8.2	6.7	5.9	5.1	4.3
P15	L	2.70	0.6		100.0	100.0	100.0	78.7	51.8	29.9	22.2	17.6	13.4	11.6	10.6	9.7	8.8

Table A-37 (continued)

Mixture ID	Type of rock	Average density (Mg/m³)	Water absorption (%)	Gradation													
				Sieve size (mm)	14	12.5	10	8	6.3	4	2.8	2	1	0.5	0.25	0.125	0.063
P16	L	2.70	0.6	% passing	100.0	100.0	100.0	78.7	51.5	24.7	15.8	12.1	9.2	8.0	7.3	6.7	6.0
P17	L	2.70	0.6		100.0	100.0	100.0	80.5	55.6	31.6	23.0	18.8	15.2	13.8	12.9	12.2	11.2
P18	L	2.70	0.6		100.0	100.0	100.0	76.2	46.1	21.1	14.2	11.5	9.5	8.7	8.3	7.8	7.3
P19	L	2.70	0.6		100.0	100.0	100.0	79.5	53.7	33.5	25.5	19.9	14.5	12.2	10.9	9.7	8.5
P20	L	2.70	0.6		100.0	100.0	100.0	77.6	49.7	32.8	27.1	22.6	18.0	16.1	14.9	14.0	12.8
P21	L	2.70	0.6		100.0	100.0	100.0	73.4	40.2	21.7	16.5	12.4	8.3	6.6	5.6	4.7	3.8
P22	L	2.70	0.6		100.0	100.0	100.0	78.3	51.1	30.2	22.7	17.8	13.1	11.2	10.1	9.1	8.1
P23	L	2.70	0.6		100.0	100.0	100.0	78.5	51.3	27.5	19.5	15.5	12.0	10.7	9.8	9.1	8.3
P24	L	2.70	0.6		100.0	100.0	100.0	96.4	90.2	56.0	36.1	25.9	16.8	13.1	11.0	9.1	7.4
P25	L	2.70	0.6		100.0	100.0	100.0	97.2	91.8	58.6	38.5	27.7	17.9	14.0	11.7	9.7	7.8
P26	L	2.70	0.6		100.0	100.0	100	96.8	91	57.6	37.7	27.1	17.5	13.7	11.4	9.5	7.7
P27	L	2.70	0.6		100.0	100.0	100	96.1	89.3	53.1	33.4	24.2	16.4	13.4	11.5	10	8.4
P28	L	2.70	0.6		100.0	100.0	100	97	91.3	56.2	36.5	26.9	18.7	15.4	13.5	11.8	10.2
P29	L	2.70	0.6		100.0	100.0	100	94.3	85.7	55.3	37.2	26.9	17.4	13.6	11.3	9.4	7.6
P30	L	2.70	0.6		100.0	100.0	100	93.6	84.3	55.9	38.8	28.6	19.1	15.2	12.9	10.9	9

Table A-37 (continued)

Mixture ID	Type of rock	Average density (Mg/m³)	Water absorption (%)	Gradation													
				Sieve size (mm)	14	12.5	10	8	6.3	4	2.8	2	1	0.5	0.25	0.125	0.063
P31	L	2.70	0.6		100.0	100.0	100	93.3	83.1	47.6	29.9	22.3	16.1	13.7	12.3	11	9.7
P32	L	2.70	0.6		100.0	100.0	100	95.7	88.3	48.9	29	21	14.7	12.3	10.9	9.7	8.4
P33	L	2.70	0.6		100.0	100.0	100	94.5	85.8	50	31.1	22.4	15.1	12.2	10.5	9.1	7.6
P34	L	2.70	0.6		100.0	100.0	100	93.2	83.1	51.6	34.3	25.4	17.5	14.3	12.4	10.8	9.2

Table A-38: Comparing physics engine output to output from model equations developed in Chapter 5.

Mixture ID	Mastic (cm ³)			Number of Aggregates		
	Eqn. (5-14) output (a)	Nomograph output (b)	Estimability of Eqn. (5-14), % (a/b * 100)	Eqn. (5-15) output (c)	Nomograph output (d)	Estimability of Eqn. (5-15), % (c/d * 100)
V1	35.91	35.91	100.0	1348	1348	100.0
V2	33.36	33.36	100.0	1317	1295	101.7
V3	35.74	35.74	100.0	1318	1316	100.1
V4	35.76	35.78	100.0	1264	1251	101.0
V5	37.26	37.26	100.0	1214	1196	101.5
V6	31.64	31.64	100.0	1203	1202	100.1
V7	30.51	30.52	100.0	1311	1303	100.6
V8	31.79	31.80	100.0	1277	1285	99.4
V9	34.40	34.40	100.0	1203	1206	99.7
Average			100.0	100.5		

Table A-39: Properties of asphalt mixtures for the development of a model to select filling mixtures.

Mixture ID	Bitumen type	Compaction temperature (°C)	No. of blows	BC (%)	AVC (%)	Max. density (Mg/m ³)
P1	PG 40/60	150.0	2 x 50	6.0	5.4	2.477
P2	PG 40/60	150.0	2 x 50	6.0	6.3	2.483
P3	PG 40/60	150.0	2 x 50	6.0	7.8	2.473
P4	PG 40/60	150.0	2 x 50	6.0	22.9	2.505
P5	PG 40/60	150.0	2 x 50	5.0	16.0	2.533
P6	PG 40/60	150.0	2 x 50	6.0	10.5	2.488
P7	PG 40/60	150.0	2 x 50	8.0	3.4	2.419
P8	PG 40/60	150.0	2 x 50	6.0	3.5	2.475
P9	PG 40/60	150.0	2 x 50	5.5	2.4	2.499
P10	PG 40/60	150.0	2 x 50	5.5	22.2	2.518
P11	PG 40/60	150.0	2 x 50	4.5	29.3	2.56
P12	PG 40/60	150.0	2 x 50	5.5	12.4	2.516
P13	PG 40/60	150.0	2 x 50	6.0	5.9	2.56
P14	PG 40/60	150.0	2 x 50	5.2	5.2	2.498
P15	PG 40/60	150.0	2 x 50	6.0	16.7	2.496
P16	PG 40/60	150.0	2 x 50	5.5	15.6	2.513
P17	PG 40/60	150.0	2 x 50	6.6	10.4	2.474
P18	PG 40/60	150.0	2 x 50	5.4	15.3	2.511
P19	PG 40/60	150.0	2 x 50	5.5	9.1	2.481
P20	PG 40/60	150.0	2 x 50	6.5	8.3	2.473
P21	PG 40/60	150.0	2 x 50	4.0	20.4	2.513
P22	PG 40/60	150.0	2 x 50	5.5	13.3	2.513
P23	PG 40/60	150.0	2 x 50	5.4	15.6	2.516
P24	PG 40/60	150.0	2 x 50	5.0	3.7	2.477
P25	PG 40/60	150.0	2 x 50	5.0	3.4	2.472
P26	PG 40/60	150.0	2 x 50	5.0	3.6	2.477
P27	PG 40/60	150.0	2 x 50	5.0	4.7	2.472
P28	PG 40/60	150.0	2 x 50	5.0	4.1	2.522
P29	PG 40/60	150.0	2 x 50	5.0	4.5	2.519
P30	PG 40/60	150.0	2 x 50	5.0	4.8	2.562

Table A-39 (continued)

Mixture ID	Bitumen type	Compaction temperature (°C)	No. of blows	BC (%)	AVC (%)	Max. density (Mg/m ³)
P31	PG 40/60	150.0	2 x 50	5.0	6.3	2.489
P32	PG 40/60	150.0	2 x 50	5.0	5.6	2.502
P33	PG 40/60	150.0	2 x 50	5.0	5.5	2.513
P34	PG 40/60	150.0	2 x 50	5.0	5.6	2.516
Slab	PG 40/60	150.0	Roller	5.5	4.0	2.492

Table A-40: Simulated and experimental characteristics of asphalt mixtures for digitally designing the pothole-filling mixtures.

Mixture ID	MV (cm ³)	NA	E (cm ³ /s)	S (kN)	F (mm)
M1	31.8	1268	85.5	7.7	1.7
M2	27.8	1129	101.1	6.8	1.4
M3	44.9	1283	57.9	11.7	7.1
M4	22.6	522	160.6	7.1	1.2
M5	26.7	655	90.7	8.3	1.8
M6	42.4	874	64.3	10.9	5.8
M7	55.1	869	48.9	14.5	9.3
M8	37.9	1272	70.9	10.1	3.0
M9	39.5	1087	71.1	9.1	4.0
M10	23.6	664	144.8	7.7	1.8
M11	17.3	510	213.8	6.6	1.0
M12	30.2	614	79.2	9.3	1.8
M13	41.1	750	82.4	9.2	3.2
M14	23.4	1537	141.1	7.5	1.4
M15	23.8	722	153.7	8.6	1.5
M16	23.8	802	162.7	7.6	1.4
M17	32.2	753	97.2	9.1	2.1
M18	27.0	681	103.7	8.0	1.1
M19	30.7	775	96.4	9.7	1.7
M20	35.2	647	69.2	8.5	3.4
M21	20.7	710	152.6	7.7	1.2
M22	28.8	693	87.5	7.4	2.0
M23	26.6	676	85.1	7.5	1.7
M24	34.8	1342	67.0	10.2	3.0
M25	36.5	1357	63.0	10.5	3.5
M26	35.91	1348	13.1	10.2	3.3
M27	33.36	1295	11.2	9.7	3.1
M28	35.74	1316	13.3	9.9	3.6
M29	35.78	1251	13.5	10.1	3.6
M30	37.26	1196	13.6	10.4	3.6
M31	31.64	1202	9.2	9.8	2.6
M32	30.52	1303	10.4	9.6	2.4
M33	31.80	1285	11.2	9.8	2.4
M34	34.40	1206	12.5	10.6	3.1

Appendix B
Pavement Distresses

Table B-41: Cracking types associated with flexible pavements [153,180,181,316–318].







Crack type	Crack description	Possible causes	Possible remedy	Image
Fatigue cracking	Series of connected cracks that resembles the skin of an alligator	<ul style="list-style-type: none"> Repeated traffic loading causing failure of surface or base layer. Poor drainage Aging of bitumen and temperature. 	<ul style="list-style-type: none"> Small – remove crack and patch. Large -fix drainage and reconstruct. 	
Transverse cracking	<ul style="list-style-type: none"> Almost perpendicular to the centreline of the carriageway Regularly spaced Not load related 	<ul style="list-style-type: none"> Hydraulically bound base Asphalt shrinkage due to climatic conditions 	<ul style="list-style-type: none"> Crack sealing Overlay 	
Longitudinal cracking	Runs parallel to the centreline along wheel patch	<ul style="list-style-type: none"> Mainly caused by traffic loading. Crack in middle of carriageway may be due to poor construction or utility line. 	<ul style="list-style-type: none"> Reseal Rehabilitate pavement 	
Reflective cracking	Crack in top layer (usually in an overlay) propagated from the bottom layers (usually old layers). That is, crack beneath reappear in top layer	Weak or cracked foundation layers	<ul style="list-style-type: none"> Properly seal cracks and overlay Use polymer grids beneath overlay to slow crack propagation 	

Table B-41 (continued)

Crack type	Crack description	Possible causes	Possible remedy	Image
Slippage cracking	<ul style="list-style-type: none"> Half-moon shaped cracks facing oncoming vehicles 	<ul style="list-style-type: none"> Poor surface course-binder course bonding Horizontal traffic forces Water and dirt between interlayers deficient asphalt mix 	<ul style="list-style-type: none"> Remove slipped area, tact coat binder course surface and relay surface course. 	
Block cracking	Interconnected giant rectangular shaped cracks	<ul style="list-style-type: none"> Extreme asphalt temperature. Poor compaction during construction Not traffic related 	<ul style="list-style-type: none"> Small blocks - seal Severe blocks - overlay 	
Edge cracking	Similar to longitudinal crack in appearance but starts on the side of the road and then spread toward the centre over time	<ul style="list-style-type: none"> Lack of support at shoulder from weak material or moisture 	<ul style="list-style-type: none"> Low severity – fill cracks Severe - remove and patch 	